Late Quaternary glacier-climate reconstructions from the Southern Alps, New Zealand

Levan Tielidze

A thesis
submitted to the Victoria University of Wellington
in partial fulfilment of the requirements for the
degree of Doctor of Philosophy

Te Herenga Waka – Victoria University of Wellington
Te Puna Pātiotio – Antarctic Research Centre
Te Kura Tātai Aro Whenua – School of Geography, Environment and Earth Sciences
2022

To my parents

ვუძღვნი ჩემს მშობლებს

Thank you for your dedication and for everything you both have done for me.

გმადლობთ თქვენი თავდადებისთვის და ყველაფრისთვის,

რაც თქვენ ორივემ ჩემთვის გააკეთეთ.

ABSTRACT

One of the outstanding problems in modern geoscience is identifying the cause of past climate changes, particularly the drivers of rapid climate change during Quaternary glacial cycles. Changes in the physical geography of Earth's surface during the Late Quaternary are mainly dependent on glacial dynamics – periods of rapid warming produced significant amounts of meltwater that reshaped the landscape, changed global sea-level and influenced climate. Identifying the timing of key climate transitions during past warming episodes, such as the last glacial termination, may help to understand the future evolution of Earth's climate system (e.g. Denton et al., 2021).

In this thesis, using geomorphological mapping and sixty-six cosmogenic ^{10}Be surface exposure ages obtained from ice sculpted bedrock surfaces and deposited moraine landforms, I constrain the local Last Glacial Maximum and subsequent timing of last glacial termination in the Ahuriri River valley, Southern Alps, New Zealand (44°15′S, 169°36′E). Using the maximum elevation of lateral moraine (MELM) and accumulation area ratio (AAR) methods, along with application of a temperature lapse rate, I estimate the equilibrium-line altitude (ELA) and associated temperatures from the same periods. The largest glacial event in the Ahuriri River valley occurred at 19.8±0.3 ka when the former Ahuriri Glacier reached its maximum extent, which coincides with the global Last Glacial Maximum. By 16.7±0.3 ka, ice had retreated ~18 km up-valley from the LGM position and deglaciation was accompanied by the formation of a shallow proglacial lake. Surface exposure ages from moraines situated in a tributary of the upper Ahuriri River valley indicate that a subsequent advance of the palaeo glacier culminated at 14.5±0.3 ka, while the next readvance or still stand occurred at 13.6±0.3 ka. About 1000 yr later (12.6±0.2 ka), the former glacier built another prominent terminal moraine ridge in the lower section of the upper right tributary valley.

Reconstructions of past glacier geometries indicate that the local ELA was depressed by ~880 m and climate was 5±1 °C colder than present (1981–2010) at 19.8±0.3 ka, while ELA was depressed by ~770 m and climate was 4.4±0.9 °C colder at 16.7±0.3 ka. Subsequent estimations suggest ELA elevations at 14.5±0.3 ka, 13.6±0.3 ka, and 12.6±0.2 ka were ≤700 m, ≤630 m, and ~360 m lower than today. This equates to air temperatures of ≤3.9 °C, ≤3.5 °C, and 2.3±0.7 °C colder than today, assuming no changes in past precipitation.

The results reported here provide the first dataset of Late Quaternary glacial maximum extent and deglaciation along with quantitative paleoclimate reconstructions from the Ahuriri River

valley, Southern Alps, New Zealand. The small amount of warming estimated in this study between 19.8±0.3 and 16.7±0.3 ka differs somewhat from glacial reconstructions in other major valleys in the Southern Alps, specifically from Rakaia River valley (e.g. Putnam et al., 2013a) where a much larger amount of warming may have occurred during the same time. Robust constraints of glacier changes in the Ahuriri valley between 14.5±0.3 and 12.6±0.2 ka confirm that an early glacier readvance occurred in New Zealand at this time, which has been previously recognised with only limited evidence (e.g. Kaplan et al., 2010; Putnam et al., 2010a). The reconstructed ELA suggests that the coldest part of the Late Glacial reversal occurred at 14.5±0.3 ka.

The new constraints from glacial records in the Ahuriri River valley presented in this study offer the opportunity to test hypotheses about the climate system, to better understand the processes that drove ice retreat and readvance during the Last Glacial Maximum and subsequent termination.

ACKNOWLEDGEMENTS

Working on this thesis for the last three and a half years was only possible because of being supported by my wonderful supervisors Shaun Eaves and Kevin Norton from Victoria University of Wellington, and Andrew Mackintosh from Monash University. Shaun, I feel very privileged for being your PhD student. You are a brilliant supervisor and a massive thank you for your fruitful, helpful, and intense discussions, and suggestions during this time. Thank you for making the prospect of writing this thesis and for always being with me during the Ahuriri field campaigns. Thank you also for your support not only in working on the thesis but also in involving me in other interesting projects and field trips in the Southern Alps of New Zealand. Kevin, thank you for spending hours teaching me laboratory data processing and sample analysis. Without your guidance, I don’t think my laboratory work would have been possible. Andrew, thank you for giving me this opportunity to earn my PhD at the Antarctic Research Centre. I have always been feeling your support during my study. I also appreciate the time I have spent with your family and how it helped me feel at home both in Wellington and Melbourne. Last but not least, thank you for thinking about my further career development. Looking forward to joining a wonderful community at Monash Earth, Atmosphere and Environment.

I want to thank Jane Chewings for her help in the laboratories at School of Geography, Environment and Earth Sciences (SGEES), Victoria University of Wellington. Discussions with, and various help or support from staff and students in the Antarctic Research Centre and SGEES – Brian Anderson, Claire Lukens, Luisa Ashworth, Ross Whitmore, Emily Moore, Lisa Dowling, Dina Fieman, Jamey Stutz, Warren Dickinson, Lauren Vargo, Arran Whiteford, Rob McKay, Michelle Dow, Dao Polsiri, Pasan Herath, Hamish Hirschberg, Mario Krapp, Jürgen Österle, Kosta Tashkoff, Frans Gerber, and Aleksandr Beliaev have been very helpful.

I would like to thank my examiners Dr Cliff Atkins from SGEES, Dr Andrew Lorrey from the National Institute of Water and Atmospheric Research (NIWA), and Dr Margaret Jackson from the Trinity College Dublin for the careful reading of my thesis, constructive review, and useful sugesstions.

I am grateful to Jamie Howarth and Huw Horgan for reviewing and useful suggestions on my proposal at an early stage of my study. I would also like to thank Paul Mayewski and Andrei Kurbatov from University of Maine, and Roger Wheate from University of Northern British Columbia for being my references for the Victoria Doctor Scholarship.

Special thanks to Dee Ninis-Mackintosh for her endless help and for thinking of me and my family from almost the first day of my study. All your support and attempt in making my children's lives more fun in a foreign country is very much appreciated. Many thanks to Ruzika (Ruschle) Dadic, for her warm attitude and helpful suggestions, and for always being attentive and trying to help me and my family.

I would like to thank my landlord Robbie Schneider, his brilliant mother – Jenny Schneider, and his wonderful family for their honest support and help with many aspects, especially during the challenging times over the last few years. I gratefully acknowledge all the sincere effort and care from my Georgian friends Marina Alexander-Despotashvili and Nugzar Nachkebia making my life easier far away from home. Thank you also for hosting in Hawke's Bay where we had a really good time.

Thank you to all my Wellingtonian friends for supporting and encouraging me over the last few years. I want to specifically thank Jennifer O'Donoghue for her endless help, and for always being there for my family. Jennifer, your enviable sense of humor has always made life easier even in difficult times. I still hope that one day you will win millions and decide to visit us again. I also thank Anneta and Mikhail Visotskiy, Michael and Francesca Black, Keti and Milena Saginashvili, and Giorgi Tavkelishvili for their help, support and hospitality during our stay in Wellington.

Special thanks to my beautiful wife Tamar Bragvadze for her patience, understanding, unconditional support, and love. Tamar, I could not have done this without you and thank you for always being with me in this adventure. I also thank our children, Ioane and Andria, for always giving me the motivation and energy to never give up.

Finally, I thank my parents for giving me my love of science. Mom, I can't thank you enough for everything you have done for me. Forgive me that I left you alone... Dad, you would have been proud of me!

The primary source of funding for this research came from Victoria University of Wellington's Doctoral Scholarship and the Royal Society of New Zealand (Marsden Fund – E3230). Additional funding was provided by the Antarctic Research Centre Eggers Fund scholarship. All sample analyses have been carried out at Lawrence Livermore National Laboratory (LLNL) Center for Accelerator Mass Spectrometry (CAMS) by Alan Hidy.

TABLE OF CONTENTS

LIST OF FIGURES

LIST OF TABLES

Supplement

CHAPTER 1: INTRODUCTION

1.1 Overview

Earth's climate system is currently undergoing rapid change that is unprecedented in human history (IPCC, 2019). Some climate proxy records have indicated that the system can change rapidly over a variety of timescales (e.g. abrupt (year-decade) to multi-millennial (e.g. glacial cycles) (Hays et al., 1976; Dansgaard et al., 1984; Denton et al., 2010), but we do not fully understand why these changes occurred. Understanding such changes helps constrain sensitivities and tipping points in the climate system.

Past climate variations are a natural part of the earth system (Bentley, 2010) and therefore paleoclimate studies are playing an increasingly important role in understanding current and future climate change (Tierney et al., 2020). Anthropogenic activities increase the concentration of carbon dioxide (CO_2) in the atmosphere and is one of the key factors in climate change (IPCC, 2019). Throughout the Quaternary Period (last 2.6 million years) the Earth's climate has oscillated many times (Lisiecki and Raymo, 2005), although CO_2 levels (which have mirrored temperature variations) never have been higher at any point than now (Yan et al., 2019). Climate models predict that global warming will exceed the warmest temperatures of the Holocene by 2100, regardless of which greenhouse gas emission scenario is followed (Marcott et al., 2014; Kaufman et al., 2020). In this context, reconstructing past climate changes can provide a window into future climate changes (Burke et al., 2018). Geological records are useful observational sources of information on how the climate system operated in a past state much different than the present (Bentley, 2010).

The Late (Upper) Pleistocene period is currently estimated to span the time between c. 129 ka and c. 11.5 ka (Cohen et al., 2020) characterised by extremes in climate with several cooling and warming phases (Ehlers and Gibbard, 2003). The Last Glacial Maximum (27–20 ka) was the most recent period during the Late Pleistocene when global ice volume peaked, and the global mean sea level dropped by about 120 m (Clark and Mix, 2002). After the Last Glacial Maximum, the ice cover began to decrease significantly with relatively small readvances. The time interval when glaciers were declining (20–11.5 ka) is known as the last glacial termination (Denton et al., 2010).

One of the main questions of last glacial termination in New Zealand is concerned with the nature of deglaciation. The first half of the last glacial termination deserves special attention due to various results supporting both the large (Putnam et al., 2013a; Barrell et al., 2019; Denton et al., 2021) and gradual (Shulmeister et al., 2010; 2018a; Rother et al., 2014; Moore et al., 2022) climate warming and retreat of mountain glaciers over the period of 20–17 ka. Developing a more complete picture of past glacier changes in the first half of the last glacial termination is crucial for understanding of past climate changes in the Southern Hemisphere.

Another puzzle of the last glacial termination is related to the later stages of this time period known as the Late Glacial interval (15–11.5 ka). During the Late Glacial, the warming trend recorded in Antarctic ice cores was interrupted by the Antarctic Cold Reversal (ACR, 14.5–12.5 ka) (Jouzel et al., 1995), which was subsequently identified from the southern mid to high latitudes, including New Zealand. Although existing studies suggest a general trend of deglaciation during the Late Glacial in New Zealand, the structure of climate changes during this time period is only supported by limited evidence (e.g. Putnam et al., 2010a; Kaplan et al., 2010; Kaplan et al., 2013). Climate fluctuations during the Late Glacial are important because they provide an example of abrupt, non-linear climate change during a past period of global warming, thus they have relevance for present day climate change (Kaplan et al., 2013).

The primary aim of this thesis is to constrain the timing and extent of glacier fluctuations in the Southern Alps of New Zealand over the Last Glacial Maximum and subsequent termination (including Antarctic Cold Reversal), as well as to improve our understanding of orbital- and millennial-scale climate drivers.

To achieve this aim, I complete the following objectives:

Objective 1 – Map the distribution of glacial landforms in the Ahuriri River valley.

Objective 2 – Determine the ages of these landforms using cosmogenic surface exposure dating methods.

Objective 3 – Reconstruct past equilibrium line altitudes and air temperature anomalies associated with past glacier geometries.

Objective 4 – Compare results from the Ahuriri with similar records elsewhere in New Zealand from South America and southern Australia.

In completing these objectives, I make three major following original contributions:

i) compiled the large-scale (1:38 000) glacial geomorphological map of the Ahuriri River valley (Chapter 4);

ii) established a new moraine chronology determining the timing and extent of Late Quaternary glaciation in the Ahuriri River valley between 19.8±0.3 and 12.6±0.2 ka (Chapters 5 and 6);

iii) reconstructed ELA and associated quantitative palaeotemperatures for the Last Glacial Maximum and the Late Glacial climate reversal (Chapters 5 and 6).

1.2 Organisation of this thesis

In Chapter 2, I present a literature review and introduction to the study region. At the end of this chapter, I identify the research questions to be addressed by this study. In Chapter 3, I describe and justify the methodological approaches that were used in this thesis. In Chapters 4–6, I present original research designed and carried out during my doctoral studies. Some of these chapters have already been published in international peer-reviewed journals (see Section 1.3, below), thus these chapters are formatted in the style of full scientific journal articles. In Chapter 7, I readdress the original research questions of the thesis in light of the results.

1.3 Statement on the contributions made to this thesis by the author, supervisors, and collaborators

This thesis consists of five major components: i) field work, such as sample collection and field mapping. These were conducted by myself, Shaun Eaves, Lisa Dowling, and Emily Moore. ii) Computer-based geomorphological mapping was performed by myself with the assistance of Shaun Eaves and Kevin Norton. iii) Laboratory work, such as sample physical preparation and geochemistry. These were accomplished by myself with the assistance of Kevin Norton, and Shaun Eaves. iv) $^{10}Be/^{9}Be$ ratio measurement by accelerator mass spectrometry at Lawrence Livermore National Laboratory (CA, USA) was completed by Alan Hidy. Calculation of ages was done by myself with the assistance of Shaun Eaves and Kevin Norton. v) Writing the individual chapters was achieved by myself based on input and feedback from all three supervisors (mainly from Shaun Eaves) and collaborators.

The project, which was the main source of funding (E3230) was supervised by Andrew Mackintosh (Monash University) and Brian Anderson (Antarctic Research Centre). All supervisors and main collaborators are co-authors of published papers. Below I present research papers with all co-authors that have been published or submitted based on this thesis.

Chapters 3–4: Tielidze L. G., Eaves S. R., Norton, K. P., and Mackintosh A. N. (2021). Glacial geomorphology of the Ahuriri River valley, central Southern Alps, New Zealand. Journal of Maps, 17:2, 73-86, doi:10.1080/17445647.2021.1876777.

Chapters 3, 5, and section 7.2.4.1: Tielidze L. G., Eaves S. R., Norton, K. P., Mackintosh A. N. and Hidy, A. J. (2022). Cosmogenic ^{10}Be constraints on deglacial snowline rise in the Southern Alps, New Zealand. Quaternary Science Reviews, 286, 107548, doi.org/10.1016/j.quascirev.2022.107548.

Chapters 3, 6 and section 7.2.4.2: Tielidze L. G., Eaves S. R., Norton, K. P., Mackintosh A. N. Pedro, J. B., and Hidy, A. J. (2022). Early glacier advance in New Zealand during the Antarctic Cold Reversal. Journal of Quaternary Science. Accepted for final publication.

CHAPTER 2: BACKGROUND

2.1 Regional settings of the Southern Alps

2.1.1 Location

The Southern Alps are located in the Southern Hemisphere in South Island of New Zealand (Figure 2.1a), and span approximately 700 km from north-east (41°S, 173°E) to the south-west (45°S, 167°E). Both western and eastern slopes of the mountain range are occupied by glacial valleys, many of which are infilled with glacial lakes, especially on the eastern side. There are seventeen mountain peaks in the Southern Alps that exceed 3,000 metres above sea level (a.s.l.) with Aoraki/Mount Cook – the highest point in New Zealand (3,724 m a.s.l.).

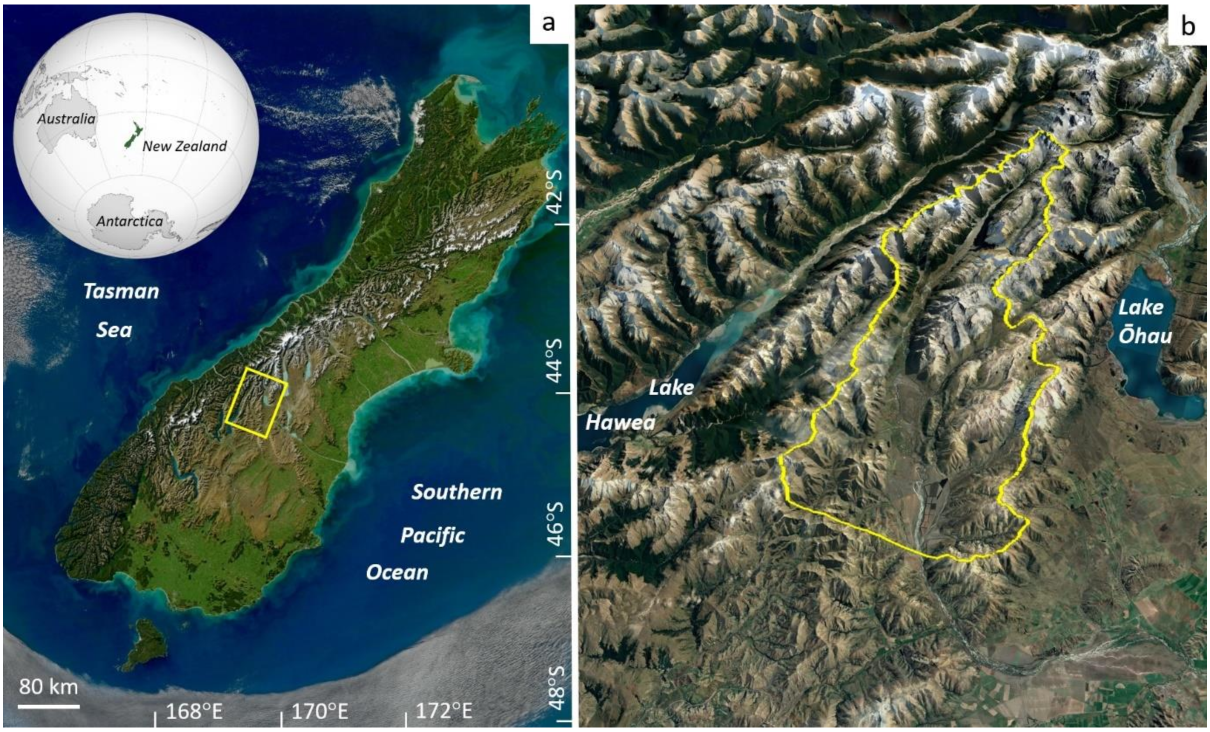

Figure 2.1 *a – Overview map of the South Island of New Zealand. Regional location of New Zealand is given on insert map. b – Location of the Ahuriri River valley is shown with a yellow outline (© Google Earth).*

2.1.2 Climate

The mountain range of the Southern Alps lies perpendicular to the prevailing westerly flow of air masses, dividing South Island into strongly different climate regions. The western facing part of the island is the wettest across the range (4,000–10,000 mm mean annual) and all of New Zealand, whereas the eastern slopes of the mountains are drier (<1,000 mm) (Chinn et al., 2014). The high precipitation of the western-facing slopes of the Southern Alps sustains glaciers that descend to just a few hundred meters above sea level (Purdie et al., 2014). Large glaciers and snowfields can mostly be found west of, or on, the highest peaks of the main ranges with smaller glaciers further east. The largest, Tasman Glacier (at about 100 km^2), east of the main divide.

Relatively low elevation locations towards the coast of the South Island have a mean annual temperature of between 10 °C and 11 °C, whereas inland areas generally observe a slightly lower mean annual temperature of between 9 °C and 10 °C (Macara, 2018). Temperatures decrease at a rate of about ~1 °C for every 200 m of altitude (Norton, 1985) providing low temperatures on many mountain summits that are sufficiently high to enable perennial survival of snow and thus ice formation (Chinn et al., 2014).

The analysis of annual equilibrium line altitudes (ELA) for 34 glaciers in the central Southern Alps demonstrates that regional variability of the ELA is much dependent on the aspect of glaciers. e.g. south-facing glaciers have a lower ELA: ~1750 m in the south-west while those glaciers facing the north-west have an ELA of ~2070 m (Carrivick and Chase, 2011). Recent study by Lorrey et al. (2022) analysed ELA change for 41 index glaciers from New Zealand between 1980 and 2010 indicating a trend towards higher regional snowlines since the 1990s that has been steepening in recent decades. An average ELA for all 41 glaciers was 1820 m a.s.l.

2.1.3 Geology and tectonics

2.1.3.1 Tectonic history

The Southern Alps covers a variety of geological terrains. Three main tectonic regimes such as – ***Tuhua Orogeny*** (Devonian and Carboniferous), the ***Rangitata Orogeny*** (Cretaceous), and the ***Kaikoura Orogeny*** (Cenozoic to present) can be distinguished in this area.

The oldest rocks in the Southern Alps were deformed and uplifted by the ***Tuhua Orogeny***, approximately 370 and 330 million years BP when New Zealand was part of Gondwanaland. The Tuhua Orogeny produced severe folding, faulting, and intrusions. The New Zealand Geosyncline developed and filled only after approximately 200 million years when the island arc system was formed. This period was marked by deposition of colossal thicknesses of sandstones that later became the greywacke of the axial part of the Southern Alps (Fitzsimons and Veit, 2001).

The ***Rangitata Orogeny*** peaked approximately 130 million years BP when deposition in the New Zealand Geosyncline ended and produced a new land area. After approximately 80 million years BP, similar to Australia and Antarctica, the land area of New Zealand had broken away from Gondwanaland (late Cretaceous Peneplain). Most of New Zealand still was below sea level for that time and a series of early to middle Tertiary sediments accumulated (Kingma, 1959; Fitzsimons and Veit, 2001).

Kaikoura Orogeny is known as the most recent and relatively simple phase of deformation in New Zealand (compared with the previous orogenies). During this time much of the sediment in the South Island has been removed by the joint effects of erosion and uplift. The main orographic units of the Southern Alps were formed at the beginning of the Kaikoura Orogeny approximately 26 million years ago, as the Pacific Plate collided with the Indo-Australian Plate (Kingma, 1959; Korsch and Wellman, 1988; Fitzsimons and Veit, 2001).

The ~500 km long oblique-slip fault zone called the Alpine Fault is a major transcurrent reverse fault of dextral displacement in New Zealand. It bounds the western edge of the Southern Alps running from Lake Rotoiti in the north to Milford Sound in the south (Williams, 1991; Fitzsimons and Veit, 2001). Evidence of rapid uplift are found on the western side of the South Island, just to the east of the Alpine Fault where convergence is strongest (Williams, 1991). The uplift of the Southern Alps is continuing today at a rate of about 5 to 10 mm per year (Fitzsimons and Veit, 2001; Little et al., 2005), therefore, it has had a large impact on regional environments in New Zealand during the Quaternary period.

2.1.3.2 Tertiary (Pliocene) landscape development

The Tertiary landscape in the southern island are presented as sediment fragments of the early Pleistocene Porika Glaciation (~2.2 Ma) in Nelson (Suggate, 1990) and Ross Glaciation (~2.5 Ma) in Westland (Fitzsimons et al., 1996). In general, there is very little evidence of Tertiary landscape development in the Southern Alps because most of the uplift has occurred since the Pliocene (~5.3–2.5 Ma). However, on the eastern side of the Southern Alps (e.g. Canterbury Plains), there are widespread Tertiary marine sediments deposited during a middle Tertiary marine transgression (Fitzsimons and Veit, 2001). A big gap in glacial history (approximately 1 million years) after the Porika Glaciation allowed the uplift and erosion to play the dominant role in the gradual establishment of the present pattern of the landscape in New Zealand (Suggate, 2004).

2.2 Geomorphological division of the Southern Alps

On the basis of contrasting tectonic uplift rates, erosion processes, precipitation, glaciation, and landform groups, three geomorphological domains were identified across the Southern Alps by Whitehouse (1988). These regions are: i) Western Southern Alps – characterised by very steep, heavily eroded slopes formed by fluvial erosion and debris avalanches; ii) Axial Southern Alps – mostly dominated by high level of glacier cover; and iii) Eastern Southern Alps – with two sub-regions, such as the basin and range sub-region (moderately eroded, scree-covered ranges separated by large valleys with braided rivers) and eastern front range sub-region (eroded greywacke mountains with rounded ridge crests and V-shaped valleys).

Based on structural geology and rock type, Williams (1991) distinguished four first-order and several second-order morphological divisions for New Zealand. The first-order morphological divisions are: 1. The Axial Ranges (run diagonally across the both islands of New Zealand); 2. Basin and Range Provinces (symmetrically placed on both sides of the axis); 3. Taupo Volcanic Zone (North Island); and 4. Major Lowlands and Sedimentary Basins. Based on this classification the headwater of Ahuriri River valley is placed in South Island Axial Range's zone, while the rest of the territory belongs to the Canterbury Faulted and Folded Belt zone.

2.3 Glacial geomorphological studies

2.3.1 Early study period

The first studies of New Zealand's glacial history date back to the 1860's (Fleming, 1959; Haast, 1864; Hector, 1865), while the 1960s is regarded as the end of a century-long pioneering phase when a chronological scheme for New Zealand's glacial stratigraphy was set out by Suggate (1965). Suggate mapped the extent of Late Pleistocene glaciation and systematically named stratigraphic units for mapping purposes. The history of past glaciation studies in New Zealand is described more in detail by Gage (1985), Suggate (1990, 2004) and Barrell (2011).

New Zealand was very poorly covered by topographical maps until the Second World War. Only after 1941 topographic mapping on a 1:63,360 scale was started for military purposes. Even though those first surveying maps were very simple, no other data exists from this time and these maps are the most reliable source of information. By 1945 aerial photos had already covered post-glacial landforms on the west coast of South Island, while by the late 1950s a geological map on a scale 1:250,000 was considered. The implementation of this mapping programme started only after seven years, in 1957 and was carried out over the next eleven years. The new mapping programme covered the whole country in 28 sheets at a scale of 1:250,000. This new survey provided evidence of ice advances in major valleys of the South Island, however, correlation between valley systems for the entire island was not carried out. Such an attempt was only made later when the Quaternary geological map of New Zealand at a scale of 1,000,000 was created in 1973 (New Zealand Geological Survey, 1973) for the INQUA congress held in New Zealand (Gage, 1985, Suggate, 2004). Since the 1990s the mapping capacities of Quaternary glacial deposits has been significantly enhanced by the availability of complete coverage of the country with large scale (1:50,000) topographical maps and high-resolution satellite imagery. Old geological maps (scale 1:250,000) have also been enhanced and updated nationwide by GNS Science in 1993–2010 (e.g. Rattenbury et al., 2010; Turnbull, 2000).

2.3.2 Recent study period

During the last decade a lot of new scientific data about the Late Quaternary glaciation has been obtained across New Zealand. Furthermore, new methods of landscape assessment have been launched (e.g. LiDAR) and improved methods of dating techniques have been applied (e.g. luminescence and surface exposure dating techniques). Meanwhile, significant glacial geomorphological studies have been carried out both at the regional scale (Barrell et al., 2011), and for individual catchments in the Mackenzie River basin, Southern Alps (e.g. Putnam et al., 2013a; Borsellino et al., 2017; Strand et al., 2019; Sutherland et al., 2019a).

The glacial geomorphology of both the eastern and western side of the central Southern Alps was documented by Barrell et al. (2011) on a five sheet 1:100,000 scale geomorphological map and in an associated monograph. This work shows the distributions of a range of landforms, such as glaciers, moraines, and outwash plains. These landforms are placed in broad age groups, emphasizing different climatic events. Particular attention is paid to glacial landforms of Late Quaternary age.

Further detailed glacial-geomorphological mapping has been carried out in individual river basins following Barrell et al. (2011). For example, Putnam et al. (2013b) presented a record of palaeo glacier behavior during the local Last Glacial Maximum from near Lake Ohau. Based on detailed glacial geomorphological mapping and ^{10}Be surface-exposure dating methods they produced a robust chronology of well-preserved terminal moraines. Overall, they distinguished six major moraine landforms across the study area. Borsellino et al. (2017) provided a large-scale 1:20,000 glacial geomorphological map of the Brabazon and Butler Downs. They mapped and subdivided glacial landforms into three main zones, such as kame terraces, kettles and meltwater channels, and lateral moraines. Strand et al. (2019) used glacial geomorphological mapping along with ^{10}Be surface-exposure dating in order to study the left-lateral moraine sequence of the palaeo Pukaki Glacier. They identified six different moraine landforms dating to the Last Glacial Maximum. Sutherland et al. (2019a) used a 1 m digital elevation model (DEM) based on airborne LiDAR data along with high-resolution aerial imagery and field observations to analyse well-preserved glacial geomorphology surrounding Lake Tekapo. They distinguished a group of Last Glacial Maximum moraines and described in detail landform assemblages such as the glacio-lacustrine, glacio-fluvial, supra-glacial, sub-glacial, and recessional ice-marginal features.

2.4 Late Quaternary glaciation in a global context, and the orbital theory of Ice Ages

The Quaternary glaciation, also known as the Pleistocene glaciation, refers to the Quaternary period that began 2.58 million years ago and was characterised a series of glacial (colder) and interglacial (warmer) periods (Ehlers and Gibbard, 2011). The Last Glacial Period (LGP) is intended to be the fourth division of the Quaternary glaciation (or Pleistocene Epoch) encompassing the period 115–11.7 ka which is known in Europe as the Würm (Alpine) or Devensian (Great Britain) or Weichselian glaciation (northern Europe); these are broadly equated with the Wisconsin glaciation (North America), though technically that began much later (NEEM community members, 2013). This time-period with a little earlier onset (~129–11.7 ka) is also often referred to as the Late Pleistocene (Cohen et al., 2020). Within the Last Glacial Period (or Late Pleistocene), the Last Glacial Maximum was approximately between 26 ka and 19 ka years ago (Clark et al., 2009). The initiation of conditions that caused Quaternary glaciation resulted from the long-term declining cooling trend in global climate.

Overall, Quaternary glaciation is hypothesised as a product of the internal variability of the Earth climate system (e.g. carbon cycle and ocean currents), interacting with external forcing by phenomena outside the climate system, such as, for example, changes in Earth's orbit (Milankovitch, 1941). Variation in the Earth's orbit through time causes changes in the amount and distribution of solar radiation reaching Earth's surface.

The hypothesis that variation in Earth's orbit causes glacial-interglacial cycles was first proposed by James Croll (1864) in the late 19th century. However, Milutin Milankovitch (1920, 1941) extended Croll’s theory with robust calculation of orbital parameters, and popularised it in about 1920. He calculated that these irregularities in Earth's orbit could cause the climatic cycles now known as Milankovitch cycles. Milankovitch's hypothesis was not widely accepted until the 1970s when a sufficiently long and detailed chronologies of the Quaternary temperature and ice volume changes from marine sediments first became available. According to his calculations, three orbital parameters, (eccentricity, obliquity, and precession) are responsible in causing fluctuations in ice cover on Earth (e.g. Broecker, 1966):

Eccentricity: The Earth's orbit around the sun is not a circle, but rather it is an ellipse (Figure 2.2). The shape of the elliptical orbit, which is measured by its eccentricity, varies from between one and five percent through time. The eccentricity affects the difference in the amounts of radiation Earth's surface receives at aphelion (the point on its orbit when Earth is farthest from the sun) and at perihelion (the point on its orbit when the Earth is closest to the sun). The effect of the radiation variation is to change the seasonal contrast in the northern and southern hemispheres, although the amount of change in radiation is less than 0.2%. Changes in the orbital eccentricity of Earth occur on a cycle of approximately 100,000 years (Figure 2.3a and 2.4).

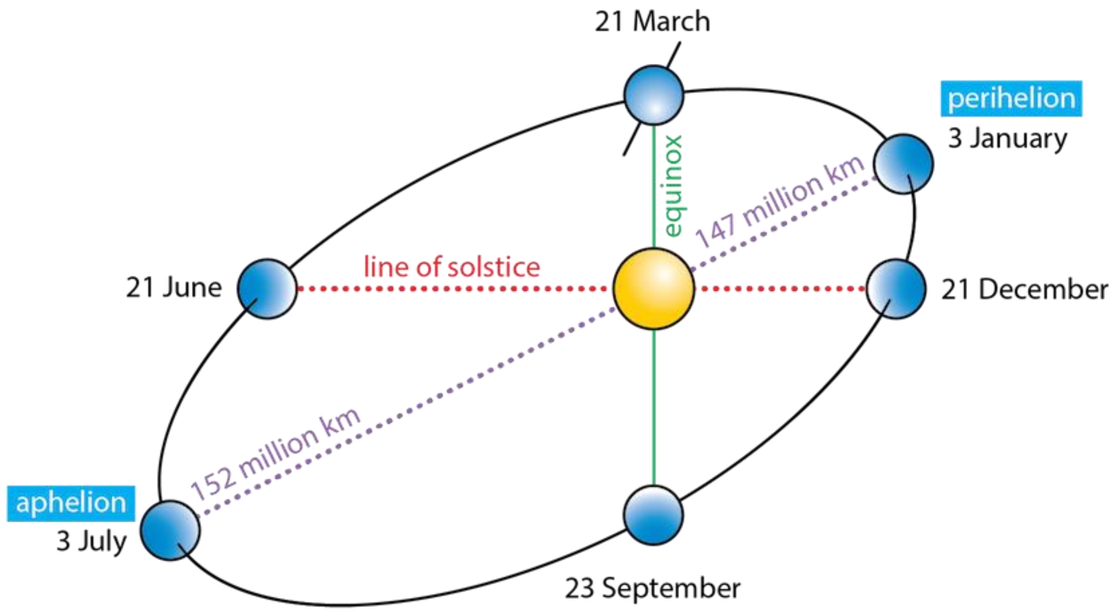

Figure 2.2 *The motion of the Earth in an elliptical orbit and the principle of Eccentricity theory.*

Obliquity: The Earth's axis is tilted by about 23.5° with respect to its orbit around the sun (Figure 2.4). The inclination, or tilt, of Earth's axis varies periodically between 21.6° and 24.5° in a cycle 41,000 years long (Figure 2.3b and 2.4). The tilt of Earth's axis is responsible for the seasons. The greater the tilt, the greater the contrast between summer and winter temperatures at high latitudes and in the length of the winter dark period at the poles but very little effect on low latitudes. The effects of tilt on the amount of solar radiation reaching the Earth are closely linked to the effects of precession. Variation in these two factors cause radiation changes of up to 15% at high latitudes. Radiation variation of this magnitude greatly influences the growth and melting of ice sheets.

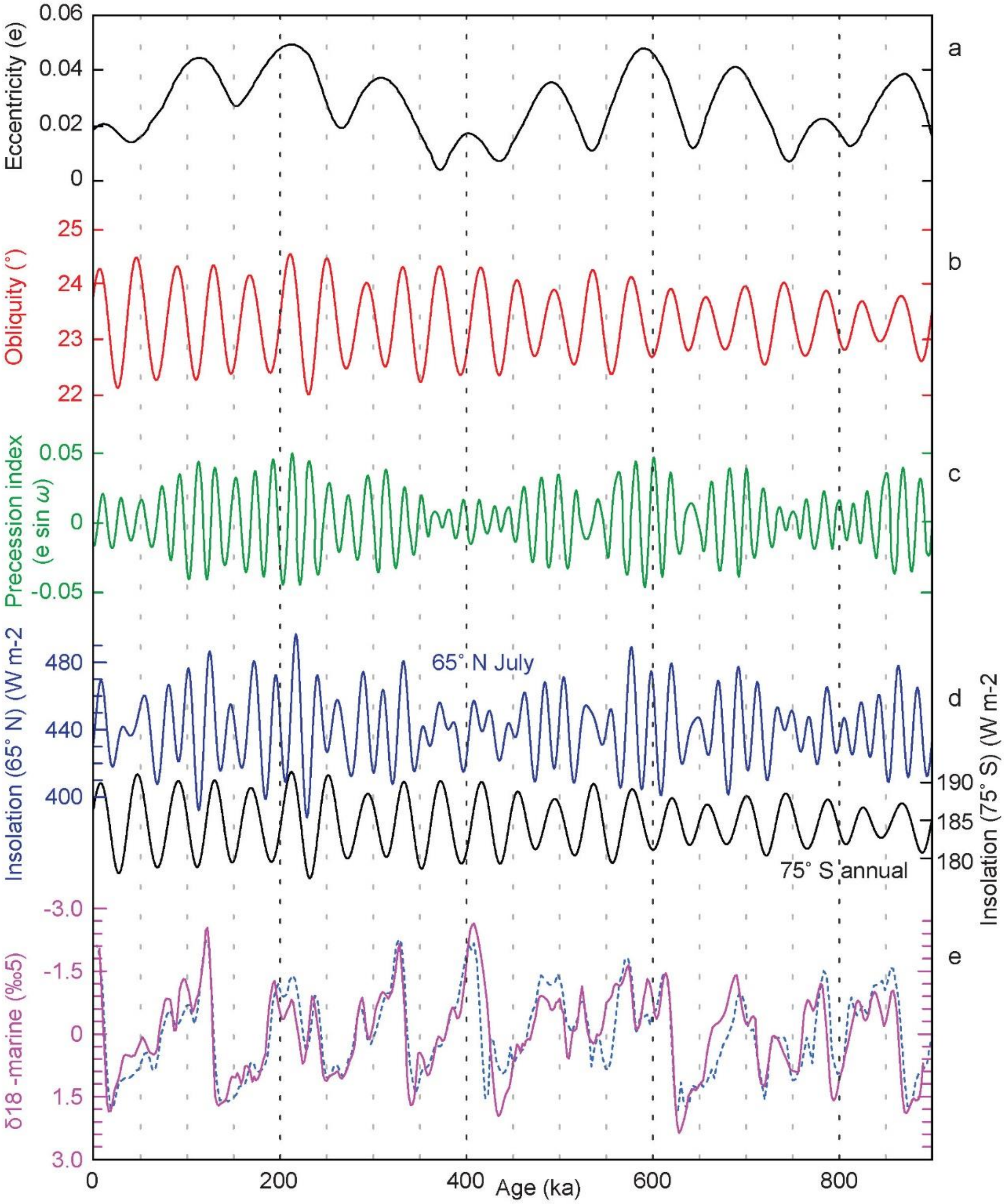

Figure 2.3 *a – Axial eccentricity; b – obliquity; c – precessional index (e sin ω). Values calculated using the code of Huybers and Eisenman (2006). d – mid-summer (July) insolation intensity at 65 °N and annual insolation intensity at 75 °S. Values calculated using the code of Berger and Loutre (1991). e – Stages of glacial cycles from marine oxygen isotope record (solid purple line. Site MD900963 and ODP6773) (Bassinot et al., 1994). The dashed blue line indicates the uncertainties in the marine records (ODP site 677) (Imbrie et al., 1993).*

Precession: Twice a year, the sun is located directly over the equator (equinoxes). Currently the equinoxes occur on approximately March 21 and September 21. However, because the Earth's axis of rotation "wobbles" (like a spinning top), the timing of the equinoxes changes which is known as precession (Figure 2.3c and 2.4). Although the timing of the equinoxes is not in itself important in determining climate, the timing of the Earth's aphelion and perihelion also changes. Similar to the timing of the equinoxes, the timing of the aphelion and perihelion is also affected by the wobble of the axis of rotation. The changing aphelion and perihelion are important for climate because it affects the seasonal balance of radiation. The aphelion and perihelion change position on the orbit through a cycle of 360 degrees which has two periods of approximately 19,000 and 23,000 years. Together these combine to produce a generalised periodicity of about 22,000 years (Figure 2.3c).

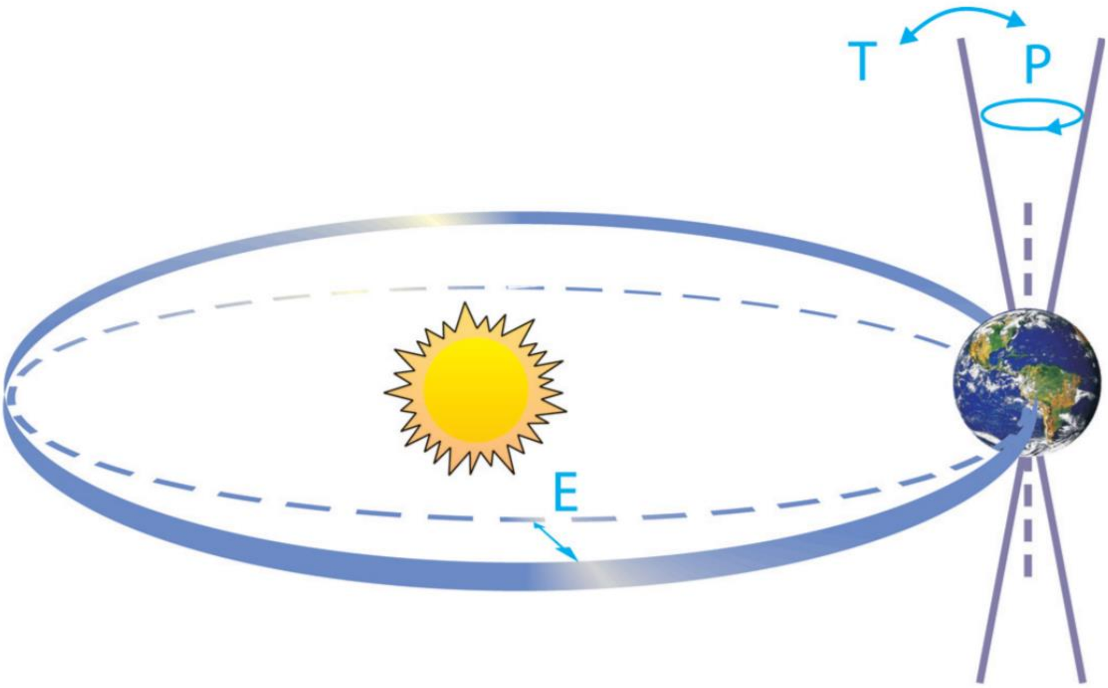

Figure 2.4 *Schematic of the Earth's orbital changes (Milankovitch cycles) that drive the ice age cycles. 'T' represents changes in the tilt (or obliquity) of the Earth's axis, 'E' represents changes in the eccentricity of the orbit (due to variations in the minor axis of the ellipse), and 'P' represents precession, that is, changes in the direction of the axis tilt at a given point of the orbit (Rahmstorf and Schellnhuber, 2006; Jansen et al., 2007).*

Studies of deep-sea cores (Emiliani, 1955; Broecker, 1966; Hays et al., 1976; Broecker et al., 1978), and the fossils contained in them, along with ice cores from Greenland (Dansgaard et al., 1969, 1982) and Antarctica (Epstein et al., 1970; Lorius et al., 1985; Jouzel et al., 1987) indicate that the fluctuation of climate during the last few hundred thousand years is remarkably close to that predicted by Milankovitch.

There are also other processes known to play an important role in the transitions between glacials and interglacials such as changes in the ocean thermohaline system (through changing fluxes of fresh water) and changes in atmospheric carbon dioxide (CO_2) (as an important greenhouse gas). As recorded in Antarctic ice cores, CO_2 was closely tracked with Antarctic temperature variations over the last 800,000 years (Petit et al., 1999; Siegenthaler et al., 2005; Lüthi et al., 2008). Low CO_2 contents correspond to cold glacial periods, and high CO_2 to warm interglacial periods. However, other studies by (Joos and Prentice, 2004; 2008) indicate that CO_2 may not be the primary cause of the interglacial-glacial transitions, but instead acts as a feedback. The explanation for this observed CO_2 variation "remains a difficult attribution problem" (Joos and Prentice, 2004; 2008).

2.5 Late Quaternary glaciation in New Zealand

2.5.1 Pre-Last Glacial Maximum (before 35 ka)

The Southern Alps have experienced multiple glaciations during the Quaternary, as indicated by the many large glacially-eroded troughs and multiple belts of lateral and terminal moraines (Barrell, 2011). Four major glaciations, the Nemona, Waimaunga, Waimea, and Ōtira, occured in the Middle and Late Pleistocene in New Zealand (Suggate, 1990). During the last glacial cycle of the Late Pleistocene, the extent of the glaciation differed very little from that of the Pleistocene glacial maximum in New Zealand, i.e. glacier tongues were only slightly smaller than during earlier events (Barrell, 2011). A large complex of palaeo glacier systems during that time extended approximately 700 km along the Southern Alps and averaged ~100 km in width (Barrell, 2011).

Geomorphic evidence of pre-Last Glacial Maximum glacier advances in many valleys is now heavily reworked or even removed. However, locally well-preserved glacial deposits and Late Quaternary stratigraphic sequences provide insight into pre-LGM glaciation in New Zealand

(Sutherland et al., 2007; Shulmeister et al., 2010). For example, using the luminescence dating of sediments Preusser et al. (2005) indicate that Late Pleistocene glaciers reached their last maximum extent in North Westland during the early part of the Otira (Last) Glaciation (~64 ka). Furthermore, initial dating evidence on coarse alluvial deposits in the lowlands indicates their formation during MIS 5b (85 ka) and MIS 5d (111 ka). The stratigraphic record of the palaeo Rakaia Glacier margin by Shulmeister et al. (2010) indicate six significant advances occurred in early MIS 6, mid-MIS 6, MIS 5b (100–90 ka), MIS 5a/4 (~80 ka), mid-MIS 3 (~48 ka), and late MIS 3 (~40 ka). The ^{10}Be chronology combined with a model simulation by Schaefer et al. (2015) demonstrates that the former Pukaki Glacier reached its maximum position of the last glacial cycle during the MIS 4 (65.1±2.7 ka), while other peaks of readvance occurred at 44±1.0, 41.8±1.1, and 36.5±0.9 ka (Strand et al., 2019).

2.5.2 Last Glacial Maximum (35–18 ka) and onset of the deglaciation

More is known about the most recent glacial period. The Last Glacial Maximum occurred between ~35 and ~18 ka when a comprehensive and interconnected mountain ice field formed over the Southern Alps, and glaciers generally advanced. However, some warmer intervals during the Last Glacial Maximum saw advance and retreat of glaciers in the Southern Alps, with variations on the number and timing of advances in different regions (e.g. Suggate 1990; Pillans 1991; Suggate and Almond 2005).

Significant progress has been made recently in reconstructing the Last Glacial Maximum and subsequent deglaciation in the Southern Alps using surface exposure dating. However, the amount of ice retreat and temperature decrease during this time is still subject to debate, as different proxy records provide different constraints (see further discussion below).

Using ^{10}Be surface-exposure dating methods for seventy-three samples and detailed glacial geomorphological mapping, Putnam et al. (2013b) produce a robust chronology of well-preserved terminal moraines deposited during the Last Glacial Maximum near Lake Ōhau. They also used a glaciological model to estimate palaeo ELA and past atmospheric temperatures from the Ōhau Glacier record. They discovered that the Last Glacial Maximum in the Ōhau valley was achieved as early as 32.5±1.0 ka, and palaeo ELA was 920±50 m below for that time relative to the present-day. This palaeo ELA corresponds to a temperature depression of about 6.25±0.5 °C. Subsequent glacier advances produced slightly inboard moraine belts at 27.4±1.3, 22.5±0.7, and 18.2±0.5 ka. Strand et al. (2019) and Doughty et al. (2015) undertook geomorphological mapping in conjunction with ^{10}Be surface-exposure dating in a previously unstudied sector of the left-lateral moraine sequence of the former Pukaki Glacier. These studies indicate that the Last Glacial Maximum advances of Pukaki Glacier occurred at ~27, ~20, and ~18 ka. A glacier modelling simulation by Golledge et al. (2012) indicated that the Last Glacial Maximum ELA was depressed by 800 m (Ōhau, Tekapo glaciers) to 875 m (Pukaki Glacier), indicating the Last Glacial Maximum (20–30 ka) annual temperature depression of 6±0.5 °C below modern in the central Southern Alps. Rowan et al. (2014) also used glacier modelling to reconstruct the Last Glacial Maximum climate, concluding that temperatures in the central Southern Alps were –8.2 °C to –5.5 °C relative to present day. A recent study by Moore et al. (2022) uses cosmogenic ^{10}Be chronology along with 2D reconstructions and equilibrium line altitude estimation from a cirque glacier situated in Fiordland. This study has identified pulses of moraine building at millennial-scale frequency during the latter half of the last glacial cycle. Specifically, they identified moraines that formed 32±11 ka, 18.7±0.2 ka, 18.1±0.1 ka, and 17.2±0.3 ka. 2D glacier reconstruction suggests the equilibrium line altitude remained depressed by c.1130 m (equivalent to 5.8±0.6 °C colder than present) during this interval.

The ^{10}Be surface-exposure chronology along with glacier modeling by Putnam et al. (2013a) suggested that the abrupt warming in the Rakaia River valley began at 17.8±0.2 ka and continued to 15.7±0.2 ka. The temperature increased from 6.25 °C to 2.25 °C relative to present during that time. i.e. large ice retreat is attributed primarily to an abrupt atmospheric warming by ~4 °C in this time-period. Approximately 3.75 °C (∼70%) of the warming occurred between ∼17.8 and ∼16.3 ka. In contrast to records from Rakaia River valley, Rother et al. (2014) and Shulmeister et al. (2018a) argue there was no evidence of a large warming or significant retreat of glaciers at 18 ka in Rangitata River valley. Furthermore, the latter study argues that the Rangitata record constitutes a more direct record of glacial response to deglacial climate than other records where glacial dynamics were influenced by large proglacial lake development (e.g. Ōhau, Pukaki, Tekapo, and north part of the Rakaia Valley). Overall, both studies support the concept of gradual warming and retreat of mountain glaciers over the 20–17 ka (Rother et al., 2014; Shulmeister et al., 2018a). Hereafter Barrell et al. (2019) recalculated the Rangitata record and identified that the substantial ice-surface lowering of the Last Glacial Maximum Rangitata Glacier was in progress shortly after c. 18 ka. The recalculated Rangitata chronology is thus compatible with dating results from other eastern valleys of the Southern Alps (e.g.

Ōhau and Rakaia), indicating moraine formation at c. 18 ka, followed by sustained glacier recession associated with regional climatic amelioration. The recent study by Moore et al. (2022) from the former cirque glacier situated in Fiordland indicated that the reduction of ice volume between 19 ka and 17 ka may have occurred in response to only a minor rise (<50 m) in the ELA or slight warming, and onset of the significant warming occurred only after 17.2±0.2 ka.

To conclude, the timing and magnitude of ice retreat along with amount of atmospheric warming during the first half of last deglaciation (20–16 ka) is still not sufficiently understood, as different proxy records provide different estimates suggesting that the last glacial termination in the Southern Alps is remaining subject of debate.

2.5.3 Late Glacial (15–11.5 ka)

The Late Glacial period refers to the later stage of the last deglaciation spanning ~15–11.5 ka. In New Zealand only a small number of moraine chronologies have been documented for this interval. Based on detailed landform mapping, a high-precision ^{10}Be chronology, and snowline reconstruction from the Irishman Stream in the Ben Ohau Range (Lake Ōhau basin) Kaplan et al. (2010) provide evidence that a cold event during the Late Glacial culminated at 13 ka. Putnam et al. (2010a) also used ^{10}Be surface exposure ages from the well-defined Birch Hill lateral moraine complex on the west flank of the Tasman River valley to assess whether the glacier advance was associated with the Antarctic Cold Reversal (ACR, 14.5–12.5 ka). They found that widespread glacier resurgence culminated at and 13 ka, at the peak of Antarctic cooling. However, a limited number of samples (n=2) from the same study also suggests that the glacier may have readvanced much earlier at 14.1 ka. Using geomorphologic mapping of moraines, ^{10}Be surface-exposure dating, snowline reconstructions, and numerical modeling, Kaplan et al. (2013) studied glacier fluctuation during Late Glacial time in the Ben Ohau Range, Lake Pukaki basin. With a limited number of older ages (n=4 from two different moraine ridges) this study suggests that glaciers were larger early Antarctic Cold Reversal at around 14.5 ka, while the main readvance occurred at ~13 ka.

Numerical modeling experiments from the Ben Ohau Range (Kaplan et al., 2013) suggest that air temperature during the Antarctic Cold Reversal was between 1.8 °C and 2.6 °C cooler than today, with similar (±20%) prescribed precipitation. Glaciological modelling of the former

Irishman Stream Glacier by Doughty et al. (2013) suggests that the snowline was ~400 m lower during the Antarctic Cold Reversal in New Zealand than the present-day, corresponding to a 2–3 °C cooler climate than today. Similar values of snowline lowering (ca 400 m relative to present) have been proposed by Eaves et al. (2017) based on manual ELA reconstructions and numerical glacier modelling from the Arthur's Pass during the last glacial-interglacial transition (ca.16–14 ka). They indicated that the Arthur's Pass moraines formed in a climate that was 2.2–3.5 °C colder than present. General cooling evidence the during the Late Glacial period was also confirmed from pollen records (Burrows and Russell, 1990; McGlone, 1995; Newnham and Lowe, 2000; Turney et al., 2003; McGlone et al., 2004; Vandergoes et al., 2008) and sediment cores (Vandergoes et al., 2008) from around New Zealand which support the notion that temperatures during the ACR in New Zealand were 2–3 °C cooler than today.

In summary, existing studies in several valleys of the Southern Alps provide evidence that a cold event during the Late Glacial culminated at 13 ka (e.g. Kaplan et al., 2010; Putnam et al., 2010a), coincident with Antarctic Cold Reversal. However, some moraine records from New Zealand also include older ages that suggest glaciers were larger at around 14.5 ka (Kaplan et al., 2013) and 14.1 ka (Putnam et al., 2010a). Due to the limited number of ages available, these glacier records do not provide sufficiently robust information about the climate of the early part of the Late Glacial. Hence, questions remain about the timing of glacier readvances and climate changes during the Antarctic Cold Reversal in New Zealand.

2.6 Study site – Ahuriri River valley

2.6.1 Location

The Ahuriri River originates on the eastern slopes of the central Southern Alps and forms the border between the Canterbury and Otago regions. The river flows approximately 70 km from the north-west (Mt. Huxley 2505 m a.s.l., 44°4'15.31"S, 169°40'42.56"E) to the south-east (conjunction with Lake Benmore 44°30'30.18"S, 170°3'26.51"E), within the Waitaki (Mackenzie) River basin.

A detailed glacial geomorphological work relating to the Ahuriri study site is presented in Chapter 4 and Tielidze et al. (2021). The study area selected for this thesis includes the upper portion of the Ahuriri River catchment, spanning about 45 km from the headwater (Figure 2.1b).

2.6.2 Orography

The upper section of the Ahuriri River valley (~20 km from the headwater) is surrounded by the Huxley (western side) and Barrier (eastern side) ranges and is relatively narrow with steep slopes and high elevation with several peaks exceeding 2200 m a.s.l. (Figure 2.5). Canyon Creek on western valley side, and Watson Stream and Hodgkinson Creek on the eastern side, are the main tributaries of the Ahuriri River in this upper region. In the middle and lower sections, the Ahuriri River valley has a very low bed slope (~5 m/km). The bottom of the lower and middle section of the valley contains prominent terminal and lateral (hummocky) moraine systems that were selected for this study, hereafter called moraine belts 3, 2, and 1 (see chapter 5). The bottom of the lowest section of the valley is very subtle and reaches its maximum width (~5 km) at the area of a large prominent hummocky moraine system (44°23'54"S, 169°39'48"E) (Figure 2.6).

Figure 2.5 *The upper section of the Ahuriri River valley. View from north to south (Photo by: W. Dickinson).*

Figure 2.6 *The lower section of the Ahuriri River valley. View from south to north.*

2.6.3 Stratigraphy

Despite the geochronological study that was accomplished during this thesis, the overall geochronology of the Ahuriri River valley is poorly studied. Thus, I am only giving here the relative ages based on 1:250,000 geological maps by Rattenbury et al. (2010) and Turnbull (2000).

The the Ahuriri River basin contains Late Pleistocene to Holocene formations. Holocene material encompasses angular, unsorted, blocky rock debris (scree), boulder till, and variable mixtures of rock debris, sand, silt (colluvium), and cirque moraines. These mainly located in the headwater of the Ahuriri River and its tributaries. The upper section of the valley contains alluvial deposits such as plains composed of gravel, sand, mud and minor peat, while fans composed of gravel and sand commonly occur along with large boulders from landslides and rockfalls. Late Pleistocene glacial deposits in the middle and lower valley comprise poorly sorted, generally unweathered boulder (greywacke) till with interlayered silt. In the lower section the Ahuriri River bed is cut into the Late Pleistocene (Hawera series) alluvial (including glacial outwash) deposits and tills. Peat swamp deposits with interbedded mud and gravel are mainly present at the lower section of the valley as well.

2.6.4 Tectonic setting

The Southern Alps has a rapid uplift rate of about 8±3 mm/year in the central section (Norris and Cooper, 2001), along with the major active transcurrent Alpine Fault (Kamp and Tippett, 1993). As a part of the central Southern Alps, there are several active and inactive fault lines in the Ahuriri River basin mainly stretching from north-east to south-west of the catchment (see main map in supplement). The largest fault occurs in the main river bed from the headwater to the Birch Creek conjunction from where it branches into two fault lines: the first turns south-west and almost follows the watershed between Ahuriri and Dingle Burn, while the second trends in the south-east direction, right parallel to the main river stream (Rattenbury et al., 2010; Turnbull, 2000) (Figure 2.7).

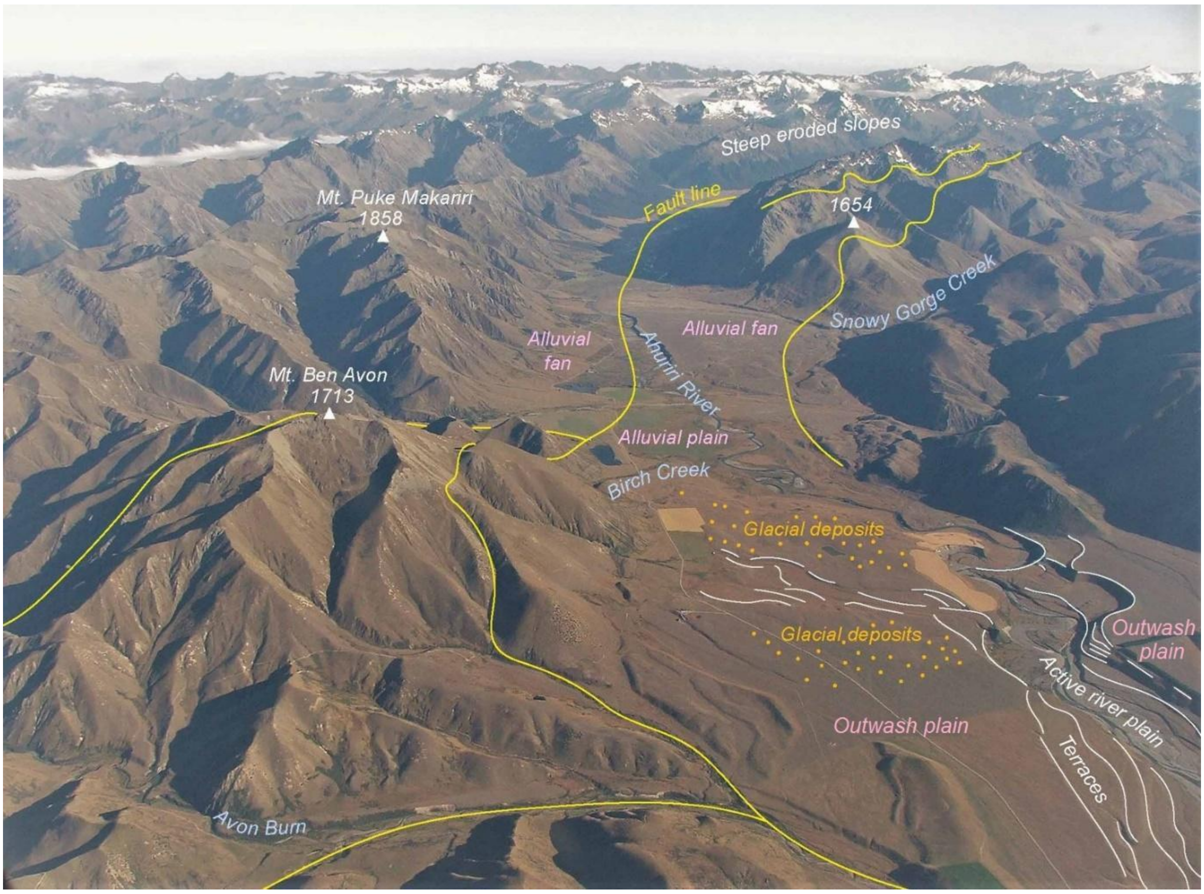

Figure 2.7 *Oblique image of the Ahuriri River valley and fault lines according to Rattenbury et al. (2010) and Turnbull, (2000). View from south to north (Photo by: K. Norton).*

In the upper section, there is one more right branch of this main fault line which perpendicularly crosses the Canyon Creek valley. Another large fault runs between the crest of the Barrier

Range and Snowy Gorge Creek bed, which crosses the Snowy Gorge Creek in the downstream and turns in a south-east direction. Relatively small faults occur at the left slope of the main river valley in the upper portion, almost parallel to the Ahuriri River bed, while the even smaller fault line is located at the headwater of Hodgkinson Creek (Rattenbury et al., 2010; Turnbull, 2000).

Areas of younger deposits or landforms in the Ahuriri River valley such as young floodplains and river terraces, accumulating fans of stream sediment at the mouths of valleys, gullies, and steep, eroding mountain or hill slopes, are commonly younger than the most recent fault movements. However, the ice-age landforms, such as the river plains, and glacially-sculpted landforms, although youthful in a geological sense, are old enough to have been affected by some of the most recent active faults and fold movements (Barrell, 2016).

2.7 Research questions

The previous sections have detailed existing knowledge about the last glacier termination in the Southern Alps of New Zealand. The specific research questions of this thesis are (each of which is addressed in one or more specific thesis chapters):

1. What was the timing and extent of palaeo Ahuriri Glacier advance and retreat during the Last Glacial Maximum and at the onset of the last deglaciation? (Chapter 5)

2. How did the Ahuriri Glacier respond to the Late Glacial climate reversal and when was the largest glacier readvance during that time? (Chapter 6)

3. What was the snowline depression and associated temperature changes during the Last Glacial Maximum and subsequent deglaciation? (Chapter 5–6)

4. What climate processes (at the millennial scale) could be responsible for glacier advance and retreat? (Chapter 5–6)

CHAPTER 3: METHODS

3.1 Geomorphological mapping

Geomorphological mapping is an established tool for reconstructing and documenting landscape development (Seijmonsbergen, 2013). There are two primary approaches in geomorphological mapping (Chandler et al., 2018): i) Classical – with mapping all geomorphological features and different landforms. This approach of mapping also defines the formation of all landscape terrain located at any given area. This approach is mainly used in Europe (e.g. Klimaszewski, 1990; Rączkowska and Zwoliński, 2015). ii) Thematic – e.g. detailed geomorphological mapping in glacial environments which mainly emphasis glacial and periglacial landforms and processes (e.g. Darvill et al., 2014; Bendle et al., 2017; Izagirre et al., 2018). This type of mapping helps us in understanding past glacier behaviour and processes in any particular place.

3.1.1 The geomorphologic approach used in this thesis

A number of glacial-geomorphological studies have recently been published on both individual river basins in New Zealand (Wallace, 2001; Evans, 2008; Borsellino et al., 2017) and regionally in the central Southern Alps (Barrell et al., 2011). In this study, I used the methodology of Barrell et al. (2011) as a baseline for my geomorphological approach. I used this thematic mapping method, because mapping is the first step towards making a climate reconstruction from the glacial history – and achieving this goal requires consideration of all landscape elements as the interaction of glacial and non-glacial landforms (e.g. cross-cutting relationships) can inform the glacial history. In total, four general land surface features were mapped as polygon, line, and point symbols based on their geomorphologic characteristics: hillslope landform features, moraine landform features, fluvial landform features, and other landform features (Table 3.1). In addition, I was guided by the glacial landform interpretations developed within recent studies listed in Table 3.1.

Table 3.1 *Identification criteria, uncertainties, interpretation, and references used for mapping geomorphological landforms.*

Landform Category	**Landform type**	**Morphology/general description**	**Possible identification errors**	**Interpretation**	**Reference**
Hillslope landform features	General bedrock terrain	Land surface developed on bedrock, beyond the limits of Late Quaternary glaciers. Commonly has irregularly dissected surface texture produced by fluvial gullying or gravitational erosion processes.			Barrell et al., 2011
	Ice-sculpted bedrock	Widespread exposures of bare or lightly vegetated bedrock, sometimes containing small lake basins. Evidence for extensive areas of former ice at pressure melting point.	Possible underestimation where bedrock is obscured by vegetation.	Marks former areas of relatively thick, fast-flowing and warm-based ice causing efficient subglacial erosion.	Glasser and Jansson, 2008 Izagirre et al., 2018 Leger et al., 2020
	Steep eroded slope	Cliff face or steep slope formed on poorly consolidated deposits. Large-scale version of the terrace edge landform feature.	Potential for confusion with active scree slopes.		Barrell et al., 2011
	Active scree slopes	Accumulations of debris on steep valley slopes at the foot of rockwalls.	Possible, but unlikely, confusion with steep eroded slope.		

	Vegetated stable scree slopes	Vegetated accumulations of debris on valley slopes at the foot of active scree slopes.	Possible misinterpretation as alluvial fans.		
Moraine landform features	Moraine ridge	Ridges of positive relief that display arcuate, crenulate or saw-tooth planform, and sharp crestlines.	Very low-relief ridges may be difficult to detect in imagery and possible confusion with trimlines.	Indicate former ice-front position. Characteristic landform features are ice-contact slopes.	Barrell et al., 2011 Bendle et al., 2017 Izagirre et al., 2018 Leger et al., 2020
	Hummocky moraine terrain	Hummocky or irregular surface texture of rises or troughs developed on ice-deposited (glaciogenic) sediments. Crestlines are less well defined than moraine ridges. Includes lateral and terminal moraine.	Boundaries of individual ridges are difficult to delimit. Linear patterns are difficult to map in the field. Will be missed in areas not covered by high-resolution aerial photography.	Marks former ice-marginal zone, or zone of stagnant ice.	Barrell et al., 2011 Darvill et al., 2014 Bendle et al., 2017
Fluvial landform features	Outwash plain	Large, open, approximately flat surfaces graded to former ice-limits (e.g. moraines). Often dissected by meltwater channels and relict stream networks.	Exact limits of outwash are often difficult to define. Surface grading is often only apparent in the field or over large distances on high-resolution aerial photos. Often form narrow corridors, so can be difficult to distinguish from channels.	Indicates former pathways of meltwater during glacier advance or still-stand. Characteristic landform features are terrace edges.	Barrell et al., 2011 Darvill et al., 2014 Bendle et al., 2017 Leger et al., 2020

	Alluvial plain	As for outwash, but where the water source was mainly from non-glaciated catchments.			Barrell et al., 2011
	Alluvial fan	Sub-horizontal fans on valley sides and on distal parts of the outwash plains, often fed by meltwater channels or streams.	Possible misinterpretation as ice contact deposit.	Reworking of unconsolidated material by contemporary meltwater channels and streams.	Glasser and Jansson, 2008 Izagirre et al., 2018
	Debris cone	Cone- or fan-shaped accumulations of sediment at the base of a steep gully, chute or tributary valley. Typically, steeper than alluvial fans, which are similar morphologically.	Possible misinterpretation as rockfall.	Record the deposition of successive debris flows.	Chandler et al., 2019
	River terrace	Raised, relatively flat areas located immediately adjacent to, or near, a stream or river. Characteristic landform features are terrace edges.	Potential for confusion with linear features such as palaeo shorelines.	The result of periods of aggradation and incision.	Chandler et al., 2019
Other landform features	Peak	Mountain peaks, often pyramidal in shape due to glacial and periglacial erosion on two or more sides.	Possible misplacement due to snow or ice on the summit. A DEM helps to pinpoint the exact summit.	Divides one or more present or former ice masses.	Izagirre et al., 2018
	Cirque	Up-slope crest of a formerly glaciated, amphitheatre-shaped basin (corrie).	Possible, but unlikely, confusion with mass movement or landslip	Records local cirque glaciation during phases of glacier advance/retreat.	Glasser and Jansson, 2008 Barrell et al., 2011

			Scars.		Izagirre et al., 2018
	Contemporary glacier	Bare ice, snow and debris. Surface structures such as crevasses and seracs are common.	Possible overestimation in glacier extent if confused with snow cover.		Izagirre et al., 2018
	Rock glacier	Wrinkled or undulatory surface developed on an accumulation of angular rock debris, with ridges transverse to the down-slope direction.	Possible, but unlikely, misinterpretation as rockfall deposit.		Barrell et al., 2011
	Hanging Valley	Mouth of a formerly glaciated valley where it adjoins a larger, deeper, formerly glaciated valley. Line is oriented, so that it can be symbolised with teeth that point upstream into the hanging valley.			Barrell et al., 2011
	Landslide terrain	Prominent breaks on the slope originating a steeped topography with presence of linear features and small lacustrine basins or mass wasting deposits with signs of downslope flow associated to semi-circular scarps in the headwall.	No significant changes in color in comparison with moraine ridges or moraine terrain. Flowslide deposits are similar to moraine terrain. Fieldwork and high-resolution DEM are needed for proper identification.	Indicative of slope instability.	Soteres et al., 2020

	Rock avalanche deposit	Broken bedrock deposit from a destabilised slope.	Potential for confusion with landslide deposit.		
	Active river plain	Bare river bed or the episodic floodplain of a water course. Boundaries between contiguous floodplains are drawn at confluences.			Barrell et al., 2011
	Lake	Bodies of water surrounded by land (with no link to the sea).	Not always obvious in aerial photos (a counterpart photo is sometimes necessary). Extent of many lakes is seasonally variable – so their size can vary in different imagery and in the field.	Indicate impeded drainage and can result from rock basins formed by glacial over deepening.	Glasser and Jansson, 2008 Darvill et al., 2014 Izagirre et al., 2018
	River and stream	Channels of water draining a valley.		Indicate contemporary drainage routes and may be sourced from modern glaciers.	Izagirre et al., 2018
	Waterfall	Water flows over a vertical drop or a series of steep drops in the course of a stream or river.			
	Swamp	Low-lying area with wetland vegetation.	Potential for confusion with alluvial plain.		Barrell et al., 2011

	Alluvial fan formline	Formline denoting the down-slope direction on alluvial fans. Drawn schematically to give a visual sense of fan geometry.			Barrell et al., 2011
	Fault	Topographic step produced by Late Quaternary tectonic fault displacement or buckling of the ground surface.			Turnbull, 2000 Rattenbury et al., 2010 Barrell et al., 2011
	Cliff and terrace edge	Break of slope around flat-area edges. Line is oriented, so that it can be symbolised with ticks on the downslope side.	Potential for confusion with shorelines.	Individual terraces indicate down-cutting and aggradational events.	Glasser and Jansson, 2008
	Ice contact slope	Steep escarpment of predominantly glaciofluvial sediment that was deposited against the wall of glacier ice, marking the position of relatively static ice margin; an irregular scarp against which glacier ice once rested.	Possible confusion with morainic complexes or outwash plains.	Sediments deposited by streams draining tributary valleys onto/against glacier ice. Indicate the thickness and extent of ice.	Izagirre et al., 2018
	Palaeo-shorelines	A linear, smooth-continuous sediment outline, characterised by a mono elevation-interaction with topography. Only visible in the field or from high-resolution imagery.	Potential for confusion with linear features such as terrace edge, low-relief moraine ridge or, kame terrace.	Indicates former lake surface levels. Some shorelines indicate the presence of former ice-dammed lakes.	Glasser and Jansson, 2008 Leger et al., 2020

3.1.2 Compilation of a glacial geomorphological map

The glacial geomorphology of the area surrounding the Ahuriri River valley was mapped using a combination of remote sensing analysis and field work. The geomorphological mapping was conducted by visual interpretation of high-resolution (40 cm) individual co-registered aerial imagery (140 sheets) from the New Zealand (NZ) national dataset (2014). High-resolution Google Earth images were also used for the mapping in areas where cloud cover was present in photos, or where the three-dimensional (3D) landscape visualisation was required. Basic topographic variables (e.g. contours, rivers) are derived from the NZ LINZ Topographic online collection (Data Information NZ). The images and maps were overlain on a 15 m resolution digital elevation model (DEM) (Columbus et al., 2011) to provide topographic context, elevation range and to aid landform type (or shape) identification in areas of complex terrain.

Field campaigns in April 2019, February 2020, and November 2020 allowed me to crosscheck features mapped from remote imagery and maps. We did not cover the entire ~532 km^2 study area on the ground due to its remote and challenging nature, however we accessed the major landform features by helicopter, 4x4 vehicle, and general hiking tracks in the main river and side valleys.

From this field work and detailed visual analysis I mapped the shape, size, position and surface composition of glacier-related landform systems visible in the aerial imagery and topographical maps. All the landforms and objectives were mapped using ESRI ArcMap software (version 10.6.1). All files were projected in the New Zealand Transverse Mercator 2000 (NZTM2000) grid system. The map was exported into the Adobe Illustrator CS7 from ArcGIS for final editing (see main map in supplement). The full data sources used in this study are listed in Figure 3.1.

3.2 Cosmogenic surface exposure dating

Cosmogenic nuclides accumulate in the upper few meters of Earth's surface as a result of the interaction of cosmic rays and target elements in rocks and sediments. Measuring cosmogenic nuclides in rocks can give quantitative estimates of the timing and rate of geomorphological processes on the Earth (Cockburn and Summerfield, 2004). Utilising cosmogenic nuclides for surface exposure dating has become a powerful technique for Earth scientists (e.g. glacial geologists, geomorphologists, paleo-climate scientists), as it can be used to determine the age of the wide range of landforms from hundreds to millions of years old (Darvill, 2013).

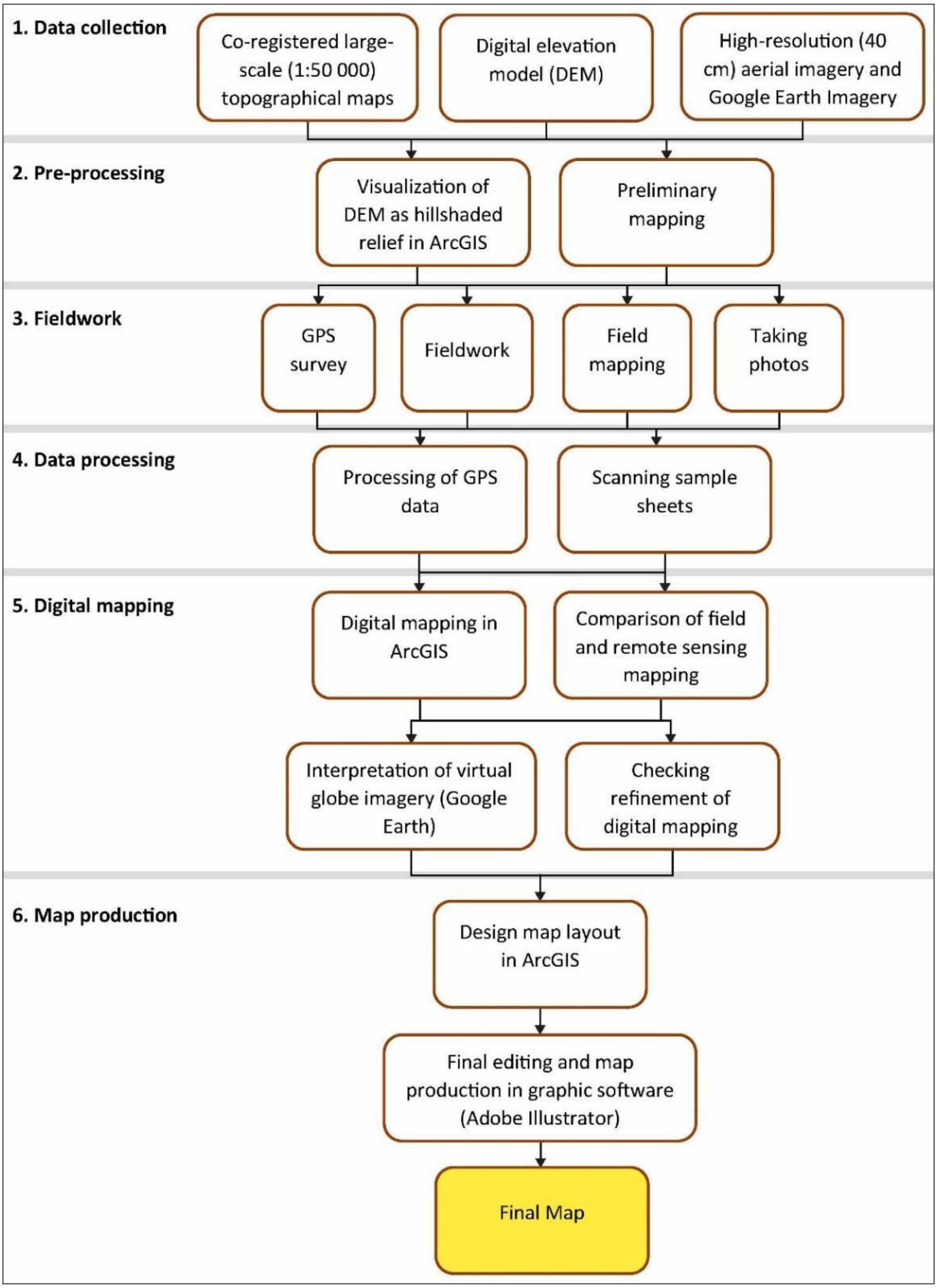

Figure 3.1 *Workflow summarising the datasets and methods used in the production of the final glacial geomorphological map of the Ahuriri River valley.*

In paleoclimate and glacial geology cosmogenic nuclides such as ^{10}Be, ^{14}C, ^{26}Al, ^{36}Cl (the radionuclides), ^{3}He, and ^{21}Ne (the stable noble gases), can provide information on when climate change has led to the growth of glaciers (von Blanckenburg and Willenbring, 2014), and can also determine the timing of ice retreat (Ivy-Ochs and Briner, 2014). A number of studies have recently used this technique to date paleo-glacial landforms all over the world (Balco, 2011). Among the suite of these cosmogenic nuclides in-situ produced ^{10}Be is one of the most widely used approaches, especially for dating the moraine boulders (e.g. Phillips et al., 1996; Heyman et al., 2011) or previously-glaciated bedrock surfaces (e.g. Bierman et al., 1999)

3.2.1 ^{10}Be surface exposure dating

Terrestrial cosmogenic nuclide measurements (^{36}Cl in this case) were first reported by Davis and Schaeffer (1955) and became popularised for ^{10}Be three decades later starting with Brown et al. (1982) when accelerator mass spectrometry became available (von Blanckenburg and Willenbring, 2014). Nowadays, ^{10}Be is the isotope used most often for dating glacial fluctuations over Quaternary timescales because it has a long half-life – 1.387 Myr (Chmeleff et al., 2010; Korschinek et al., 2010) and it is formed in quartz, which is commonly present in continental crust. In addition, ^{10}Be is used most widely, since it has the best-determined production rate and can be measured at low concentrations (Balco, 2020; Lifton et al., 2014). However, there are several restrictions associated with ^{10}Be dating approach, such as:

i) The largest potential errors in dating using the ^{10}Be nuclide comes from a sampling strategy. Since cosmic rays penetrate only the upper few centimetres of a rock, post-depositional exhumation, surface erosion, and/or movement of a boulder downslope can result in errors in the age calculated. Thus, careful and detailed visual inspections must be completed in the study area to check that the rock was deposited by the proposed mechanism, that it is in a stable position, and has not experienced surface erosion.

ii) Latitude and elevation factors must be measured and accounted for in the calculation of the exposure age since the cosmogenic nuclide production rates vary according to it. Near the poles, cosmic rays travel approximately parallel to the Earth's geomagnetic field lines, which allows all cosmic ray rigidities to enter Earth’s atmosphere (Lifton et al., 2005). Near the equator, high rigidities are required to penetrate the magnetic field in the tropics since the geomagnetic field lines are positioned approximately perpendicular to incident cosmic rays (Gosse and Phillips, 2001).

iii) Topographic shielding by adjacent mountains also affects the production rate of cosmogenic nuclides (Dunne et al., 1999; Schildgen et al., 2005). This is because the cosmic rays, which bombard Earth at a more or less equal rate from all sectors of the sky, will be reduced if the view of the sky is shielded. Therefore the 360 degrees skyline for each boulder must be carefully measured at each sampling site and ages are corrected for topographic shielding (where present).

3.2.2 Approach used in this thesis

In this thesis, I use the in-situ cosmogenic ^{10}Be nuclide to constrain the timing of glacier fluctuations in the Ahuriri River valley. The primary reason for using this nuclide is the lithology of the moraine boulders and glaciated bedrock surfaces at this site. Greywacke boulders and bedrock surfaces are frequently used in cosmogenic nuclide dating in New Zealand (e.g. Putnam et al., 2013a; 2013b; Strand et al., 2019), as they have large amounts of quartz minerals and veins, which yields ^{10}Be. ^{10}Be in quartz represents the most commonly used in situ nuclide-mineral pair. This is primarily because the production of in situ ^{10}Be is relatively simple due to the chemical structure of quartz (SiO_2), with little scope for compositional variability. In addition, the potential contaminants can be readily removed from quartz through simple acid leaching procedures, due to the lack of cleavage of quartz, which reduces the surface available for meteoric ^{10}Be adsorption (Eaves et al., 2018).

Application of cosmogenic ^{10}Be surface exposure dating requires numerous steps. Below I provide a detailed working protocol that I used mainly with my supervisors during the compilation of this thesis, such as sample collection (fieldwork), laboratory procedures, and exposure age calculations.

3.2.2.1 Field work

In the 2019–2020 austral summer, we targeted ice sculpted bedrock surfaces and the greywacke boulders embedded in well-preserved moraine ridges for cosmogenic surface exposure dating located middle and lower sections of the Ahuriri River valley as well as from the Canyon Creek and the upper right tributary of the Ahuriri River valley (Figure 3.2–3.4). Many of the boulders contained quartz veins of various thicknesses (5–30 mm). We targeted the top central surfaces (sample depths = 1–7 cm) of large, unmodified greywacke boulders that were deposited within the moraine surface. Boulders with steep sloping tops or displaying evidence for post-depositional surface erosion (e.g., fresh-looking surfaces, evidence of human activities etc.) were excluded.

Figure 3.2 *Sampled boulders from inner (northern) portion of the Ahuriri terminal moraine terrain. Moraine belt-3 (see chapter 5).*

Figure 3.3 *Sampled boulders from the prominent terminal/lateral moraine system. Moraine belt-1 (see chapter 5).*

Quartz veins were targeted using a portable rock saw, hammer, and chisel. For measuring the location and altitude of individual samples we used the Trimble GeoXH and eTrex 20 Garmin GPS. We measured the angle of the surrounding horizon using a clinometer and geological compass, which were combined with strike and dip observations of each boulder surface to calculate topographic shielding of the cosmic ray flux using the online exposure (formerly known as CRONUS-Earth) calculator (Balco et al., 2008). The dimension of each boulder (length, width, height) was measured by measuring tape. Each boulder has been photographed several times relative to the surrounding area (Figure 3.2–3.4). All field observations are given below in Chapter 5 and 6 (Tables 5.1–5.2 and 6.1–6.2).

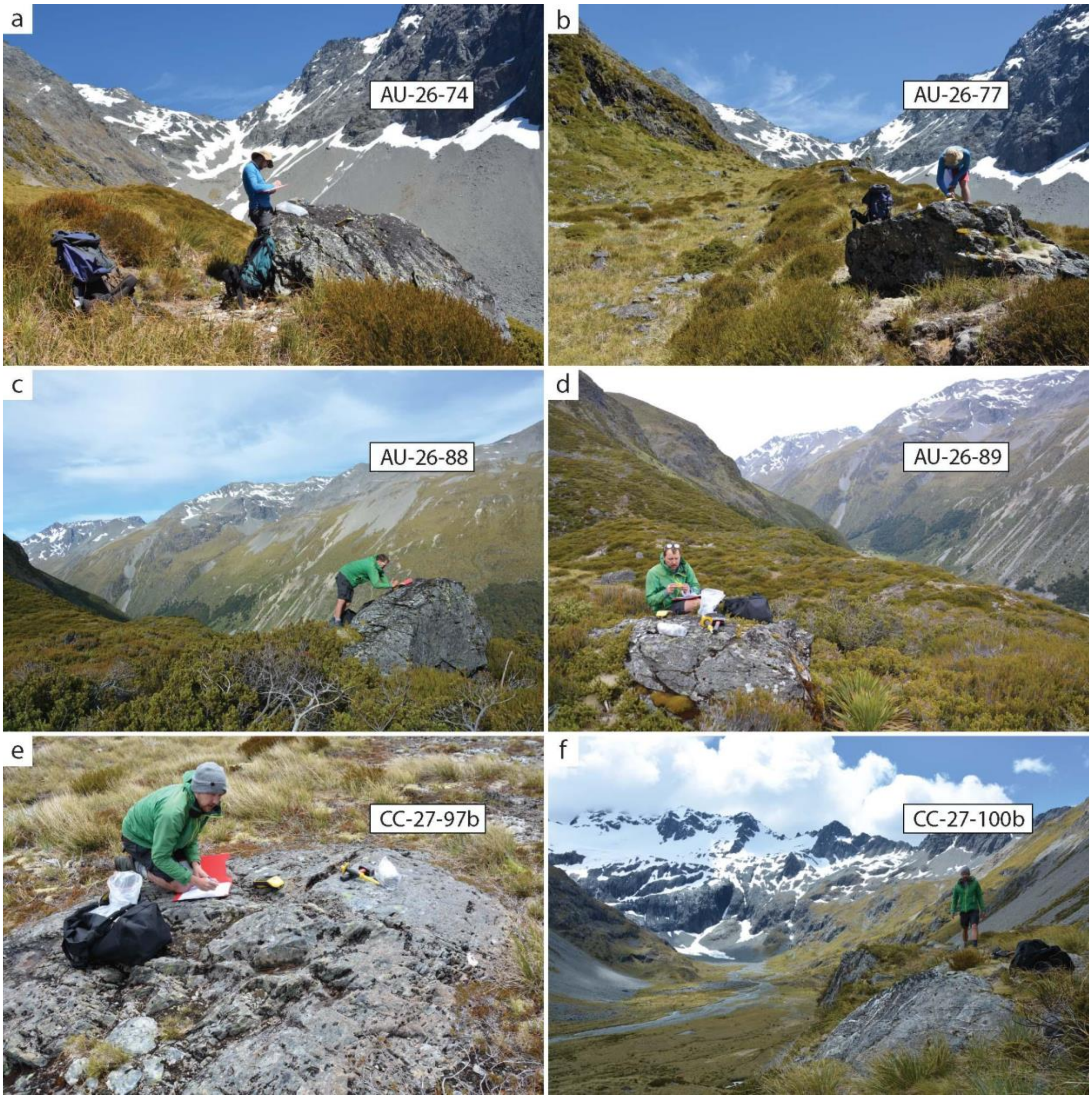

Figure 3.4 *Sampled boulders from inner (a–b) and terminal-lateral (c–d) moraine ridges, upper right tributary of the Ahuriri River valley. Sampled bedrock surfaces from Canyon Creek valley (e–f) (see chapter 6).*

3.2.2.2 Laboratory work

Physical and chemical preparation of samples for ^{10}Be dating took place at the Victoria University of Wellington laboratories. The thickness of all the collected samples, relative to the surface, was measured by digital callipers before jaw-crushing and sieving to isolate the 250–710 μm fraction. Each sample was then repeatedly passed through the Frantz magnetic separator to remove the magnetic minerals from quartz-rich fractions (Figure 3.5).

Figure 3.5 *Some illustrations from the laboratory work. a – partially crushed Graywacke sample; b – leached quartz fraction (250–710 μm); c – processing of the Iron (Ferum) columns; d – dried samples after Iron columns; e – precipitated beryllium; f – targeted samples.*

Next, three leaching steps were performed: i) twice in a 10% HCl solution for 24 hours each, ii) once in a 5% HF / 1% HNO_3 solution for 24 hours, and finally, iii) twice in a 2.5% HF / 0.5% HNO_3 solution for 48 hours each (Kohl and Nishiizumi, 1992). Samples were rinsed in MQ water and dried down following steps i and iii. The final leach has been done by 7M HF and Aqua Regia (concentrated HNO_3+HCl). A 1008.4 ppm ^{9}Be carrier from University of Melbourne was added to clean quartz (~280μg ^{9}Be to each sample, Tables 5.1 and 6.1) and was digested in concentrated HF. Beryllium was isolated using ion exchange chromatography (von Blanckenburg et al., 2004; Norton et al., 2008) to remove contaminants and $BeOH_2$ was precipitated at pH9 (Ochs and Ivy-Ochs, 1997). All the samples were calcined over a flame, mixed with niobium (Nb) powder at a ratio of 2:3 (BeO:Nb by volume) and packed into stainless steel targets.

3.2.2.3 Exposure age calculations

^{10}Be/^{9}Be ratios of all targets were measured by accelerator mass spectrometry at Lawrence Livermore National Laboratory (CA, USA). Samples were measured relative to the 07KNSTD standard (^{10}Be/^{9}Be = 2.85 x 10^{-12}) (Nishiizumi et al., 2007). Moraine exposure ages were calculated using the Macaulay calibration dataset of Putnam et al. (2010b). For comparison, I also present ages using the primary global production rate calibration dataset of Borchers et al. (2016). I assumed a rock density of 2.7 g/cm^3 and applied a sample thickness correction for each sample based on laboratory measurements made prior to crushing (Tables 5.1 and 6.1).

Age calculations were carried out using the online exposure (formerly CRONUS-Earth) calculator, version 3 (Balco, 2011). This version calculates exposure ages using the scaling methods: St (Stone, 2000), Lm (Balco et al., 2008), and LSD (Lifton et al., 2014). In addition, the chi-squared outlier detection routine was used from the exposure age calculator version 3 (Balco, 2017a, 2017b) to assess if the spread in ^{10}Be exposure ages for a single moraine belt is consistent with a synchronous period of deposition. For consistency with previous studies from the Southern Alps (e.g. Putnam et al., 2013a; 2013b; Strand et al., 2019), I use results from the Lm scaling method and this scaling decision does not affect overall conclusions.

Canyon Creek and the upper right tributary of the Ahuriri River valley (see chapter 6) lie above the elevation (~1200 m) at which snow lies persistently during the winter months in the Southern Alps, raising the possibility that exposure to cosmic radiation at our samples may have been partially shielded by seasonal snow cover. Kaplan et al. (2010) observed that snow cover at ~1500 m a.s.l. in Irishman Stream basin (~35 km from my study sites) has rarely been thicker than 2 m or so over the last few decades allowing salient boulders to stand out prominently from the snow blanket. Most of the boulder heights from my study site range from ~1 to 3 m and they are located on the crest of the moraine ridges, thus I am confident that snow shielding at these sites is negligible relative to other uncertainties (e.g. measurement, production rate scaling). For bedrock samples, snow cover may be more significant, yet the magnitude and duration of seasonal cover remains unconstrained. Theory indicates that a 1 m of average density snow (0.3 g/cm^3) covering a rock surface for 4 months of the year reduces ^{10}Be production via spallation by ~5 % (Gosse and Phillips, 2001), which equates to 500-600 years for my bedrock sample sites. I present ages without this speculative correction, but acknowledge that the apparent ages may underestimate the true age by a few centuries. Overall, bedrock samples comprise only a small portion of my data and my assumptions outlined above do not alter the main conclusions of this study.

3.3 Palaeo climate reconstruction

3.3.1 Mountain glaciers as a palaeoclimate proxy

Mountain glaciers are highly visible indicators of global climate change as they are sensitive to variations in temperature and precipitation (Oerlemans and Fortuin, 1992). Furthermore, mountain glaciers affect local geomorphological processes and hydrology (Benn and Evans, 1998); building records of their past changes yield important data concerning the timing and magnitude of past climate-landscape change (Mackintosh et al., 2017; Balco, 2020).

The type of mountain glacier depends on the shape of the landscape as well as glacier size, which is dependent on local climate. e.g. valley glaciers flow at least in part down a valley and are longer than they are wide, while the cirque glaciers are short and wide, limited to valley-heads. Glaciers can be divided into areas of accumulation and ablation, separated by the equilibrium line altitude (ELA) (often called the summer snowline, or simply the snowline) where the accumulation equals ablation on a yearly time scale (Ohmura et al., 1992), i.e. accumulation of snow is exactly balanced by ablation. There is therefore a very close connection between the ELA and local climate, particularly air temperatures and solid precipitation (Benn and Lehmkuhl, 2000).

Glaciers always flow in the direction of the ice surface slope. The flow, speed (velocity), and movement of a glacier are controlled by several factors (Jiskoot et al., 2011) such as ice thickness and steepness, ice temperature and density, valley geometry, bedrock conditions (hard, soft, frozen or thawed bed), subglacial hydrology, terminal environment (land, sea, ice shelf, sea ice), and mass balance (rate of accumulation and ablation). When the ice in a valley glacier moves from accumulation area to that of ablation, it acts like a conveyor belt – picks up rock debris from the valley walls and floor, transporting it in, on, or under the ice. When this debris material reaches the lower, peripheral parts of the glacier, it exits the glacier margins and accumulates in landforms known as moraines. Moraines formed along the lateral glacier margins are termed lateral moraines, while those formed immediately in front of the glacier are termed terminal moraines. In general, lateral moraines have high preservation potential as less subject to postglacial fluvial erosion but do not always allow for the clear constraint of past glacier length, while the terminal moraines are more useful since they record the maximum extent of the glacier during a given glaciation, but have the low potential of preservation. Palaeoclimatic reconstructions based on the terminal and lateral moraine deposits commonly make use of estimates of the associated equilibrium-line altitudes (ELAs) (Benn and Lehmkuhl, 2000) which can be used to extract quantitative information about paleo temperature and precipitation (Mackintosh et al., 2017). In New Zealand, this has also been done for 26 glaciers using the Little Ice Age (LIA) moraine sequences (Lorrey et al., 2014).

Well preserved moraines from the Southern Alps provide a good opportunity to develop an improved understanding of ice ages and glacial-interglacial transitions (Putnam et al., 2013a). Dating of the moraines using cosmogenic exposure techniques such as ^{10}Be is providing exciting and important information on the duration, timing, and scale of the Late Quaternary glaciation, as well as providing additional information about the past climate (Balco, 2011, 2020).

3.3.2 Reconstruction of equilibrium line altitude

The accurate reconstruction of past equilibrium-line altitude (ELA) (commonly called ‘snowline’) requires accurately determining the extent and morphology of the former glaciers.

This along with the determined age of the reconstructed glacier enable us to use past snowline as a proxy for palaeo climatic conditions (e.g. Porter, 1975; Benn et al., 2005). Detailed geomorphological mapping (e.g. Chandler et al., 2018) is required for accurate reconstruction of past glacier extent. Furthermore, sufficient geomorphic evidence, such as terminal-lateral moraines and trimlines allow the shape of the former glacier to be most accurately reconstructed (Benn et al., 2005).

The most common methods in reconstructing former ELAs or snowlines are:

a) Balance ratio (BR),

b) Accumulation area ratio to the total area (AAR),

c) Maximum elevation of lateral moraines (MELM),

d) Toe-to-headwall altitude ratio (THAR),

e) Median elevation of glaciers (MEG),

f) Lowest cirque elevations or Cirque-floor altitudes.

a) The Balance ratio (BR) method was established by Furbish and Andrews (1984) and is based on two assumptions: (i) the accumulation and ablation gradients are approximately linear; and (ii) the ratio between these two components is known. The method can only be used where good topographic data are available, allowing for detailed reconstruction of the former glacier surface contours (e.g. Benn and Gemmell, 1997). The BR method is well-adjusted for snow-fed, clean glaciers in well-studied regions, but it is not suitable for glaciers with a strong influence of debris cover in ablation areas or snow avalanches in accumulation areas (Benn and Lehmkuhl, 2000).

b) The Accumulation area ratio (AAR) method is well-suited for snow-fed, clean glaciers in well-studied regions. Similar to the Balance ratio (BR) method the AAR method also requires contoured maps of former glacier surfaces, and can therefore only be applied where detailed topographic maps are available. This method is based on the assumption that the steady-state AAR of former glaciers is 0.6±0.05 a value derived from temperate glaciers from different regions of the world (Porter, 1975), however, steady-state AARs can also be changed through time on a single glacier system (Clark et al., 1994). This method assumes that the accumulation area of a glacier occupies a fixed proportion of the total glacier area (Benn and Gemmell, 1997). Knowledge of mass-balance gradients is not required for this method, however a 2D reconstruction of the former glacier surface is needed to calculate the AAR. Supra-glacial debris cover on snouts of mountain glaciers strongly affects the AAR. Glaciers with extensive debris-cover in ablation areas have lower AARs than debris-free glaciers, due to the effect of thick debris on lowering ablation and increasing the size of the ablation area required to balance accumulation (Clark et al., 1994).

c) Maximum elevation of lateral moraines (MELM) method is based on the highest lateral moraine ridges that would give a good indication of the minimum altitude of a former snowline, because net annual glacier ablation, and hence ice-marginal deposition, only occur below the snowline. Thus, the former snowline must lie above the highest elevation of the lateral moraines (Benn and Lehmkuhl, 2000). However, sometimes it is difficult to assess whether moraine deposition started immediately downglacier of the snowline or whether or not a lateral moraine is preserved entirely in the upper part. Thus, again, only a lower limit for snowline can be estimated (Atle, 1992). The MELM method does not require accurate topographic information for the whole glacier but the only accurate determination of lateral moraines is sufficient.

d) Toe-to-headwall altitude ratio (THAR) (ELA = Lowest elevation of the glacier plus vertical range multiplied by a ratio) assumes that the ELA lies at some fixed proportion of the vertical distance between the lowest and highest glacier limits (a ratio between the maximum and minimum altitude of a glacier). This method has been used as a quick estimate to calculate the ELA with the ratios of 0.35–0.4 for the best results (e.g. Meierding, 1982; Murray and Locke 1989). The THAR method is very simple and does not require glacier hypsometry or mass balance. Instead, defining the effective upper limit of palaeo glaciers can be questionable, or impossible in some cases (Benn and Lehmkuhl, 2000). In New Zealand, this method was used by Chinn (1996) to examine LIA positions for the snowline/ELA.

e) The median elevation of glaciers (MEG) (e.g. Manley, 1959; Østrem, 1966). This method gives best results at small, geometrically regular glaciers with "normal" area/altitude distribution (Porter, 1981). Otherwise, empirical evidence from modern glaciers (e.g. Meier and Post, 1962) proposes that the MEG overestimates the ELA. Furthermore, this method fails to consider changes in valley morphology, which strongly impact the area-elevation distribution of a glacier (Atle, 1992).

f) Lowest cirque elevations or cirque-floor altitudes have been widely used as a measure of the ELA of former cirque glaciers (Hastenrath, 1971; Andrews, 1975). Although this method is rapid, the elevation of a cirque basin does not necessarily closely correspond to the ELA of the former glacier (Richardson and Holmlund, 1996). This method is also highly subjective because cirque floors are not always easily identifiable (Murray and Locke, 1989). In addition, in some cases cirque-floor altitudes are strongly controlled by pre-existing relief, particularly the location of Tertiary erosion surfaces (e.g. Haman and Embleton, 1988). Further limiting their usefulness as palaeoclimatic indicators is that cirques develop cumulatively over multiple glacial cycles and cannot be assigned to any particular glacial event (Benn and Lehmkuhl, 2000). This method, is, however, better for a regional approximation of ELA (Andrews, l975) by implication, average climatic conditions over long time periods (Robinson et al., 1971).

3.3.3 Approach used in this thesis

In this study I used the accumulation area ratio (AAR) of 2:1 or 0.67/0.33 which is well adopted and frequently used technique for snowline estimation in New Zealand (e.g. Porter, 1975; Kaplan et al., 2010; Eaves et al., 2016, 2017). The lowest terminus limits used in this study is based on my ages from the terminal moraine features. Other glacier limits (e.g., marginal, headwall) were defined from a detailed glacial geomorphological map (Tielidze et al., 2021) and high-resolution aerial imagery. For the palaeo glacier area uncertainty I used a buffer method which is broadly adopted for modern glacier mapping (e.g., Granshaw and Fountain 2006; Tielidze and Wheate, 2018). A buffer width of 50 m was created along the glacier outline, and the uncertainty term was calculated as an average ratio between the original glacier area and the area with a buffer increment. I manually mapped the past glacier outlines and reconstructed glacier surface contours at 50 m intervals. Contour lines were drawn mimicking a typical glacier surface topography (consistent with principles of glacier flow): convex near the terminus, horizontal at mid-elevations, and concave near the headwall. I assume that the largest source of error associated with this method is the reconstruction of glacier surface contours. Nevertheless, this uncertainty is considered to be randomly distributed and unlikely to introduce major deviations (Nesje and Dahl, 2000).

Based on the reconstructed glacier contour lines I created 30 m resolution digital elevation models (DEMs) in ArcGIS software 10.6.1. The area between each pair of successive contours was measured automatically in ArcGIS by ELA calculation toolbox (Pellitero et al., 2015). Empirical studies of modern glaciers have shown that under steady-state conditions the AAR typically falls between 0.5 and 0.8, meaning that the accumulation area occupies approximately two-thirds of the glacier's total area (Meier and Post, 1962). The AAR of 0.67 with a nominal 1 standard deviation uncertainty of 0.05 is used in this study, which is standard for New Zealand glaciers (Chinn et al., 2012) and the commonly-adopted value for palaeoglacial reconstructions in this region (e.g. Kaplan et al., 2010; Putnam et al., 2012; Eaves et al., 2016, 2017).

I also used the Maximum Elevation of Lateral Moraines (MELM) method as a supplementary tool for snowline estimation. This was due to the absence of a terminal moraine feature that could potentially accompany the prominent lateral moraine ridges in Canyon Creek (44°11'28"S, 169°35'34"E) and in the upper right tributary of the Ahuriri River valley (outer-1, 44°7'57"S, 169°38'34" E and outer-2, 44°7'55"S, 169°38'30"E) (see chapter 6). In this study, the highest point of lateral moraine feature was taken as the lower limit of palaeo snowline in the Canyon Creek and in the upper right tributary of the Ahuriri River valley (outer moraine 1 and 2) (see chapter 6).

3.3.4 Palaeo temperature reconstruction

In order to reconstruct past temperature conditions (relative to present (1981–2010) (NIWA, 2012)) associated with the palaeo ELA, I translate the magnitude of ELA change, relative to present to temperature change using a lapse rate and assuming no change in precipitation. To reflect the high uncertainty in the key variables for ELA-temperature estimation, Eaves et al. (2016, 2017) employed a Monte-Carlo approach that repeatedly resampled distributions of the present-day ELA, the AAR value for the reconstructed glacier, and the temperature lapse rate. Here I follow the same approach. To derive estimates of the present-day ELA, I used recently mapped modern glacier outlines from the Ahuriri River valley (Tielidze et al., 2021) along with a medium resolution (15 m) DEM (Columbus et al., 2011) and applied the AAR automatic approach (Pellitero et al., 2015) with the same ratio (0.62–0.72). This gave me an elevation of present-day ELA at 2000±50 m a.s.l. This value closely matches with a recently-reported snowline elevation of 1957 m a.s.l. for Thurneyson Glacier based on four-decades (19981-2010) of snowline observations from the National Institute of Water and Atmospheric Research (Lorrey et al., 2022). The present-day temperature lapse rate in New Zealand is assumed to be

~5 °C km^{-1} (Norton, 1985; Tait and Macara, 2014), although it is poorly constrained by observations. Thus, I follow Eaves et al. (2016) in selecting temperature lapse rates from an evenly-distributed range from –4 to –7 °C km^{-1}. The algorithm repeatedly resamples these input parameters providing a population of *p*ELA and *d*T estimates that represent the window of parameter uncertainty.

The approach that I apply to reconstruct past temperatures assumes that temperature changes are the main driver of glacier changes in the Southern Alps, and specifically that precipitation changes and other meteorological variables (e.g. cloud cover) play a minor role. While this assumption is a simplification, it is justifiable given the evidence from mass balance sensitivity studies on present-day glaciers in the Southern Alps (e.g. Anderson et al., 2010; Anderson and Mackintosh, 2012) as well as sensitivity analyses conducted in palaeoglaciological modelling studies that target a similar time period (Doughty et al., 2013; Eaves et al., 2017). I revisit this assumption and its influence on my findings in the discussion (section 6.4.3).

CHAPTER 4: GLACIAL GEOMORPHOLOGY OF THE AHURIRI RIVER VALLEY

4.1 Introduction

Detailed geomorphological mapping of ice-related and post-glacial landforms is widely used to explain past glacial fluctuations and dynamics (Chandler et al., 2018). Late Quaternary glaciation has created well-preserved landforms in the Ahuriri River valley that can be used to understand palaeo-glacier extent and behaviour. Thus, there was a need to provide a detailed geomorphological description and map for this area.

In this chapter I present the first detailed glacial geomorphological description of the landform assemblages produced by the former Ahuriri Glacier. My goal was also to create a detailed 1:38,000 scale glacial geomorphological map of this area and provide a geomorphological context to support future geochronological work. For this purpose, I selected a region extending approximately 45 km downstream from the headwaters of the Ahuriri River covering an area of about 532 km^2 (Figure 4.1). I provided high-resolution spatial information for all the glacial-related landforms shown on the map (see main map in supplement). This map provides an essential basis for constructing reliable geomorphological and geochronological reconstructions in the southern mid-latitudes.

4.2 Results

The 1:38,000 scale glacial geomorphological map of the Ahuriri River valley (see main map in supplement) presents a variety of glacial-related landform assemblages that are summarised below and in Table 3.1. These include modern glaciers, rock glaciers, cirques, ice-scoured bedrocks, ice-contact slopes, moraines (moraine ridges and hummocky moraines), outwash plains, and alluvial fans. All landform types were classified and manually digitised as polyline and polygon shapefiles. The main map also includes other landform types (e.g. steep eroded slopes, active scree slopes, vegetated scree slopes, debris cones, river terraces, active river plains, alluvial plains, etc.) and topographic features (e.g. rivers, lakes, peaks, fault lines, etc.), which are useful for topographic and physiographic context.

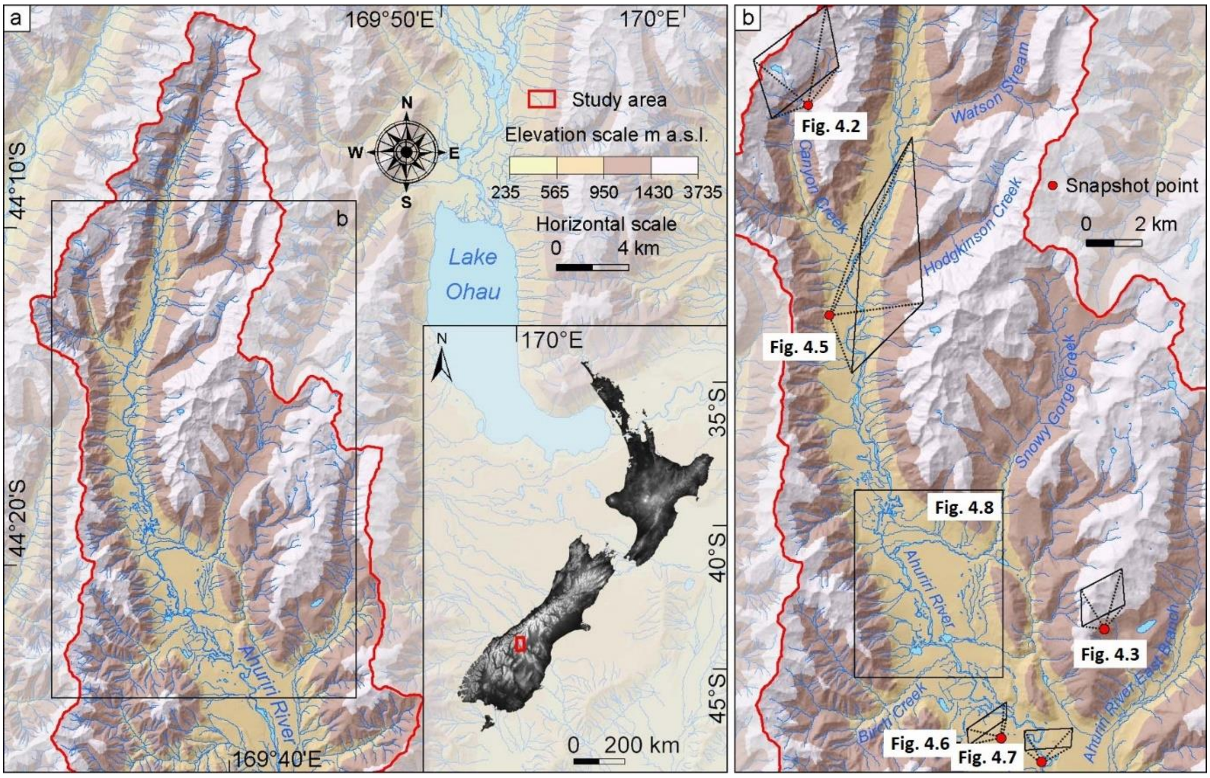

Figure 4.1 *a – Hillshaded 15 m Digital Elevation Model (Columbus et al., 2011) showing the area covered by the map presented with this chapter. b – The red circles indicate photograph locations.*

4.2.1 Modern glaciers

There are very few modern glaciers in the Ahuriri River basin and they are mainly located in the headwater of the main river. The largest glacier of the entire catchment (Thurneysen Glacier – 0.9 km^2) is located in the headwater of the Canyon Creek (44°9'56"S, 169°35'55"E) (Figure 4.2). Modern glaciers were identified using the most current version of the Global Land Ice Measurements from Space (GLIMS) glacier database. These outlines come to GLIMS via the Randolph Glacier Inventory (version6 – Pfeffer et al., 2014). Original outlines are primarily from Chinn (2001), which were derived by manual delineation using geodetic maps and oblique aerial photography collected in 1978. The GLIMS database has had several regional updates (e.g. Gjermundsen et al., 2011), with the first comprehensive revision published recently by Baumann et al. (2020). This recent update used semi-automatic classification, based on average resolution (~15m) Landsat 8 and Sentinel 2 imagery from the year 2016. While this approach is well-suited for national-scale assessment, the resolution is less appropriate for a larger-scale mapping such as that presented here. I thus took an independent approach to glacier delineation, which involved manual modification of the previous GLIMS outlines. This manual classification high-resolution (40 cm) aerial imagery from Land Information New Zealand (Data Information NZ). Overall, I identified 22 modern glaciers in the Ahuriri River basin with total area of about 2.2 km^2.

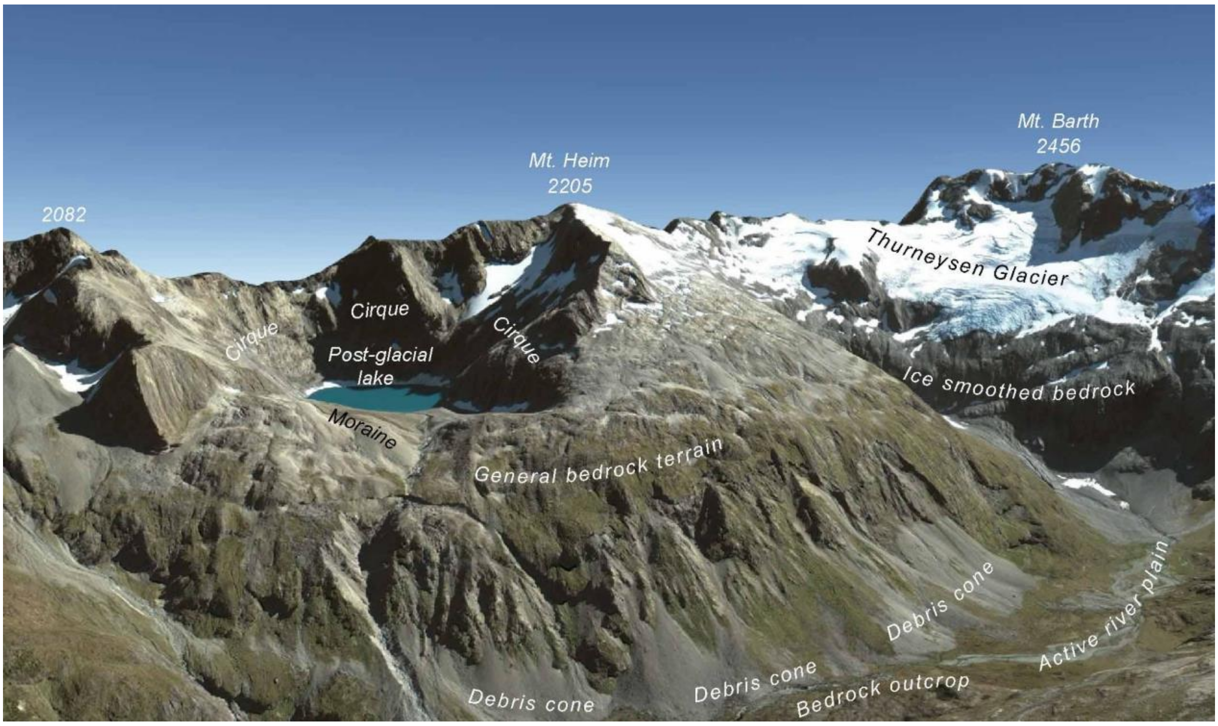

Figure 4.2 *Modern glacier and postglacial landscape in the Canyon Creek valley (© Google Earth 07/03/2010). Figure 4.1 shows exact location of this area.*

4.2.2 Rock glaciers

Surface morphology and size makes rock glaciers easily identifiable in high-resolution imagery. Based on permafrost presence and mobility of rock glacier, three activity states are distinguished: active (containing ice, moving), inactive (containing ice, not moving), and relict rock glaciers (not containing ice, not moving) (Martin and Whalley, 1987). Latest rock glacier inventory for the Southern Alps has been recently completed by Sattler et al. (2016) accounting majority of rock glaciers to the east of the Main Divide in high-altitude areas (Sattler et al., 2016). Based on this study almost 60% of the mapped rock glaciers were classified as relict features that no longer contain ice. Rock glaciers from the Ahuriri River valley were omitted in this study.

Morphological evidence for rock glacier identification includes ridges and furrows, lateral slopes and steep front, collapse structures, flow structures and distinct changes of the slope in the rooting zone (Schmid et al., 2015). For digitization of the individual rock glacier boundaries I also followed the most recent polygon-based rock glacier inventory by Wagner et al. (2020). The distribution of rock glaciers in the Ahuriri River valley is mainly related to the local topography and climate of the Southern Alps and related effects such as Quaternary glaciation history. In total, ten rock glaciers are identified with total area of ~0.7 km^2. Prominent rock glaciers are located at the headwater of the main river valley (44°4'33"S, 169°40'15"E) and at the headwater of the Watson Stream (44°9'52"S, 169°42'40"E). Remaining rock glaciers are located in the Ahuriri River East Branch basin (Figure 4.3). The largest rock glacier (44°20'55"S, 169°43'19"E), with total area of ~0.2 km^2, is situated ~500 m above Dumb-bell Lake.

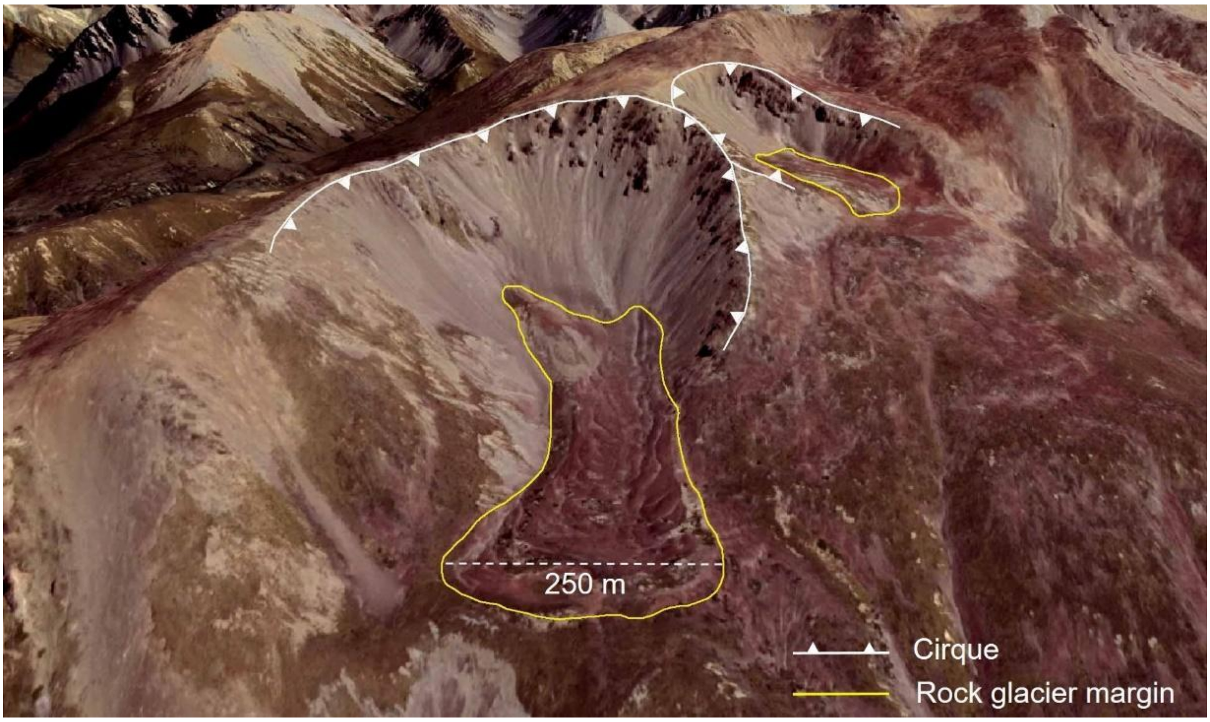

Figure 4.3 *Rock glacier terrain in the Ahuriri River East Branch basin (© Google Earth 26/01/2018). Figure 4.1 shows exact location of this area.*

Based on imagery interpretation using commonly recognised visual diagnostics, such as appearance of the upper surface, morphology, convexity, and steepness of the frontal slope, I considered the majority in the Ahuriri River valley as inactive or relict rock glaciers. Although distinguishing inactive rock glaciers from active or relict features is generally difficult even based on high-resolution aerial imagery and thus essentially associated with high uncertainty (Nyenhuis, 2006). Similar relict rock glaciers were also found by Sattler et al. (2016) on the eastern slope of the Ōhau Range, next to the Ahuriri River East Branch (e.g. 44°18'42"S, 169°46'42E).

4.2.3 Cirques

Cirques are amphitheatre-shaped hollows on the headwater slopes of the main river valley (e.g. 44°4'29"S, 169°39'51"E). They usually display sharp boundaries with the surrounding terrain. Cirques are concentrated in areas that have been deglaciated since the Last Glacial Maximum and the concave shapes of glacial cirques are open on the downhill side. The features are particularly well-developed in tributary valleys such as Ahuriri River East Branch (44°17'57"S, 169°43'31"E), Snowy Gorge Creek (44°15'38"S, 169°39'22"E), and Canyon Creek (44°10'43"S, 169°34'38"E). The floor of some cirques most often contain small lakes (tarns) behind the dam (moraine or bedrock), which mark the downstream limit of the glacial over deepening (Figure 4.2).

4.2.4 Ice-sculpted bedrock

Many examples of ice-sculpted bedrock landforms are found in my study area. They include broad benches and flattened spurs on former glacier valley sides as well as valley floors and cirque basins. A prominent example is found on the eastern slope of the main river valley at the conjunction of Watson Stream next to the largest landslide terrain (44°12'22"S, 169°38'15"E). Also notable is the Canyon Creek valley, where the full spectrum of ice sculpted bedrock is presented, ranging from cirque headwalls (44°10'9"S, 169°35'11"E) to the valley floor (44°11'26"S, 169°35'23"E) (Figure 4.2 and 4.4). Relatively small features of ice-sculpted bedrock are present at the head of the main river valley (44°5'3"S, 169°40'57"E), as well as Ahuriri River East Branch (44°17'5"S, 169°45'5"E) and Watson Stream (44°8'42"S, 169°41'34"E). The ice-sculpted bedrock terrain in the study area has been primarily identified using satellite and aerial imagery due to difficulty of access, although ice-sculpted bedrock in the middle and lower sections of the main river valley were confirmed in the field.

Figure 4.4 *Ice sculpted bedrock presented in the valley floor and the eastern slopes of the Canyon Creek valley.*

4.2.5 Ice-contact slopes

These accumulations represent ice-contact glaciofluvial deposits that have been mainly formed over the floor of the valley or low-lying bedrock outcrops. The topography marks former marginal or terminal positions of both Ahuriri and side valley glaciers. The best example of this feature is presented in the middle section of the main river valley (largest terminal-lateral moraine ridge), while relatively small features are present in the Ahuriri River East Branch basin. Even smaller and relatively young ice-contact slopes are also located in the headwater of the main river valley.

4.2.6 Moraine terrains

Moraines can form as a result of a different geomorphological processes, depending on ice dynamics, sediment characteristics, and the location on the glacier at which the moraine forms (Benn and Evans, 1998). Processes of moraine formation can be conditionally divided into active and passive. Active processes form or rework moraine deposits directly through glaciotectonism. This includes moraine ridges of pushing and thrusting blocks, which often consist of tills and reworked proglacial deposits (Bennett, 2001). Passive processes include the placement of chaotic supra-glacial deposits around a former glacier margin with limited processing (reworking), usually with the formation of hummocky or hilly moraines. These moraines are composed of supraglacial deposits from the ice surface (Kjær and Krüger, 2001).

4.2.6.1 Moraine ridges

The mapped moraine ridges in the Ahuriri River valley are mainly single, linear or curvilinear, elongate features exhibiting ∼5 to 40 m relief that demarcates the limits of former glacier margins. They are often discontinuous, and it is rare to find entire lateral-terminal moraine ridges. The prominent terminal-lateral moraine system (44°15'44"S, 169°36'41"E) runs for approximately four kilometres in the middle section of the main river valley between 760 and 800 m a.s.l. This feature comprises fragmentary crested ridges (divided by meltwater channels or river streams), usually up to a few hundred metres long and less than 40 metres high (Figure 4.5). Other lateral moraine ridges are present on the left bank of the Ahuriri River (44°22'36"S, 169°40'6"E; between Snowy Gorge Creek and Ahuriri River East Branch). Two more less-well defined ridges located at the lowest section of the main valley, between Ahuriri and Avon Burn rivers. The length of this first possible moraine ridge is ~2.1 km (44°25'11"S, 169°39'51"E) while the second one is ~1.7 km long (44°25'40"S, 169°40'50"E). A smaller ~1 km-long moraine ridges extends below a well-preserved cirque in the Ahuriri River East Branch basin at an elevation between 1440–1220 m a.s.l. (44°19'4"S, 169°42'38"E). Several well-preserved terminal and lateral moraine systems are discovered near the head of the valley (the unnamed third right tributary) of the Ahuriri River, at an elevation of 1280 and 1190 m a.s.l., ranging from 150 to 500 meters long (44°7'56"S, 169°38'39"E). Groups of minor and relatively recent moraine ridges are frequent in the headwater of the main river valley, Canyon Creek, and Snowy Gorge Creek, where they exhibit sharp crest lines.

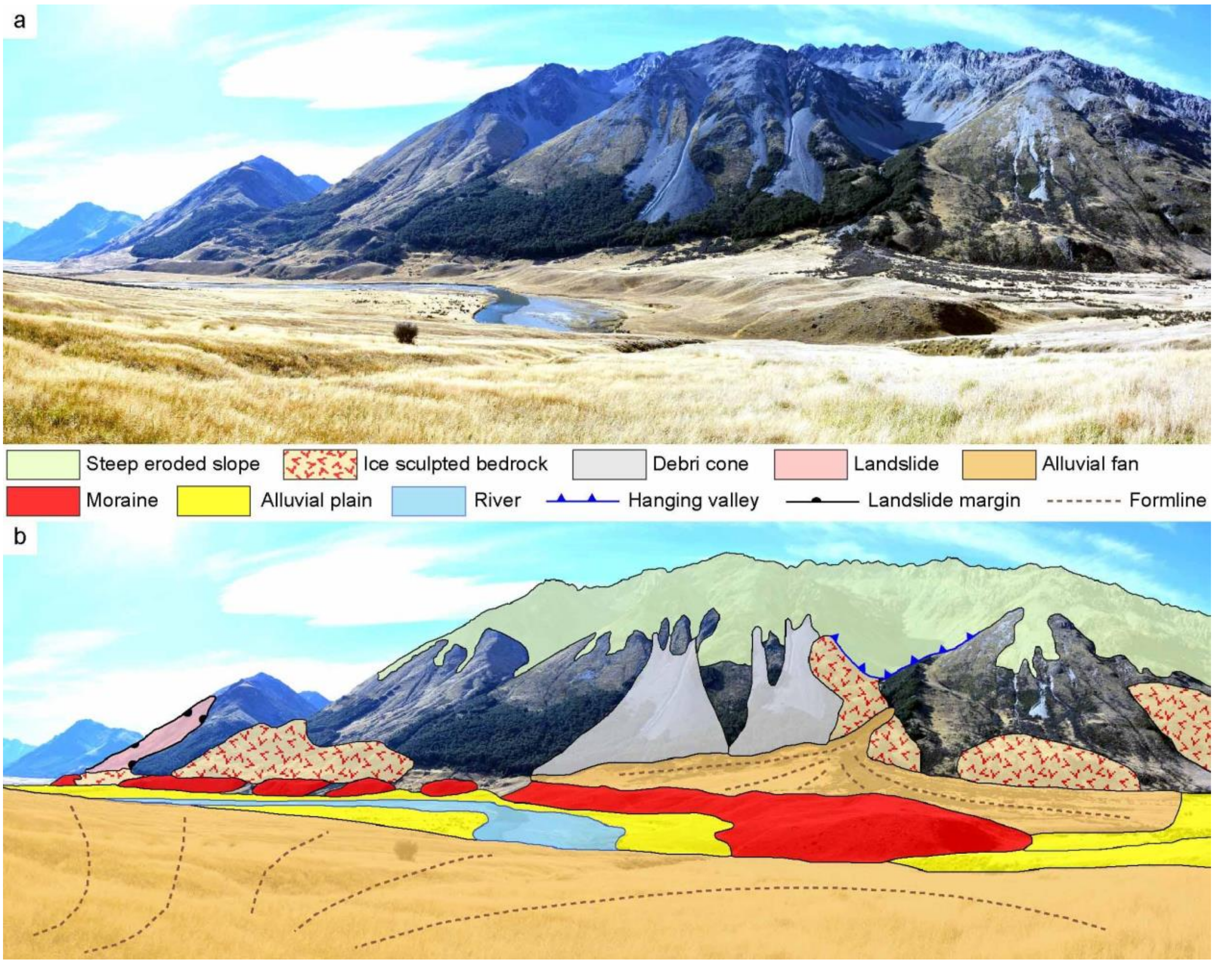

Figure 4.5 *Glacial geomorphological mapping comparison in 3D. a – Lateral-terminal moraine ridge in the middle section of the Ahuriri River valley with surrounding area. b – Key landscape elements are shown in the accompanying sketch. Figure 4.1 shows exact location of this area.*

4.2.6.2 Hummocky moraines

One large hummocky moraine unit (~3.5 km length and 1.6 km width) was identified in the lower section of the main river valley, defining a former ice margin (~760 m a.s.l.). The surface of this landform is significantly broader than moraine ridges described above and are not sharp-crested, however, it is often scattered with large 1 to 2 metre (diameter) sized greywacke boulders. Two small ponds occur on the surface of this terrain. The upper surfaces of the hummocky moraine in some places are occasionally lined by low hardly distinguishable relief ridges that range in height from 1 to 5 metres above the smoothed rounded surface (Figure 4.6).

The middle part of the terrain is cut by meltwater channels dividing it into two parts, northern (inner) (44°23'54"S, 169°39'48"E) and southern (outer) (44°24'36"S, 169°40'25"E).

A smaller hummocky moraine system was identified near the confluence of Ahuriri River and Snowy Gorge Creek (44°21'6"S, 169°39'16"E). The surface of this terrain is strongly modified by meltwater channels and possible by Snowy Gorge Creek. Several small pond and swamps occur on the surface of this hummocky system.

Figure 4.6 *Hummocky moraine surface in the lower section of the Ahuriri River valley. Figure 4.1 shows exact location of this area.*

4.2.7 Outwash plains

A large outwash plain is present in the lowest section of my study site. It is characterised by broad, gently sloping surfaces of glaciofluvial gravel and sand. The plain was identifiable on aerial imagery as a planar surface with clear meltwater channels with several terrace levels were identified within the outwash. These have been mapped separately along with main river stream and active river bed dividing the outwash surface into two sections (Figure 4.7).

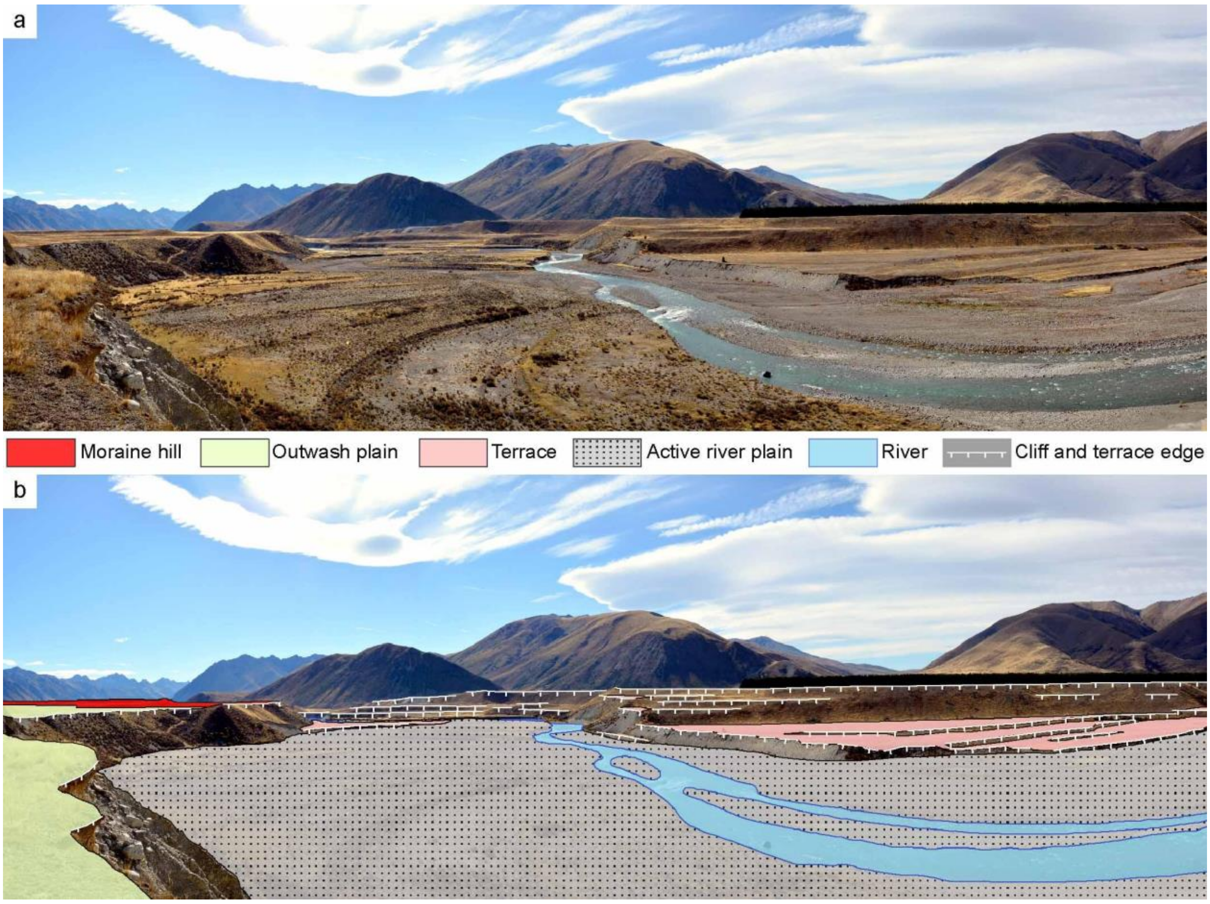

__Figure 4.7__ Glacial geomorphological mapping comparison in 3D. a – The outwash surface and incised terrace steps in the lowest section of the Ahuriri River valley cut by main river stream and active river plain. b – Key landscape elements are shown in the accompanying sketch. Figure 4.1 shows exact location of this area.

4.2.8 Alluvial fans and debris cones

Alluvial fans are common throughout the Ahuriri study site, some of them associated with drainage originating in side valleys. Fans vary greatly in size depending on the amount of source material. Most of the fans on aerial imagery are characterised by conical or semi-conical shapes. The majority of the fans are observed on the right side (west relative to Ahuriri River) slopes across the main river stream, while the largest alluvial fan is located at the conjunction of the Ahuriri and Snowy Gorge Creek (44°20'37"S, 169°38'35"E) (Figure 4.8). The surface of this fan is strongly modified by fluvial processes. Most of the other fans are less eroded and often vegetated by shrubs and grasses.

Debris cones in the Ahuriri River valley are mostly attributed to smaller creeks that increase their flow seasonally during periods of increased snowmelt or rainfall.

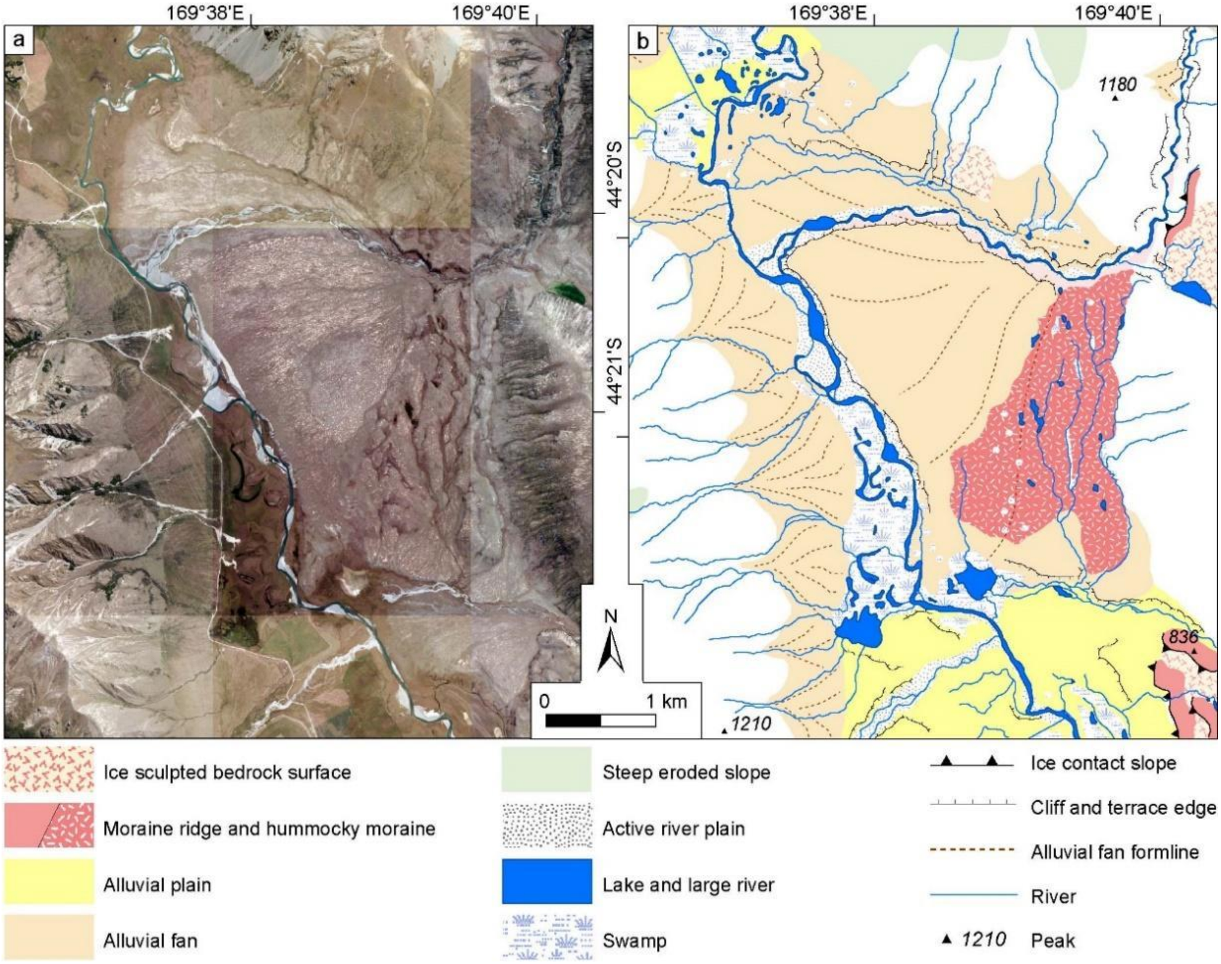

Figure 4.8 *a – High-resolution (40 cm) aerial image showing the largest alluvial fan and surrounding area in the lower section of the Ahuriri River valley. b – Digitised example of geomorphological mapping conducted for the same place. Figure 4.1 shows exact location of this area.*

4.2.9 Palaeo lake landforms

Proglacial lakes are a common feature of present-day glacier retreat in the Southern Alps (Kirkbride, 1993) and may have been pervasive after the Last Glacial Maximum (Thomas, 2018). Sutherland et al. (2019b) note several major landform features can be used to identify former proglacial lakes in the Southern Alps. These landforms are: subaqueous mass flow deposits, palaeo shorelines, grounding zone wedge, sub-lacustrine moraine, palaeo-delta, iceberg grounding structure, and below wave base lacustrine deposits. I identify the following evidence in the Ahuriri River valley:

i) multiple shorelines (44°23'25"S, 169°39'31"E) at different elevations (720–740 m a.s.l.) occur inner (upper) valley side of hummocky moraine system which likely represents initial impact of lake regression. These shorelines represent single platforms nested at single elevations and stretching from ~50 to ~300 of meters. Overall, there are three clearly visible (and a few more uncertain) shorelines running parallel to each other (Figure 4.9a);

ii) a small/thin deposit of possible lacustrine sediments was found during the field investigation, approximately 2 km upstream from the hummocky terminal moraine system. The top 1 m of this sediment consisted of fine fraction clay-mixed sand or silt, while the lower unit (0.5–1.0 m) consisted of gravels (Figure 4.9b). However, since the river has a low inclination in this section and is characterised by meanders, an alternative explanation for sediment creation can be an oxbow lake;

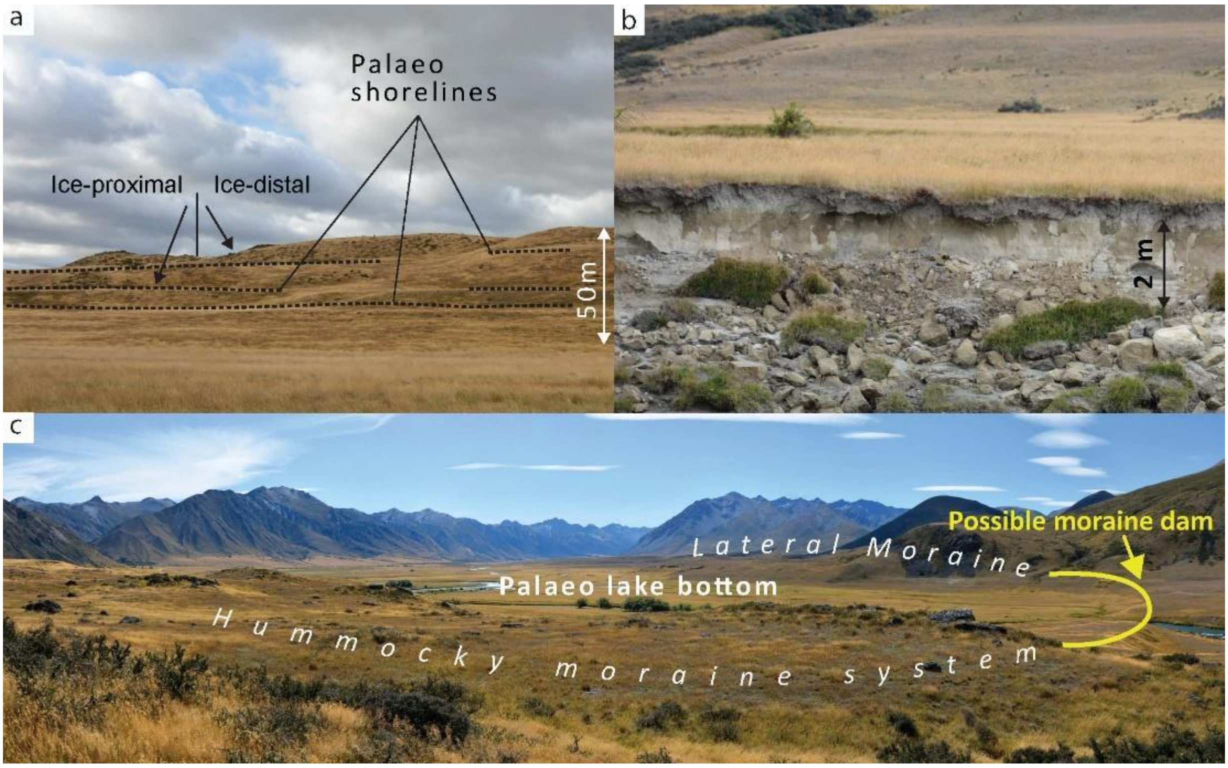

Figure 4.9 *a – Palaeo-shorelines on inner side of the hummocky moraine system. Figure 4.1 shows exact location of this area. b – Possible lacustrine sediments (gravels and sand) in 2 m-high sediment exposure at the left bench of the Ahuriri River. c – Terminal and lateral moraine systems and possible palaeo lake covered area.*

iii) the valley profile suggesting that this hummocky terminal moraine (44°23'24"S, 169°39'52"E) was likely merged with the lateral moraine at the other side of the river (44°22'55"S, 169°40'1"E), which may have created a dam (Figure 4.9c);

iv) former ice-contact lakes associated with glacier retreat after the Last Glacial Maximum in the Southern Alps are often associated with gently sloping terrain due to sedimentary infilling (Suggate and Almond, 2005; Thomas, 2018). Today, the valley floor immediately inboard of the hummocky moraines is occupied by active river plains, wetlands, alluvial plains, and alluvial fan deposits. This low-inclination (~3 m/1 km) surface may also be weak evidence of former lake presence.

In order to see the possible area that covered by a former lake I did a DEM-based simple computer calculation. Based on my hypothetical estimate, the post-glacial lake which might have occupied the Ahuriri River valley had a total area of about 14.4 km^2. It is possible that, after recession of the former Ahuriri Glacier, a lake became impounded behind the hummocky moraine system that blocked the gorge and extended for about 13 km up valley. The surface level of the lake could not have an elevation higher than the highest point of the impounding moraines (~750 m a.s.l. Figure 4.10). I think that the subtle evidence for the lake in the Ahuriri River valley today likely represents shallow/short-lived nature, which has largely been overprinted by subsequent fluvial aggradation.

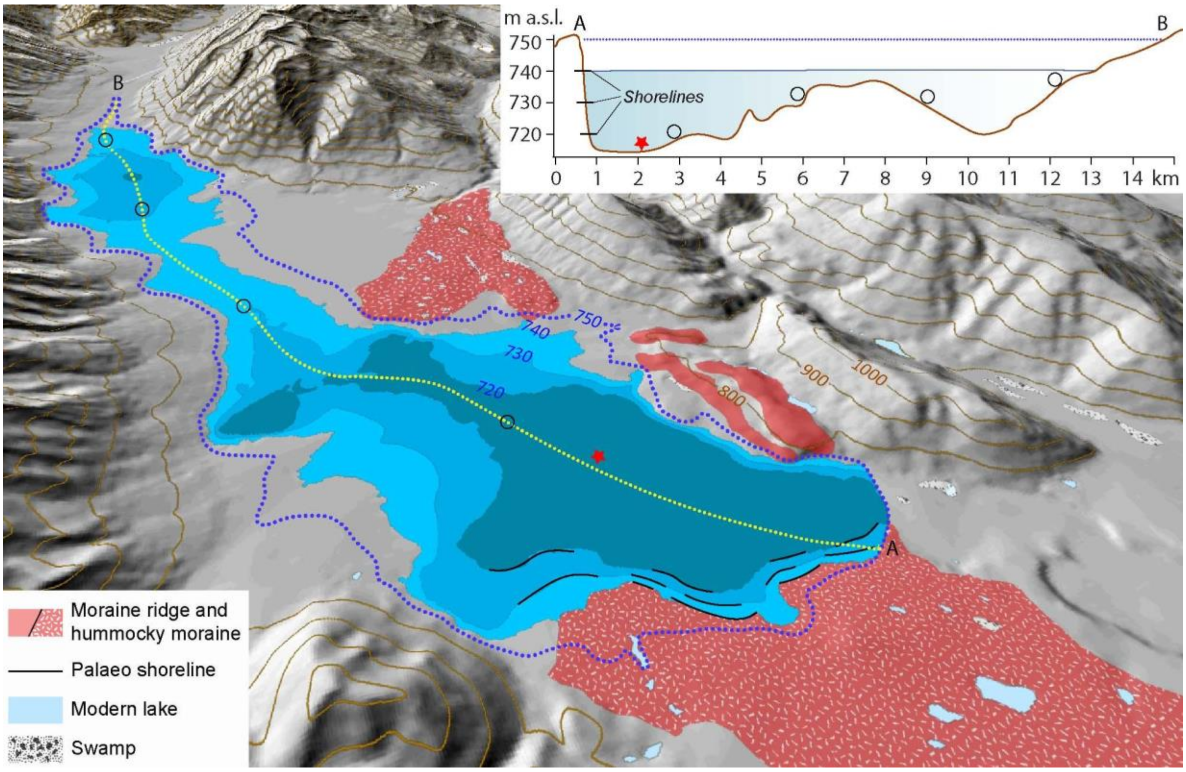

***Figure 4.10** A general overview of simulated palaeo Lake Ahuriri. Elevation profile of the possible glaciolacustrine basin is presented as an inserted diagram based on yellow dotted line (from A to B point) on main image. The lake depths are conditional for the modern day topography and are marked by circles (O) at the different distance on both images. Lake bathymetry was provided according to water depths relating to the palaeo lake shorelines based on DEM contours. Red star shows the location where lacustrine sediments were found (see also Figure 4.9b). The blue dotted line shows the maximum possible level of the lake, where the hypothesised lake level coincides with the maximum elevation of the moraines. This is a theoretical limit as I did not find any evidence confirming former lake existence at this level.*

4.3 Discussion

The spatial distribution of the glacial landform assemblages in the Ahuriri River basin provides evidence for more extensive glaciation during the Late Quaternary, as well as glacier recession and post-glacial sedimentation. Clear evidence of former extensive glaciers includes the presence of well-preserved moraine ridges in the main and tributary river valleys. Large hummocky moraine system in the lower section of the main valley (44°23'54"S, 169°39'48"E and 44°24'36"S, 169°40'25"E) outlines the maximum length (~41 km) of the former glacier. It is likely that small glaciers in tributary valleys (Canyon Creek, Watson Stream, Hodgkinson Creek, Snowy Gorge Creek, and Birch Creek) merged with main trunk of the former Ahuriri glacier at during the Last Glacial Maximum. The prominent terminal-lateral moraine ridge in the middle section of the main valley (44°15'44"S, 169°36'41"E) indicates a more limited advance or stillstand of the former valley glacier with a length of ~23 km. Other prominent but smaller size moraine landforms mostly in the tributary river valleys (see main map in supplement) also suggesting relatively small advance phases of former glaciers.

Based on this investigation it is reasonable to assume that glaciation in the Ahuriri River valley was smaller in scale than those in other river valleys in the Waitaki River basin (e.g. Putnam et al., 2013b; Strand et al., 2019; Sutherland et al., 2019a), which is broadly consistent with the lower-elevation headwaters of the Ahuriri River valley. The distribution and number of post-glacial landforms such as multiple terminal-lateral moraines in the Ahuriri River valley is relatively smaller than in other well-mapped valleys in the central Southern Alps. For example, I found only one well-preserved moraine ridge in the middle section of the main valley and two terminal hummocky moraine system at the lower section of the valley, while Putnam et al. (2013b) and Strand et al. (2019) described at least six different moraine landforms that were formed by the Ōhau and Pukaki glaciers during the Last Glacial Maximum.

Geomorphic evidence for a lake to have ever existed in the Ahuriri River valley is weak, but present. If such a lake did exist during deglaciation then it was likely shallow, and has since silted up entirely, unlike other larger lakes, Pukaki, Tekapo, etc., which receive much higher sediment inputs (Hicks et al., 2011). The main evidence for episodic lake occupation suggests that Lake Ahuriri did not persist for very long and thus was likely shallow, exerting little influence on glacier length changes. A similar pattern of post-glacial lake evidence elsewhere in New Zealand was found by Barrell et al. (2019) in current lake-free the upper Rangitata River valley.

4.4 Conclusions

This chapter presents the first comprehensive map of the glacial geomorphology of the Ahuriri River valley, in the central Southern Alps, New Zealand. Geomorphological mapping from high-resolution aerial imagery, large scale topographical maps, average resolution DEM (15 m), and several field investigations allowed me to produce this 1:38,000 scale map for the entire study site covering an area of about 532 km^2 (see main map in supplement). Mapped landforms consist of modern glaciers, rock glaciers, cirques, ice-scoured bedrocks, former ice-contact slopes, moraine terrain (moraine ridges and hummocky moraines), outwash plains, and alluvial fans, which have not been previously recorded. This map will provide the necessary context for robust dating of the former Ahuriri Glacier limits and will assist future investigations on the glacial history of this study site.

The main findings highlight several important characteristics of the glacial geomorphology:

i) Even though the surface morphology of the Ahuriri River valley has been modified (eroded or buried) by post-glacial fluvial processes (e.g. alluvial fans, debris fans) there are still well-preserved glacial landforms allowing us to understand past glacier behaviour.

ii) Hummocky moraines at the base of the Ahuriri River valley suggest that the maximum length of the former glacier could have been ~41 km. Furthermore, the ~18 km distance between two prominent moraine landforms (well-preserved moraine ridge in the middle section and hummocky moraine system at the lower section of the valley) suggests at least two major advances or stillstands of former glacier occurred during the Late Quaternary.

iii) Geometric and field investigation of the lower valley suggest the potential occurrence of a small, shallow proglacial lake shortly after the former glacier retreated from its maximum extent. The lake area could not have exceeded ~14.4 km^2 with a length ~13 km. In comparison, the former Lake Ahuriri was about four times smaller than Lake Ōhau today (~54 km^2). Such a restricted lake is unlikely to have affected glacier response to climate change.

CHAPTER 5: GLACIER-CLIMATE RECONSTRUCTIONS FROM THE AHURIRI RIVER VALLEY DURING THE EARLY LAST GLACIAL TERMINATION

5.1 Abstract

Geochronological dating of glacial landforms, such as terminal and lateral moraines, is useful for determining the extent and timing of past glaciation and for reconstructing the magnitude and rate of past climate changes. In the Southern Alps of New Zealand, well-dated glacial geomorphological records constrain the last glacial cycle across much of the Waitaki River basin (e.g. Ōhau, Pukaki, Tekapo) but its southern sector such as the Ahuriri River valley remains comparatively unconstrained. Recently, there has been debate on the scale and rapidity of mountain glacier retreat during the last glacial termination, particularly the 20–17 ka period in New Zealand. Missing from this debate is well-constrained equilibrium-line altitude (ELA) and associated temperature reconstructions, particularly over the period around 17 ka, which can help us to develop a more complete picture of how past temperature changes drove glacier retreat. In this chapter I report the glacial chronology dataset from the Last Glacial Maximum (LGM) and subsequent deglaciation from the Ahuriri River valley, Southern Alps, New Zealand (44°23'54"S, 169°39'48"E) based on thirty-eight beryllium-10 (^{10}Be) surface-exposure ages from terminal moraine systems and glaciated bedrock situated at the lower and middle sections of the valley. The results show that the former Ahuriri Glacier reached its maximum extent at 19.8±0.3 ka, which coincides with the global Last Glacial Maximum. By 16.7±0.3 ka, the glacier had retreated ~18 km up-valley suggesting at least ~43% glacier-length loss relative to its full LGM extent. This deglaciation was accompanied by the formation of a shallow proglacial lake. Using the accumulation area ratio (AAR) method, I estimate that the ELA was lower than present by ~880 m (~1120 m a.s.l.) at 19.8±0.3 ka, and ~770 m lower (~1230 m a.s.l.) at 16.7±0.3 ka. Applying an estimate for temperature lapse rate, this ELA anomaly implies that local air temperature was 5±1 °C colder than present (1981–2010) at 19.8±0.3 ka, while it was 4.4±0.9 °C colder at 16.7±0.3 ka, assuming no change in precipitation. The substantial glacier retreat in response to a relatively small accompanying increases in ELA (110 m) and temperature (0.6±1.0 °C) may have been a result of the high glacier-length sensitivity of this glacier system due to its low gradient of former ice surface. This low warming estimate differs markedly from other deglaciation studies, specifically from Rakaia River valley, which reports a much larger temperature increase at the onset of the last deglaciation. This precisely-dated moraine record along with reconstructed ELA as proxies for atmospheric conditions, provides new insight into post LGM glacier behaviour and climate conditions in New Zealand.

5.2 Introduction

Past glacial maxima and their terminations provide important information on the dynamics of the climate system, particularly the relationships between the atmosphere, hydrosphere and the cryosphere (Clark et al., 2009; Denton et al., 2010). Such information is fundamental for assessing the stability of Earth's climate considering ongoing climate change (IPCC, 2019). Identifying the timing of key climate transitions during past warming episodes, such as the last glacial termination, may help to understand the future evolution of Earth's climate system (e.g. Denton et al., 2021).

Mountain glaciers are highly sensitive to climate change (Oerlemans and Fortuin, 1992) and provide proxy information for regional and global climate (Oerlemans, 2005; Mackintosh et al., 2017). Exposure dating of moraines using terrestrial cosmogenic nuclides such as ^{10}Be provides new information on the duration, timing, and scale of the Late Quaternary glaciation (Balco, 2011; 2020). The high sensitivity of glaciers to climate change also permits quantitative reconstruction of past temperature and precipitation (Mackintosh et al., 2017), which may be used to test hypotheses about past climate change mechanisms (e.g. Dowling et al., 2021).

Late Quaternary glacier-based climate reconstructions from the Southern Alps are of particular interest since very few glacier-covered mountain regions exist in the mid latitudes of the Southern Hemisphere (Figure 5.1). The climate in New Zealand and the southwest Pacific region was markedly different from present during the last glacial termination (Lorrey and Bostock, 2017). Despite the high utility of glaciers as climatic indicators, glacier-based estimates of the onset and rate of air temperature rise during this time-period lack consensus. Several studies advocate for rapid deglaciation, in response to regional warming beginning at 18 ka (Putnam et al., 2013a; Barrell et al., 2019; Denton et al., 2021). However, this is countered by suggestions that proglacial lake development at such sites may have compromised the relationship between glacier length and surface mass balance (Shulmeister et al., 2010; 2018a) and that air temperatures may have remained depressed until 15–16 ka (Rother et al., 2014).

These uncertainties remain, despite relatively abundant moraine chronologies, in large part due to the paucity of associated quantitative climate reconstructions. While glaciers are of high utility as climate proxies, the magnitude of length changes is not only reflective of regional climate, but also glacier geometry, which is largely reflects catchment topography. Qualitative inference of climate change from chronological information alone, may thus overlook key aspects of glacier response to climate change (e.g. Eaves et al., 2019). In this chapter I pair cosmogenic ^{10}Be exposure dating of a sequence of glacial landforms that are sufficiently preserved to permit reconstruction of past glacier equilibrium line altitude, thus affording quantitative information of both the timing and magnitude of climatic change in the Southern Alps at the onset of the glacial termination.

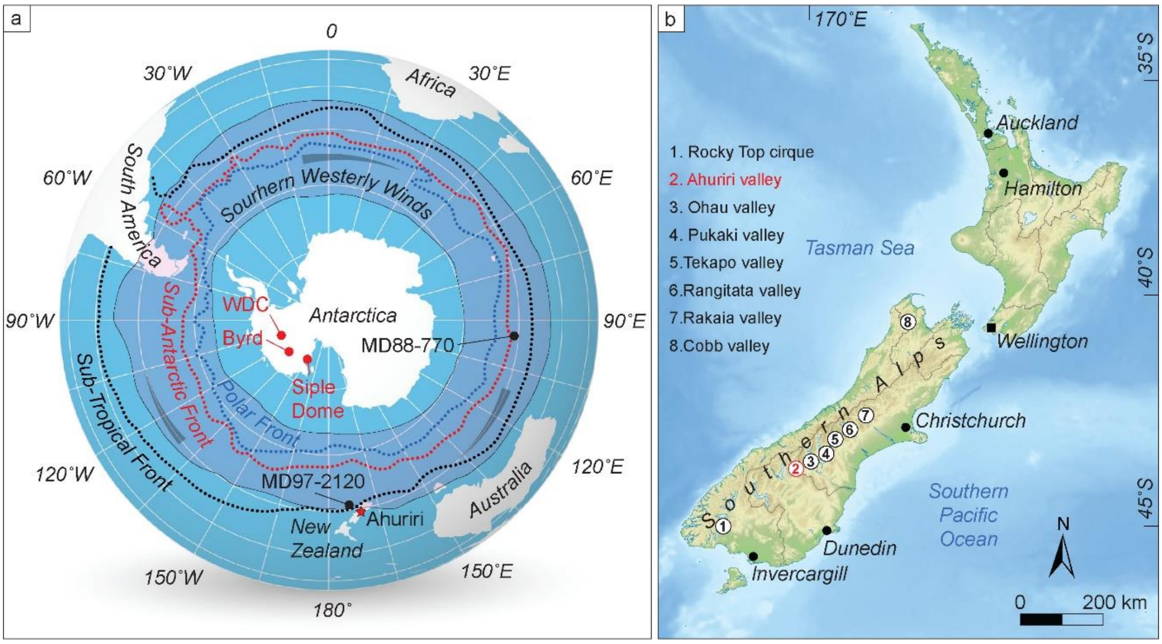

***Figure 5.1** a – Map of the Southern Hemisphere. Light grey – showing the approximate positions of the Southern Westerly Winds (SWW) belt (Sime et al., 2013); Light grey arrows – direction of the SWW belt; The blue dotted line – Polar Front; The red dotted line – Sub-Antarctic Front; The black dotted line – Sub-Tropical Front (Darvill et al., 2016); The red star – location of the Ahuriri River valley; The black dots – locations of key marine core palaeoclimate records illustrated in Figure 5.7 and mentioned in the text (Pahnke et al., 2003; Barrows et al., 2007); The red dots – locations of key ice core palaeoclimate records mentioned in the text (Pedro et al., 2011; WAIS Divide Project Members, 2013). b – Location map of New Zealand showing all sites mentioned in the text.*

Detailed glacial geomorphological mapping of the Ahuriri study site is presented in the previous chapter (Chapter 4) or in Tielidze et al. (2021). This chapter only describes three distinct terminal and lateral (hummocky) moraine systems. These moraine features are located at the bottom of the lower and middle section of the valley (Figure 5.2) and are hereafter called moraine belts 3, 2, and 1.

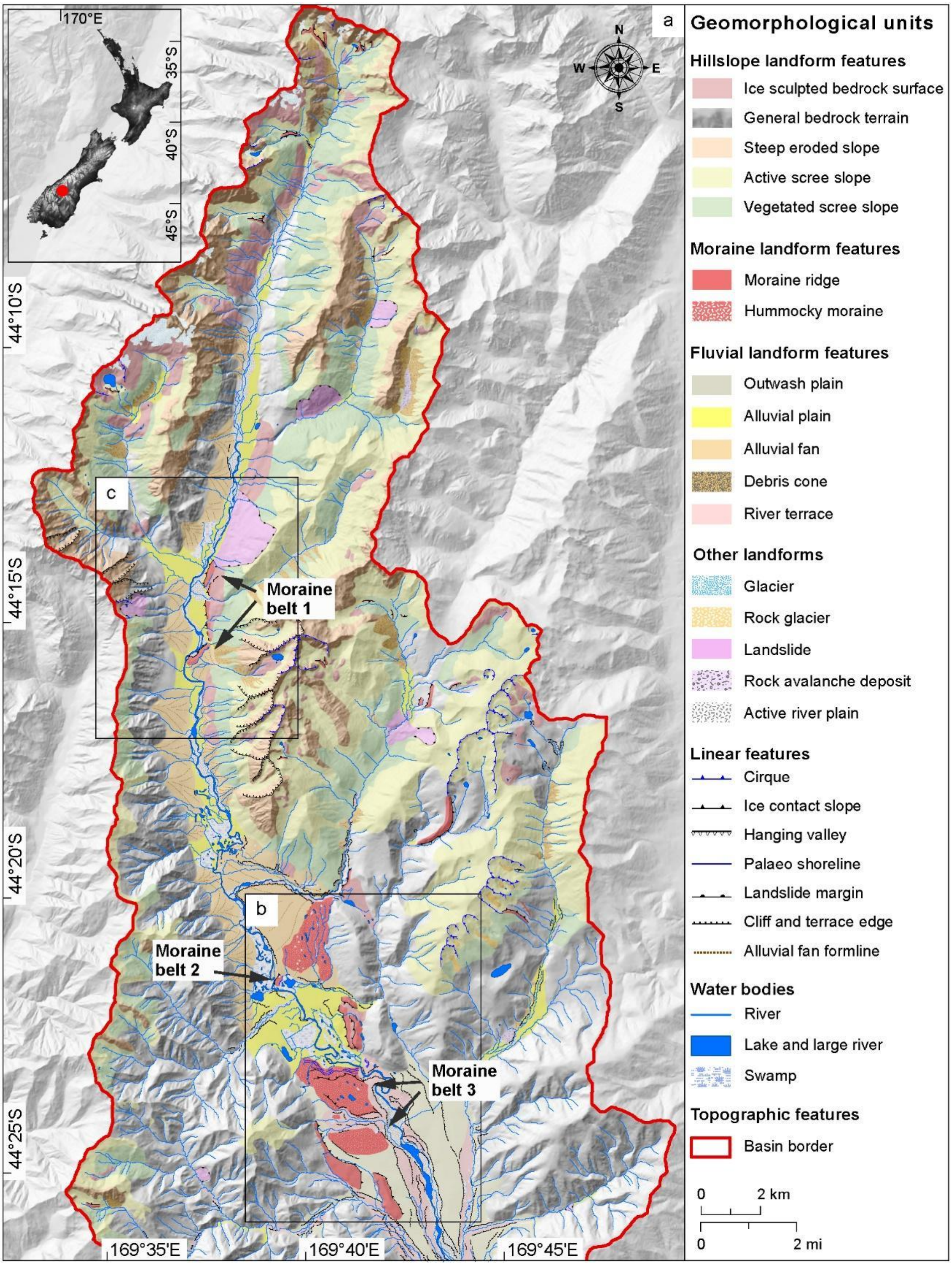

Figure 5.2 *a – Simplified overview map of the glacial geomorphology of the Ahuriri River valley (Tielidze et al., 2021). Study area location is given on regional New Zealand insert map. b – terminal moraine systems selected for this study (moraine belts 3 and 2) along with surrounding area. c – terminal-lateral moraine system (moraine belt-1) in the middle valley along with surrounding area. Detailed glacial geomorphological maps of these panels are shown in Figure 5.3 and 5.4.*

5.3 Results

5.3.1 Moraine belt-3

A large terminal moraine unit (∼3.5 km long and 1.6 km wide) at an elevation of about 760 m a.s.l. was identified in the lower section of the Ahuriri River valley, defining a former ice margin. Large 1 to 2 m (diameter) sized greywacke boulders are scattered on the surface of this landform. which is broad and lacks sharp crests. The upper surface of the moraine is in some places lined by low, broad ridges that range in height from 1 to 5 metres above the general moraine surface. Two small ponds occur on the surface of this terrain. The middle part of the moraine is incised by a meltwater channel, which divides the moraine into two parts, inner (44°23'54"S, 169°39'48"E) and outer (44°24'36"S, 169°40'25"E) (Figure 5.3). The inner (northern) part of the moraine has a hummocky nature and is characterised by relatively shorter, steeper angle up-glacier ice-contact margins, and longer, low down-glacier margins. Multiple former shorelines (44°23'25"S, 169°39'31"E) at different elevations (~720–740 m a.s.l.) occur on the ice-margin contact slopes of the hummocky moraine belt which likely represents a palaeo lake and its subsequent recession (Tielidze et al., 2021). These shorelines manifest as multiple platforms nested at several elevations (~725, 734, and 740 m a.s.l.) that extend horizontally between ∼50 and ∼300 metres length. In total, I identified three clear (and several possible) former shorelines running parallel to each other. The outer (southern) section of the moraine belt is more subtle and flat.

Sample details for surface exposure ages from all moraine systems are given in Table 5.1, while cosmogenic ^{10}Be exposure ages are listed in Table 5.2. All age calculations are referenced to calendar year before sample collection (2019).

Eleven samples from the inner (northern) part of a moraine belt-3 show individual apparent exposure ages ranging from 17.6±0.4 to 20.9±0.5 ka (Table 5.2 and Figure 5.3). The ages from this moraine belt were grouped around an exposure age of 20.1±0.4 ka (n=10; 1 outlier – AL-27-61, see methods for details), based on the internal error-weighted mean of the eleven exposure ages. Eleven exposure ages from the outer (southern) moraine range from 19.1±0.4 to 20.0±0.6 ka (Table 5.2 and Figure 5.3). These eleven ages yield internal error-weighted mean age of 19.5±0.4 ka (n=11; no outliers). Because the mean ages of the Ahuriri moraine belt-3 at the inner and outer sites are within error of each other, I interpret this feature as one continuous moraine that formed 19.8±0.3 ka ago. The entire moraine was probably divided by a meltwater channel when the glacier was located nearby. These results suggest that 19.8±0.3 ka ago, the glacier margin was located at the outermost terminal moraine system of the Ahuriri valley at an elevation of ~760 m a.s.l. Overall, a comparison of exposure ages from all the different scaling or calibration models (St, Lm, LSD, and Global) shows that this conclusion is insensitive to the choice of scaling model (Table 5.2), thus I proceed using the Lm model of Balco et al., (2008).

5.3.2 Moraine belt-2

Approximately 4 km upstream from moraine belt-3, on the eastern side of the Ahuriri River, I identified a left-lateral moraine sequence that descend in elevation from ~785 m a.s.l on the valley side down to ~710 m a.s.l close to the present-day riverbank. The outermost portion of this sequence grades down-valley to intersect with moraine belt-3, thus I interpret the inner parts of this sequence to represent a recessional sequence that records glacier surface lowering after 19.8±0.3 ka.

I targeted the lowest, innermost section of this moraine sequence for surface exposure dating, to bracket the timing of glacier thinning at this location. My target moraine is a prominent, isolated moraine hummock situated immediately adjacent (east of) the present-day Ahuriri River at the edge of largest alluvial fan in the middle-lower section of Ahuriri River valley (Figure 5.3) (44°21'46"S, 169°38'15"E). A single former shoreline at elevation of 721 m a.s.l. occurs on the outer face of this moraine belt, which likely represents a subsequent recession of a palaeo lake. The surroundings of the moraine belt are swampy with several small ponds. Several greywacke boulders are embedded in the slopes and crest of the moraine, ranging in elevation between 720–740 m a.s.l.

Five samples from moraine belt-2 range from 9.9±0.3 to 12.2±0.5 ka (Table 5.2 and Figure 5.3). The ages from this moraine belt were grouped around an exposure age of 11.3±0.7 ka (n=4; 1 outlier – AML-28-105), based on the internal error-weighted mean of the five exposure ages. Although these ages are morphostratigraphically consistent with moraine belt-3, they are unusually young for their situation in the lower valley and are inconsistent in age relative to moraine belt-1 below. As such, it is hard to believe these ages represent the timing of deposition by ice and I discuss the possible reasons for this discrepancy in the discussion (section 5.6.2), below.

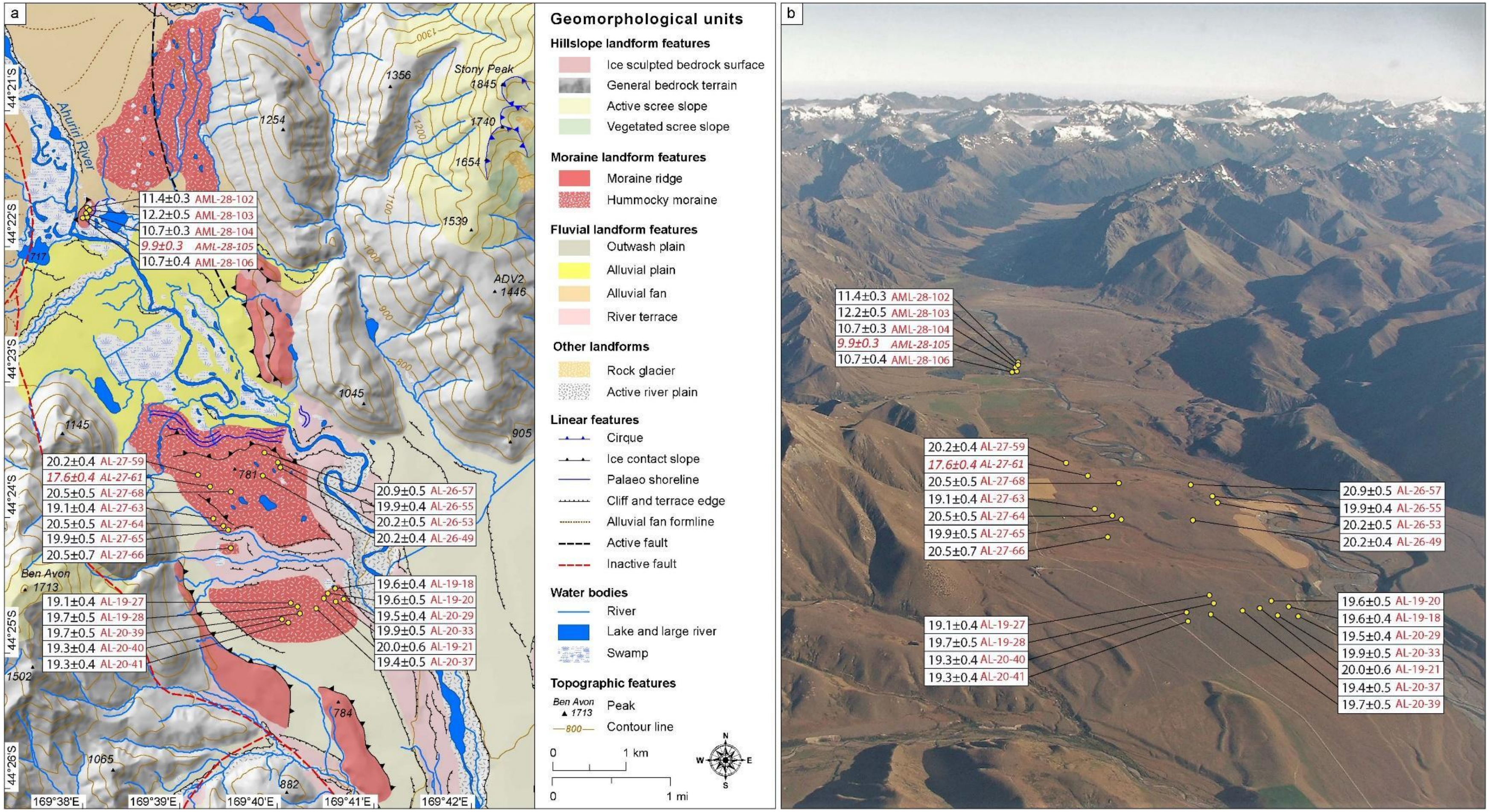

Figure 5.3 *a – Glacial geomorphological map of the Ahuriri terminal moraine systems (moraine belts 3 and 2) and surrounding area described in this chapter. See Figure 5.2 for map location with respect to the Ahuriri River valley. b – Oblique aerial view of the Ahuriri River valley from south to north (Photo by: K. Norton). Yellow dots on both panels indicate the location of the samples (see Table 5.1 and 5.2 for more details). The outlier samples are given by red italic text (see discussion section below).*

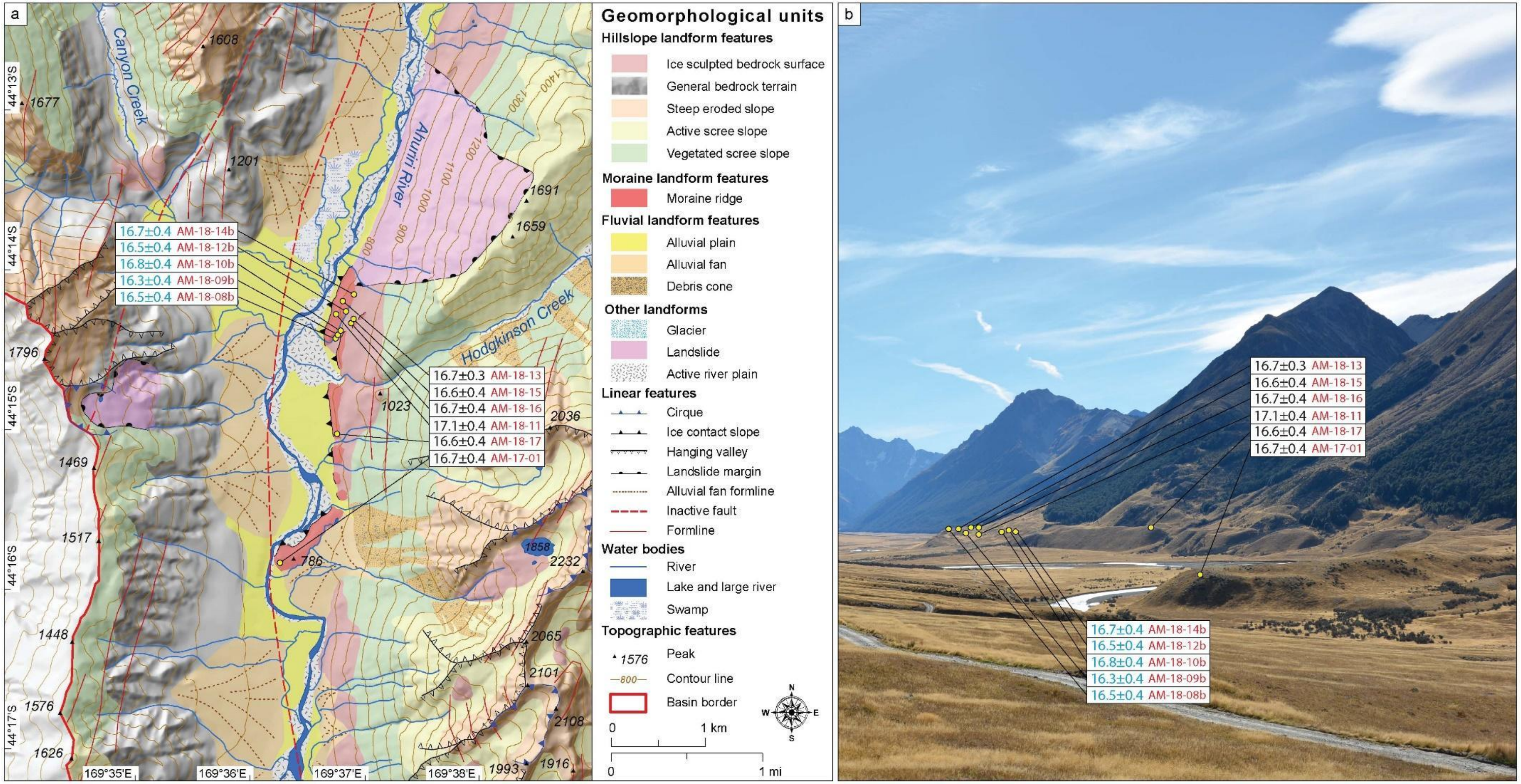

Figure 5.4 *a – Glacial geomorphological map of the Ahuriri terminal moraine system (moraine belt-1) and surrounding area. See Figure 5.2 for map location with respect to the Ahuriri River valley. b – Field photo of the Ahuriri moraine belt-1. Yellow dots on both panels indicate the location of the samples (see Table 5.1 and 5.2 for more details). The black ages are from boulders while the blue ages are from bedrock.*

***Table 5.1** Surface-exposure sample details and ^{10}Be data of moraine systems from the Ahuriri River valley. Italic ages indicate outliers that were excluded from the chi-squared test (Balco, 2017a; 2017b). See Table 5.2 for the calculated ages and Figure 5.3–5.4 for sample location.*

Sample field ID	LLNL ID	Boulder/ Bedrock	Latitude (S)	Longitude (E)	Elevation (m a.s.l.)	Boulder size (L×W×H) (cm)	Sample thickness (average cm)	Shielding correction	Quartz weight (g)	^{9}Be added (mg)	^{10}Be/^{9}Be ± 1σ (10–^{14})	[^{10}Be] ± 1σ (10^{4}) (atoms/gram qtz.)
Moraine belt-3 (inner) (44°23′54″S, 169°39′48″E)												
AL-26-49	BE48600	Boulder	-44.395441	169.666723	774	170×140×95	2.3	0.998195	13.338	0.2837	11.20±0.21	15.82±0.35
AL-26-53	BE48601	Boulder	-44.393977	169.669205	774	180×95×80	4.0	0.990586	13.543	0.2846	11.11±0.21	15.50±0.35
AL-26-55	BE48602	Boulder	-44.393104	169.668986	768	240×228×78	2.8	0.993362	13.310	0.2864	10.76±0.20	15.37±0.34
AL-26-57	BE48603	Boulder	-44.391977	169.666613	765	300×280×150	2.8	0.998693	13.680	0.2859	11.64±0.22	16.16±0.36
AL-27-59	BE48604	Boulder	-44.394375	169.655063	769	144×138×36	1.7	0.996929	13.681	0.2874	11.32±0.21	15.79±0.35
AL-27-61	*BE48605*	Boulder	*-44.395731*	*169.658087*	*766*	*211×110×24*	*2.4*	*0.998627*	*13.152*	*0.2850*	*9.48±0.18*	*13.62±0.30*
AL-27-63	BE48606	Boulder	-44.400109	169.657308	767	332×150×64	2.4	0.995922	12.746	0.2873	9.91±0.18	14.82±0.32
AL-27-64	BE48607	Boulder	-44.401301	169.659033	769	268×262×171	2.5	0.992318	13.598	0.2845	11.43±0.21	15.88±0.35
AL-27-65	BE48608	Boulder	-44.401771	169.659769	769	157×102×67	2.7	0.998846	13.426	0.2863	10.91±0.21	15.45±0.35
AL-27-66	BE48609	Boulder	-44.403993	169.659257	774	420×350×130	2.8	0.995555	12.989	0.2858	10.91±0.33	15.93±0.52
AL-27-68	BE48610	Boulder	-44.396934	169.660573	768	182×147×69	3.8	0.991419	12.832	0.2862	10.60±0.21	15.69±0.35
Blank	BE48611	-	-	-	-	-	-	-	-	0.2770	0.08±0.02	-
Moraine belt-3 (outer) (44°24′36″S, 169°40′25″E)												
AL-19-18	BE48481	Boulder	-44.409645	169.678879	757	160×110×60	1.9	0.990779	11.617	0.2783	9.81±0.17	15.08±0.33
AL-19-20	BE48482	Boulder	-44.410053	169.677258	759	201×171×81	2.0	0.998955	12.134	0.2780	10.29±0.22	15.15±0.39
AL-19-21	BE48483	Boulder	-44.410519	169.677116	759	244×144×90	2.3	0.998955	13.360	0.2785	11.51±0.29	15.49±0.45
AL-19-27	BE48484	Boulder	-44.41137	169.67104	761	163×132×65	2.7	0.998955	15.161	0.2781	12.44±0.23	14.77±0.33
AL-19-28	BE48485	Boulder	-44.41184	169.67271	757	266×127×57	4.3	0.998955	13.793	0.2807	11.38±0.24	14.95±0.37
AL-20-29	BE48486	Boulder	-44.41072	169.68034	753	251×210×138	2.1	0.998955	14.678	0.2805	12.17±0.23	15.05±0.34
AL-20-33	BE48487	Boulder	-44.41117	169.67877	762	357×173×170	2.0	0.974704	14.504	0.2736	12.35±0.25	15.07±0.36

AL-20-37	BE48488	Boulder	-44.41179	169.67583	755	207×184×80	2.9	0.998955	14.125	0.2789	11.65±0.22	14.86±0.35
AL-20-39	BE48489	Boulder	-44.41282	169.67349	756	182×133×55	2.3	0.998680	14.399	0.2798	12.10±0.23	15.21±0.35
AL-20-40	BE48490	Boulder	-44.41389	169.6703	758	443×365×66	2.6	0.998955	14.042	0.2775	11.65±0.22	14.87±0.34
AL-20-41	BE48491	Boulder	-44.41443	169.6712	753	112×98×41	2.1	0.976371	15.149	0.2810	12.14±0.21	14.57±0.32
Blank	BE48492	-	-	-	-	-	-	-	-	0.2760	0.4±0.04	-
Moraine belt-2 (44°21′46″S, 169°38′15″E)												
AML-28-102	BE49454	Boulder	-44.362613	169.637987	738	150×130×40	1.1	0.996832	13.562	0.2795	6.47±0.16	8.55±0.24
AML-28-103	BE49455	Boulder	-44.362858	169.637718	738	200×160×70	4.1	0.994472	7.727	0.2805	3.95±0.14	8.96±0.36
AML-28-104	BE49456	Boulder	-44.363229	169.637915	736	110×80×40	2.2	0.994472	14.160	0.2812	6.25±0.14	7.95±0.21
AML-28-105	*BE49457*	Boulder	*-44.363044*	*169.637183*	*731*	*130×90×80*	*2.6*	*0.992993*	*14.026*	*0.2816*	*5.64±0.14*	*7.22±0.20*
AML-28-106	BE49458	Boulder	-44.362497	169.637083	727	120×100×70	3.0	0.997196	13.508	0.2817	5.87±0.18	7.82±0.27
Blank	BE49459	-	-	-	-	-	-	-	-	0.2777	0.3±0.04	-
Moraine belt-1 (Boulders) (44°15′44″S, 169°36′41″E)												
AM-17-01	BE47757	Boulder	-44.264579	169.605771	775	185×90×156	1.1	0.927932	15.173	0.3016	9.35±0.16	12.23±0.30
AM-18-11	BE47761	Boulder	-44.241326	169.614783	800	231×145×110	1.4	0.984798	16.720	0.3012	11.46±0.26	13.52±0.35
AM-18-13	BE47763	Boulder	-44.239497	169.616435	813	172×131×65	1.3	0.986981	13.793	0.2973	9.56±0.15	13.39±0.27
AM-18-15	BE47765	Boulder	-44.239671	169.619302	863	75×50×48	0.9	0.976531	15.417	0.2975	10.87±0.21	13.71±0.32
AM-18-16	BE47766	Boulder	-44.239705	169.619328	863	97×75×45	0.9	0.969833	12.943	0.2965	9.25±0.17	13.74±0.31
AM-18-17	BE47767	Boulder	-44.25119	169.61516	804	320×175×80	2.6	0.979546	15.642	0.2932	10.60±0.20	12.93±0.29
Blank	BE47768	-	-	-	-	-	-	-	-	0.3002	0.3±0.03	-
Moraine belt-1 (Bedrock) (44°15′44″S, 169°36′41″E)												
AM-18-08b	BE47758	Bedrock	-44.241709	169.614529	798	Bedrock	1.6	0.988486	15.592	0.3005	10.38±0.19	13.04±0.29
AM-18-09b	BE47759	Bedrock	-44.241693	169.614466	798	Bedrock	1.6	0.981724	15.391	0.2993	10.13±0.19	12.77±0.29
AM-18-10b	BE47760	Bedrock	-44.241688	169.61446	797	Bedrock	2.5	0.944171	15.469	0.3002	10.02±0.19	12.62±0.29
AM-18-12b	BE47762	Bedrock	-44.241384	169.614766	800	Bedrock	1.2	0.991202	16.817	0.2996	11.28±0.21	13.13±0.30
AM-18-14b	BE47764	Bedrock	-44.23724	169.617903	820	Bedrock	1.3	0.985638	16.234	0.3316	10.08±0.19	13.45±0.30
Blank	BE47768	-	-	-	-	-	-	-	-	0.3002	0.3±0.03	-

Table 5.2 *Cosmogenic ^{10}Be exposure ages (with internal 1-sigma uncertainties) from the moraine belts in the Ahuriri River valley. Three scaling schemes: St (Stone, 2000), Lm (Balco et al., 2008), LSD (Lifton et al., 2014) and the "Macaulay" production rate (Putnam et al. 2010b) was used for exposure age calculations. Ages calculated using a global production rate (Borchers et al., 2016) are also presented without external uncertainties that are much higher due to the large uncertainties in the global ^{10}Be production rate calibration dataset. Italic ages indicate outliers that were excluded from the chi-squared test (Balco, 2017a; 2017b).*

Sample field ID	St age and internal uncertainty	**Lm age and internal uncertainty**	LSDn age and internal uncertainty	Lm age and internal uncertainty Global prod. rate
Moraine belt-3 (inner) (44°23′54″S, 169°39′48″E)				
AL-26-49	20924±464	**20204±448**	20032±444	19272±427
AL-26-53	20963±469	**20241±453**	20068±449	19307±432
AL-26-55	20604±458	**19906±442**	19747±438	18987±421
AL-26-57	21631±479	**20859±462**	20679±458	19899±441
AL-27-59	20896±463	**20178±447**	20010±443	19246±426
AL-27-61	*18118±403*	***17569±391***	*17463±389*	*16752±373*
AL-27-63	19781±424	**19138±410**	18998±407	18250±391
AL-27-64	21255±469	**20512±453**	20336±449	19567±432
AL-27-65	20561±467	**19866±451**	19706±447	18948±430
AL-27-66	21226±701	**20485±677**	20305±671	19541±645
AL-27-68	21258±483	**20515±466**	20341±462	19570±444
Error-weighted mean (n=10)	20859±151 (360)	**20144±146 (350)**	19977±144 (340)	19214±139 (913)
Moraine belt-3 (outer) (44°24′36″S, 169°40′25″E)				
AL-19-18	20312±450	**19636±435**	19491±431	18727±414
AL-19-20	20228±524	**19558±506**	19413±503	18652±483
AL-19-21	20729±606	**20025±585**	19868±580	19100±558
AL-19-27	19772±450	**19131±435**	18994±432	18243±415
AL-19-28	20352±508	**19674±491**	19527±487	18763±468
AL-20-29	20194±463	**19526±448**	19386±444	18621±427
AL-20-33	20563±499	**19869±482**	19714±478	18951±460
AL-20-37	20037±470	**19380±454**	19242±451	18482±433
AL-20-39	20413±468	**19730±452**	19584±449	18818±431
AL-20-40	19962±459	**19309±444**	19170±441	18414±423
AL-20-41	20003±436	**19348±422**	19212±419	18451±402
Error-weighted mean (n=11)	20201±144 (348)	**19533±140 (338)**	19390±139 (330)	18628±133 (885)
All samples error-weighted mean (n=21)	20516±104 (338)	**19826±101 (329)**	19672±100 (319)	18909±96 (893)
Moraine belt-2 (44°21′46″S, 169°38′15″E)				

AML-28-102	11538±326	**11391±322**	11446±324	10860±307
AML-28-103	12423±509	**12204±500**	12228±501	11665±478
AML-28-104	10864±293	**10747±290**	10798±291	10267±277
AML-28-105	*9958±287*	***9904±285***	*9977±288*	*9462*±273
AML-28-106	10799±380	**10688±376**	10742±378	10208±359
Error-weighted mean (n=4)	11406±756 (777)	**11258±707 (729)**	11304±695 (716)	10750±677 (844)
Moraine belt-1 (Boulders) (44°15′44″S, 169°36′41″E)				
AM-17-01	17233±419	**16730±406**	16646±404	15946±387
AM-18-11	17639±455	**17115±442**	17013±439	16314±421
AM-18-13	17238±355	**16733±344**	16623±342	15948±328
AM-18-15	17054±399	**16551±388**	16414±384	15777±369
AM-18-16	17224±392	**16717±381**	16568±377	15933±363
AM-18-17	17071±390	**16570±379**	16472±377	15795±361
Error-weighted mean (n=6)	17226±163 (315)	**16720±158 (307)**	16606±157 (300)	15937±150 (763)
Moraine belt-1 (Bedrocks) (44°15′44″S, 169°36′41″E)				
AM-18-08b	17007±386	**16510±374**	16419±372	15737±357
AM-18-09b	16775±383	**16295±372**	16210±370	15528±355
AM-18-10b	17352±395	**16844±383**	16746±381	16056±365
AM-18-12b	17002±384	**16506±373**	16414±371	15733±356
AM-18-14b	17241±389	**16736±378**	16620±375	15950±360
Error-weighted mean (n=5)	17071±173 (318)	**16574±168 (311)**	16478±167 (304)	15797±160 (758)
All samples error-weighted mean (n=11)	17154±119 (293)	**16652±115 (287)**	16546±114 (279)	15871±110 (753)

5.3.3 Moraine belt-1

Approximately 11.5 km upstream from moraine belt-2, a prominent terminal-lateral moraine system extends for approximately 4 km in the middle section of the Ahuriri River valley between 760 and 800 m a.s.l. (Figure 5.4) (44°15'44"S, 169°36'41"E). The middle section of this moraine is linear, while the lower section is curvilinear and demarcates the limits of former glacier margin. This feature comprises fragmentary crested ridges (divided by meltwater channels or river streams) exhibiting ~30 m relief from the present valley floor and usually up to a few hundred metres long. The surface of upstream section of the moraine terrain is broad and exhibits distinct ridge crests. Here ice-moulded bedrock ridges, streamlined in the former direction of ice flow, protrude through the overlying moraine. Large sized (1 to 2 m diameter) greywacke boulders are found in many places on the crest of the fragmented moraine ridges. I collected samples from a mixture of erratic boulders (n=6) and ice-moulded bedrock surfaces (n=5).

Six ages from the boulders of moraine belt-1 are tightly clustered and range from 16.6±0.4 to 17.1±0.4 ka (Table 5.2 and Figure 5.4). The ages from these boulders were grouped around an error-weighted mean exposure age of 16.7±0.3 ka (n=6; no outliers). Five exposure ages from the bedrock surfaces of moraine belt-1 range from 16.3±0.4 to 16.8±0.4 ka (Table 5.2 and Figure 5.4). These five ages yield internal error-weighted mean age of 16.6±0.3 ka (n=5; no outliers).

The ages from the boulders, which are situated on the moraine ridge crests, represent the final stages of moraine formation. Meanwhile, the bedrock ages record the withdrawal of ice and onset of bedrock exposure. As the two sample populations date complementary events in the glacier history, I expect them to be similar in age. As this is the case, I consider a combined age 16.7±0.3 ka to best represent the culmination of moraine building and withdrawal of ice from this site.

5.3.4 Palaeo glacier geometry

Based on recent geomorphological mapping (Tielidze et al., 2021), a 15 m DEM (Columbus et al., 2011), high-resolution aerial imagery, and oblique aerial photographs I reconstructed the approximate area and thickness of the palaeo glacier occupying the Ahuriri River valley. According to this calculation, the former glacier covered at least 219±18 km^2 at 19.8±0.3 ka (Figure 5.5a). The length of the main trunk of the ice (from headwater of the valley to the moraine belt-3) was ~41 km. Canyon Creek was the only large tributary that flowed into the former glacier from the western (right) side, while three large tributaries (Watson Stream, Hodgkinson Stream, and Snowy Gorge Creek) joined the glacier from the eastern (left) side.

The main trunk of the Ahuriri Glacier was relatively narrow (1.5 km) in its upper section. By the middle section, the former glacier doubled in width (~3.0 km), and in its lowest sections, its width was much expanded (~4.0 km) (Figure 5.5b). The palaeo glacier had also a very low surface inclination in its lower section.

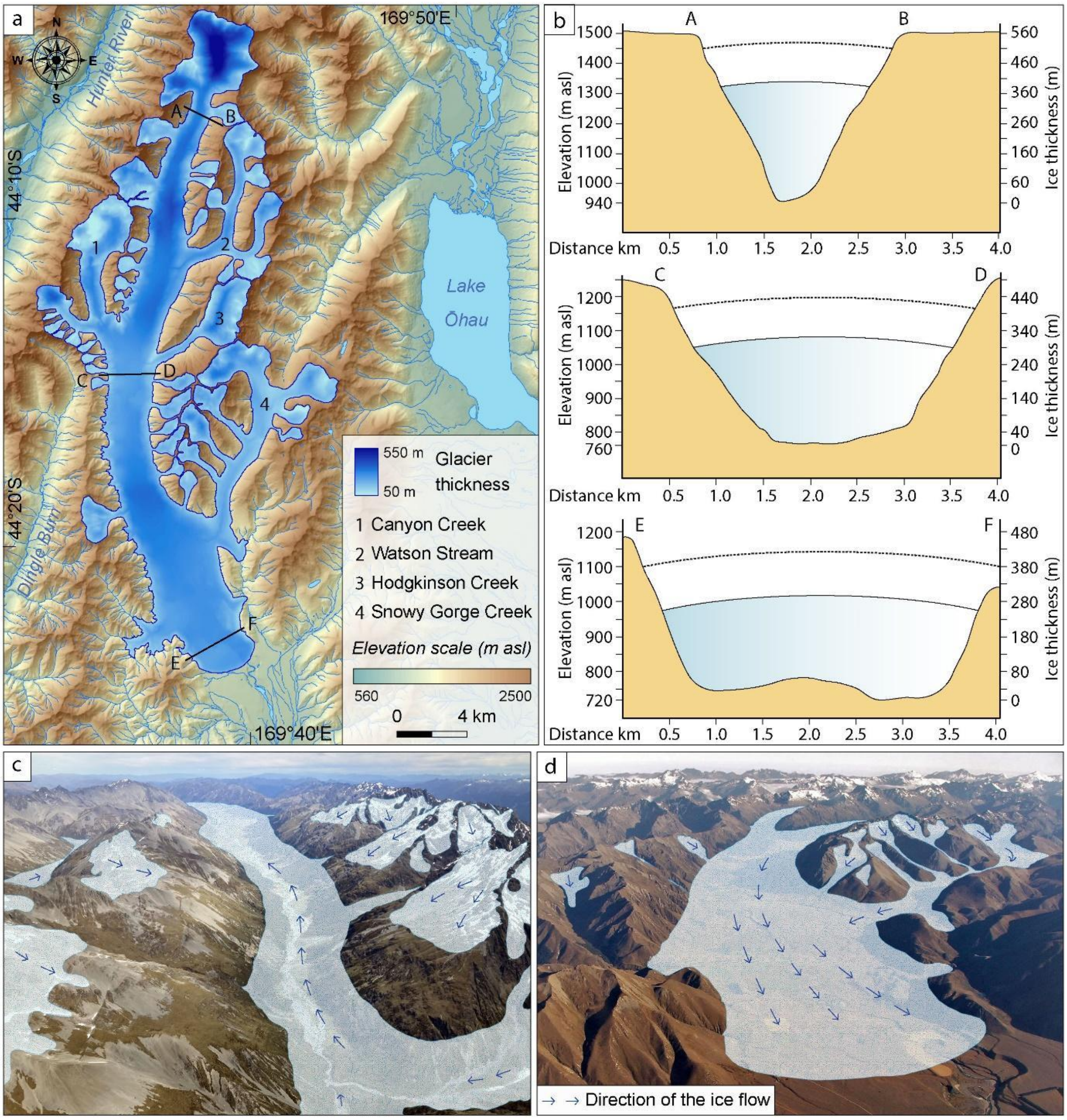

Figure 5.5 *a – Manually derived palaeo Ahuriri Glacier at 19.8±0.3 ka. b – reconstructed ice thickness based on three cross-sections in the upper, middle, and lower sections of the glacier at 19.8±0.3 ka. The black dotted lines show the maximum height that ice could have been for that time. Oblique imagery and GIS simulation show palaeo glacier expansion in the upper (c – view from north to south) and lower (d – view from south to north) valley (photos by: W. Dickinson and K. Norton).*

According to the three different profiles, the thickness of the palaeo glacier was at least ~450 m in the upper section, ~350 m in the middle section, and ~300 m in the lower section (Figure

5.5b). I note that my ice thickness estimate was produced based on modern and manually reconstructed DEMs and it does not consider post-glacial changes in the valley profile resulting from sediment fill. It is likely that the sediment-cover was thinner and the valley floor lower during the glacial period relative to today, thus ice thickness estimates are likely minimum constraints. However, this uncertainty is irrelevant for equilibrium line altitude reconstruction.

My reconstructions indicate that glacier area decreased significantly between 19.8±0.3 and 16.7±0.3 ka. The estimated area of all separated ice bodies for 16.7±0.3 ka was 117±15 km^2, while the area of single Ahuriri Glacier was 86±8 km^2 (Figure 5.6). This indicates that ~18 km (or ~580 m/0.1 ka) of terminus retreat of the palaeo Ahuriri Glacier occurred between 19.8±0.3 and 16.7±0.3 ka.

5.3.5 Palaeo ELA and air temperature

Uncertainties in the knowledge of former ice geometries affect the accuracy of reconstructed ELAs for any particular glacier. Manually reconstructed palaeo Ahuriri glaciers are shown in Figure 5.6. Using an AAR of 0.67, my estimate the modern ELA (*m*ELA) at 2000 a.s.l. for the Ahuriri catchment, while the palaeo ELAs (*p*ELAs) are estimated at 1120 m a.s.l. and 1230 m a.s.l, for 19.8±0.3 ka and 16.7±0.3 ka, respectively. This calculation represents an ELA lowering relative to present (*d*ELA) of 880 m and 770 m for 19.8±0.3 ka and 16.7±0.3 ka, respectively. Altering the AAR by ±0.05 (0.62–0.72) yields *p*ELAs of 1170–1060 m a.s.l. for the 19.8±0.3 ka glacier, which represent *d*ELAs of 830–940 m. Similarly, altering the AAR by ±0.05 (0.62–0.72) yields *p*ELAs of 1280–1170 m a.s.l. for the 16.7±0.3 ka glacier, which represents *d*ELAs of 720–830 m.

The temperature lapse rate at the Last Glacial Maximum is not known, and hence I use a range of lapse rate values to estimate the temperature lowering that equates to the *d*ELA. The mean annual temperature lapse rate for upland (>300 m) New Zealand (–5.1 °C km^{-1}; Norton, 1985) gives me temperature lowering of –4.5 °C and –3.9 °C relative to present for the ELA depression of 880 and 770 m for 19.8±0.3 ka and 16.7±0.3 ka respectively. A standard environmental lapse rate (–6.5 °C km^{-1}) increases the temperature depression to –5.7 °C and –5.0 °C for the same times relative to present.

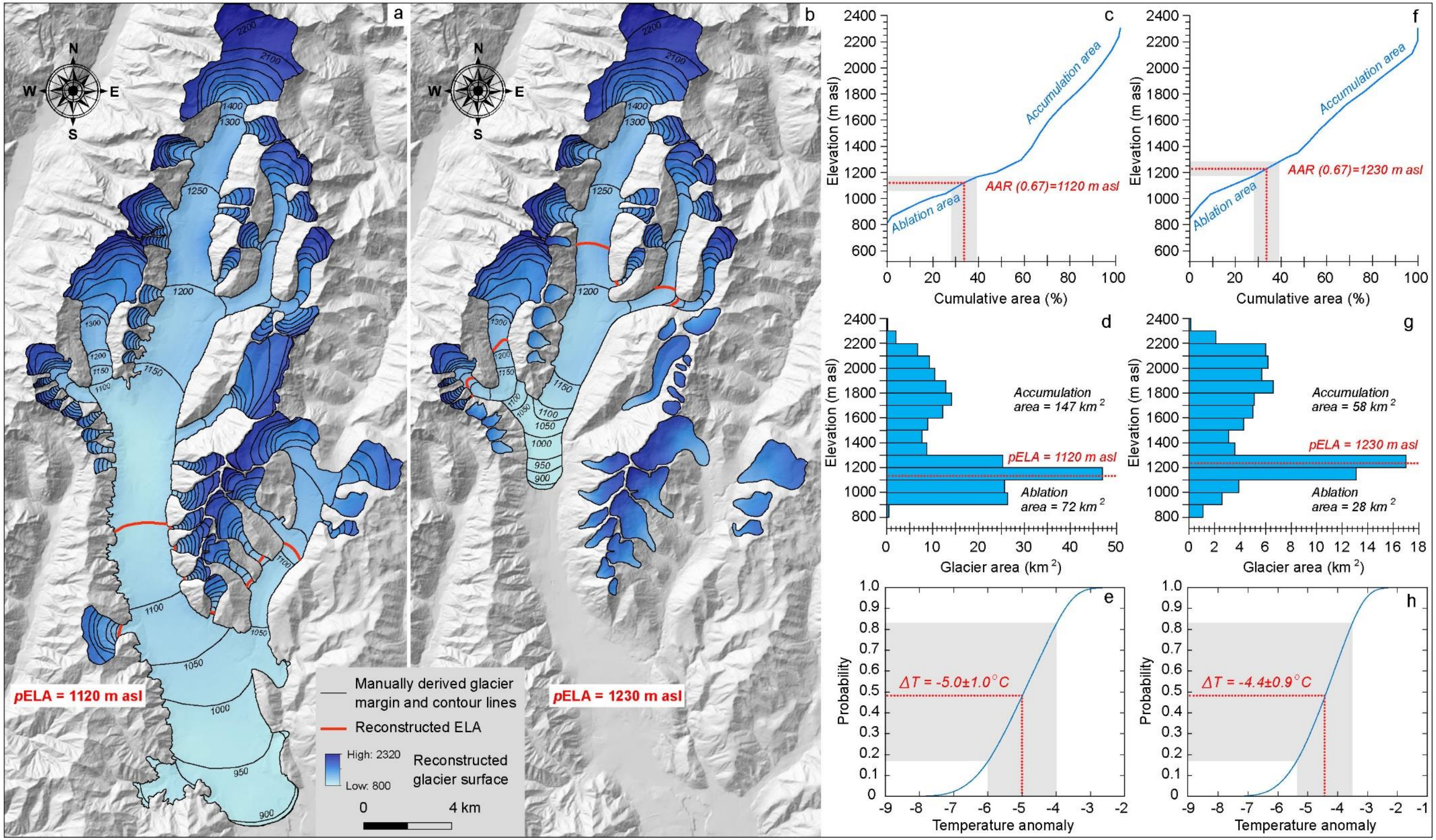

a
b
c
d
e
f
g
h
pELA = 1120 m asl
pELA = 1230 m asl
Manually derived glacier margin and contour lines
Reconstructed ELA
High: 2320
Low: 800
Reconstructed glacier surface
0
4 km
AAR (0.67)=1120 m asl
AAR (0.67)=1230 m asl
Accumulation area
Ablation area
Elevation (m asl)
Cumulative area (%)
Accumulation area = 147 km 2
Ablation area = 72 km 2
pELA = 1120 m asl
Accumulation area = 58 km 2
Ablation area = 28 km 2
pELA = 1230 m asl
Glacier area (km 2)
Probability
ΔT = -5.0±1.0°C
ΔT = -4.4±0.9°C
Temperature anomaly

Figure 5.6 *Reconstructed surface of the palaeo Ahuriri Glacier (based on manually derived contour lines) and reconstructed ELA (AAR=0.67) for 19.8±0.3 ka (a) and 16.7±0.3 ka (b). Cumulative curve (surface profile) of the palaeo Ahuriri Glacier for 19.8±0.3 ka (c) and 16.7±0.3 ka (f). The palaeo ELA is shown by the dashed line and shaded box. Hypsometry and reconstructed ELA of palaeo Ahuriri Glacier for 19.8±0.3 ka (d) and 16.7±0.3 ka (g). Cumulative distribution function for the palaeo temperature estimate associated with the Ahuriri terminal moraines for 19.8±0.3 ka (e) and 16.7±0.3 ka (h). Shaded box defines the 1-sigma uncertainty interval*[1].

Using a Monte Carlo technique (Eaves et al., 2016, 2017) to combine uncertainties in each variable (*m*ELA, *p*ELA, AAR, and temperature lapse rate), I derive an estimated temperature anomaly of –5.0±1.0 °C (1σ) relative to present for 19.8±0.3 ka and –4.4±0.9 °C (1σ) relative to present for 16.7±0.3 ka (Figure 5.6e, h).

5.6 Discussion

5.6.1 Last Glacial Maximum

The exposure age data from moraine belt-3 provide robust constraints on the timing of maximum glacier advance during the Last Glacial Maximum in the Arhuriri River valley. Given the ~2.5 km spread of the terminal morainal sequence at moraine belt-3, I anticipated that this landform may have accumulated during several glacial advance events, perhaps across several millennia. However, with the exception of one anomalously young sample, there is no significant difference in boulder ages across this landform within age uncertainties (Figure 5.3, Table 5.2). I thus conclude that this moraine formed during a single glacial advance or stillstand and we combine the ages to give the timing of moraine formation as 19.8±0.3 ka. The absence of any older ages from the outer parts of this landform suggests that the largest advance of the

[1] The extent of separate ice bodies on panel “b” is theoretical, as I did not extract any ages at these sites. Therefore, these are not included in the ELA measurements. i.e. the panels “f”, “g”, and “h”, in the Figure 5.6, are created based on a single Ahuriri Glacier (without separate ice bodies).

last glacial cycle in the Ahuriri valley occurred at ~20 ka, at the height of the global Last Glacial Maximum (Clark et al., 2009).

Comparison of this new data with proximal moraine exposure chronologies shows that the timing of this glacier advance in the Ahuriri valley is consistent with other published ^{10}Be data from the left-lateral moraine system at Lake Pukaki, situated ~60 km to the northeast of my study site. There, a prominent portion of the Mt. John moraine formation is robustly dated to 20.3±0.6 ka (Doughty et al., 2015) and 20.0±0.5 ka (Strand et al., 2019) (Figure 5.7), which is indistinguishable within uncertainties from the Ahuriri moraine belt-3. However, while the moraine belt-3 advance in the Ahuriri valley represents the largest of the last glacial cycle, the geomorphic records at Lake Pukaki and other nearby sites (e.g. Lake Ōhau – Putnam et al., 2013b) record a much richer history of earlier, slightly more extensive glacier advances spanning much of oxygen isotope stages 2–3 (Denton et al., 2021). Differences in moraine presence between Ahuriri and the Pukaki/Ōhau records are unlikely to be attributable to large scale climatic forcing, given the proximity of all sites to one another. Instead, I consider these differences arise from the local topographic settings, which may influence both glacier response to climate (e.g. response times, and length sensitivity), as well as moraine preservation potential. For example, several studies have noted the potential feedback effect of subglacial erosion as a modulator of glacier length in the Pukaki catchment, whereby the large temperate glaciers advancing over and eroding thick packages of unconsolidated sediment may decrease bed elevation and reduce glacier length over time (McKinnon et al., 2012), thus enhancing the preservation potential of older moraines (Barr and Lovell, 2014). There is limited scope for such feedbacks in the Ahuriri River valley, where sediment fluxes are lower, and the low surface gradient of the former glacier (Figure 5.6a) restricted ice velocity, thus increasing the potential for obliterative overlap of moraines by successive glacier advances (Gibbons et al., 1984; Kirkbride and Brazier, 1998).

Despite lower potential for preserving moraines from glacial advances of similar extent, the prominent terminal moraine (moraine belt-3) in Ahuriri does afford clear delineation of past ice extent, which permitted 2D reconstruction of the former ice mass.

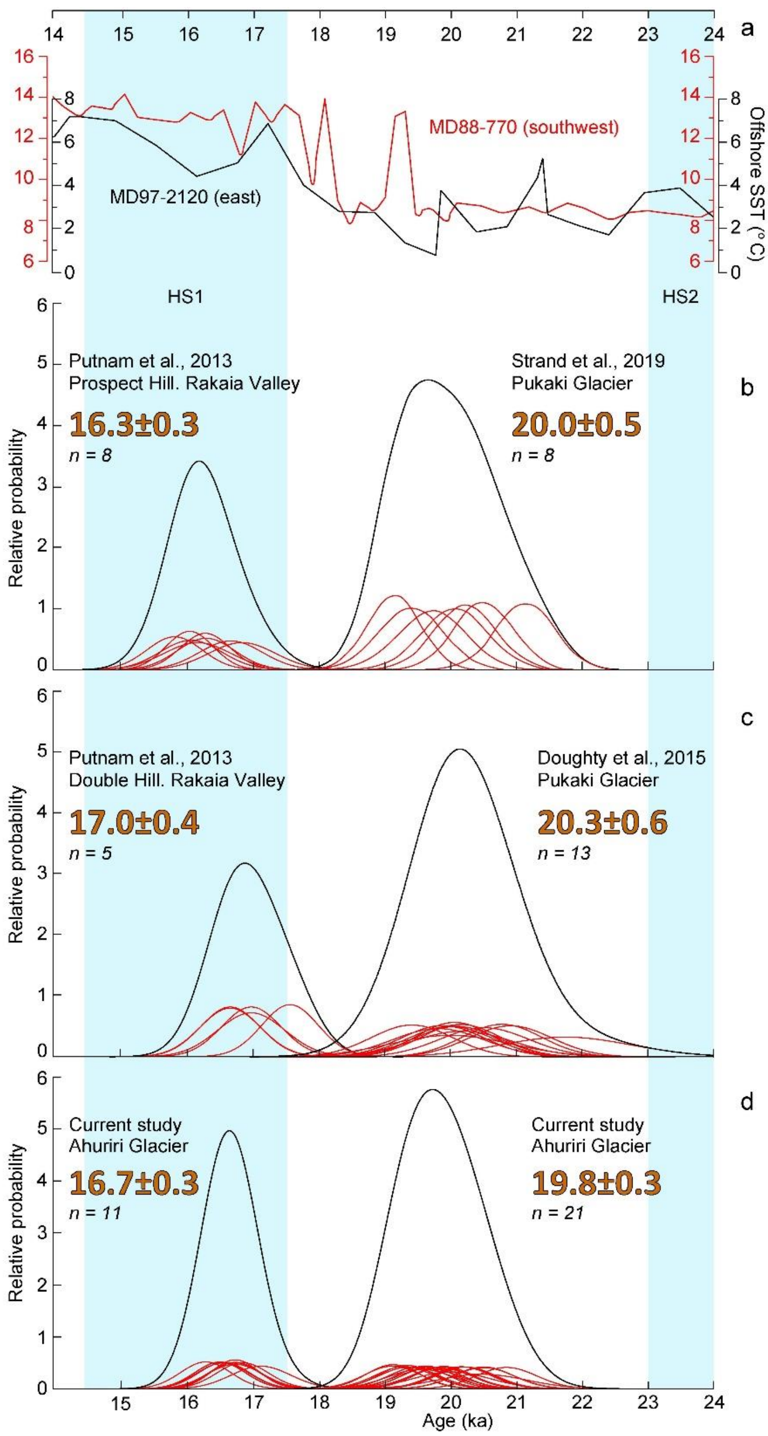

Figure 5.7 *a – Southern Ocean sea-surface temperature (SST) records for 24–14 ka: black – fauna based sediment cores MD88-770 (Barrows et al., 2007); red – Mg/Ca sediment cores MD97-2120 (Pahnke et al., 2003). See also Figure 5.1 for the location of the coring sites. b–c – A normal kernel density plots or "camel plots" from Pukaki and Rakaia glaciers (Putnam et al., 2013a; Doughty et al., 2015; Strand et al., 2019). d – Ahuriri terminal moraine belts (1 and 3). Outlier sample from current study camel plot was excluded. Blue bands correspond to Heinrich Stadials 1 (HS1) and 2 (HS2).*

My constraint from moraine belt-3 is in good agreement with glacier chronologies from southern mid-latitudes of South America (Patagonia) (Kaplan et al., 2008; García et al., 2019; Leger et al., 2021; Soteres et al., 2022) and Australia (Tasmania and Mt Kosciusko) (Barrows et al., 2002; Kiernan et al., 2004; Mackintosh et al., 2006) that indicate glacier advance at ~20 ka.

Using the AAR method, I estimated *p*ELA depression of 830–940 m for the former Ahuriri Glacier at ~19.8±0.3 ka. Porter (1975) also used AAR method (0.6±0.05 ratio) for *p*ELA estimation during the Last Glacial Maximum in the Lake Pukaki drainage basin, and suggested that *p*ELA was 875 m lower during construction of the equivalent Mt. John formation (26.5–18.0 ka; Barrell and Read, 2014). In addition, a glacier modelling simulation by Golledge et al. (2012) indicated that the Last Glacial Maximum ELA was depressed by 800 m (Ōhau, Tekapo glaciers) to 875 m (Pukaki Glacier), consistent with my *p*ELA calculations. Furthermore, modelling experiments by Putnam et al. (2013b) indicate snowline lowering of 920±50 m relative to present since the Last Glacial Maximum at the palaeo Ōhau Glacier.

Good agreement was found in the reconstruction of palaeo temperature between the manual and Monte Carlo method in our study. Both methods indicate that local temperature was 5±1 °C lower than present when the Ahuriri moraine belt-3 was formed (19.8±0.3 ka). This finding is consistent with modelling studies indicating the Last Glacial Maximum (24–21 ka) temperature depression of 5.8 °C below to the modern values from the Cobb valley (e.g., Eaves et al., 2019) or 5.8±0.6 °C from Fiordland in 19–17 ka time interval (e.g., Moore et al., 2022). However, while my finding agrees within uncertainty with modelling studies indicating the Last Glacial Maximum temperature depression of 6.25±0.5 °C below to the modern values from the Lake Ōhau (e.g., Putnam et al., 2013b) or 6–6.5 °C from the entire Southern Alps (e.g., Golledge et al., 2012), it is on the low side of the temperature range of these previous reconstructions. A likely explanation for this difference is that the simulation of 'maximum' LGM extent corresponds to the earliest ice advances between 32.5±1.0 ka and 27.4±1.3 ka from the Lake Ōhau (Putnam et al., 2013b) or between 30 ka and 27 ka from the entire Southern Alps (Golledge et al., 2012), while I only constrain the latest stage of the LGM (19.8±0.3 ka) in this study. My temperature depression also corresponds with pollen-based estimates of temperature lowering by 6.01±1.91 °C for New Zealand at the ~21 ka (Newnham et al., 2013). Multiple studies showing excellent agreement give high confidence to these LGM temperature estimates, providing a robust target for assessment of paleoclimate simulations using climate models (e.g. Kageyama et al., 2017).

A close linkage between Southern Ocean sea surface temperatures (SSTs) and mid-latitude glacier activity was proposed by Barrows et al. (2007) and later supported by Doughty et al. (2015) and Shulmeister et al. (2018b). Sediment core MD97-2120, 300 km east from the Southern Alps at 45°S (Pahnke et al., 2003) and sediment core MD88-770 (R/V Marion Dufresne), situated southwest of Australia at 46°S (Barrows et al., 2007) (Figure 5.1) highlight a Southern Ocean temperature drops of 4–5 °C below present at the height of the Last Glacial Maximum (Figure 5.7). Overall, the agreement between the estimated age of the Ahuriri moraine belt-3 and the cooling at ~20 ka suggests that the deposition of this moraine was not a local event. Rather, it was likely caused by regional or hemispheric cooling during at this time.

5.6.2 Last glacial termination

5.6.2.1 Onset of glacier retreat

The former Ahuriri Glacier retreated from the prominent LGM terminal moraine (moraine belt-3) at or shortly after 19.8±0.3 ka. A sequence of left-lateral moraines situated 2–4 km upstream (44°21'6"S, 169°39'24"E) from moraine belt-3 records the downwasting of the glacier at this time. I attempted to constrain the timing of this ice-thinning event by targeting the innermost moraine of the recessional sequence, termed here moraine belt-2 yield exposure ages from 9.9±0.3 ka to 12.2±0.5 ka. These dates are unusually young for their situation relative to LGM ice limits and morphostratigraphically inconsistent with the age of moraine belt-1 (16.7±0.3 ka), thus I do not believe these accurately reflect the timing of moraine-belt-2 deposition.

Anomalously young outliers are not uncommon in alpine moraine datasets (Heyman et al., 2011). However, young outliers are often isolated cases, that occur perhaps due to unrecognised surface erosion or rotation of individual boulders, and stand apart from a more secure population of samples that centre close to the true depositional age (e.g. sample AL-27-61 from moraine belt-3 in this study; Table 5.1). However, the clustering of inaccurate ages from moraine belt-2 ages suggests the cause is a process that worked more uniformly across these boulders. One possibility is that I have misinterpreted the genesis of this landform. Landslide and rock avalanches are frequent occurrences in the tectonically active Southern Alps, and can generate hummocky landforms of unconsolidated, poorly sorted sediment that resemble moraines (McColl and Davies, 2011). However, the position of this landform close to the centre of the valley away from nearby hillslopes, coupled with the relatively low-elevation valley sides that seem unlikely to generate large runout mass movements, leads me to rule out such a misinterpretation. Furthermore, the connection of my sample site (44°21'46"S, 169°38'15"E) to the clear flight of left-lateral moraines (44°21'6"S, 169°39'24"E) that grade to moraine belt-3 gives me confidence that my samples were similarly deposited by the waning former glacier.

I consider that the consistent age underestimation of samples from moraine belt-2 is likely to represent suppression of ^{10}Be production due to submergence beneath a shallow water body that developed during glacier retreat. Earlier mapping by Tielidze et al. (2021) revealed multiple shorelines imprinted on the ice-contact slope of moraine belt-3, which indicate former lake existence with former water levels (~725, 734, and 740 m a.s.l., Figure 5.8a). Crucially, the elevation of the uppermost shoreline is higher than the elevation of the boulders sampled (727-738 m a.s.l., Table 5.1), indicating that the boulders could have been submerged by this former water body. Using a cosmogenic nuclide production model, which incorporates the recent muon production model of Balco (2017c; Method 1A), I show that in situ cosmogenic ^{10}Be production declines rapidly even in shallow water, largely due to the rapid attenuation of spallogenic production (Figure 5.8b).

As a further test, the hypothetical modelling was undertaken to explore the lake depths and duration of boulder submergence that could explain my observed ^{10}Be concentrations. I assume that the proglacial lake existed continuously for a single period (rather than drying and refilling repeatedly) and that this period of lake cover began at 19 ka, shortly after moraine belt-3 deposition. Figure 5.8c shows that if water depth above our samples was 1–5 m, then minor sub-aqueous production could occur, and such a shallow lake would need to persist for 7–15 kyr to produce my measure concentrations. However, water depths >5 m effectively shutoff production. Thus, for a deeper lake (>5 m), my concentrations would imply lake persistence for ~7 kyr. While the lake depth is poorly constrained, these insights suggest that my concentrations require persistence of a glacial lake in Ahuriri River valley at least until the onset of the Holocene Epoch (c. 12 ka). Progressively falling lake levels, as indicated by the mapped shorelines (Figure 9–10 in Tielidze et al., 2021) may reflect down-cutting of the lake outlow into the glacio-fluvial outwash plains as indicated by the impressive flights of fluvial terraces situated immediately outboard of moraine belt-3 (Figure 5.3). Further chronological investigation of these sequences may afford critical examination of my inferred chronology of proglacial lake evolution.

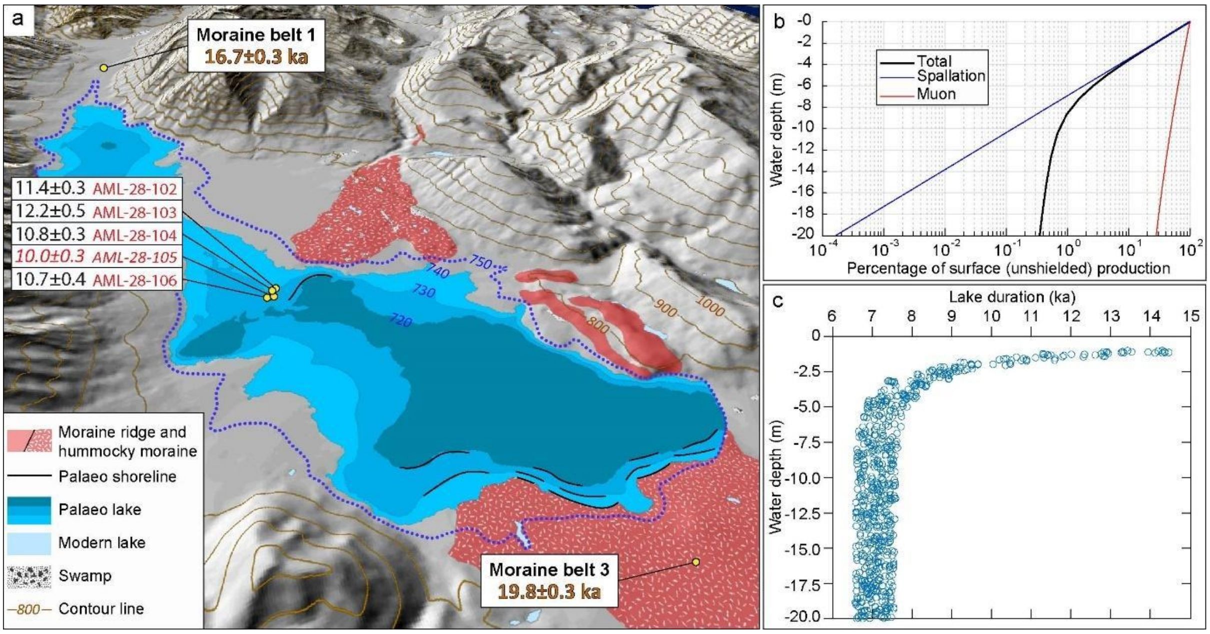

Figure 5.8 *a – Five ^{10}Be exposure data from moraine belt-2 and simulated palaeo Lake Ahuriri. Lake bathymetry was provided according to the palaeo lake shorelines based on DEM contours. The blue dotted line shows the maximum possible level of the lake, where the hypothesised lake level coincides with the maximum elevation of the moraines. b – ^{10}Be production decreases beneath water according to Balco (2017c). c – hypothetical modelling to constrain the lake depths and duration of existence that could explain observed ^{10}Be concentrations.*

5.6.2.2 Rate of deglacial warming

The available chronological information from the lower Ahuriri valley indicates that glacier retreat began at 19.8±0.3 ka, although the precise timing of ice withdrawal from the lower valley remains uncertain. However, surface-exposure ages from the moraine belt-1 confirm that the second readvance or stillstand of the former Ahuriri Glacier occurred at 16.7±0.3 ka, which shows that a significant retreat of the palaeo Ahuriri Glacier occurred between 19.8±0.3 and 16.7±0.3 ka. These data constrain an 18 km retreat in glacier length (43% retreat of the LGM length) of the former Ahuriri Glacier. My glacier reconstructions indicate that this retreat occurred in response to an ELA rise of c. 110 m, from ~1120 m a.s.l. to ~1230 m a.s.l., which corresponds to just ~0.6±1.0 °C of warming between those two time-periods (Figure 5.9) (assuming no change in precipitation occurred).

The large length change in response to relatively minor ELA rise suggests that the former Ahuriri glacier, in its LGM configuration, was highly sensitive to even minor climatic variability. Such high sensitivity may be a function of the very low inclination (~5 m/km) of the former Ahuriri Glacier in its middle to lower section (Figure 5.6). This characteristic of some former valley glaciers was recently demonstrated in the Cobb River valley, where physics-based modelling shows that a low-angle glacier reduced in length by half during the LGM in response to just 0.5 °C rise in air temperature (Eaves et al., 2019). The former Ahuriri Glacier exhibits similar characteristics to former Cobb valley glacier, namely a low surface slope and lower altitude source area, especially in comparison to neighbouring Ōhau and Pukaki glaciers, which were sourced from the highest parts of the Southern Alps. These characteristics may be responsible for the observed difference in moraine sequences at these locations.

In contrast to the LGM, few quantitative estimates of air temperature changes during the last glacial termination exist for the Southern Alps. In one of the few glacial studies to provide such data, Putnam et al. (2013a) reported 3.25 °C warming (from −6.25 to −3.0 °C) between 17.8±0.2 and 16.3±0.4 ka from the Rakaia River valley, situated on the eastern side of the Southern Alps. At face value this rate of warming appears much greater than my ~0.6 °C temperature increase between 19.8±0.3 ka and 16.7±0.3 ka (Figure 5.9), however there are several possible explanations for this discrepancy.

It may represent a real difference, whereby there was substantial heterogeneity in the timing and rate of warming across the Southern Alps. The interplay of topography and atmospheric circulation, particularly the orientation of the Southern Alps relative to prevailing circulation, has been recognised to create distinct climate districts that exhibit different responses to changes in synoptic atmospheric conditions (Kidson, 2000; Lorrey et al., 2007; 2010). There is general consensus that the westerly winds contracted southwards during the last glacial termination (Anderson et al., 2009; Buizert et al., 2018; Denton et al., 2021), which would lead to an increase in blocking, relative to trough regimes (Lorrey et al., 2012; Lorrey and Bostock, 2017). However, such a regime shift tends to have fairly uniform temperature effects across the country, while flattening the west-east precipitation gradient (Lorrey et al., 2007). Neither of these climatic impacts are consistent with greater rates of recession of glaciers in the Rakaia, relative to the Ahuriri.

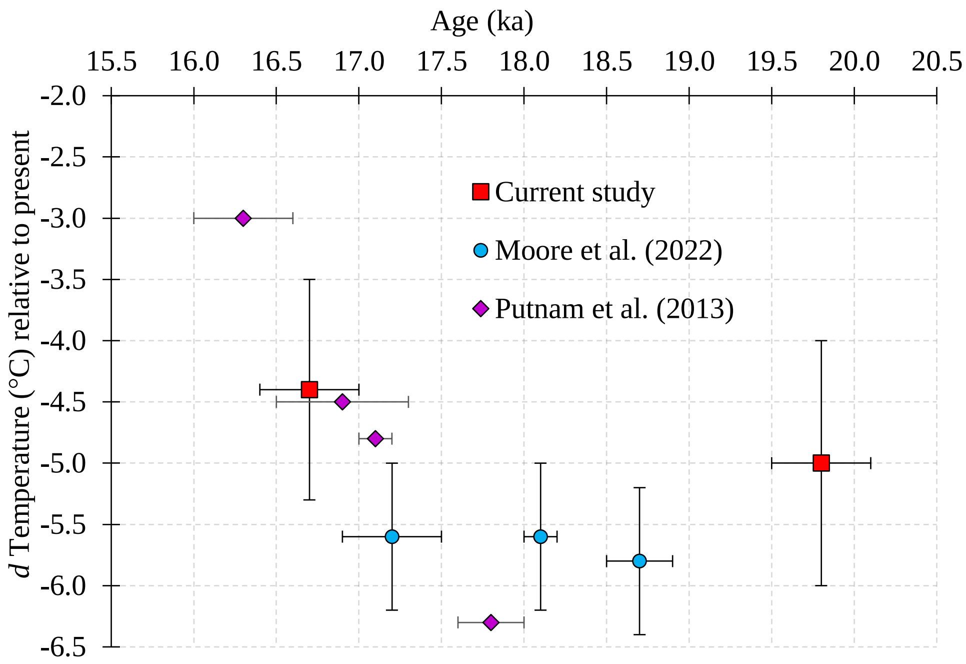

Figure 5.9 *Comparison of the dTemperature (°C) change relative to present (1981–2010) between current study, Moore et al. (2022) and Putnam et al. (2013a) at the onset of last glacial termination.*

Alternatively, both glacier-based temperature reconstructions may be accurate, but the difference may be caused by relatively low resolution of the dating method, relative to the rate of climate change. Despite precise local constraint of the in situ ^{10}Be production rate in New Zealand (Putnam et al., 2010b), exposure ages of landforms typically have a 1σ (68% confidence interval) uncertainties of a few centuries at best, largely due to geological scatter. Thus, it is possible that this imprecision may reduce the ability to pinpoint the onset of deglaciation if those the climatic changes were abrupt (i.e. occurring over a few centuries or less) (Balco, 2020). This effect may be relevant to the onset of deglaciation in New Zealand. For example, Denton et al. (2021) demonstrate using climate model experiments how a southward shift in the westerly winds at the onset of the last glacial termination can cause several degrees of warming in the Tasman Sea over centennial timescales. Such a shift, which is supported by marine sea-surface temperature proxies (Bostock et al., 2015), may have occurred more rapidly than the cosmogenic dating method can resolve.

Recent studies have suggested that differences in the timing and rates of glacier retreat between nearby catchments may reflect local topo-climatic influence. For example, retreat of large valley glaciers, such as the former Rakaia Glacier, into overdeepened basins may have promoted proglacial lake formation that enhanced the overall sensitivity of glacier mass balance to atmospheric forcing (Shulmeister et al., 2010). Sutherland et al. (2020) show that under similar climate conditions, glaciers calving into proglacial lakes may experience enhanced retreat relative to land-terminating glaciers. The modelling simulations of Putnam et al. (2013a) do not account for this possible feedback, likely due to the lack of constraint on former bed geometry, therefore it is possible their inferred temperature changes overestimate the rate of deglacial warming.

Finally, it is possible that methodological differences between my manual approach to ELA reconstructions and other numerical modelling approaches may be the cause of differences in the inferred temperature anomalies. Previous work has shown that temperature reconstructions are comparable between these methods (e.g. Kaplan et al., 2010; Doughty et al., 2013; Eaves et al., 2017), however these studies largely focus on relatively small former glaciers with simple geometries. My application of manual glacier reconstruction method to the large, former Ahuriri Glacier requires extrapolation of ice surface over several 10s of kilometres without direct constraint by geomorphological evidence. Errors in the reconstructed glacier geometry may thus propagate over such distances with potential to impact the ELA estimation via the AAR method. However, temperature estimation via numerical modelling of former glaciers also involves assumptions (e.g. precipitation rate, bed geometry) that may cause inaccuracies (e.g. Rowan et al., 2014), which could also factor into the discrepancy between my deglacial temperature curve and that of Putnam et al. (2013a). It is noteworthy that a recent study from southern New Zealand demonstrates that the local ELA remained close to LGM values, with little evidence for warming, until at least 17.2±0.2 ka (Moore et al., 2022) (Figure 5.9). This reconstruction, from a simple former cirque glacier, is unlikely to be affected by uncertainties in past bed geometry or possible lake calving feedbacks, thus may represent a robust estimate of atmospheric conditions. My record from the Ahuriri valley mirrors the ELA-inferred temperature changes from Moore et al. (2022), with gradual ELA-rises during the late stages of the LGM (see Eaves et al., 2019), with the majority of deglacial warming occurred after 17 ka.

5.7 Conclusions

To investigate the maximum extent and deglaciation of the former glacier during the Last Glacial Maximum, I report the dataset with thirty-eight ^{10}Be surface-exposure ages from three different sites of the Ahuriri River valley, central Southern Alps, New Zealand. The main findings of this chapter are:

i) The former Ahuriri Glacier reached its maximum extent at 19.8±0.3 ka. This advance appears to be the largest event of the last glacial cycle in the Ahuriri River valley.

ii) A GIS-based glacier reconstruction indicates that the palaeo Ahuriri Glacier had an ELA of 1170–1060 m a.s.l. at 19.8±0.3 ka, which is 830–940 m lower than the present ELA on nearby glaciers. This equates to a temperature difference of –5±1 °C relative to present (1981–2010), which agrees within uncertainty with other regional climate proxy reconstructions for this time.

iii) Onset of glacier retreat after 19.8±0.3 ka coincided with development of a proglacial lake that imprinted shorelines on the LGM moraines and partially submerged recessional moraines. Anomalously young ^{10}Be exposure ages (11–12 ka) from submerged moraines suggest this lake persisted at c. 740 m a.s.l. or higher until at least 12 ka.

iv) By 16.7±0.3 ka the Ahuriri Glacier had retreated ~18 km from its LGM position, in response to a c. 110 m rise in ELA, which equates to a 0.6±1.0 °C rise in temperature. This small amount of warming contrasts with a previous estimate of local deglacial warming at this time interval from the Rakaia River valley (Putnam et al. 2013a). These differences may in part reflect the approaches taken to reconstruct past temperature from glaciers (ELA reconstructions using the AAR method versus glacier models), but the correspondence between this study and similar ELA-inferred temperature changes from Fiordland (Moore et al., 2022) shows that my finding may be real and warrants further investigation.

This study shows that the Ahuriri Glacier was at its LGM position at 19.8±0.3 ka and then receded by 16.7±0.3 ka but these ages do not constrain the timing of termination onset. Thus, the precise timing of ice withdrawal from the lower Ahuriri valley remains uncertain. Further dating, particularly of the left lateral moraines near Moraine belt-2, may shed light on this.

CHAPTER 6: GLACIER-CLIMATE RECONSTRUCTIONS FROM THE AHURIRI RIVER VALLEY DURING THE LATE GLACIAL

6.1 Abstract

Glacial landscapes preserve records of past climate change. Investigating the glacier-climate system over the Late Quaternary provides information about past climate change and context for present day glacier response to climate warming. Using twenty-eight beryllium-10 (^{10}Be) surface exposure dates and snowline reconstructions, I present glacier fluctuations and climate changes for the Late Glacial reversal in the Ahuriri River catchment, Southern Alps of New Zealand (44°7'50"S, 169°38'29"E). Prominent terminal and lateral moraine features from the upper right tributary of the Ahuriri River valley have exposure ages of 14.5±0.3 ka, 13.6±0.3 ka, and 12.6±0.2 ka, suggesting episodic advance and retreat of the glacier during the Antarctic Cold Reversal. Maximum elevation of lateral moraines (MELM) and accumulation area ratio (AAR) suggest snowline elevations at these ages were ≤700 m, ≤630 m, and ~360 m lower than today, respectively. This equates to air temperatures of ≤3.9, ≤3.5 °C, and 2.3±0.7 °C colder than today (1981–2010), assuming no changes in past precipitation. Ice-sculpted bedrock surfaces bound by a lateral moraine at nearby Canyon Creek have an age of 13.1±0.3 ka, indicating the moraine correlates with those in the Ahuriri upper right tributary. MELM and AAR reconstructions from the Canyon Creek suggest that snowline elevations at 14.5–13.6 ka were ≤500 or ~380 m lower than today, corresponding to air temperatures of ≤2.8 or 2.4±0.7 °C cooler than the present-day (1981–2010). These new results provide insight into the structure of the Antarctic Cold Reversal in the Southern Alps, showing that the largest glacier advance occurred at the start of this interval at c. 14.5±0.3 ka and was followed by smaller episodic advances interspersed by retreat. I hypothesize that the early cooling and glacier readvance in New Zealand at the onset of Antarctic Cold Reversal were triggered by a latitudinal shift of the Southern Hemisphere westerly wind belt.

6.2 Introduction

Worldwide glacial retreat during the last major deglaciation coincided with a large-scale reorganization of oceanic and atmospheric circulation patterns, global sea-level rise, and changes in greenhouse gas concentrations (Mix et al., 2001). This period of time, known as last glacial termination (or last deglaciation) extends from the end of the Last Glacial Maximum

(LGM, 19–20 ka; Clark et al., 2009) to the onset of the Holocene (11.7 ka; Denton et al., 2010). The later stages of the last deglaciation between 15.0 and 11.5 ka are known as the Late Glacial interval. During the Late Glacial, the warming trend recorded in Antarctic ice cores was interrupted by the Antarctic Cold Reversal (ACR, 14.5–12.5 ka) (Jouzel et al., 1995), which was subsequently also recognised in the southern mid-latitudes, including New Zealand (e.g. Putnam et al., 2010a; Kaplan et al., 2010; Kaplan et al., 2013; Pedro et al., 2016). Climate fluctuations during the Late Glacial are important because they provide an example of abrupt, non-linear climate change during a past period of global warming, that may have relevance for present day climate change (Kaplan et al., 2013).

Mountain glaciers are very responsive to climate fluctuations and provide crucial information on regional and global climate (Oerlemans, 2005). Cosmogenic exposure dating techniques using nuclides such as ^{10}Be are a widely used tool to understand past glacial fluctuations (Balco, 2011, 2020). Glacier snowlines are also frequently used to extract quantitative information about paleo temperature and precipitation for former glaciers (Mackintosh et al., 2017). Glacier records from New Zealand situated in the southwestern Pacific provide a rare record of Southern Hemisphere climate changes, and are ideal tools for testing hypotheses about the competing drivers of Late Glacial climate change (Kaplan et al., 2010).

In the Southern Alps, where the present work focuses, only a small number of Late Glacial cosmogenic moraine chronologies have been documented. These records provide evidence that a glacier-advance event during the Late Glacial culminated at ~13 ka (e.g. Kaplan et al., 2010; Putnam et al., 2010a) (See Figure 6.1 for site locations), suggesting close agreement with Antarctic ice core temperature records that indicate warming abruptly resumed at this time (Jouzel et al., 2001; Pedro et al., 2011). Some of these moraine records also include older ages that suggest glaciers may have been slightly larger at around 14.5 ka (Kaplan et al., 2013) and 14.1 ka (Putnam et al., 2010a). However, due to the limited number of ages available, the significance of these data for understanding millennial-scale climate events of the Late Glacial remains uncertain. Further records of glacier change from well-preserved moraine sequences are required to provide more complete information about the structure of mid-latitude climate variability during this millennial-scale event.

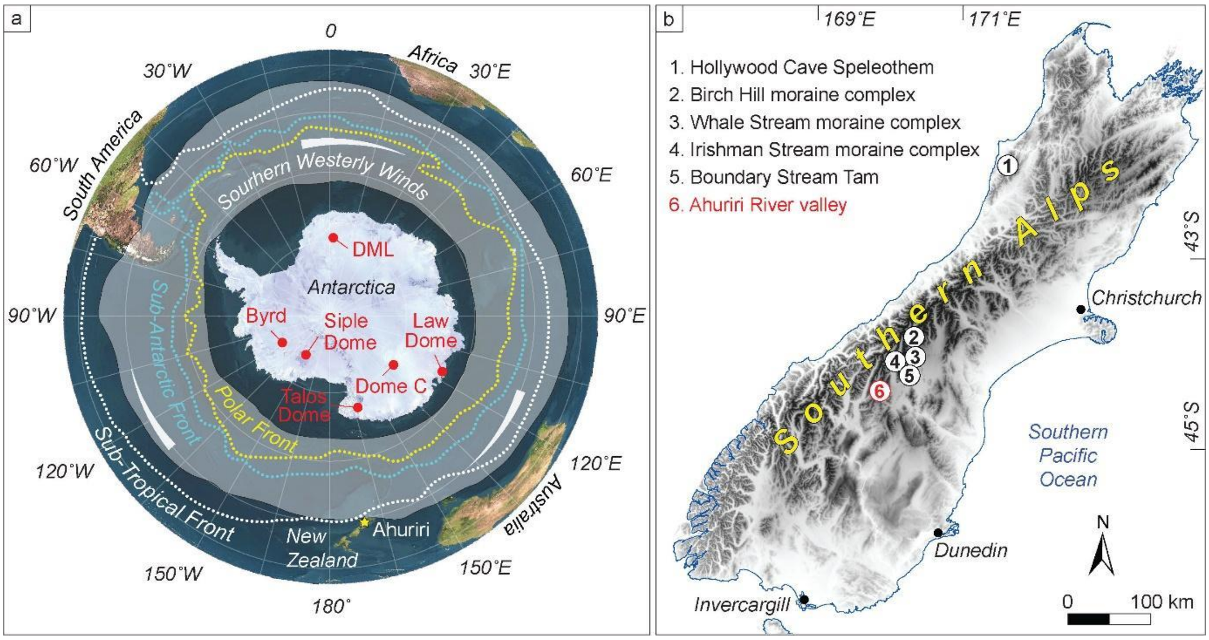

Figure 6.1 *a – Map of the Southern Hemisphere and location of Ahuriri River valley (yellow star). Light grey shading shows the approximate positions of the Southern Westerly Winds (SWW) belt (Sime et al., 2013). White arrows indicate direction of the SWW belt. The yellow, blue, and white dotted lines represent positions of the Polar Front, Sub-Antarctic Front, and Sub-Tropical Front, respectively (Darvill et al., 2016). The red dots are locations of key ice core palaeoclimate records illustrated in Figures 6.11 and 6.13 and mentioned in the text (Dronning Maud Land (DML), Byrd, Siple Dome, Talos Dome, Dome C, Law Dome) (Jouzel et al., 2001; Bereiter et al., 2015; Pedro et al., 2011; Stenni et al., 2011). b – Location map of South Island of New Zealand showing study sites mentioned in the text and the Ahuriri River valley, the focus of this study. See Figure 6.2 for a detailed view of the selected field sites.*

Here, I target glacial landforms of Late Glacial age at two different sites in the Ahuriri River valley in the Southern Alps of New Zealand such as the upper right tributary and the Canyon Creek (Figure 6.2). These two sites were chosen because moraines and glaciated bedrock sequences are well preserved. Furthermore, the former glaciers occupied single valleys of simple geometry, avoiding potential complications associated with tributary glaciers, making these basins ideal for reconstructing past snowlines (e.g. Pellitero et al., 2015).

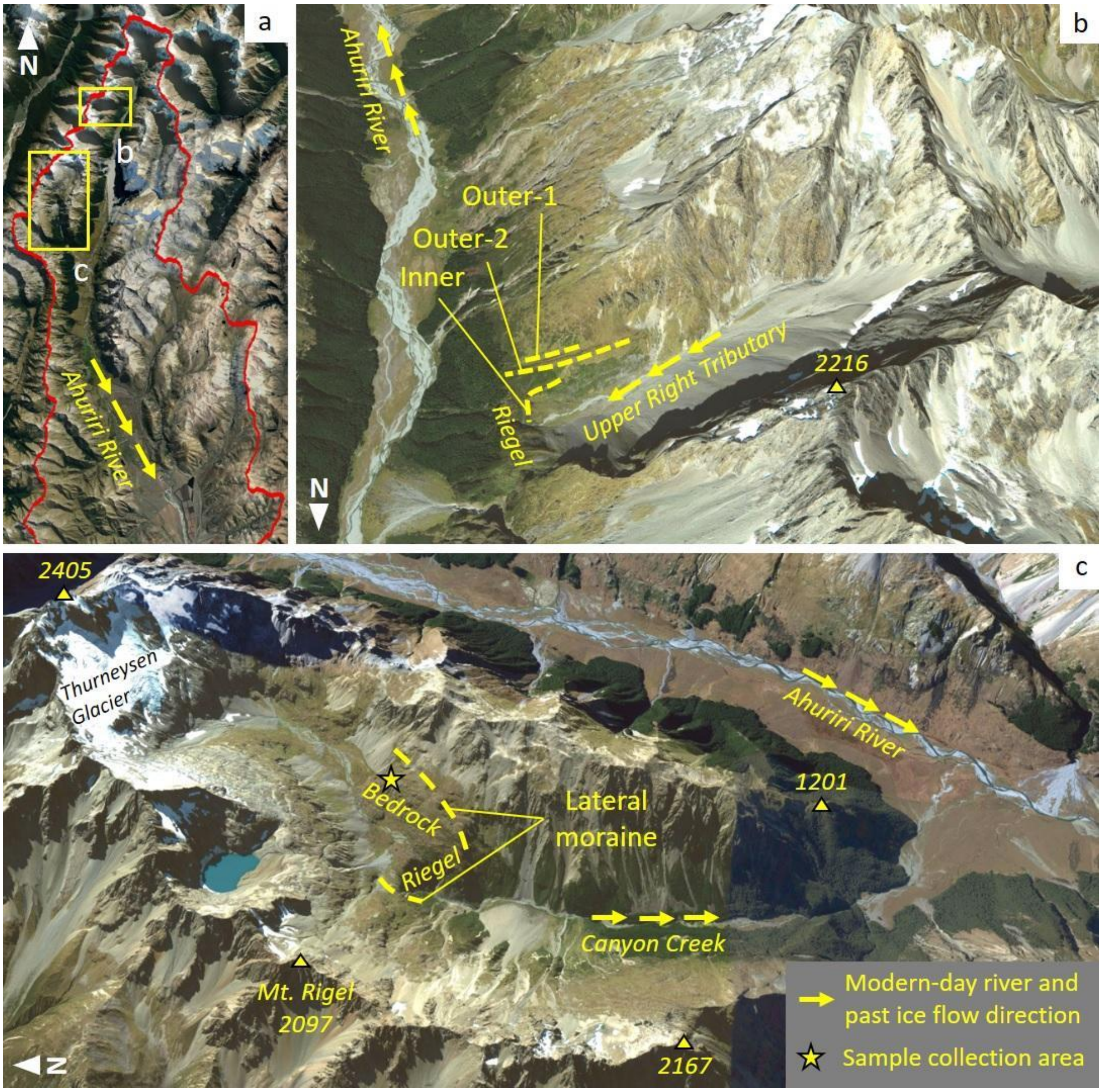

Figure 6.2 *a – Study area locations in the Ahuriri River catchment (Google Earth image). b – Upper right tributary of the Ahuriri River valley along with terminal and lateral moraine features and surrounding area. c – Canyon Creek along with lateral moraine features and surrounding area. Google Earth image (7/03/2010) is used as a background of panel b and c). Detailed glacial geomorphological maps of these panels are shown in Figure 6.3 and 6.5.*

6.3 Results

The spatial distribution of moraine and bedrock features across the upper right tributary of the Ahuriri River valley and Canyon Creek suggests the occurrence of several glacial readvance or stillstand periods during the Late Glacial. The timing of these glacial phases is constrained by twenty-eight ^{10}Be surface exposure ages spanning from 14.5±0.3 to 12.6±0.2 ka. Sample details for surface exposure ages from all moraine systems are given in Table 6.1, while cosmogenic ^{10}Be exposure ages are listed in Table 6.2 and Figure 6.3, 6.5. All age calculations are referenced to calendar year before sample collection (2020).

6.3.1 The upper right tributary of the Ahuriri River valley

A small tributary valley with a length of ~2.7 km connects to the upper western side of the Ahuriri River valley (44°7'41"S, 169°37'52"E). The main part of this valley is surrounded by steep, eroded slopes (especially the northern bench) resulting in extensive debris deposits (colluvium) on the lower valley walls and floor. The upper section of the valley reaches its maximum altitude at ~2360 m a.s.l., while the lowest part descends to an elevation of ~1150 m a.s.l. The lowest portion of the valley is represented by a glacial riegel (rock bar) that has been exposed by ice erosion. The surface of this riegel is fractured and partly vegetated.

Several lateral and terminal moraines exist at different altitudes in the lower part of the valley. Two clearly visible lateral moraine ridges hereafter called outer-1 (44°7'57"S, 169°38'34"E) and outer-2 (44°7'55"S, 169°38'30"E) run parallel to each other, ~20 m apart, on the southern flank of the valley (Figure 6.2). These moraines project into the main valley indicating that the former glacier exited the tributary and terminated in the Ahuriri River valley at the time of moraine formation. An additional well-preserved terminal moraine ridge (hereafter called inner) is situated ~140 m lower in elevation relative to the outer ridges 1 and 2 represents a thinner and shorter glacier that terminated just inboard of the riegel (44°7'54"S, 169°38'42"E). There are further ridges of uncertain origin running parallel to each other on the northern bench of the lower valley slope (44°7'44"S, 169°38'52"E) that were not investigated during the field campaign.

Table 6.1 *Surface-exposure sample details and ^{10}Be data of moraine systems and bedrock surface from the upper right tributary of the Ahuriri River valley and Canyon Creek. Italic ages indicate the outliers that were excluded through the chi-squared test (Balco, 2017a, 2017b). See Table 6.2 for the calculated ages and Figure 6.3 and 6.5 for sample location.*

Sample field ID	LLNL ID	Boulder/ Bedrock	Latitude (S)	Longitude (E)	Elevation (m a.s.l.)	Boulder size (L×W×H) (cm)	Sample thickness (average cm)	Shielding correction	Quartz weight (g)	^{9}Be added (mg)	^{10}Be/^{9}Be ± 1σ (10–^{14})	^{10}Be ± 1σ (10^{4}) (atoms/gram qtz.)
Upper right tributary of the Ahuriri River valley												
Outer lateral moraine ridge-1 (44°7'57" S 169°38'34" E)												
AU-26-75	BE50002	Boulder	-44.132107	169.64134	1315	400×190×170	3.7	0.941083	13.143	0.2873	11.06±0.25	15.95±0.41
AU-26-78	BE50005	Boulder	-44.13243	169.64223	1287	200×110×120	1.2	0.941901	13.774	0.2882	11.40±0.27	15.74±0.41
AU-26-79	BE50006	Boulder	-44.13243	169.64231	1286	160×130×60	1.6	0.946035	11.671	0.2879	9.93±0.23	16.14±0.42
AU-26-81	BE50008	Boulder	-44.132666	169.64315	1264	105×90×75	2.4	0.952138	12.918	0.2877	11.03±0.22	16.21±0.38
Blank	BE50010	-	-	-	-	-	-	-	-	0.2882	0.14±0.02	-
Outer lateral moraine ridge-2 (44°7'55" S 169°38'30" E)												
AU-26-73	BE50000	Boulder	-44.131838	169.64007	1339	280×200×60	1.2	0.943362	13.836	0.2873	11.59±0.22	15.90±0.35
AU-26-74	BE50001	Boulder	-44.13192	169.64091	1324	330×250×120	3.3	0.928704	9.482	0.2866	7.42±0.14	14.71±0.34
AU-26-76	*BE50003*	*Boulder*	*-44.132274*	*169.6422*	*1292*	*370×320×230*	*3.9*	*0.941555*	*11.356*	*0.2882*	*9.96±0.28*	*16.65±0.51*
AU-26-77	BE50004	Boulder	-44.132367	169.64261	1281	310×180×190	1.4	0.948823	13.479	0.2884	11.09±0.22	15.66±0.36
AU-26-80	BE50007	Boulder	-44.132513	169.64295	1270	400×290×150	2.5	0.951419	13.605	0.2878	10.42±0.19	14.53±0.32
AU-26-82	BE50009	Boulder	-44.132424	169.64321	1263	520×470×280	4.5	0.949802	13.952	0.2880	10.49±0.22	14.27±0.34
Blank	BE50010	-	-	-	-	-	-	-	-	0.2882	0.14±0.02	-
Inner lateral-terminal moraine ridge (44°7'54"S 169°38'42"E)												
AU-26-84	BE49516	Boulder	-44.131726	169.64395	1203	130×90×70	3.08	0.938499	14.902	0.2863	10.31±0.21	12.70±0.31
AU-26-85	BE49517	Boulder	-44.131726	169.64452	1188	750×390×390	2.46	0.946756	14.984	0.2878	10.48±0.22	12.91±0.33

AU-26-86	BE49518	Boulder	-44.131834	169.64462	1186	120×95×46	1.17	0.946756	14.537	0.2872	10.14±0.19	12.83±0.30
AU-26-87	BE50011	Boulder	-44.13173	169.6451	1178	135×67×64	6.10	0.952172	7.0129	0.2881	4.94±0.12	12.42±0.38
AU-26-88	BE49519	Boulder	-44.13198	169.64525	1175	420×350×210	1.21	0.952172	14.908	0.2876	10.80±0.20	13.37±0.31
AU-26-89	BE49520	Boulder	-44.132115	169.64543	1171	230×210×160	3.19	0.955393	13.755	0.2880	9.62±0.20	12.86±0.32
AU-27-91	*BE49522*	*Boulder*	*-44.131055*	*169.64544*	*1179*	*490×320×230*	*1.64*	*0.952291*	*14.468*	*0.2887*	*8.75±0.18*	*11.11±0.28*
AU-27-92	BE49523	Boulder	-44.130957	169.64545	1178	not recorded	3.67	0.951371	14.612	0.2877	9.76±0.21	12.28±0.32
AU-27-93	BE49524	Boulder	-44.13088	169.64524	1181	not recorded	2.73	0.952522	13.131	0.2882	9.15±0.21	12.80±0.35
AU-27-94	BE49525	Boulder	-44.130879	169.64523	1181	not recorded	2.55	0.952522	9.8891	0.2885	7.05±0.14	12.92±0.32
AU-27-95	*BE49526*	*Boulder*	*-44.130751*	*169.64523*	*1182*	not recorded	*3.19*	*0.952291*	*14.711*	*0.2884*	*1.95±0.12*	*19.99±0.17*
Blank	BE49527	-	-	-	-	-	-	-	-	0.2890	0.42±0.05	-
Riegel-bedrock near the Inner lateral-terminal moraine ridge (44°7'56"S 169°38'44"E)												
AU-26-90b	BE49521	Bedrock	-44.132226	169.64577	1163	-	7.00	0.955393	14.760	0.2879	10.70±0.33	13.40±0.46
Blank	BE49527	-	-	-	-	-	-	-	-	0.2890	0.42±0.05	-
Canyon Creek bedrock (44°11'22"S 169°35'28"E)												
CC-27-96b	BE49447	Bedrock	-44.186078	169.59321	1307	-	1.84	0.957296	5.3886	0.2781	4.44±0.12	14.21±0.47
CC-27-97b	BE49448	Bedrock	-44.18629	169.59321	1307	-	2.49	0.957296	3.7191	0.2778	3.21±0.12	14.42±0.64
CC-27-98b	*BE49449*	*Bedrock*	*-44.186441*	*169.59378*	*1314*	-	*2.48*	*0.957296*	17.765	0.2791	*11.57±0.22*	*11.82±0.27*
CC-27-99b	BE49450	Bedrock	-44.18664	169.59427	1318	-	1.88	0.957296	18.112	0.2792	15.03±0.28	15.15±0.34
CC-27-100b	BE49451	Bedrock	-44.188254	169.59521	1353	-	2.01	0.894639	17.867	0.2803	14.59±0.32	14.97±0.38
CC-27-101b	BE49452	Bedrock	-44.188254	169.59521	1353	-	2.02	0.894639	18.142	0.2799	14.25±0.27	14.36±0.32
Blank	BE49453	-	-	-	-	-	-	-	-	0.2803	0.26±0.04	-

Table 6.2 *Cosmogenic ^{10}Be exposure ages (with internal 1-sigma uncertainties) from the upper right tributary of the Ahuriri River valley and Canyon Creek. Three scaling schemes: St (Stone, 2000), Lm (Balco et al., 2008), LSD (Lifton et al., 2014) and the "Macaulay" production rate (Putnam et al. 2010b) was used for exposure age calculations. Ages calculated using a global production rate (Borchers et al., 2016) are also presented without external uncertainties that are much higher due to the large uncertainties in the global ^{10}Be production rate calibration dataset. Italic ages indicate the outliers that were excluded through the chi-squared test (Balco, 2017a, 2017b).*

Sample field ID	St age and internal uncertainty	**Lm age and internal uncertainty**	LSDn age and internal uncertainty	Lm age and internal uncertainty Global prod. rate
Upper right tributary of the Ahuriri River valley				
Outer lateral moraine ridge-1 (44°7'57" S 169°38'34" E)				
AU-26-75	14750±380	**14364±370**	13994±360	13700±353
AU-26-78	14548±384	**14170±374**	13832±365	13523±356
AU-26-79	14920±391	**14526±381**	14167±371	13850±363
AU-26-81	15254±354	**14842±345**	14490±336	14148±328
Error-weighted mean (n=4)	14883±188 (299)	**14490±183 (293)**	14135±179 (282)	13819±175 (671)
Outer lateral moraine ridge-2 (44°7'55" S 169°38'30" E)				
AU-26-73	14095±311	**13746±303**	13399±295	13109±289
AU-26-74	13637±314	**13317±306**	12993±299	12719±293
AU-26-76	*15688±484*	***15236±470***	*14865±458*	*14542±448*
AU-26-77	14459±335	**14086±326**	13758±319	13443±312
AU-26-80	13626±302	**13307±295**	13013±288	12709±281
AU-26-82	13694±328	**13374±320**	13075±313	12768±305
Error-weighted mean (n=5)	13888±142 (259)	**13553±138 (254)**	13235±135 (245)	12938±132 (621)
Inner lateral-terminal moraine ridge (44°7'54"S 169°38'42"E)				
AU-26-84	12768±312	**12522±306**	12310±301	11970±292
AU-26-85	12946±329	**12683±323**	12473±317	12121±308
AU-26-86	12757±298	**12511±292**	12309±288	11960±279
AU-26-87	12871±396	**12615±388**	12413±382	12057±371
AU-26-88	13342±309	**13041±302**	12824±297	12464±289
AU-26-89	13035±330	**12764±323**	12560±318	12197±309
AU-27-91	*11082±284*	***10961±281***	*10817±277*	*10482±269*
AU-27-92	12477±322	**12256±317**	12073±312	11721±303
AU-27-93	12873±353	**12617±346**	12414±340	12059±331
AU-27-94	12971±325	**12706±318**	12499±313	12142±304
AU-27-95	*2010±168*	***1984±166***	*1919±161*	*1886±158*

Error-weighted mean (n=9)	12894±109 (229)	**12637±107 (226)**	12432±105 (218)	12078±102 (575)
Riegel-bedrock near the Inner lateral-terminal moraine ridge (44°7'56"S 169°38'44"E)				
AU-26-90b	14110±485	**13764±473**	13522±464	13125±451
Error-weighted mean (n=1)	14110±485	**13764±473**	13522±464	13125±451
Canyon Creek bedrock (44°11'22"S 169°35'28"E)				
CC-27-96b	12780±428	**12532±420**	12261±411	11980±402
CC-27-97b	13034±583	**12762±571**	12481±559	12196±546
CC-27-98b	*10621±243*	***10547±241***	*10341±236*	*10076±230*
CC-27-99b	13516±305	**13197±298**	12889±291	12614±284
CC-27-100b	13909±357	**13575±349**	13207±339	12950±333
CC-27-101b	13346±302	**13042±295**	12726±288	12467±282
Error-weighted mean (n=5)	13405±162 (265)	**13102±159 (260)**	12787±155 (250)	12518±151 (606)

6.3.1.1 Outer moraine ridge-1

The outer moraine feature-1 is a single ridge, ~170 m long at an elevation ranging from 1230–1300 m a.s.l. Four exposure ages from this moraine ridge are tightly clustered and range from 14.2±0.4 to 14.8±0.3 ka (Figure 6.3–6.4). These four ages yield internal error-weighted mean age of 14.5±0.3 ka (n=4; no outliers).

6.3.1.2 Outer moraine ridge-2

The outer moraine landform-2 is inboard of outermost moraine feature-1. It is much longer than outer-1 stretching to about 560 m. The crest of this moraine feature ranges in altitude from ~1160 to ~1370 m a.s.l. and is scattered by large 1 to 3 m (diameter) sized greywacke boulders. Six samples from this lateral moraine feature returned ^{10}Be ages from 13.3±0.3 to 15.2±0.5 ka. The ages from outer moraine ridge-2 were grouped around an exposure age of 13.6±0.3 ka (n=5; 1 outlier – AU-26-76), based on the internal error-weighted mean of the six exposure ages (Table 6.2; Figure 6.3–6.4).

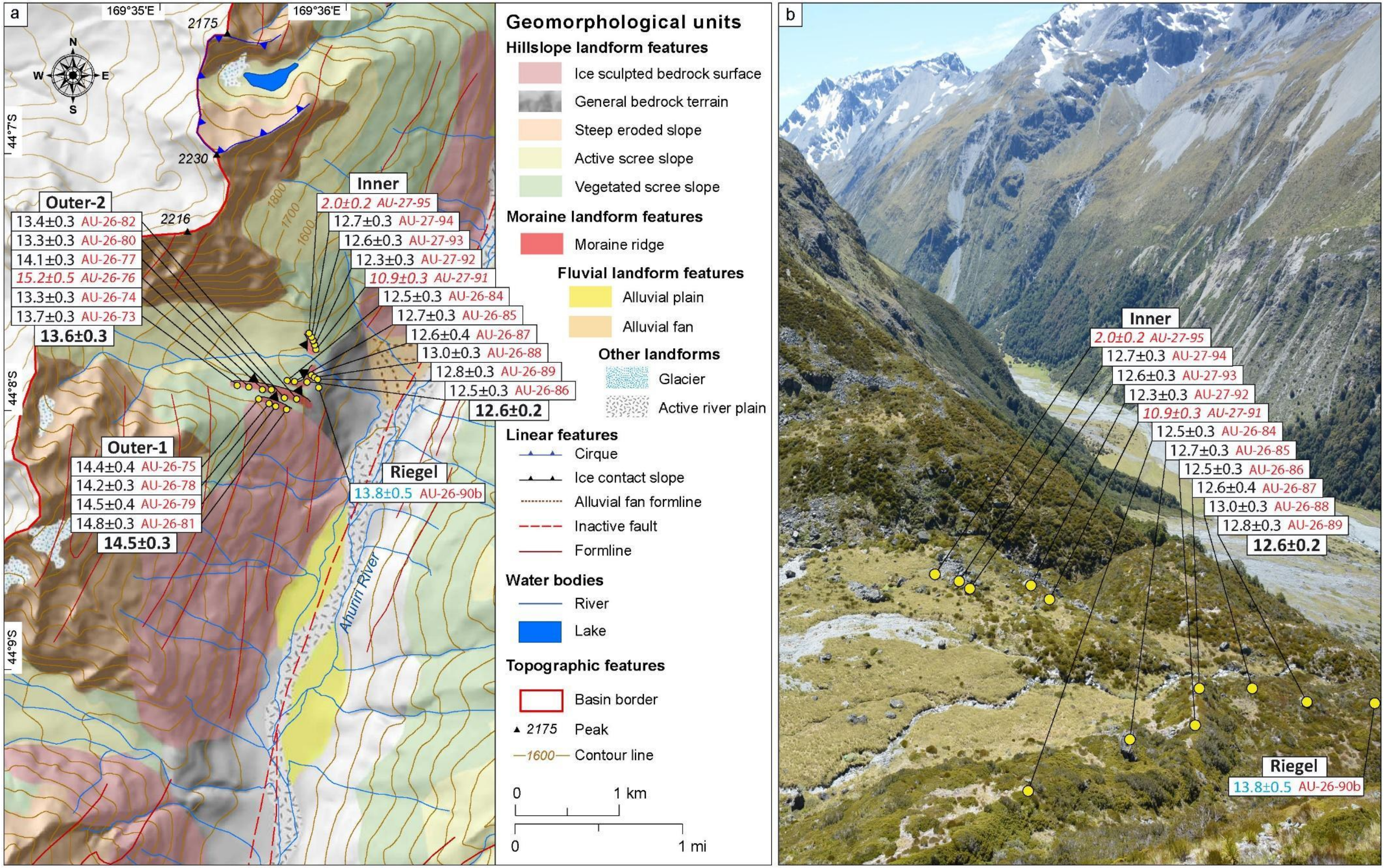
a
169°35'E
169°36'E
44°7'S
44°8'S
44°9'S
2175
2230
2216
1800
1700
1600
Ahuriri River
Outer-2
13.4±0.3 AU-26-82
13.3±0.3 AU-26-80
14.1±0.3 AU-26-77
15.2±0.5 AU-26-76
13.3±0.3 AU-26-74
13.7±0.3 AU-26-73
13.6±0.3
Inner
2.0±0.2 AU-27-95
12.7±0.3 AU-27-94
12.6±0.3 AU-27-93
12.3±0.3 AU-27-92
10.9±0.3 AU-27-91
12.5±0.3 AU-26-84
12.7±0.3 AU-26-85
12.6±0.4 AU-26-87
13.0±0.3 AU-26-88
12.8±0.3 AU-26-89
12.5±0.3 AU-26-86
12.6±0.2
Outer-1
14.4±0.4 AU-26-75
14.2±0.3 AU-26-78
14.5±0.4 AU-26-79
14.8±0.3 AU-26-81
14.5±0.3
Riegel
13.8±0.5 AU-26-90b
Geomorphological units
Hillslope landform features
Ice sculpted bedrock surface
General bedrock terrain
Steep eroded slope
Active scree slope
Vegetated scree slope
Moraine landform features
Moraine ridge
Fluvial landform features
Alluvial plain
Alluvial fan
Other landforms
Glacier
Active river plain
Linear features
Cirque
Ice contact slope
Alluvial fan formline
Inactive fault
Formline
Water bodies
River
Lake
Topographic features
Basin border
2175 Peak
1600 Contour line
0 1 km
0 1 mi
b
Inner
2.0±0.2 AU-27-95
12.7±0.3 AU-27-94
12.6±0.3 AU-27-93
12.3±0.3 AU-27-92
10.9±0.3 AU-27-91
12.5±0.3 AU-26-84
12.7±0.3 AU-26-85
12.5±0.3 AU-26-86
12.6±0.4 AU-26-87
13.0±0.3 AU-26-88
12.8±0.3 AU-26-89
12.6±0.2
Riegel
13.8±0.5 AU-26-90b

Figure 6.3 *a – Glacial geomorphological map of the upper right tributary of the Ahuriri River valley and surrounding area described in this chapter. See Figure 6.2 for map location with respect to the Ahuriri River valley. b – Field photo of the inner terminal-lateral moraine ridge. Yellow dots on the both panels indicate the location of the samples (see Table 6.1 and 6.2 for more details). The bedrock sample is given by blue text while the outlier samples are shown in red italic text.*

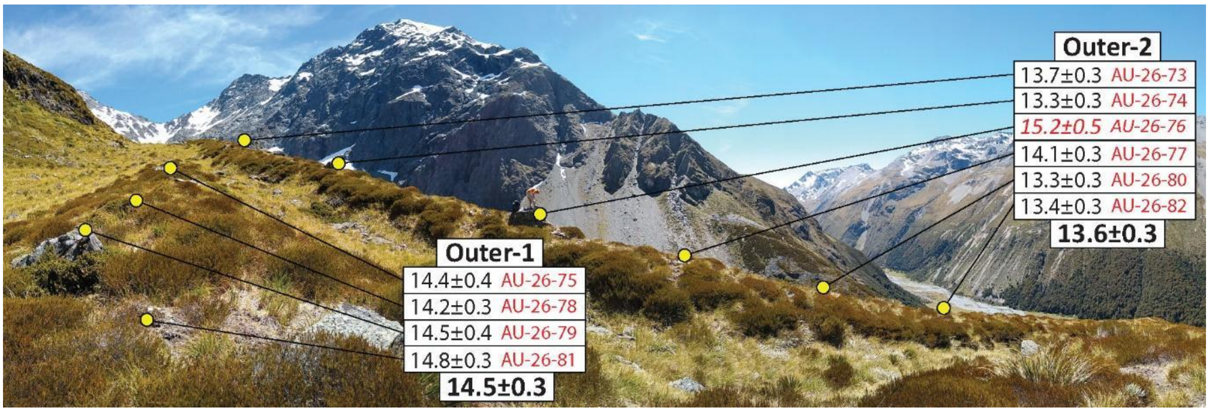

Figure 6.4 *Photo of the outer lateral moraine ridges 1 and 2 (Photo by: S. Eaves). Yellow dots indicate the location of the samples. The outlier sample is given by red italic text (see Table 6.1 and 6.2 for more details).*

6.3.1.3 Inner moraine ridge

The crest of the inner terminal moraine feature ranges from 1160 to 1230 m a.s.l. Eleven samples from this moraine ridge show individual apparent exposure ages ranging from 2.0±0.2 to 13.0±0.3 ka (Table 6.2 and Figure 6.3). Two boulders (AU-27-91 and AU-27-95) with youngest ages of 2.0±0.2 and 11.0±0.3 ka are not situated on the main moraine ridge. I consider that these boulders fell from a nearby slope and came to rest on an older deposit. Thus, I do not include these ages in our calculation of the mean landform age. The remainder of the nine samples from this terminal moraine ridge show individual apparent exposure ages ranging from 12.3±0.3 to 13.0±0.3 ka. The ages from this moraine landform were grouped around an exposure age of 12.6±0.2 ka (n=9; 2 outliers), based on the internal error-weighted mean of the eleven exposure ages.

6.3.1.4 Riegel-bedrock near the Inner moraine ridge

A glacial riegel (rock bar) is situated at the lowest portion of the valley at an elevation of 1150 m a.s.l. One bedrock sample (AU-26-90b) from this riegel was collected about 80 m away from the crest of inner moraine ridge. This sample with an age of 13.8±0.5 ka is stratigraphically consistent with the age of the inner moraine ridge and thus provides some constraint on the timing of glacier retreat and exposure of the riegel. The age is consistent with the abandonment of outer moraine ridge-2 (13.6±0.3 ka), suggesting that the glacier retreated from outer moraine ridge-2 to a position inside the tributary valley at this time.

6.3.2 Canyon Creek

Canyon Creek is one of the largest tributaries of the Ahuriri River. The upper western section of this valley is surrounded by Huxley Range with mountain peaks reaching ~2200 m a.s.l. The Huxley Range also separates Canyon Creek from Hunter River (Lake Hāwea basin) to the west. Other mountain peaks at the crest of the western surrounding ridge reach ~1800 m a.s.l. The largest extant glacier of the Ahuriri River catchment (Thurneysen Glacier – 0.9 km^2) is located in the headwater of this valley (44°9'56"S, 169°35'55"E). Separately, a large cirque exists on the western headwater slope of the Canyon Creek valley. The floor of this cirque contains a small lake (tarn) which is bound by fresh moraines that likely indicate late Holocene deglaciation. Several small alluvial fans and debris cones are observed mainly on the right side (west relative to Canyon Creek) slopes across the river. The full spectrum of ice sculpted bedrock is presented, in this valley, ranging from cirque headwalls (44°10'9"S, 169°35'11"E) to the valley floor (44°11'26"S, 169°35'23"E).

A large bedrock outcrop is situated on the floor of the middle section of Canyon Creek and cut through by the river. The largest exposure is represented on the true left side (44°11'22"S, 169°35'28"E) (Figure 6.5). Several small ponds occur on the surface of this bedrock while the rest of the area is partly vegetated. The elevation of this bedrock ranges from 1250 to 1500 m a.s.l.

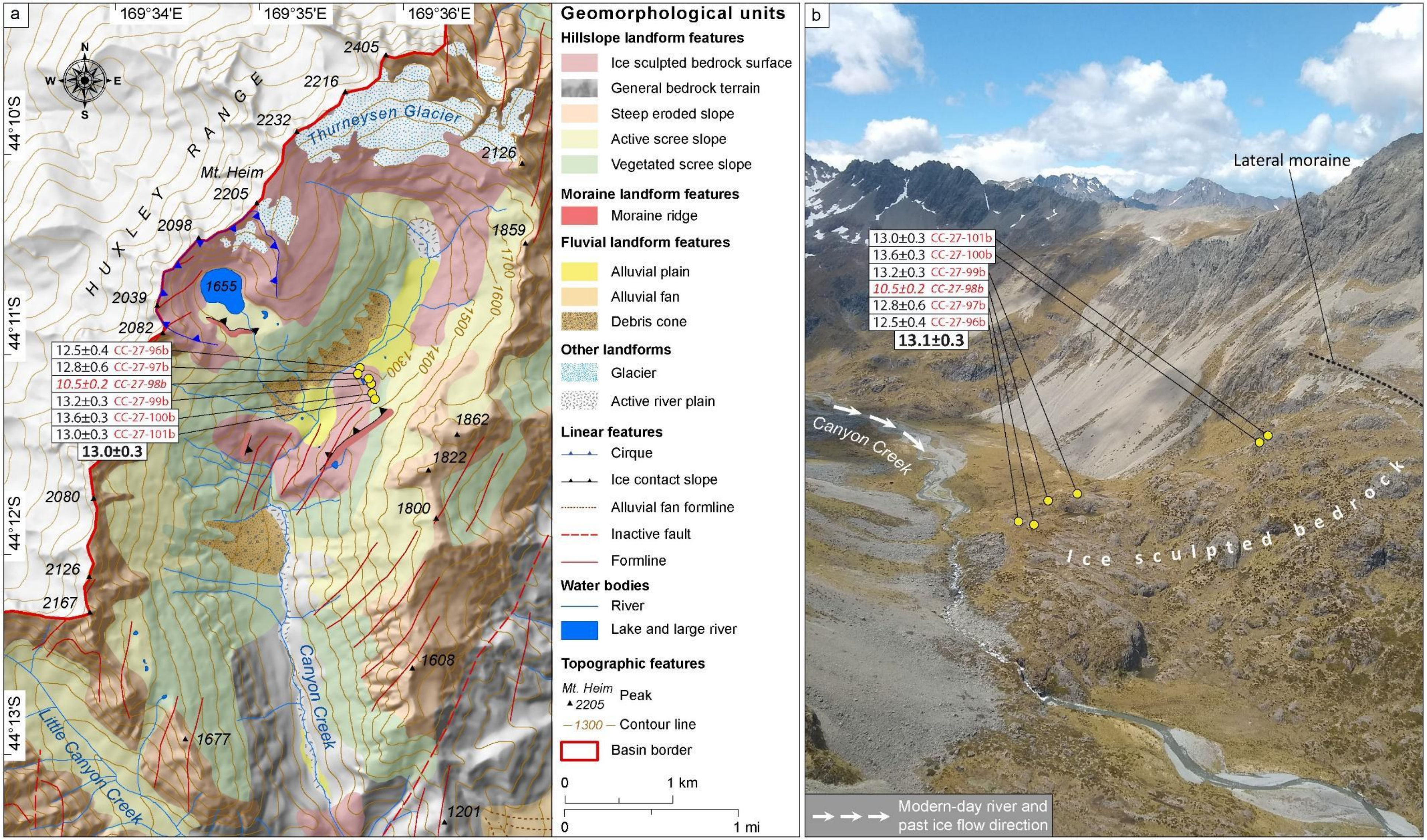
a
169°34'E
169°35'E
169°36'E
44°10'S
44°11'S
44°12'S
44°13'S
HUXLEY RANGE
Thurneysen Glacier
Mt. Heim
2205
2405
2216
2232
2126
2098
2039
2082
1655
1859
1862
1822
1800
2080
2126
2167
1608
1677
1201
Canyon Creek
Little Canyon Creek
12.5±0.4 CC-27-96b
12.8±0.6 CC-27-97b
10.5±0.2 CC-27-98b
13.2±0.3 CC-27-99b
13.6±0.3 CC-27-100b
13.0±0.3 CC-27-101b
13.0±0.3
Geomorphological units
Hillslope landform features
Ice sculpted bedrock surface
General bedrock terrain
Steep eroded slope
Active scree slope
Vegetated scree slope
Moraine landform features
Moraine ridge
Fluvial landform features
Alluvial plain
Alluvial fan
Debris cone
Other landforms
Glacier
Active river plain
Linear features
Cirque
Ice contact slope
Alluvial fan formline
Inactive fault
Formline
Water bodies
River
Lake and large river
Topographic features
Mt. Heim 2205 Peak
1300 Contour line
Basin border
0
1 km
0
1 mi
b
Lateral moraine
13.0±0.3 CC-27-101b
13.6±0.3 CC-27-100b
13.2±0.3 CC-27-99b
10.5±0.2 CC-27-98b
12.8±0.6 CC-27-97b
12.5±0.4 CC-27-96b
13.1±0.3
Canyon Creek
Ice sculpted bedrock
Modern-day river and past ice flow direction

Figure 6.5 *a – Glacial geomorphological map of the Canyon Creek and surrounding area. See Figure 6.2 for map location with respect to the Ahuriri River valley. b – Field photo of the sampled bedrock massif (Photo by: S. Eaves). Yellow dots on both panels indicate the location of the samples (see Table 6.1 and 6.2 for more details). The outlier sample is given by red italic text.*

A prominent linear lateral moraine ridge is situated on the eastern slope (relative to Canyon Creek) of the valley (44°11'28"S, 169°35'34"E) just above on the mentioned bedrock massif. This ridge is almost 800 m long and ranges in elevation from 1305 m to 1500 m a.s.l. The orientation of the moraine ridge is not parallel to the valley (or to the river bed), but the crest of the moraine descends towards the riverside, suggesting that the palaeo glacier terminated not far down-valley from this moraine. A smaller (~180 m length) and the less visible fragment of another lateral moraine ridge is preserved on the opposite slope, ranging from 1230 to 1275 m a.s.l. (44°11'30"S, 169°34'47"E). These paired lateral moraines are separated by glacial riegel of approximately 200 m relief.

Six exposure ages from the bedrock surface situated on left side (east relative to Canyon Creek) of the river (44°11'22"S, 169°35'28"E) range from 10.5±0.2 to 13.6±0.3 ka. The ages from this bedrock surface have a mean exposure age of 13.1±0.3 ka (n=6; 1 outlier – CC-27-98b), based on the internal error-weighted mean of the six exposure ages (Table 6.2 and Figure 6.5). The Canyon Creek bedrock ages suggest that this site was covered by ice during lateral moraine formation (outer-1 – 14.5±0.3 ka and outer-2 – 13.6±0.3 ka) at the upper right tributary of the Ahuriri River valley. One prominent moraine ridge from Canyon Creek (44°11'28"S, 169°35'34"E) is situated immediately outboard of the sampled bedrock outcrop, tentatively suggest that this moraine ridge correlates to the lateral moraine ridges 1 and 2 (14.5–13.6 ka) in the upper right tributary of the Ahuriri River valley.

6.3.3 Palaeo glacier geometry, snowline and temperature estimation

6.3.3.1 Upper right tributary of the Ahuriri River valley

I reconstructed the geometry of the former glacier when the terminus was at the inner latero-terminal moraine position at 12.6±0.2 ka in the upper right tributary of the Ahuriri River valley.

Based on this reconstruction, the glacier had a total surface area of ~1.8±0.2 km^2 while its length was ~2.5 km. The thickness of the former glacier was ~150 m. The AAR-based estimation shows that snowline for this tributary glacier at 12.6±0.2 ka was approximately 1640±50 m a.s.l., which is approximately 360 m lower than present-day (2000±50 m a.s.l., from nearby Thurneysen Glacier. See chapter 3.3.4). This magnitude of snowline depression equates to a temperature anomaly of –2.3±0.7 °C relative to present-day (Figure 6.6–6.7), assuming no change in precipitation.

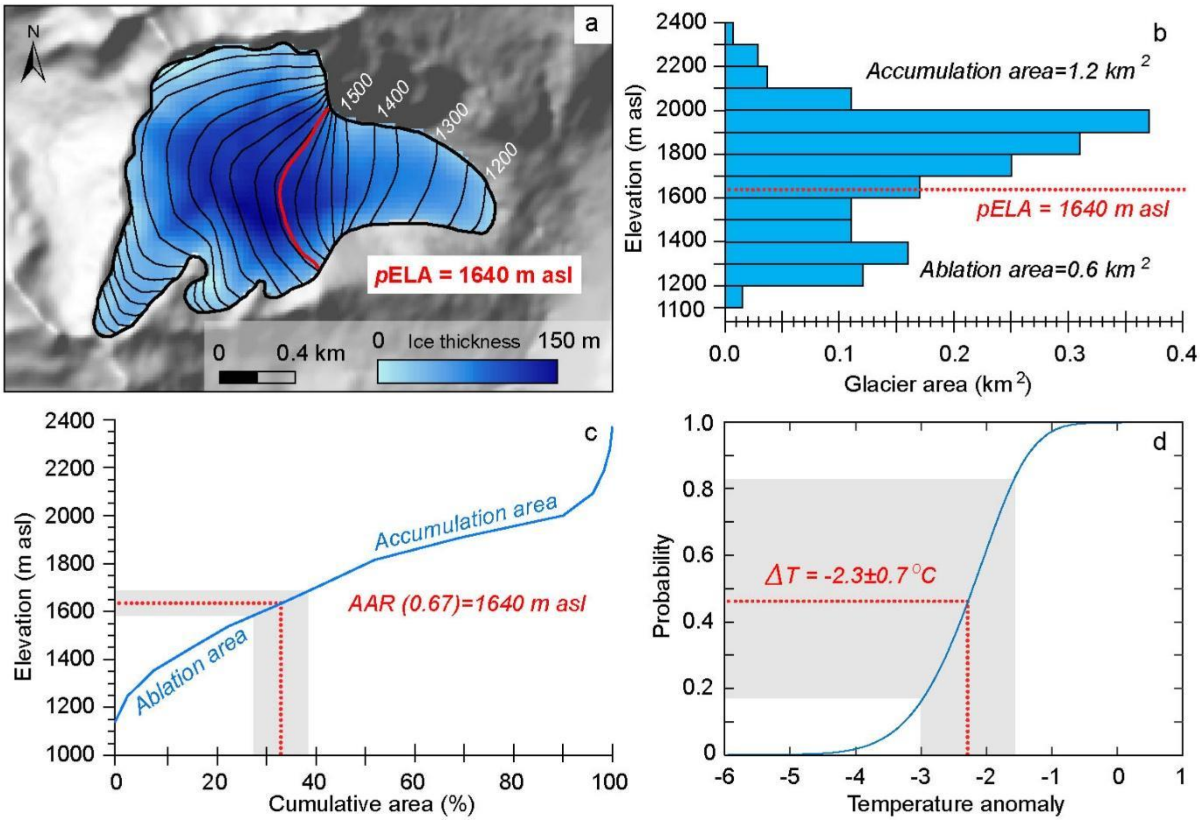

Figure 6.6 *a – Surface of the palaeo glacier (based on manually derived contour lines) and reconstructed ELA (AAR=0.67) for 12.6±0.2 ka in the upper right tributary of the Ahuriri River valley. b – Hypsometry and reconstructed ELA of palaeo glacier for 12.6±0.2 ka. c – Cumulative curve (surface profile) and reconstructed ELA of palaeo glacier for 12.6±0.2 ka. d – Cumulative distribution function for the palaeo temperature estimate associated with the terminal-lateral moraine for 12.6±0.2 ka. Shaded box defines the 1-sigma uncertainty interval.*

The two prominent outer moraine ridges (1 and 2) in the upper right tributary of the Ahuriri River valley are spaced approximately 20 m apart (Figure 6.3–6.4), however, the maximum elevation of the outer moraine feature-1 is about 70 lower (1300 m a.s.l.) than those for moraine feature-2 (1370 m a.s.l.) providing a broad maximum for the difference in the modern and palaeo snowlines based on the MELM method. i.e. the MELM technique only affords a maximum estimate of ELA depression due to the poor preservation of the upper portions of outer moraine ridges (1 and 2). These observations indicate that the snowline was ≤700 m lower than present-day snowline at 14.5±0.3 ka and ≤630 m lower than present-day snowline during the 13.6±0.3 ka suggesting that local air temperature was ≤3.9 and ≤3.5 °C colder than present respectively.

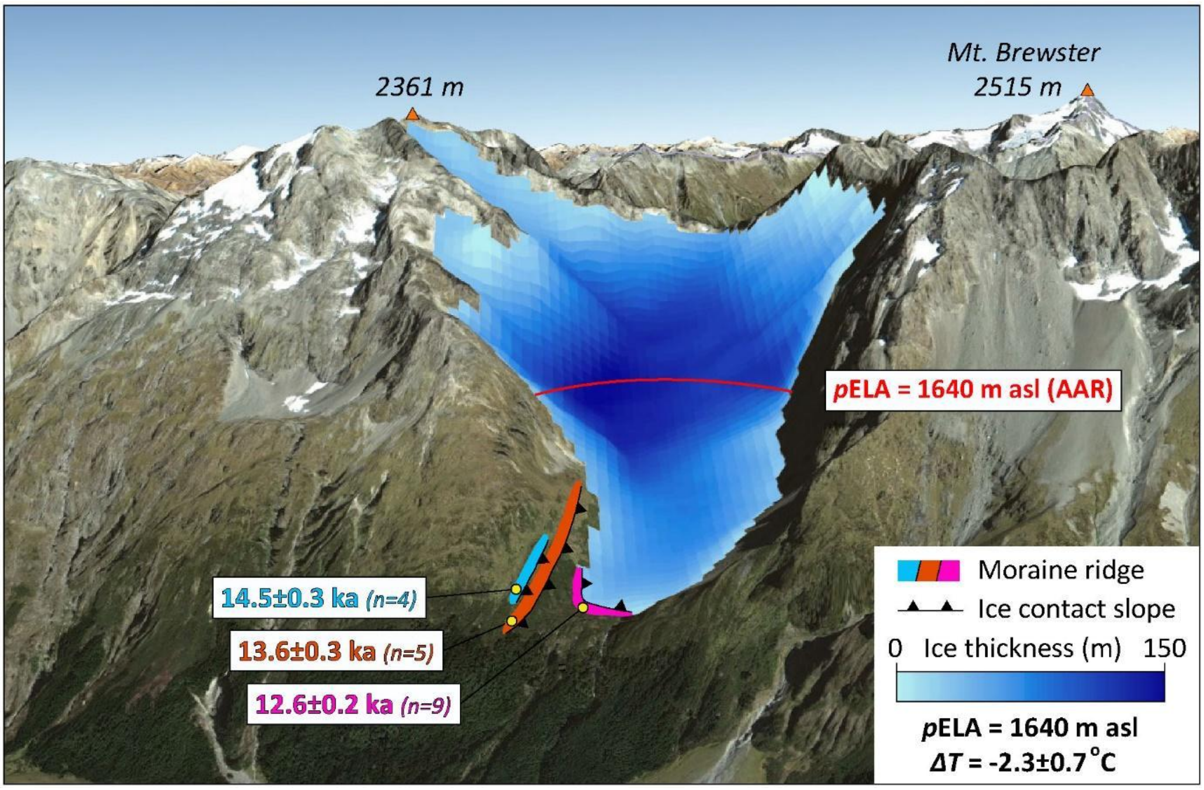

Figure 6.7 *Reconstructed palaeo Glacier and snowline at 12.6±0.2 ka from the upper right tributary of the Ahuriri River valley in 3D. Google Earth image (07/03/2010).*

6.3.3.2 Canyon Creek

Sampled bedrock surfaces from Canyon Creek are situated immediately inboard of a prominent left lateral moraine ridge (44°11'28"S, 169°35'34"E) which must have been deposited before the bedrock became exposed at 13.1±0.3 ka (Figure 6.5). Thus, I tentatively suggest that this moraine likely correlates with the outer-1 and outer-2 moraine ridges from the upper right tributary of the Ahuriri River valley, which were deposited at 14.5–13.6 ka. Consequently, these moraine features from both Canyon Creek and the upper right tributary are likely to indicate the timing of formation (re-advance or stillstand) of both palaeo glaciers (Canyon Creek and upper right tributary) at 14.5–13.6 ka.

Based on this geomorphic and age relationships between those two sampled sites we reconstructed the geometry of the palaeo glacier from Canyon Creek. During the 14.5–13.6 ka interval the glacier had a total surface area of 6.0±0.8 km^2 while its length and thickness was ~5.5 km, and ~300 m respectively. The estimated snowline based on the AAR method was approximately 1620±60 m a.s.l., while the lowest limit of palaeo snowline based on MELM method was at about ≥1500 m a.s.l. These correspond with a snowline depression of ~380 m (AAR) or ≤500 m (MELM) relative to the present-day, which represents a temperature of –2.4±0.7 °C or ≤2.8 °C cooler than present during the moraine formation in the Canyon Creek at 14.5–13.6 ka (Figure 6.8–6.9), assuming no change in precipitation.

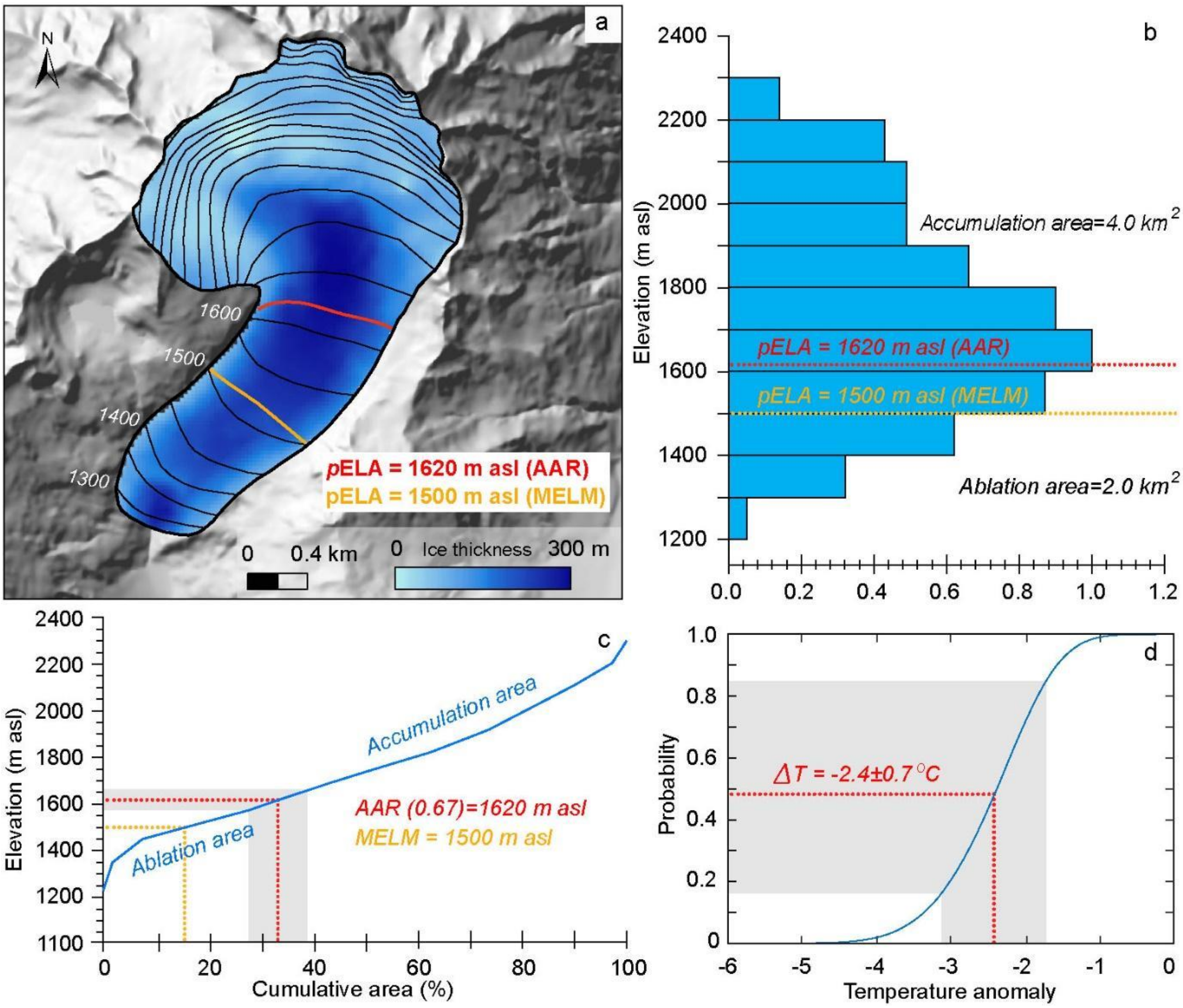

__Figure 6.8__ a – Surface of the former Canyon Creek or Thurneysen Glacier (based on manually derived contour lines) from Canyon Creek for 14.5–13.6 ka and reconstructed ELAs using the AAR (0.67) and MELM methods. b – Hypsometry and reconstructed ELAs of palaeo glacier for 14.5–13.6 ka. c – Cumulative curve (surface profile) and reconstructed ELAs of palaeo glacier for 14.5–13.6 ka. d – Cumulative distribution function for the palaeo temperature estimate associated with the lateral moraines for 14.5–13.6 ka. Shaded box defines the 1-sigma uncertainty interval.

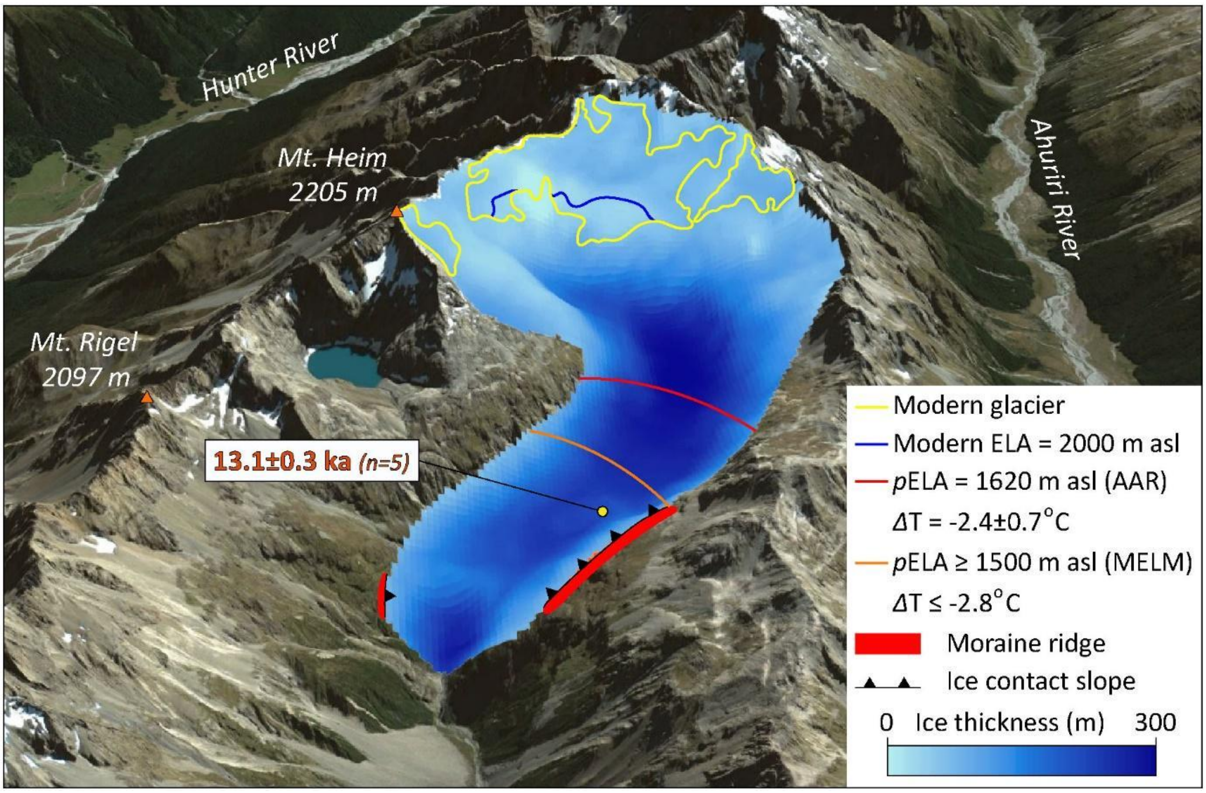

***Figure 6.9** Reconstructed palaeo Thurneysen Glacier at 14.5–13.6 ka from Canyon Creek in 3D. Google Earth image (07/03/2010).*

6.4 Discussion

6.4.1 Moraine chronology

The new surface-exposure chronology from the upper right tributary moraines of the Ahuriri River basin indicates that an advance of the palaeo glacier culminated at 14.5±0.3 ka (outer moraine ridge-1), while the next readvance or still-stand phase occurred at 13.6±0.3 ka (outer moraine ridge-2). About 1 kyr later (12.6±0.2 ka), the former glacier had lowered approximately 140 m and built another prominent moraine ridge in the lower section of the valley. I did not estimate geometry of the palaeo glacier at 14.5±0.3 and 13.6±0.3 ka from this valley since both lateral moraine features (1 and 2) do not indicate the terminus position of the former glacier, but only the lateral-marginal locations.

The ^{10}Be constraints from the Canyon Creek valley indicate the prominent, valley-floor bedrock outcrop became free from ice cover at 13.1±0.3 ka. This result is consistent with the upper right tributary where my ages also recorded ice thinning and glacier retreat at this time (i.e. between outer-2 and inner moraines).

6.4.2 Early glacier advance in the Late Glacial

Previous studies in the Southern Alps, for example at Irishman Stream (Kaplan et al., 2010) and Birch Hill (Putnam et al., 2010a) argue that the coldest part of the Late Glacial was at ~13.0 ka, at the end of the Antarctic Cold Reversal (Figure 6.10d–e). However, a few studies indicate that the maximum Late Glacial advance or stillstand was earlier. For example, Kaplan et al. (2013) provide ages for a glacier advance at 14.5±0.4 ka (n=4) from two adjacent moraine ridges (two ages per moraine ridge) (Figure 6.10e). Two boulders of similar age have also been constrained at the Birch Hill outboard moraine ridge (14.1±0.4 ka, n=2) (Figure 6.10d) (Putnam et al. 2010a).

This new data clearly demonstrates the structure of this early Late Glacial event in the Southern Alps, with a large glacier advance evident at the start of this interval at c. 14.5±0.3 ka, a small decrease in ice extent between 14.5±0.3 ka and 13.6±0.3 ka, a larger recession between 13.6 ka and 12.6 ka, and one more readvance or stillstand at 12.6 ka (Figure 6.10g). Consequently, my study provides confirmation that a glacier readvance or stillstand occurred at 14.5±0.3 ka, suggesting that the coldest part of the Late Glacial reversal was earlier than previously thought in New Zealand (e.g. Kaplan et al., 2010; Putnam et al., 2010a), assuming no changes in precipitation. This new finding is comparable with that from outlet glaciers in Torres del Paine (51°S, south Patagonia, Chile) which reached their maximum extent at 14.2±0.6 ka (García et al., 2012).

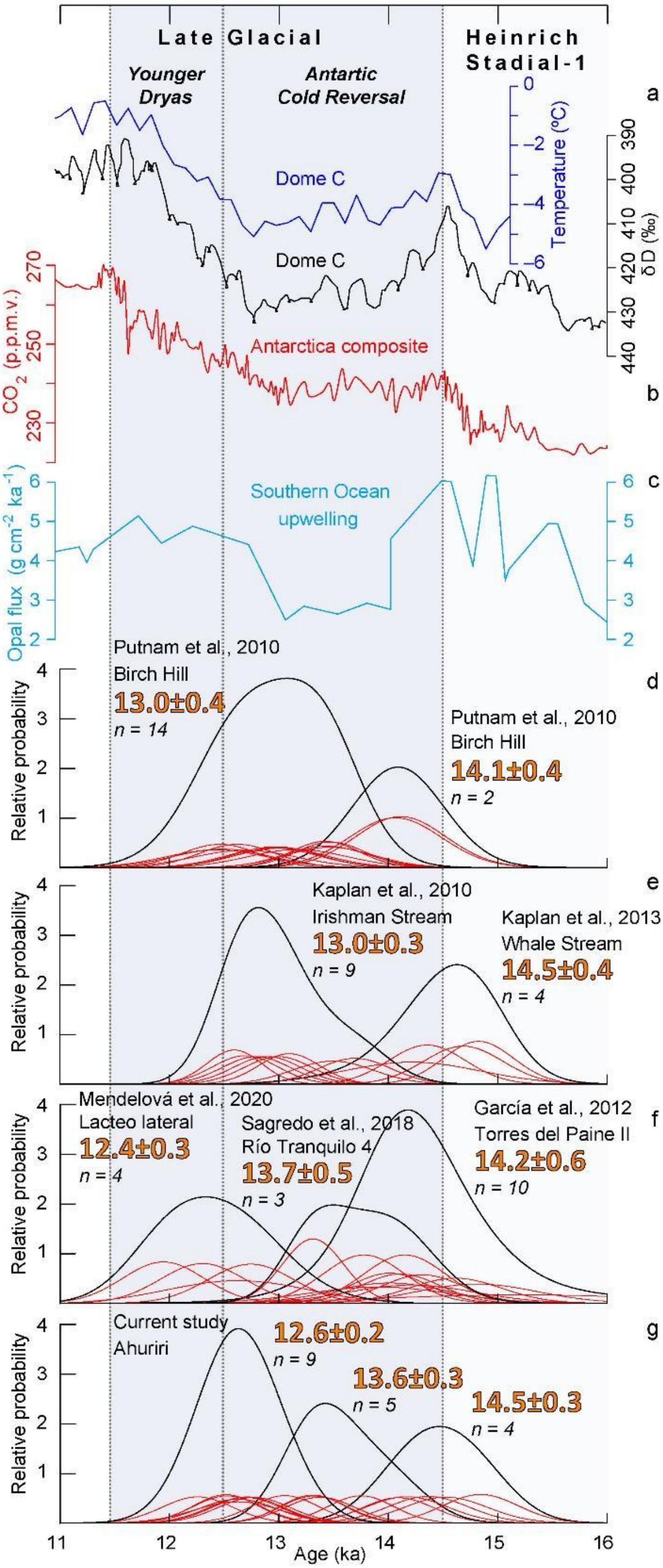

Late Glacial
Heinrich Stadial-1
Younger Dryas
Antartic Cold Reversal
Dome C
Dome C
Temperature (ºC)
δD (‰)
CO_2 (p.p.m.v.)
Antarctica composite
Southern Ocean upwelling
Opal flux (g cm^{-2} ka^{-1})
a
b
c
d
e
f
g
Putnam et al., 2010
Birch Hill
13.0±0.4
n = 14
Putnam et al., 2010
Birch Hill
14.1±0.4
n = 2
Kaplan et al., 2010
Irishman Stream
13.0±0.3
n = 9
Kaplan et al., 2013
Whale Stream
14.5±0.4
n = 4
Mendelová et al., 2020
Lacteo lateral
12.4±0.3
n = 4
Sagredo et al., 2018
Río Tranquilo 4
13.7±0.5
n = 3
García et al., 2012
Torres del Paine II
14.2±0.6
n = 10
Current study
Ahuriri
12.6±0.2
n = 9
13.6±0.3
n = 5
14.5±0.3
n = 4
Relative probability
Age (ka)

Figure 6.10 *a – δD (deuterium) and temperature anomalies (Jouzel et al., 2001; Röthlisberger et al., 2002) from Dome C, Antarctica. b – Composite CO_2 record from Antarctica (Bereiter et al., 2015). c – Biogenic opal flux (wind-driven upwelling) (Anderson et al., 2009). d-e – Normal kernel density plots from New Zealand: Birch Hill (Lake Pukaki basin) (Putnam et al., 2010a); Irishman Stream (Lake Ōhau basin) (Kaplan et al., 2010) and Whale Stream (Lake Pukaki basin) (Kaplan et al., 2013) (based on two different moraine ridges – two ages from per moraine). e – Normal kernel density plots from South America: Torres del Paine-II (García et al., 2012); Río Tranquilo-4 (Sagredo et al., 2018); Lacteo lateral (Mendelová et al., 2020). g – Normal kernel density plots from the upper right tributary of the Ahuriri River valley (current study).*

The results from outer moraine ridge-2 (13.6±0.3 ka) and inner terminal moraine ridge (12.6±0.2 ka) show consistent long-term trends with existing dated glacier landforms and snowline reconstructions from the Southern Hemisphere. For instance, my ^{10}Be constraints from the outer moraine ridge-2 (13.6±0.3 ka) are consistent with ^{10}Be ages of 13.3±0.3 ka at Mid-Macaulay moraines (middle ridge, Tekapo basin) (Tekapo basin) in the Southern Alps (Putnam et al., 2010a). My ages are also in good agreement with a glacier record from Monte San Lorenzo (47°S), central Patagonia, which show that the Río Tranquilo Glacier readvanced at 13.9±0.7 and 13.7±0.5 ka (Sagredo et al., 2018). The youngest Late Glacial advances in the upper right tributary of the Ahuriri River valley (inner terminal moraine – 12.6±0.2 ka) are overlapping in age with the 12.7±0.5 ka at the intermediate moraine in the outer part of Irishman Stream (Ōhau basin) in the Southern Alps (Kaplan et al., 2010). This is also consistent with a moraine deposit dated at 12.4±0.3 ka from Lacteo valley in Monte San Lorenzo, central Patagonia (Mendelová et al., 2020).

6.4.3 Early cooling in the Late Glacial

My geologically-constrained estimates of equilibrium line altitude changes, relative to present, afford quantitative insights of climate changes associated with past glacier geometries. Glacier mass balance is primarily determined by temperature and precipitation, while other variables such as solar radiation, wind speed and relative humidity also contribute to varying degrees depending on the climatic setting (Oerlemans, 2001; Mackintosh et al., 2017). In New Zealand, previous studies have shown that air temperature changes dominate over other variables because of their control on the elevation of the snow/rain threshold, and also the melt process via the exchange of turbulent heat (Anderson et al., 2010). In addition, glacier modelling studies show that in effect this means that large precipitation changes (much larger than what we see in present-day interannual variability) are needed to offset the effects of relatively small temperature changes on New Zealand glaciers (Anderson and Mackintosh, 2006). For example, Doughty et al. (2013) showed that a c. 3.5x increase in precipitation (relative to modern levels) is required for precipitation alone to drive glacier advance during the Antarctic Cold Reversal. This study and that of Eaves et al. (2017) also show that more reasonable precipitation changes of ±20% only alter Late Glacial temperature estimates by <0.5 °C. Thus, while it is likely that precipitation may have varied during the Late Glacial (e.g. Whittaker et al., 2011), the absence of quantitative estimates, coupled with the relatively low sensitivity of New Zealand glaciers to this variable, means that I choose to present my ELA-based climate estimates purely as a temperature signal. The studies above and the conclusions of Rowan et al. (2014) indicate that this assumption imparts uncertainty to my temperature reconstructions on the order of <0.5 °C.

My estimate of ≤700 m snowline depression at 14.5±0.3 ka based on the MELM method equates to air temperatures of ≤3.9 °C colder than today (1981–2010), assuming no changes in past precipitation. This finding compares to the previously estimated LGM and post-LGM ELA depression from the Ahuriri River valley by ∼880 m and ∼770 m at 19.8±0.3 ka and 16.7±0.3 ka, respectively (Figure 6.11) (Tielidze et al., 2022). These previously reconstructed ELA anomalies implied that local air temperature was 5.0±1.0 °C colder than present (1981–2010) at 19.8±0.3 ka, while it was 4.4±0.9 °C colder at 16.7±0.3 ka, assuming no change in precipitation (Tielidze et al., 2022). Together these results suggest there was at least 0.5 °C of warming between 16.7±0.3 ka and 14.5±0.3 ka (Figure 6.11).

My MELM and AAR based estimate of snowline depression by, ≤630 m and ~360 m along with ≤3.5 and 2.3±0.7 °C cooler climate at 13.6±0.3 and 12.6±0.2 ka from the upper right tributary of the Ahuriri River valley is comparable with other Late Glacial studies from New Zealand. For example, AAR analysis of reconstructed glaciers by Porter (1975) show that the Late Glacial equilibrium-line altitude (ELA) in the Tasman River catchment (inside the Birch Hill moraine limit) was 500±50 m lower than modern. Numerical modelling results by Kaplan et al. (2013) suggest that a mean annual temperature of 2.2±0.4 °C cooler than today is required to simulate a glacier to the Late Glacial (between 15.4 and 12.9 ka) moraine loop at the Whale

Stream area (Pukaki basin). Manual glacier reconstruction and glacier modelling suggest that the ELA of the former Otira Glacier near Arthur's Pass, was 540–330 m lower between 16–14 ka corresponding 3.5–2.2 °C colder climate than present-day (Eaves et al., 2017). The coupled energy-balance and ice-flow model also demonstrate an annual temperature ~3.2–2.3 °C cooler at 13.0 ka than present, at nearby Irishman Stream, corresponding 400 m lower equilibrium-line altitude than present-day (Doughty et al., 2013) (Figure 6.11). Numerical glacier modelling from Mt. Ruapehu in central North Island of New Zealand show that the ELA on Mt. Ruapehu was c. 400 m lower than present between 14 and 11 ka, which equates to a temperature anomaly of 3–2 °C lower than present (Eaves et al., 2019). My snowline-based temperature increase of ~1.2 °C between 13.6±0.3 and 12.6±0.2 ka from the upper right tributary of the Ahuriri River valley is also comparable with temperature increase of 0.25–1.0 °C from the Irishman Basin between 13–12 ka (Kaplan et al., 2010).

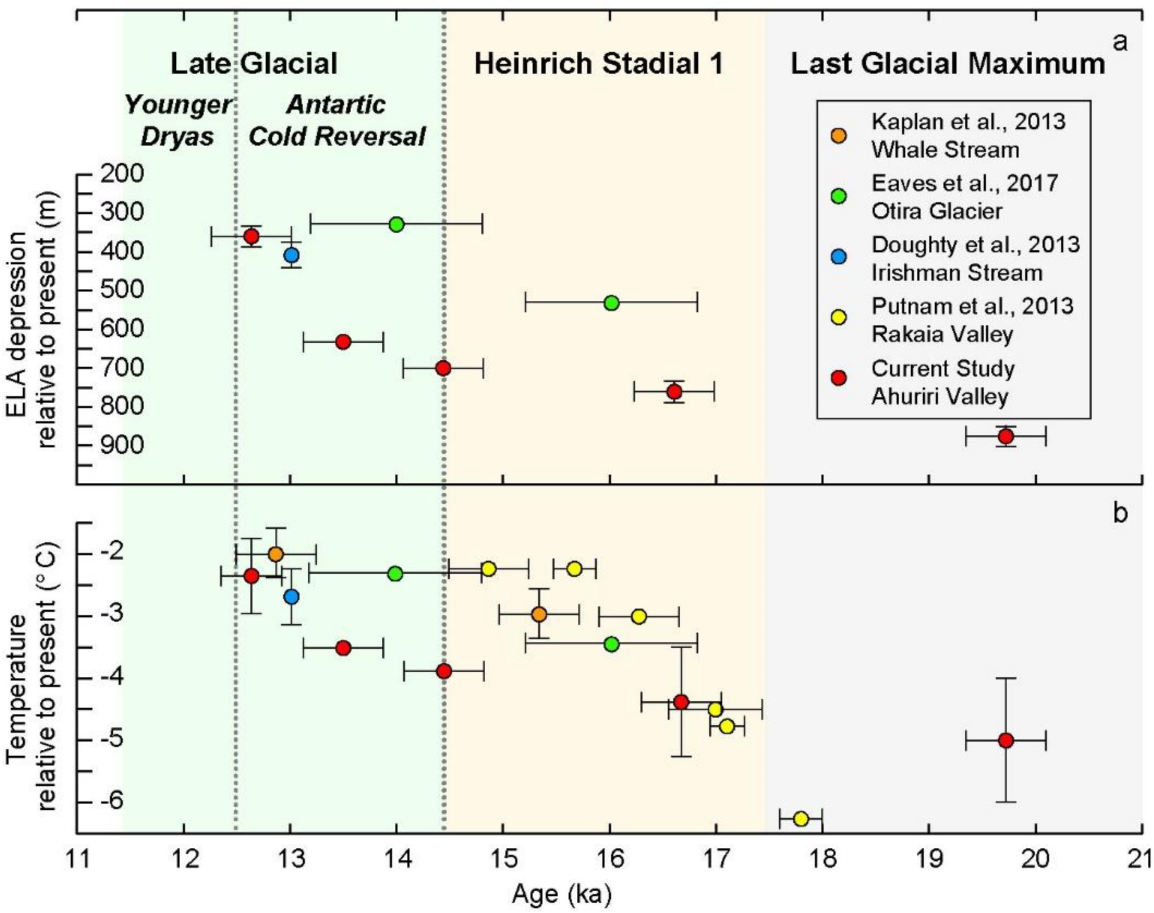

Figure 6.11 *Evolution of snowline (a) and temperature (b) in the Ahuriri River valley between 20 and 12 ka relative to the other studies in the Southern Alps of New Zealand based on* ^{10}*Be-dated moraines and numerical modelling (Kaplan et al., 2013; Eaves et al., 2017; Doughty et al., 2013; Putnam et al., 2013a).*

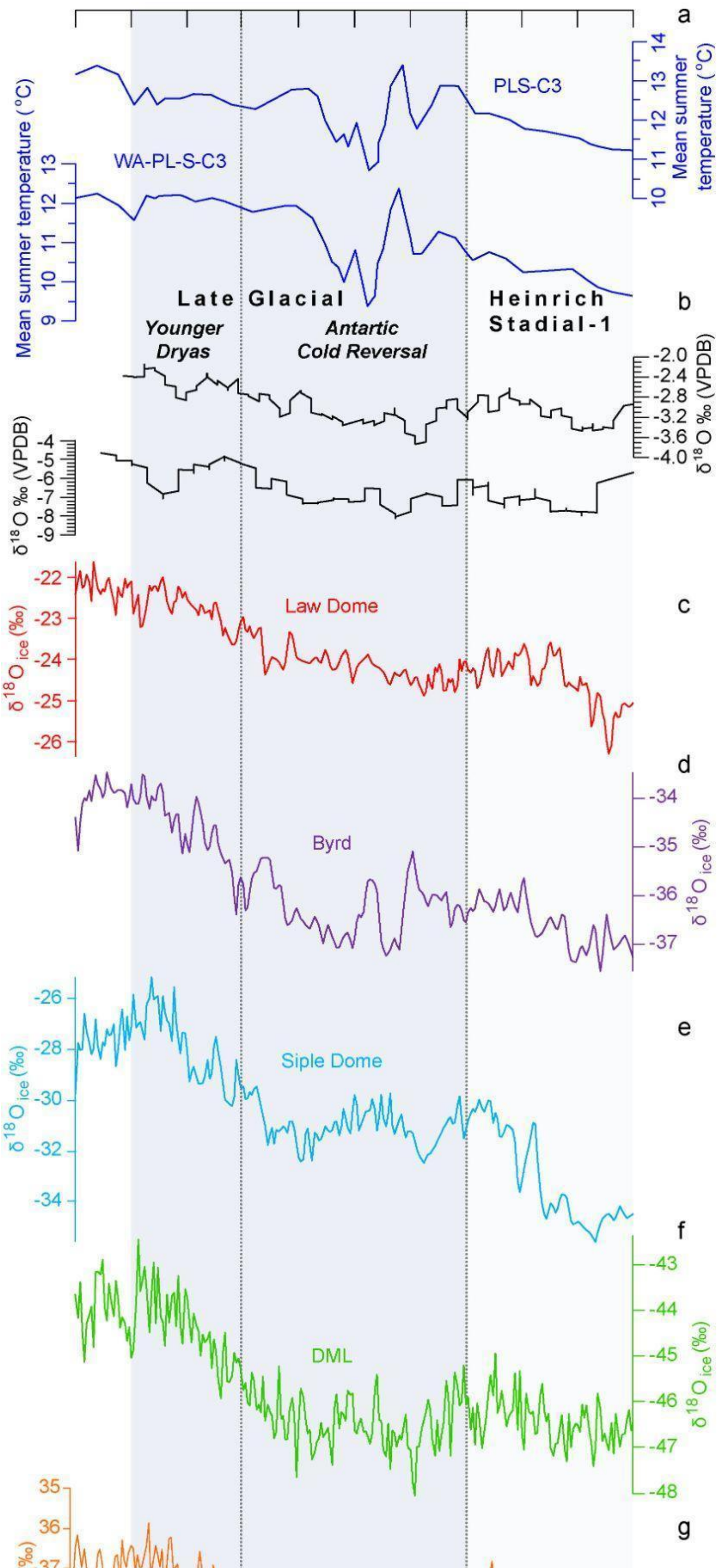
a
PLS-C3
Mean summer temperature (°C)
WA-PL-S-C3
Mean summer temperature (°C)
b
Late Glacial
Heinrich Stadial-1
Younger Dryas
Antartic Cold Reversal
δ18O ‰ (VPDB)
δ18O ‰ (VPDB)
c
Law Dome
δ18O ice (‰)
d
Byrd
δ18O ice (‰)
e
Siple Dome
δ18O ice (‰)
f
DML
δ18O ice (‰)
g
Talos Dome
δ18O ice (‰)
Age (ka)

Figure 6.12 *a – Boundary Stream Tarn (Lake Pukaki area) chironomid temperature records (Vandergoes et al., 2008). b – Isotope ratio profiles (5-point means) from stalagmite HW3 from Hollywood Cave, South Island, New Zealand (Whittaker et al., 2011). c–f – Deglacial $\delta^{18}O$ ice core records from Law Dome, Byrd, Siple Dome, and Dronning Maud Land (DML), Antarctica (Pedro et al., 2011). g – Deglacial $\delta^{18}O$ ice core record from Talos Dome, Antarctica (Stenni et al., 2011).*

Multiple atmospheric and oceanic climate proxy records from across Southern high latitudes reveal that the cooling of the Late Glacial period started at around 14.6 ka and reached its cooling peak at the end of the Antarctic Cold Reversal after ~13 ka (Figure 6.10a–d). This is in contrast to my results which suggest lower temperatures at 14.5±0.3 ka and 13.6±0.3 ka than at 12.6±0.2 ka. My suggestion of lower temperatures early in the Late Glacial is more similar to the radiocarbon-dated pollen and chironomid record from Boundary Stream Tarn at Lake Pukaki (Figure 6.12a). This data suggests that early cooling of the Late Glacial occurred between 14.2 and 14.0 ka when temperatures decreased to 1.5–2.0 °C below modern summer (1981–2008) air temperature (Vandergoes, et al., 2008). The onset of this cooling period at 14.2 ka matches within uncertainty with our oldest moraine ages of 14.5±0.3 ka. A short interruption to this cooling occurred at ~13.9 ka, when mean summer temperature increased to around 2.5 °C, or slightly above present-day level. Over the next 300–500 years interval (i.e. between 13.6–13.4 ka), average mean summer temperatures dropped to around 2.0–2.9 °C below the present day and in the most extreme case as much as 3.9 °C lower (Vandergoes, et al., 2008) (Figure 6.12a). Again, this fits within uncertainty of my moraine ages of 13.6±0.3 ka. Isotope ratio profiles from Hollywood Cave stalagmite (HW3), South Island, New Zealand also suggests that the coldest Late Glacial climate occurred between 14.2 and 13.9 ka (Whittaker et a., 2011) (Figure 6.12b) coinciding within uncertainty of my 14.5±0.3 ka ages. Furthermore, five different ice core records from Antarctica (Law Dome, Byrd, Siple Dome, Dronning Maud Land, and Talos Dome) show a strong cooling trend from the onset of Antarctic Cold Reversal at ca ~14.6±0.2 ka to ~14±0.2 ka then period of variability without significant cooling trendng until ~13 ka (Pedro et al., 2011; Stenni et al., 2011) (Figure 6.12c–g), again consistent with my lowest temperatures from outer moraine ages of 14.5±0.3 ka.

6.5 Conclusions

In this chapter, I aimed to improve our understanding of the glacier behaviour and climate events during the Antarctic Cold Reversal in the Southern Alps of New Zealand using cosmogenic exposure dating and snowline reconstructions. Based on several moraine features and twenty-eight ^{10}Be ages, I reconstructed the geometries of former glaciers in two different tributary river basins of the Ahuriri River valley. Using the AAR and MELM methods I also estimated associated snowline elevations. Furthermore, based on the reconstructed glacier snowline I estimated palaeo temperatures during the Antarctic Cold Reversal.

My results give insight to the structure of the Antarctic Cold Reversal event in New Zealand. The 14.5±0.3 ka outer moraine feature from the upper right tributary of the Ahuriri River valley confirms the largest glacier advance in New Zealand occurred in the first centuries of this millennial-scale event. By 12.6±0.2 ka, the local snowline had risen ~340 m (from ~1300 m to ~1640 m a.s.l.), which corresponds to approximately 1.6 °C of warming during the Antarctic Cold Reversal.

CHAPTER 7: SYNTHESIS

7.1 Introduction

The primary aim of this thesis was to constrain the timing and extent of glacier fluctuations in the central Southern Alps of New Zealand over the Last Glacial Maximum and subsequent termination including the Antarctic Cold Reversal, as well as, to investigate orbital- and millennial-scale climatic drivers. In response to this aim I first applied geomorphological mapping of glacier-related landforms (see main map in supplement) which helped me to understand and describe past glacier behaviour and dynamics in the Ahuriri River valley. I then developed a glacier chronology based on cosmogenic ^{10}Be surface exposure dating and glacier related landforms (Figure 7.1) along with past equilibrium line altitudes and associated air temperatures (Figure 7.2). I also investigated possible climate processes that could be responsible for this glacier timing. The combination of geomorphological mapping, cosmogenic surface exposure dating and ELA/temperature reconstruction provides new insights into the regional and hemispheric climate system. In the following section (7.2), I summarize and discuss the main findings of this thesis in the context of my specific research questions (see section 2.7). In the final section (7.3) I highlight outstanding questions that I consider important for future research.

Two peer-reviewed papers (Tielidze et al., 2021; 2022) have already been published from this doctoral thesis, and therefore there is some overlap between Chapters 3–4 and Tielidze et al. (2021), between chapters 3, 5, section 7.2.4.1, and Tielidze et al. (2022) and between chapters 3, 6, section 7.2.4.2, and Tielidze et al. (2022 under review) (see also section 1.3).

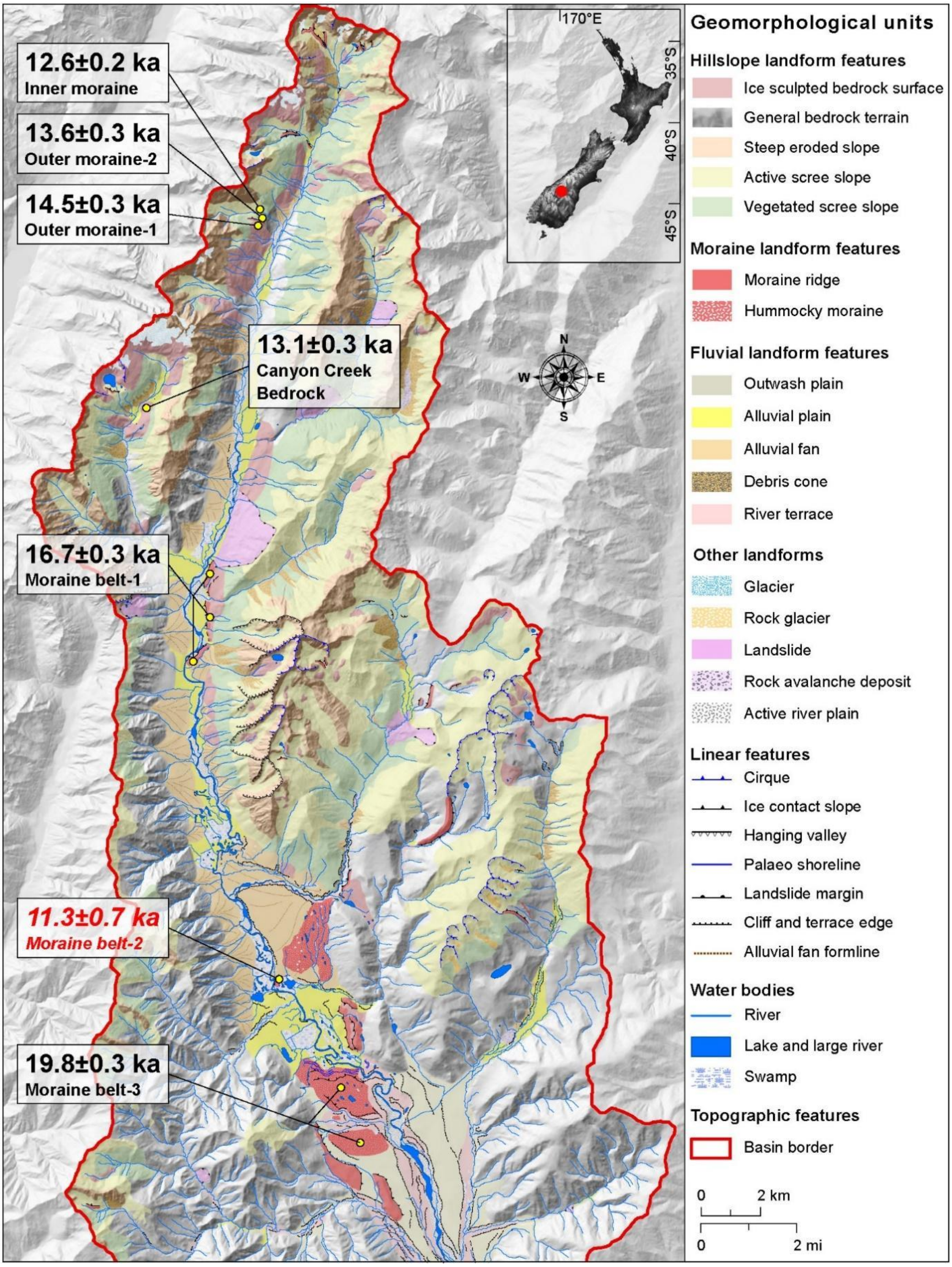

Figure 7.1 *Ahuriri Glacier chronology constrained in this study based on geomorphological mapping and cosmogenic surface exposure dating.*

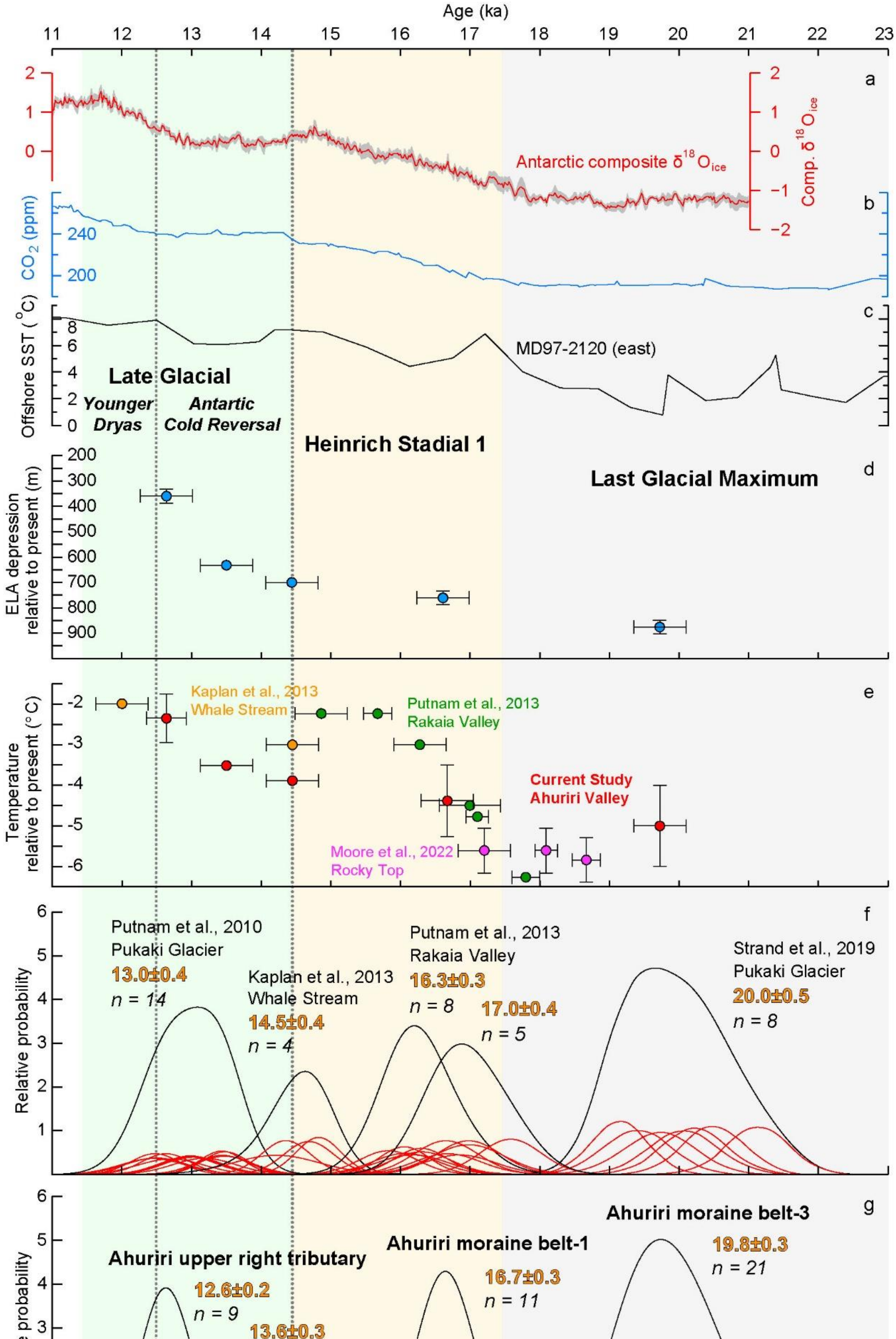

Age (ka)
Antarctic composite δ18Oice
Comp. δ18Oice
CO2 (ppm)
Offshore SST (°C)
MD97-2120 (east)
Late Glacial
Younger Dryas
Antartic Cold Reversal
Heinrich Stadial 1
Last Glacial Maximum
ELA depression relative to present (m)
Temperature relative to present (°C)
Kaplan et al., 2013 Whale Stream
Putnam et al., 2013 Rakaia Valley
Current Study Ahuriri Valley
Moore et al., 2022 Rocky Top
Relative probability
Putnam et al., 2010 Pukaki Glacier 13.0±0.4 n = 14
Kaplan et al., 2013 Whale Stream 14.5±0.4 n = 4
Putnam et al., 2013 Rakaia Valley 16.3±0.3 n = 8
17.0±0.4 n = 5
Strand et al., 2019 Pukaki Glacier 20.0±0.5 n = 8
Ahuriri upper right tributary
12.6±0.2 n = 9
13.6±0.3 n = 5
14.5±0.3 n = 4
Ahuriri moraine belt-1 16.7±0.3 n = 11
Ahuriri moraine belt-3 19.8±0.3 n = 21

Figure 7.2 *a – Atmospheric CO_2 concentrations during the 23–11 ka (Ahn and Brook, 2008). b – The Antarctic composite $\delta^{18}O_{ice}$ by the standard error (grey shading) for 21–11 ka based on the five sites – Law Dome, Byrd, Siple Dome, Dronning Maud Land (DML), and Talos Dome (Pedro et al., 2011; Stenni et al., 2011). c – Southern Ocean sea-surface temperature (SST) records for 23–11 ka based on Mg/Ca sediment cores MD97-2120 (Pahnke et al., 2003). See also Figure 6.1 for location of ice and sediment coring sites. d – Evolution of snowline in the Ahuriri River valley between 19.8±0.3 ka and 12.6±0.6 ka based on ^{10}Be-dated moraines. e – Evolution of air temperatures in the Ahuriri River valley between 19.8±0.3 ka and 12.6±0.2 ka based on snowline estimation relative to previous studies from New Zealand. f – a normal kernel density plot based on previous studies from New Zealand. g – a normal kernel density plots from the Ahuriri River valley.*

7.2 Research Questions

7.2.1 What was the timing and extent of palaeo Ahuriri Glacier during the Last Glacial Maximum and at the onset of the last deglaciation?

Combining glacial geomorphology and geochronological dating of glacial landforms is a powerful method for understanding past glacier responses to climate change. In Chapter 4, I present a detailed glacial geomorphological description of glacier related landforms of the Ahuriri River valley, while in Chapter 5, I report the glacial chronology dataset from the Last Glacial Maximum and subsequent deglaciation based on thirty-eight beryllium-10 (^{10}Be) surface-exposure ages from terminal moraine systems and glaciated bedrock situated at the lower and middle sections of the valley.

The new glacial chronology dataset suggests that the former Ahuriri Glacier reached its maximum extent at 19.8±0.3 ka, which coincides with the global Last Glacial Maximum. By 16.7±0.3 ka, the glacier had retreated ~18 km up-valley suggesting at least ~43% glacier-length loss relative to its full LGM extent. This deglaciation was accompanied by the formation of a shallow proglacial lake. These ages do not constrain the timing of termination onset. Thus, the precise timing of ice withdrawal from the lower Ahuriri valley remains uncertain.

Glacier advance at 19.8±0.3 ka in the Ahuriri valley is consistent with other published ^{10}Be data from the left-lateral moraine system at Lake Pukaki that was dated to 20.3±0.6 ka

(Doughty et al., 2015) and 20.0±0.5 ka (Strand et al., 2019) (Figure 5.7). However, while the 20 ka advance in the Ahuriri valley represents the largest of the last glacial cycle, the geomorphic records at Lake Pukaki and other nearby sites (e.g. Lake Ōhau – Putnam et al., 2013b) record a richer history of earlier, slightly more extensive glacier advances spanning much of oxygen isotope stages 2–3 (Denton et al., 2021). Differences in moraine presence between Ahuriri and the Pukaki/Ōhau records are unlikely to be attributable to large-scale climatic forcing, given the proximity of all sites to one another. Instead I consider these differences arise from the local topographic settings, which may influence both glacier response to climate (e.g. response times, and length sensitivity), as well as moraine preservation potential.

In contrast to the Last Glacial Maximum, very few quantitative constraints of glacier readvance at 16–17 ka exist for the Southern Alps. However, the surface-exposure ages from moraine belt-1 formed at 16.8±0.3 ka, confirms glacier readvance during that time and is similar to observations from the former Rakaia Glacier that readvanced at 16.3±0.4 ka (Putnam et al., 2013a) after having also retreated substantially.

Significant retreat of the palaeo Ahuriri Glacier between two readvances at 19.8±0.3 ka and 16.7±0.3 ka is broadly consistent with moraine chronologies in South America and Tasmania. For example, the main glacier lobe at Lago Palena/General Vintter basin in northern Patagonian Andes (44°S) reached its maximum extent at 19.7±0.7 ka and then underwent a large retreat until ~16.3 ka (Soteres et al., 2022). Glaciers in Tasmanian highlands were most extensive at 20.1±1.9 ka and then retreated significantly until 17.3±1.1 ka (Barrows et al., 2002).

7.2.2 How did the Ahuriri Glacier respond to the Late Glacial climate reversal and when was the maximum readvance phase during that time?

In the Southern Alps, only a small number of Late Glacial moraine chronologies have been documented. Based on detailed glacial geomorphological mapping (Chapter 4) of the several moraine features and twenty-eight ^{10}Be exposure ages (Chapter 6), the geometries of former glaciers in two different tributary river basins of the Ahuriri River valley have been reconstructed. Prominent terminal and lateral moraine features from the upper right tributary of the Ahuriri River valley have exposure ages of 14.5±0.3 ka, 13.6±0.3 ka, and 12.6±0.2 ka. The, 14.5±0.3 and 13.6±0.3 ka moraine features formed early in the Antarctic Cold Reversal, as defined in Antarctic ice core (e.g. Jouzel et al., 1995) confirming early glacier readvance in New Zealand which has been previously recognised with only limited evidence (e.g. Kaplan et al., 2010; Putnam et al., 2010a). These moraine features may also represent steady fluctuations of climate between 14.5±0.3 ka and 13.6±0.3 ka just prior to the significant recession and greater warming between 13.6±0.3 ka and 12.6±0.2 ka, and one more readvance or stillstand at 12.6 ka.

The early glacier readvance from the upper right tributary of the Ahuriri River valley is comparable with that from outlet glaciers in Torres del Paine (51°S, south Patagonia, Chile) which reached their maximum extent at 14.2±0.6 ka (García et al., 2012). In an interhemispheric context, the early glacier readvance during the Late Glacial in New Zealand recorded by my work (14.5±0.3 ka) is also largely consistent with regional glacier records and ^{10}Be chronologies from the Northern Hemisphere and the tropics. For example, the new ^{10}Be constraints from Scandinavia suggest that the first readvance of the south-western Scandinavian Ice Sheet occurred at 14.0±0.6 ka (e.g. Briner et al., 2014), while cosmogenic ^{10}Be chronologies from Arctic Norway show that Late Glacial culmination occurred at 13.9±0.7 ka (e.g. Wittmeier et al., 2020). The new ^{10}Be moraine chronology from the northern tropical Andes suggest the largest glacial extent occurred at 14.0±0.3 ka (Jomelli et al., 2014).

The younger exposure ages (13.6±0.3 ka and 12.6±0.2 ka) from the upper right tributary of the Ahuriri River valley are similar to existing dated glacier landforms from the Southern Hemisphere. For instance, ^{10}Be constraints from the outer moraine ridge-2 (13.6±0.3 ka) are consistent with ^{10}Be ages of 13.3±0.3 ka at Mid-Macaulay moraines (middle ridge) (Tekapo basin) in the Southern Alps (Putnam et al., 2010a). These ages are also in good agreement with the Río Tranquilo Glacier (47°S), central Patagonia, and Cerro Riñón Glacier (44°S), northern Patagonian Andes that readvanced at 13.7±0.5 ka and 13.5±0.4 ka respectively (Sagredo et al., 2018; Soteres et al., 2022). The youngest Late Glacial advance in the upper right tributary of the Ahuriri River valley (inner terminal moraine – 12.6±0.2 ka) are overlapping in age with the 12.7±0.5 ka at the intermediate moraine in the outer part of Irishman Stream (Ōhau basin) in the Southern Alps (Kaplan et al., 2010). This is also consistent with a moraine deposit dated at 12.4±0.3 ka from Lacteo valley in Monte San Lorenzo, central Patagonia (Mendelová et al., 2020). No moraines of Late Glacial age are known from Tasmania, presumably because the mountains were not high enough to intersect the snowline during this time (Barrows et al., 2002).

Ice-sculpted bedrock surfaces bound by a lateral moraine at nearby Canyon Creek have an age of 13.1±0.3 ka, indicating the moraine correlates with those in the Ahuriri upper right tributary (14.5±0.3–13.6±0.3 ka). Overall, these new results clearly demonstrate the structure of the Antarctic Cold Reversal, and show that this period in New Zealand was defined by a large glacial advance at the onset, followed by overall glacier retreat interspersed with periods of stillstand or episodic ice readvance over a period of several thousand years.

7.2.3 What was the rate of snowline depression and associated temperature changes during the last glacial termination?

Palaeo equilibrium line altitudes (ELAs), which are often referred to as the snowline, are frequently estimated by using the accumulation area ratio (AAR) method. AAR based simulation applied in Chapter 5 shows that the Ahuriri Glacier ELA was lower than present by ~880 m (~1120 m a.s.l.) when the glacier reached its maximum extent during the Last Glacial Maximum at 19.8±0.3 ka, and ~770 m lower (~1230 m a.s.l.) during the second largest readvance or stillstand at 16.7±0.3 ka. This implies that local air temperature was 5±1 °C colder than present (1981–2010) at 19.8±0.3 ka, while it was 4.4±0.9 °C colder at 16.7±0.3 ka, assuming no change in precipitation.

The Maximum Elevation of Lateral Moraines (MELM) method as a supplementary tool (along with the AAR method) for the Late Glacial snowline estimation was also used in Chapter 6 from the upper right tributary of the Ahuriri River valley and the Canyon Creek. These estimations suggest that snowline elevations at 14.5±0.3 ka, 13.6±0.3 ka, and 12.6±0.2 ka were ≤700 m, ≤630 m, and ~360 m lower than today in the upper right tributary of the Ahuriri River valley. This equates to air temperatures of ≤3.9, ≤3.5 °C, and 2.3±0.7 °C colder than today (1981–2010), assuming no changes in past precipitation.

MELM and AAR reconstructions from the Canyon Creek also suggest that snowline elevations at 14.5–13.6 ka were ≤500 or ~380 m lower than today, corresponding to air temperatures of ≤2.8 or 2.4±0.7 °C cooler than the present-day (1981–2010).

Overall, my work suggests that there was a small amount of climate warming (~1.2 °C) during the first half of last glacial termination between 19.8±0.3 and 14.5±0.3 ka, while majority of the warming (~1.6 °C) occurred during the second half of the termination or Antarctic Cold

Reversal between 14.5±0.3 ka and 12.6±0.2 ka. Past glacier chronologies paired with ELA and temperature reconstructions at one site spanning the entire last glacial termination are very rare in New Zealand. Thus, direct comparisons with other ELA/temperature reconstructions in New Zealand is challenging because they either cover relatively short periods, or do not provide ELA/temperature reconstructions but only glacier chronologies. However, in one of the few glacial studies for early stage of termination to provide such data, Putnam et al. (2013a) reported 3.75 °C warming (from −6.25 to −2.5 °C) between 17.8±0.2 and 16.3±0.4 ka from the Rakaia River valley, situated on the eastern side of the Southern Alps. At face value this rate of warming appears much greater than ~0.6 °C temperature increase reconstructed between 19.8±0.3 ka and 16.7±0.3 ka in the Ahuriri River valley (Figure 5.9). There are several possible explanations for this discrepancy such as the relatively low resolution of the dating method (relative to the rate of climate change), local topo-climatic influence, palaeo proglacial lake existence, and different ELA reconstruction methods (modelling vs AAR).

My new ELA/temperature estimates for the Late Glacial period: ≤630 m and ~360 m along with ≤3.5 and 2.3±0.7 °C cooler climate at 13.6±0.3 and 12.6±0.2 ka from the upper right tributary of the Ahuriri River valley are comparable with numerical modelling results by Kaplan et al. (2013) suggesting that a mean annual temperature of 2.2±0.4 °C cooler than today is required to simulate a glacier to the Late Glacial (between 15.4 and 12.9 ka) moraine loop at the Whale Stream area (Pukaki basin). The coupled energy-balance and ice-flow model also demonstrate an annual temperature ~3.2–2.3 °C cooler than present, at 13.0 ka at nearby Irishman Stream, corresponding to a 400 m lower equilibrium-line altitude than present-day (Doughty et al., 2013). Numerical glacier modelling from Mt. Ruapehu in central North Island of New Zealand shows that the ELA on Mt. Ruapehu was c. 400 m lower than present between 14 and 11 ka, which equates to a temperature anomaly of 3–2 °C lower than present (Eaves et al., 2019). In the next section I discuss the climatic implications of these reconstructed ELAs and temperatures.

7.2.4 What climate processes (at the millennial scale) could be responsible for glacier timing?

7.2.4.1 Last glacial termination and its triggering factors

One of the key findings of my thesis is that the former Ahuriri Glacier started to retreat shortly after its maximum position at 19.8±0.3 ka. By 16.7±0.3 ka, the glacier had retreated ~18 km up-valley suggesting at least ~43% glacier-length loss relative to its full LGM extent in response to a modest amount of warming (~0.6 °C). I proposed that the substantial glacier retreat in response to a relatively small temperature increase may have been a result of the high glacier-length sensitivity of this glacier system due to its low gradient of the former ice surface. However, this may also require an additional climatic explanation.

A leading hypothesis for the last glacial termination suggests that Southern Hemisphere climate warming was triggered by rising Northern Hemisphere summer insolation intensity, which propagated southwards via oceanic and atmospheric teleconnections (Denton et al., 2010). Central to this hypothesis is the role of the oceanic bipolar seesaw mechanism, in which reduced North Atlantic Deep Water formation at 17.5 ka (McManus et al., 2004) caused sea surface warming across southern mid-high latitudes (Stocker and Johnsen, 2003; Pedro et al., 2018). However, while the timing of this proposed teleconnection correlates within dating uncertainties with the increases in glacier retreat rates in New Zealand (Putnam et al., 2013a), it does not readily explain the apparent early onset of gradual warming and glacier retreat recorded by my work in the Ahuriri, and other sites in the Southern Alps (Rother et al., 2014; Eaves et al., 2019; Moore et al., 2022).

Radiative equilibrium estimates by Huybers and Denton (2008) suggest an alternative insolation hypothesis – demonstrating that integrated summer duration over the Southern Ocean is near identical in timing and sign to northern (65°N) summer insolation intensity during the Late Pleistocene epoch. Denton et al. (2021) invoke this southern insolation hypothesis as a key driver of south-westerly winds position, which is important in explaining discrete shifts between glacial and interglacial modes of climate. The WAIS Divide team (2013) suggest such local insolation forcing may explain gradual warming over West Antarctica from 22–20 ka, as rising summer insolation reduced sea ice extent. According to Denton et al. (2021) such insolation changes may have also promoted gradual poleward shift of the southern westerly winds, permitting enhanced penetration of subtropical heat to southern mid-latitudes, which is consistent with my observations of retreating ice in the Southern Alps at this time. An advantage of this hypothesis is that it can reconcile these gradual changes with subsequent global deglaciation. Denton et al. (2021) demonstrate, using a global climate model, that a sustained poleward position of the westerlies from 18 ka (e.g. Buizert et al., 2018) can promote global-scale warming; Further model-based experiments are required to test this hypothesis further and disentangle competing influences such as rising carbon dioxide from 18 ka (e.g. Menviel et al., 2018). This might lead to a more compelling explanation for a possible early onset of warming and glacier retreat reconstructed in this study.

7.2.4.2 Possible causes of early cooling during the Late Glacial

The findings in this thesis that the maximum extent of ice and coldest temperatures occurred early in the Late Glacial (at 14.5±0.3 ka in the upper right tributary of the Ahuriri River valley) rather than at the peak of the Antarctic Cold Reversal (~13 ka) requires a climatic explanation.

The Antarctic Cold Reversal coincides with the Bølling–Allerød warm stage in the Northern Hemisphere, which is thought to be an example of the inter-hemispheric coupling of abrupt climate change (e.g. Stocker and Johnsen, 2003; Barker et al., 2009; Newnham et al., 2012; Pedro et al., 2016). Stocker and Johnsen (2003) suggested that the gradual cooling in Antarctica during Greenland interstadials such as the Bølling–Allerød results from enhanced cross-equatorial northward ocean heat transport by the Atlantic meridional overturning circulation (AMOC). In their view, increased northward heat transport during Greenland interstadials abruptly cools the South Atlantic, and more gradually cools the Southern Ocean, due to its larger thermal inertia. More recent work attributes the Southern Ocean and Antarctic cooling to gradual mixing of the South Atlantic cold signal across the Antarctic Circumpolar Current, (ACC) along with sea ice feedbacks (Schmittner et al., 2003; Pedro et al., 2018). This existing theory is consistent with moraine ages of ~13 ka in the Southern Alps (e.g. Putnam et al., 2010a), but does not explain the early onset and larger snowline lowering at 14.5±0.3 ka shown by my work.

There is new and growing evidence for fast ocean and atmospheric feedbacks that may help to explain my findings. For example, rapid ocean propagation of temperature anomalies is possible (north of the ACC) by Kelvin and Rossby wave-driven adjustment of isopycnals and thermocline depths (Pedro et al., 2018). There is growing evidence for a fast atmospheric teleconnection operating at the onset of the Antarctic Cold Reversal, and indeed at the onset of all millennial scale Antarctic cold events during the last glacial (Markle et al., 2017; Buizert et al., 2018). Specifically, ice-core deuterium excess records indicate abrupt northward shifts of the moisture source regions at Antarctic ice core sites within decades of the onsets of Greenland interstadials throughout the last glacial period, which is consistent with northward-shifted westerlies.

Models suggest that atmospheric adjustments during these millennial-scale events are a thermodynamic response to a change in the energy balance between the hemispheres during abrupt climate change. At the onset of Greenland interstadials, the abrupt northern warming shifts the thermal equator northward (Stocker and Johnsen, 2003). The atmosphere responds by fluxing more heat and momentum southward, toward the cooler hemisphere, in the cross-equatorial Hadley circulation. The increased momentum flux into the Southern Hemisphere draws the westerlies northward (Ceppi et al., 2013; Pedro et al., 2016). The thermal imbalance between the hemispheres is largest within the first centuries of the Greenland interstadials and thereafter relaxes as the interstadial progresses (Clement and Peterson, 2008).

My new work demonstrates that early cooling and the maximum Late Glacial ice extent in New Zealand occurred in the first centuries of the Antarctic Cold Reversal. I suggest that this may reflect the northward shift of the southern westerlies, which might have caused cooler temperatures and/or relatively higher precipitation in the Southern Alps. Subsequent gradual southward relaxation of the winds, causing warming and/or precipitation reduction, likely resulted in gradual glacier retreat as seen across the Late Glacial moraine records in the Southern Alps (this study; Putnam et al., 2010a; Kaplan et al., 2013). These wind changes may have been accompanied by sea surface temperature changes north of the Antarctic Circumpolar Current (ACC) induced by ocean propagation of abrupt climate change.

A recent study by Denton et al. (2021) proposes that southern insolation is a key driver of the southern westerly winds. Such insolation changes may have promoted an early equatorward shift of the southern westerly winds during the Late Glacial, allowing cooler temperatures to develop in the southern mid-latitudes, which is consistent with my observations of early glacier readvance and lower temperatures in the Southern Alps at this time.

Discriminating between the relative roles of the atmosphere and ocean is difficult in the highly-coupled system with the available data. However, I suggest that the atmospheric component provides a more physically-consistent explanation for the pattern of glacier length changes emerging in southern mid-latitudes terrestrial records. This hypothesis requires further exploration and testing (see next section).

7.3 Future work

This thesis has provided a deeper understanding of the Late Quaternary glacier-climate record of the Southern Alps through the detailed glacial geomorphological mapping, collection of new field data and analysis of published records. Several potential prospects for future research have also emerged from this research.

i. Numerical glacier modeling could be applied in order to better understand how the former Ahuriri Glacier responded to climate change relative to the current estimation during the last glacial termination. This will also help us to better explain the discrepancy between our amount of warming between 20–17 ka, and those from the previous study by Putnam et al., 2013a based on numerical glacier modeling. It would also allow the role of possible precipitation changes and their impact on temperature reconstructions to be assessed and quantified.

ii. Key questions remain associated with the timing of termination onset in the lower section of the Ahuriri River valley. More sample collections and further dating, particularly of the left lateral moraines near Moraine belt-2, may shed light on additional glacier activity during the last termination. In addition, dating of glacial outwash terraces and associated sediments can offer a more complete chronology of glacial activity than the fragmentary preserved moraine records (e.g. Hein et al., 2017). The outwash record in the Ahuriri River valley has yet to be studied in detail. Such analysis may provide a more complete record of glacier behaviour at the onset of last glacial termination.

iii. The use of Ground Penetrating Radar (GPR) along with Light Detection and Ranging (LIDAR) across the moraine belt-3 can be useful to see if that area was occupied by previous glacier advances (i.e. older than 20 ka). This type of study can reveal additional buried features that is not seeing today because it can be covered up.

iv. Further evidence for the existence of a palaeo proglacial lake may be preserved in the sediment records of the lower Ahuriri River valley. Palaeo lake shorelines could also tell us a little more about the lake level fluctuations through the time. Thus, sediment coring and shoreline dating is required for an accurate palaeo environmental reconstruction.

v. Other future work should focus on reconstructing paleo-ELAs from other regions through the deglaciation in New Zealand and comparing these with studies from similar mid-latitude sites of former glaciation in South America and south-eastern Australia. Combined with wider climate proxy data and climate model simulations, this will help us build a more complete picture of the Late Quaternary glacial-climatic fluctuations in the Southern Hemisphere. This will allow us to fully answer questions about the cause of the Last Glacial Termination and Antarctic Cold Reversal raised in this thesis.

Reference

Ahn, J. and Brook, E. J. (2007). Atmospheric CO_2 and climate from 65 to 30 ka B.P. Geophys. Res. Lett. 34. doi.org/10.1029/2007GL029551.

Anderson, B., Mackintosh, A. (2006). Temperature change is the major driver of late-glacial and Holocene glacier fluctuations in New Zealand. Geology; 34 (2): 121–124. doi.org/10.1130/G22151.1.

Anderson, R. F., Ali, S., Bradtmiller, L. I., Nielsen, S. H. H., Fleisher, M. Q., Anderson, B. E., Burckle, L. H. (2009). Wind-driven upwelling in the Southern Ocean and the deglacial rise in atmospheric CO2. Science 323, 1443-1448. doi.10.1126/science.1167441.

Anderson, B., Mackintosh, A., Stumm, D., George, L., Kerr, T., Winter-Billington, A., and Fitzsimons, S. (2010). Climate sensitivity of a high-precipitation glacier in New Zealand. Journal of Glaciology, 56(195), 114-128. doi:10.3189/002214310791190929.

Andrews, J. T. (1975). Glacial systems. An approach to glaciers and their environments. North Scituate, MA, Duxbury Press.

Atle, N. (1992). Topographical Effects on the Equilibrium-Line Altitude on Glaciers. GeoJournal. Vol. 27, No. 4, pp. 383-391. www.jstor.org/stable/41145524.

Balco, G., Stone, J. O., Lifton, N. A., Dunai, T. J. (2008). A complete and easily accessible means of calculating surface exposure ages or erosion rates from 10Be and 26Al measurements. Quat. Geochronol. 3, 174-195. doi.org/10.1016/j.quageo.2007.12.001.

Balco, G. (2011). Contributions and unrealized potential contributions of cosmogenic-nuclide exposure dating to glacier chronology, 1990-2010. Quaternary Science Reviews. 30 (1-2): p. 3-27. doi.org/10.1016/j.quascirev.2010.11.003.

Balco, G. (2017a). Documentation v3 exposure age calculator. Retrieved from https://sites.google.com/a/bgc.org/v3docs/home

Balco, G. (2017b). The online exposure age calculator formerly known as the CRONUS-Earth online exposure age calculator. Retrieved from https://hess.ess.washington.edu/math/v3/v3_age_in.html

Balco, G. (2017c). Production rate calculations for cosmic-ray-muon-produced 10Be and 26Al benchmarked against geological calibration data. Quaternary Geochronology. Vol. 39, pp. 150-173. doi.org/10.1016/j.quageo.2017.02.001.

Balco, G. (2020). Glacier Change and Paleoclimate Applications of Cosmogenic-Nuclide Exposure Dating. Annual Review of Earth and Planetary Sciences. 48:1, 21-48. doi.org/10.1146/annurev-earth-081619-052609.

Barker, S., Diz, P., Vautravers, M., Pike, J., Knorr, G., Hall, I. R., Broecker, W. S. (2009). Interhemispheric Atlantic seesaw response during the last deglaciation. Nature 457, pp. 1097–1102. doi.org/10.1038/nature07770.

Barr, I. D., and Lovell, H. (2014). A review of topographic controls on moraine distribution. Geomorphology, 226, 44-64. doi.org/10.1016/j.geomorph.2014.07.030.

Barrell, D. J. A. (2011). Quaternary Glaciers of New Zealand. Chapter in "Developments in Quaternary Sciences". Vol. 15, pp.1047-1064. doi.org/10.1016/B978-0-444-53447-7.00075-1.

Barrell, D. J. A., Andersen, B. G., Denton, G. H. (2011). Glacial geomorphology of the central South Island, New Zealand. GNS Science monograph 27. 81 p. + map (5 sheets) + legend (1 sheet). Lower Hutt, New Zealand, GNS Science.

Barrell, D. J.A., and Read, S. A.L. (2014). The deglaciation of Lake Pukaki, South Island, New Zealand - a review. New Zealand Journal of Geology and Geophysics, 57:1, 86-101. doi:10.1080/00288306.2013.847469.

Barrell, D. J. A. (2016). General distribution and characteristics of active faults and folds in the Waimate District and Waitaki District, South Canterbury and North Otago. GNS Science Consultancy Report 2015/166. 124 p.

Barrell, D. J. A., Putnam, A. E. and Denton, G. H. (2019). Reconciling the onset of deglaciation in the upper Rangitata valley, Southern Alps, New Zealand. Quaternary Science Reviews. Vol. 203, pp. 141-150. doi.org/10.1016/j.quascirev.2018.11.003.

Barrows, T. T., Stone, J. O., Fifield, L. K., and Cresswell, R. G. (2002). The timing of the Last Glacial Maximum in Australia, Quaternary Science Reviews, Vol. 21, 1–3, doi.org/10.1016/S0277-3791(01)00109-3.

Barrows, T. T., Juggins, S., De Deckker, P., Calvo, E., and Pelejero, C. (2007). Longterm sea surface temperature and climate change in the Australian-New Zealand region: Paleoceanography, v. 22, PA2215, doi:10.1029/2006PA001328.

Bassinot, F. C., Labeyrie, L. D., Vincent, E., Quidelleur, X., Shackleton, N. J., and Lancelot, Y. (1994). The astronomical theory of climate and the age of the Brunhes–Matuyama magnetic reversal. Earth and Planetary Science Letters, 126, 91–108. doi.org/10.1016/0012-821X(94)90244-5.

Baumann, S., Anderson, B., Chinn, T., Mackintosh, A., Collier, C., Lorrey, A. M., Rack, W., Purdie, H. and Eaves, S. (2020) Updated inventory of glacier ice in New Zealand based on 2016 satellite imagery. Journal of Glaciology 1-14. doi.org/10.1017/jog.2020.78.

Bendle, J. M., Thorndycraft, V. R., and Palmer, A. P. (2017). The glacial geomorphology of the Lago Buenos Aires and Lago Pueyrredón ice lobes of central Patagonia. Journal of Maps, 13, 654–673. doi:10.1080/17445647.2017.1351908.

Benn D. I. and Gemmell A. M. D. (1997). Calculating equilibrium-line altitudes of former glaciers by the balance ratio method: a new computer spreadsheet. Glacial Geol. Geomorphol. (1997), p. 7.

Benn, D. I., and Evans, D. J. A. (1998). Glaciers and glaciation. Oxford University Press.

Benn, D. I. and Lehmkuhl, F. (2000). Mass balance and equilibrium-line altitudes of glaciers in high-mountain environments. Quaternary International, 65:15–29. doi.org/10.1016/S1040-6182(99)00034-8.

Benn, D. I., Owen, L. A., Osmaston, H. A., Seltzer, G. O., Porter, S. C. and Mark, B. (2005). Reconstruction of equilibrium-line altitudes for tropical and sub-tropical glaciers, Quaternary International. Vol. 138–139, pp. 8-21, doi.org/10.1016/j.quaint.2005.02.003.

Bennett, M. R. (2001). The morphology, structural evolution and significance of push moraines. Earth-Science Reviews. 53 (3–4): 197–236. doi:10.1016/S0012-8252(00)00039-8.

Bentley, M. J. (2010). The Antarctic palaeo record and its role in improving predictions of future Antarctic Ice Sheet change. Journal of Quaternary Science, 2010. 25(1): p. 5-18. doi.org/10.1002/jqs.1287.

Bereiter, B., Eggleston, S., Schmitt, J., Nehrbass-Ahles, C., Stocker, T. F., Fischer, H., Kipfstuhl, S., and Chappellaz, J. (2015). Revision of the EPICA Dome C CO2 record from 800 to 600 kyr before present, Geophys. Res. Lett., 42, 542–549, doi:10.1002/2014GL061957.

Berger, A. and Loutre, M. F. (1991). Insolation values for the climate of the last 10 million years. Quaternary Science Reviews. 10, 297–317, doi.org/10.1016/0277-3791(91)90033-Q.

Bierman, P. R., Marsella, K. A., Patterson, C., Davis, P. T., and Caffee, M. (1999). Mid-Pleistocene cosmogenic minimum-age limits for pre-Wisconsinan glacial surfaces in southwestern Minnesota and southern Baffin Island: a multiple nuclide approach, Geomorphology, Vol. 27, 1–2, pp. 25-39, doi.org/10.1016/S0169-555X(98)00088-9.

Borchers, B., Marrero, S., Balco, G., Caffee, M., Goehring, B., Lifton, N., Nishiizumi, K., Phillips, F., Schaefer, J., and Stone, J. (2016). Geological calibration of spallation production rates in the CRONUS-Earth project. Quaternary Geochronology, 31, 188-198. doi.org/10.1016/j.quageo.2015.01.009.

Borsellino, R., Shulmeister, J., and Winkler, S. (2017). Glacial geomorphology of the Brabazon and Butler Downs, Rangitata Valley, South Island, New Zealand, Journal of Maps, 13:2, 502-510, doi:10.1080/17445647.2017.1336122.

Bostock, H. C., Hayward, B. W., Neil, H. L., Sabaa, A. T., and Scott, G. H. (2015). Changes in the position of the Subtropical Front south of New Zealand since the last glacial period. Paleoceanography, 30, pp. 824-844. doi.org/10.1002/2014PA002652.

Briner, J. P., Svendsen, J. I., Mangerud, J., Lohne, Ø. S. And Young, N. E. (2014). A ^{10}Be chronology of south-western Scandinavian Ice Sheet history during the Lateglacial period. Journal of Quaternary Science, 29: 370-380. doi.org/10.1002/jqs.2710.

Broecker, W. S. (1966). Absolute dating and the astronomical theory of glaciation. Science, 151(3708):299–304. doi:10.1126/science.151.3708.299.

Broecker, W. S. (1978). The cause of glacial to interglacial climatic change. In Evolution of Planetary Atmospheres and Climatology of the Earth, pages 165–190. Centre National d'Etudes Spatiales, Toulouse, France.

Brown, L., Klein. J., Middleton, R., Sacks, I. S., Tera, F. (1982). 10Be in island-arc volcanoes and implications for subduction. Nature Vol. 299, pp. 718-720. doi:10.1038/299718a0.

Burke, K. D., Williams, J. W., Chandler, M. A., Haywood, A. M., Lunt, D. J., and Otto-Bliesner, B. L. (2018). Pliocene and Eocene provide best analogs for near-future climates. Proc. Natl. Acad. Sci. U.S.A. 115, 13288–13293. doi:10.1073/pnas.1809600115.

Burrows, C. J. and Russell, J. B. (1975). Moraines of the upper Rakaia Valley. Journal of the Royal Society of New Zealand, 5(4):463–477. doi.org/10.1080/03036758.1975.10419363.

Buizert, C., Sigl, M., Severi, M. et al. (2018). Abrupt ice-age shifts in southern westerly winds and Antarctic climate forced from the north. Nature 563, 681–685. doi.org/10.1038/s41586-018-0727-5.

Carrivick J. L. and Chase S. E. (2011). Spatial and temporal variability of annual glacier equilibrium line altitudes in the Southern Alps, New Zealand, New Zealand Journal of Geology and Geophysics, 54:4, 415-429, doi:10.1080/00288306.2011.607463.

Ceppi, P., Hwang, Y.-T., Liu, X., Frierson, D. M. W., and Hartmann, D. L. (2013). The relationship between the ITCZ and the Southern Hemispheric eddy-driven jet, J. Geophys. Res. Atmos., 118, 5136– 5146, doi:10.1002/jgrd.50461.

Chandler, B. M. P., Lovell, H., Boston, C. M., Lukas, S., Barr, I. D., Benediktsson, Í. Ö., Benn, D. I., Clark, C. D., Darvill, C. M., Evans, D. J. A., Ewertowski, M. W., Loibl, D., Margold, M., Otto, J-C., Roberts, D. H., Stokes, C. R., Storrar, R. D., and Stroeven, A. P. (2018). Glacial geomorphological mapping: A review of approaches and frameworks for best practice, Earth-Science Reviews, Vol. 185, Pp. 806-846, doi.org/10.1016/j.earscirev.2018.07.015.

Chandler, B. M. P. Lukas, S., Boston, C. M., and Merritt, J. W. (2019) Glacial geomorphology of the Gaick, Central Grampians, Scotland, Journal of Maps, 15:2, 60-78, doi:10.1080/17445647.2018.1546235.

Chinn, T. J. (1996). New Zealand glacier responses to climate change of the past century. NZ J Geol Geophys 39:415–428. doi.org/10.1080/00288306.1996.9514723.

Chinn, T. J. H. (2001) Distribution of the glacial water resources of New Zealand. Journal of Hydrology (NZ) 40(2), 139–187. www.jstor.org/stable/43922047.

Chinn T., Fitzharris B. B., Willsman A., Salinger M. J. (2012). Annual ice volume changes 1976–2008 for the New Zealand Southern Alps. Global and Planetary Change 92: 105–118. doi.org/10.1016/j.gloplacha.2012.04.002.

Chinn, T. J, Kargel, J. S., Leonard, G. J., Haritashya, U. K. and Pleasants, M. (2014). New Zealand's Glaciers. In: Kargel, J., Leonard, G., Bishop, M., Kääb, A., Raup, B. (eds) Global Land Ice Measurements from Space. Springer Praxis Books. Springer, Berlin, Heidelberg. pp. 675–715. doi.org/10.1007/978-3-540-79818-7_29.

Chmeleff, J., von Blanckenburg, F., Kossert, K., Jakob, D. (2010). Determination of the 10Be half-life by multicollector ICP-MS and liquid scintillation counting. Nucl. Instrum. Methods Phys. Res., Sect. B, 268, 192–199. doi.org/10.1016/j.nimb.2009.09.012.

Clark, D. H., Clark, M. M., and Gillespie, A. R. (1994). Debris-covered glaciers in the Sierra Nevada, California, and their implications for snowline reconstructions. Quaternary Research 41, 139-153. doi.org/10.1006/qres.1994.1016.

Clark, P. U. and Mix, A. C. (2002). Ice sheets and sea level of the Last Glacial Maximum. Quaternary Science Reviews 21. pp. 1-7. doi.org/10.1016/S0277-3791(01)00118-4.

Clark, P. U., Dyke, A. S., Shakun, J. D., Carlson, A. E., Clark, J., Wohlfarth, B., Mitrovica, J. X., Hostetler, S. W., McCabe, A. M., (2009). The last glacial maximum. Science 325, 710. doi:10.1126/science.1172873.

Clement, A. C., and Peterson, L. C. (2008). Mechanisms of abrupt climate change of the last glacial period, Rev. Geophys., 46, RG4002, doi:10.1029/2006RG000204.

Cockburn, H. A. P. and Summerfield, M. A. (2004). Geomorphological applications of cosmogenic isotope analysis. Progress in Physical Geography, 28(1): p. 1-42. doi.org/10.1191/0309133304pp395oa.

Cohen, K. M., Finney, S. C., Gibbard, P. L., and Fan, J. X. (2020). "International Chronostratigraphic Chart". International Commission on Stratigraphy. Retrieved 23 February 2020.

Columbus, J., Sirguey, P. and Tenzer, R. (2011) A free, fully assessed 15-m DEM for New Zealand. Survey Quarterly, 66, 16-19.

Croll, J. (1864). XIII. On the physical cause of the change of climate during geological epochs. The London, Edinburgh, and Dublin Philosophical Magazine and Journal of Science, 28(187):121–137.

Dansgaard, W., Johnsen, S. J., Møller, J., and Langway, C. C. (1969). One thousand centuries of climatic record from Camp Century on the Greenland ice sheet. Science, 166(3903):377–380. doi:10.1126/science.166.3903.377.

Dansgaard, W., Clausen, H., Gundestrup, N., Hammer, C., Johnsen, S., Kristinsdottir, P., and Reeh, N. (1982). A new Greenland deep ice core. Science, 218(4579):1273–1277. doi:10.1126/science.218.4579.1273.

Dansgaard, W., Johnsen, S., Clausen, H., Dahl-Jensen, D., Gundestrup, N., Hammer, C. and Oeschger, H. (1984). North Atlantic Climatic Oscillations Revealed by Deep Greenland Ice Cores. In Climate Processes and Climate Sensitivity (eds J. E. Hansen and T. Takahashi). pp. 288-298. doi:10.1029/GM029p0288.

Darvill, C. M. (2013). Cosmogenic Nuclide Analysis, in Geomorphological Techniques, L. Clarke and J. Nield, Editors. British Society for Geomorphology: London.

Darvill, C. M., Stokes, C. R., Bentley, M. J., and Lovell, H. (2014). A glacial geomorphological map of the southernmost ice lobes of Patagonia: the Bahía Inútil – San Sebastián, Magellan, Otway, Skyring and Río Gallegos lobes. Journal of Maps, 10, 500–520. doi:10.1080/17445647.2014.890134.

Darvill, C. M., Bentley, M. J., Stokes, C. R., and Shulmeister, J. (2016). The timing and cause of glacial advances in the southern mid-latitudes during the last glacial cycle based on a synthesis of exposure ages from Patagonia and New Zealand. Quaternary Science Reviews, 149, 200-214. doi.org/10.1016/j.quascirev.2016.07.024.

Data Information New Zealand – Linz Data Service. https://data.linz.govt.nz/.

Davis, R. and Schaeffer, O. A. (1955). Chlorine-36 in nature. Annals of the New York Academy of Sciences, 62(5):107–121.

Denton, G. H., Anderson, R. F., Toggweiler, J. R., Edwards, R. L., Schaefer, J. M., and Putnam, A. E. (2010). The last glacial termination. Science, 328 (5986), pp. 1652-1656. doi: 10.1126/science.1184119.

Denton, G. H., Putnam, A. E., Russell, J. L., Barrell, D. J. A., Schaefer, J. M., Kaplan, M. R. and Strand, P. D. (2021). The Zealandia Switch: Ice age climate shifts viewed from Southern Hemisphere moraines, Quaternary Science Reviews, Vol. 257. 106771. doi.org/10.1016/j.quascirev.2020.106771.

Doughty, A. M., Anderson, B. M., Mackintosh, A. N., Kaplan, M. R., Vandergoes, M. J., Barrell, D. J. A., Denton, G. H., Schaefer, J. M., Chinn, T. J. H., and Putnam, A. E. (2013). Evaluation of Lateglacial temperatures in the Southern Alps of New Zealand based on glacier modelling at Irishman Stream, Ben Ohau Range: Quaternary Science Reviews, Vol. 74, pp. 160-169. doi:10.1016/j.quascirev.2012.09.013.

Doughty, A. M., Schaefer, J. M., Putnam, A. E., Denton, G. H., Kaplan, M. R., Barrell, D. J. A., Andersen, B. G., Kelley, S. E., Finkel, R .C., Schwartz, R. (2015). Mismatch of glacier extent and summer insolation in Southern Hemisphere mid-latitudes. Geology, 43 (5): 407–410. doi:doi.org/10.1130/G36477.1.

Dowling, L. Eaves, S. Norton, K. Mackintosh, A. Anderson, B. Hidy, A. Lorrey, A. Vargo, L. Ryan, M., and Tims, S. (2021). Local summer insolation and greenhouse gas forcing drove warming and glacier retreat in New Zealand during the Holocene. Quaternary Science Reviews, Vol. 266, p. 107068. doi.org/10.1016/j.quascirev.2021.107068.

Dunne, J., Elmore, D. and Muzikar, P. (1999). Scaling factors for the rates of production of cosmogenic nuclides for geometric shielding and attenuation at depth on sloped surfaces. Geomorphology, 27, pp. 3-11. doi.org/10.1016/S0169-555X(98)00086-5.

Eaves, S. R., Mackintosh, A. N., Anderson, B. M., Doughty, A. M., Townsend, D. B., Conway, C. E., Winckler, G., Schaefer, J. M., Leonard, G. S., and Calvert, A. T. (2016). The Last Glacial Maximum in the central North Island, New Zealand: Paleoclimate inferences from glacier modelling: Climate of the Past, v. 12, p. 943–960, doi.org/10.5194/cp-12-943-2016.

Eaves, S. R., Anderson, B. M., and Mackintosh, A. N. (2017). Glacier-based climate reconstructions for the last glacial–interglacial transition: Arthur's Pass, New Zealand (42° S): Journal of Quaternary Science, v. 32, p. 877–887, doi.org/10.1002/jqs.2904.

Eaves, S. R., Collins, J. A., Jones, R. S., Norton, K. P., Tims, S. G., and Mackintosh, A. N. (2018). Further constraint of the in situ cosmogenic ^{10}Be production rate in pyroxene and a viability test for late Quaternary exposure dating, Quaternary Geochronology, Vol. 48, pp. 121-132, doi.org/10.1016/j.quageo.2018.09.006.

Eaves, S. R., Mackintosh, A. N., and Anderson, B. M. (2019). Climate amelioration during the Last Glacial Maximum recorded by a sensitive mountain glacier in New Zealand. Geology (2019) 47 (4): 299–302. doi.org/10.1130/G45543.1.

Ehlers, J., Gibbard, P. L., (2003). Extent and chronology of glaciations. Quaternary Science Reviews 22. pp. 1561–1568. doi.org/10.1016/S0277-3791(03)00130-6.

Ehlers, J. and Gibbard, P. (2011). Quaternary glaciation. Encyclopedia of Snow, Ice and Glaciers. Encyclopedia of Earth Sciences Series. pp. 873–882. doi:10.1007/978-90-481-2642-2_423.

Emiliani, C. (1955). Pleistocene temperatures. The Journal of Geology, 63:538–578. jstor.org/stable/30080906.

Epstein, S., Sharp, R. P., and Gow, A. (1970). Antarctic ice sheet: stable isotope analyses of Byrd station cores and interhemispheric climatic implications. Science, 168(3939):1570–1572. doi:10.1126/science.168.3939.1570.

Evans, M. D. (2008). A Geomorphological and Sedimentological Investigation into the Glacial Deposits of the Lake Clearwater Basin, Mid Canterbury, New Zealand. Master thesis in Geology. University of Canterbury. Geological Sciences. https://ir.canterbury.ac.nz/handle/10092/1531.

Fitzsimons, S. J., Pollington, M., Colhoun, E. A. (1996). Palaeomagnetic constraints on the ages of glacial deposits in North-West South Island, New Zealand. Zeitschrift für Geomorphologie, 105 pp. 7-20. ISSN 0372-8854.

Fitzsimons, S. J., and Veit, H. (2001). Geology and Geomorphology of the European Alps and the Southern Alps of New Zealand. Mountain Research and Development Vol. 21 No 4. pp. 340-349. doi.org/10.1659/0276-4741(2001)021[0340:GAGOTE]2.0.CO;2.

Fleming, C. A. (1959) (Trans. and ed.). The Geology of New Zealand. Contributions to the geology of the provinces of Auckland and Nelson by Ferdinand von Hochstetter. Government Printer, Wellington.

Furbish, D. J. and Andrews, J. T. (1984). The use of hypsometry to indicate long-term stability and response of valley glaciers to changes in mass transfer. Journal of Glaciology, 30(105), 199–211. doi.org/10.3189/S0022143000005931.

Gage, M., 1985. Glaciation in New Zealand - the first century of research. Quaternary Science Reviews. 4, 189–214. doi.org/10.1016/0277-3791(85)90025-3.

García, J. L., Kaplan, M. R., Hall, B. L., Schaefer, J. M., Vega, R. M., Schwartz, R., and Finkel, R. (2012). Glacier expansion in southern Patagonia throughout the Antarctic cold reversal. Geology; 40 (9): 859–862. doi.org/10.1130/G33164.1.

García, J., Maldonado, A., De Porras, M., Nuevo Delaunay, A., Reyes, O., Ebensperger, C., Binnie, S., Lüthgens, C. and Méndez, C. (2019). Early deglaciation and paleolake history of Río Cisnes Glacier, Patagonian Ice Sheet (44°S). Quaternary Research, 91(1), 194-217. doi:10.1017/qua.2018.93.

Gibbons, A. B., Megeath, J. D. and Pierce, K. L. (1984). Probability of moraine survival in a succession of glacial advances. Geology, 12(6), pp. 327-330. doi.org/10.1130/0091-7613(1984)12<327:POMSIA>2.0.CO;2.

Gjermundsen, E. F., Mathieu, R., Kääb, A., Chinn, T., Fitzharris, B. and Hagen, J. O. (2011) Assessment of multispectral glacier mapping methods and derivation of glacier area changes, 1978–2002, in the central Southern Alps, New Zealand, from ASTER satellite data, field survey and existing inventory data. Journal of Glaciology 57(204), 667–683. doi.org/10.3189/002214311797409749.

Glasser, N. F., and Jansson, K. (2008). The glacial map of southern South America. Journal of Maps, 4, 175-196, doi:10.4113/jom.2008.1020.

Golledge, N. R., Mackintosh, A. N., Anderson, B. M., Buckley, K. M., Doughty, A. M., Barrell, D. J. A., Denton, G. H., Vandergoes, M. J., Andersen, B. G. and Schaefer, J. M. (2012). Last Glacial Maximum climate in New Zealand inferred from a modelled Southern Alps icefield, Quaternary Science Reviews, Vol. 46, pp. 30-45, doi.org/10.1016/j.quascirev.2012.05.004.

Gosse, J. C. and Phillips, F. M. (2001). Terrestrial in situ cosmogenic nuclides: theory and application. Quaternary Science Reviews Vol. 20, Issue 14, pp. 1475-1560. doi.org/10.1016/S0277-3791(00)00171-2.

Granshaw F. D. and Fountain A. G. (2006). Glacier change (1958–1998) in the North Cascades National Park Complex, Washington, USA, J. Glaciol., 52, 251–256, doi.org/10.3189/172756506781828782.

Haast, J. (1864). Glacial deposits of New Zealand. Natural History Reviews, 13, 474-476.

Haman, C., and Embleton, C. (1988). Morphometrische Analyse der Kare in den Salzburger Zentralalpen (Morphometrical analysis of cirques in the Central Alps of Salzburg province). Salzburger Geographische Arbeiten 17, 57-74.

Hastenrath, S. (1971). On the Pleistocene snowline depression in the arid regions of the South American Andes. Journal of Glaciology 10, 255-267. doi.org/10.3189/S0022143000013228.

Heyman, J. Stroeven, A. P., Harbor, J. M., and Caffee, M. W. (2011). Too young or too old: evaluating cosmogenic exposure dating based on an analysis of compiled boulder exposure ages. Earth and Planetary Science Letters 302, 71–80. doi.org/10.1016/j.epsl.2010.11.040.

Hays, J., Imbrie, J. and Shackleton, N. (1976). Variations in the earth's orbit: Pacemaker of the ice ages. Science 194, 1121–1132. doi:10.1126/science.194.4270.1121.

Hector, J. (1865). On the geology of Otago, New Zealand. The Quarterly Journal Geological Society of London, 21, 124-128.

Hicks, D. M., Shankar, U., McKerchar, A. I., Basher, L., Lynn, I., Page, M., and Jessen, M. (2011). Suspended sediment yields from New Zealand rivers. Journal of Hydrology (New Zealand), 81-142. www.jstor.org/stable/43945015.

Hein, A. S., Cogez, A., Darvill, C. M., Mendelova, M., Kaplan, M. R., Herman, F., Dunai, T. J., Norton, K., Xu, S., Christl, M., and Rodés, Á. (2017). Regional mid-Pleistocene glaciation in central Patagonia Quaternary Science Reviews, 164, pp. 77-94. doi.org/10.1016/j.quascirev.2017.03.023.

Huybers, P. and Eisenman, A. (2006). Integrated summer insolation calculations. NOAA/NCDC Paleoclimatology Program, Data Contribution Series no.2006-079.

Huybers, P. and Denton, G. (2008). Antarctic temperature at orbital timescales controlled by local summer duration. Nature Geosci 1, 787–792. doi.org/10.1038/ngeo311.

Imbrie, J., Berger, A., Boyle, E. A., Clemens, S. C., Duffy, A., Howard, W. R., Kukla, G., Kutzbach, J., Martinson, D. G., McIntyre, A., Mix, A. C., Molfino, B., Morley, J. J., Peterson, L. C., Pisias, N. G., Prell, W. L., Raymo, M. E., Shackleton, N. J., and Toggweiler J. R. (1993). On the structure and origin of major glaciation cycles 2. The 100,000-year cycle, Paleoceanography, 8(6), 699–735, doi:10.1029/93PA02751.

Ivy-Ochs, S. and Briner, J. P. (2014) Dating Disappearing Ice with Cosmogenic Nuclides. Elements; 10 (5): 351–356. doi.org/10.2113/gselements.10.5.351.

IPCC (2019). Special report on the ocean and cryosphere in a changing climate. Geneva, Switzerland 1 (3). www.ipcc.ch/srocc/

Izagirre, E., Darvill, C. M., Rada, C., and Aravena, J. C. (2018) Glacial geomorphology of the Marinelli and Pigafetta glaciers, Cordillera Darwin Icefield, southernmost Chile, Journal of Maps, 14:2, 269-281, doi:10.1080/17445647.2018.1462264.

Jansen, E., J. Overpeck, K.R. Briffa, J.-C. Duplessy, F. Joos, V. Masson-Delmotte, D. Olago, B. Otto-Bliesner, W.R. Peltier, S. Rahmstorf, R. Ramesh, D. Raynaud, D. Rind, O. Solomina, R. Villalba and D. Zhang. (2007). Palaeoclimate. In: Climate Change 2007: The Physical Science Basis. Contribution of Working Group I to the Fourth Assessment Report of the Intergovernmental Panel on Climate Change [Solomon, S., D. Qin, M. Manning, Z. Chen, M. Marquis, K.B. Averyt, M. Tignor and H.L. Miller (eds.)]. Cambridge University Press, Cambridge, United Kingdom and New York, NY, USA.

Jiskoot H. (2011). Dynamics of Glaciers. In: Singh V.P., Singh P., Haritashya U.K. (eds) Encyclopedia of Snow, Ice and Glaciers. Encyclopedia of Earth Sciences Series. Springer, Dordrecht. doi.org/10.1007/978-90-481-2642-2_127.

Jomelli, V., Favier, V., Vuille, M., Braucher, R., Martin, L., Blard, P. H., Colose, C., Brunstein, D., He, F., Khodri, M., Bourles, D. L., Leanni, L., Rinterknecht, V., Grancher, D., Francou, B., Ceballos, J. L., Fonseca, H., Liu, Z., Otto-Bliesner, B. L. (2014). A major advance of tropical Andean glaciers during the Antarctic cold reversal. Nature 513, 224–228. doi.org/10.1038/nature13546.

Joos, F. and Prentice, I. C. (2004). A Paleo-Perspective on Changes in Atmospheric CO_2 and Climate. hdl.handle.net/11858/00-001M-0000-000E-D1B9-5.

Joos, F. and Prentice, I. C. (2008). The Global Carbon Cycle: Integrating Humans, Climate, and the Natural World. Scope. 62. Washington D.C.: Island Press. pp. 165–186.

Jouzel, J., Genthon, C., Lorius, C., Petit, J., and Barkov, N. (1987). Vostok ice core-A continuous isotope temperature record over the last climatic cycle (160,000 years). Nature, 329:403–408. doi.org/10.1038/329403a0.

Jouzel, J., Vaikmae, R., Petit, J. R., Martin, M., Duclos, Y., Stievenard, M., Lorius, C., Toots, M., Mélières, M. A., Burckle, L. H., Barkov, N. I., and Kotlyakov, V. M. (1995). The two-step shape and timing of the last deglaciation in Antarctica. Climate Dynamics 11, 151-161. doi.org/10.1007/BF00223498.

Jouzel, J., Masson, V., Cattani, O., Falourd, S., Stievenard, M., Stenni, B., Longinelli, A., Johnsen, S. J., Steffenssen, J. P., Petit, J. R., Schwander, J., Souchez, R., and Barkov, N. I. (2001). Geophysical Research Letters. Vol. 28, pp. 3199-3202. doi.org/10.1029/2000GL012243.

Kageyama, M., Albani, S., Braconnot, P., Harrison, S. P., Hopcroft, P. O., Ivanovic, R. F., Lambert, F., Marti, O., Peltier, W. R., Peterschmitt, J. Y. and Roche, D. M. (2017). The PMIP4 contribution to CMIP6–Part 4: Scientific objectives and experimental design of the PMIP4-CMIP6 Last Glacial Maximum experiments and PMIP4 sensitivity experiments. Geoscientific Model Development, 10(11), pp.4035-4055. doi.org/10.5194/gmd-10-4035-2017.

Kamp, P. and Tippett, J. (1993). Dynamics of the Pacific Plate crust in the South Island (New Zealand) zone of oblique continent-continent convergence. Journal of Geophysical Research, 98: 105–116. doi.org/10.1029/93JB01091.

Kaplan, M. R., Fogwill, C. J., Sugden, D. E., Hulton, N. R. J., Kubik, P. W., Freeman, S. P. H. T. (2008). Southern Patagonian glacial chronology for the Last Glacial period and implications for Southern Ocean climate. Quaternary Science Reviews. 27, 284–294. doi.org/10.1016/j.quascirev.2007.09.013.

Kaplan, M., Schaefer, J., Denton, G. Barrell, D. J. A., Chinn, T. J. H. Putnam, A. E., Andersen, B. G., Finkel, R. C., Schwartz, R., and Doughty, A. M (2010). Glacier retreat in New Zealand during the Younger Dryas stadial. Nature 467, 194–197. doi.org/10.1038/nature09313.

Kaplan, M. R., Schaefer, J. M., Denton, G. H., Doughty, A. M., Barrell, D. J. A., Chinn, T. J. H. Putnam, A. E., Andersen, B. G., Mackintosh, A., Finkel, R. C., Schwartz, R., and Anderson, B. (2013). The anatomy of long-term warming since 15 ka in New Zealand based on net glacier snowline rise. Geology; 41 (8): 887–890. doi.org/10.1130/G34288.1.

Kaufman, D., McKay, N., Routson, C., Erb, M., Dätwyler, C., Sommer, P. S., Heiri, O., and Davis, B. (2020). Holocene global mean surface temperature, a multi-method reconstruction approach. Sci Data 7, 201. doi.org/10.1038/s41597-020-0530-7.

Kidson, J. W. (2000). An analysis of New Zealand synoptic types and their use in defining weather regimes. International Journal of Climatology 20: 299–316. doi.org/10.1002/(SICI)1097-0088(20000315)20:3<299::AID-JOC474>3.0.CO;2-B.

Kiernan, K., Fifield, L., and Chappell, J. (2004). Cosmogenic nuclide ages for Last Glacial Maximum moraine at Schnells Ridge, Southwest Tasmania. Quaternary Research, 61(3), 335-338. doi:10.1016/j.yqres.2004.02.004.

Kingma, J. T. (1959). The tectonic history of New Zealand, New Zealand Journal of Geology and Geophysics, 2:1, 1-55, doi:10.1080/00288306.1959.10431311.

Kirkbride, M. P. (1993). The temporal significance of transitions from melting to calving termini at glaciers in the central Southern Alps of New Zealand. The Holocene, 3(3), 232-240. doi.org/10.1177/095968369300300305.

Kirkbride, M. P., Brazier V. (1998). A critical evaluation of the use of glacier chronologies in climatic reconstruction, with reference to New Zealand. In L.A. Owen (Ed.), Mountain Glaciation, Quaternary Proceedings N6, Wiley, Chichester, pp. 55-64.

Kjær, K. H. and Krüger, J. (2001). The final phase of dead-ice moraine development: processes and sediment architecture, Kötlujökull, Iceland. Sedimentology. 48 (5): 935–952. doi.org/10.1046/j.1365-3091.2001.00402.x.

Klimaszewski, M., 1990. Thirty years of detailed geomorphological mapping. Geogr. Pol. 58, 11–18. www.geographiapolonica.pl/article/item/8028.html.

Kohl, C.P. and Nishiizumi, K. (1992). Chemical isolation of quartz for measurement of in-situ -produced cosmogenic nuclides. Geochimica et Cosmochimica Acta. Vol. 56, 9, pp. 3583-3587. doi.org/10.1016/0016-7037(92)90401-4.

Korsch, R. J., Wellman, H. W. (1988). The Geological Evolution of New Zealand and the New Zealand Region. In: Nairn A.E.M., Stehli F.G., Uyeda S. (eds) The Ocean Basins and Margins. Springer, Boston, MA. doi.org/10.1007/978-1-4615-8041-6_10.

Korschinek, G., Bergmaier, A., Faestermann, T., Gerstmann, U. C., Knie, K., Rugel, G., Wallner, A., Dillmann, I., Dollinger, G., Lierse von Gostomski, Ch., Kossert, K., Maiti, M., Poutivtsev, M., Remmert, A. (2010). A new value for the half-life of 10Be by heavy-ion elastic recoil detection and liquid scintillation counting. Nucl. Instrum. Methods Phys. Res., Sect. B, 268, 187–191. doi.org/10.1016/j.nimb.2009.09.020.

Leger, T. P. M., Hein, A. S., Bingham, R. G., Martini, M. A., Soteres, R. L., Sagredo, E. A., and Martínez, O. A. (2020). The glacial geomorphology of the Río Corcovado, Río Huemul and Lago Palena/General Vintter valleys, northeastern Patagonia (43°S, 71°W). Journal of Maps, 16(2), 651–668. doi.org/10.1080/17445647.2020.1794990.

Leger, T. P. M., Hein, A. S., Bingham, R. G., Rodés, Á., Fabel, D., and Smedley, R. K. (2021). Geomorphology and ^{10}Be chronology of the Last Glacial Maximum and deglaciation in northeastern Patagonia, 43°S-71°W, Quaternary Science Reviews, Vol. 272, 107194, doi.org/10.1016/j.quascirev.2021.107194.

Lifton, N., Bieber, J. W., Clem, J. M., Duldig, M. L., Evenson, P., Humble, J. E., and Pyle, R. (2005). Addressing solar modulation and long-term uncertainties in scaling secondary cosmic rays for in situ cosmogenic nuclide applications. Earth and Planetary Science Letters, 239(1), 140-161. doi.org/10.1016/j.epsl.2005.07.001.

Lifton, N., Sato, T. and Dunai, T. J. (2014). Scaling in situ cosmogenic nuclide production rates using analytical approximations to atmospheric cosmic-ray fluxes. Earth and Planetary Science Letters, 386, 149-160. doi.org/10.1016/j.epsl.2013.10.052.

Lisiecki, L. E., and Raymo, M. E. (2005). A Pliocene-Pleistocene stack of 57 globally distributed benthic δ18O records, Paleoceanography, 20, PA1003, doi:10.1029/2004PA001071.

Little, T. A., Cox, S., Vry, J. K., Batt, G. (2005). Variations in exhumation level and uplift rate along the oblique-slip Alpine fault, central Southern Alps, New Zealand. Geological Society of America Bulletin 117(5/6): 707-723. doi.org/10.1130/B25500.1.

Lorius, C., Ritz, C., Jouzel, J., Merlivat, L., and Barkov, N. (1985). A 150,000-year climatic record from Antarctic ice. Nature, 316:591–596. doi.org/10.1038/316591a0.

Lorrey, A., Fowler A. M., and Salinger, J. (2007). Regional climate regime classification as a qualitative tool for interpreting multi-proxy palaeoclimate data spatial patterns: A New Zealand case study. Palaeogeography, Palaeoclimatology, Palaeoecology. 253. pp. 407-433. doi:10.1016/j.palaeo.2007.06.011.

Lorrey, A. M, Vandergoes, M., Renwick. J, et al. (2010). A regional climate regime classification synthesis for New Zealand covering three critical periods of the late Quaternary: The last 2000 years, the mid-Holocene, and the end of the Last Glacial Coldest Period. NIWA Client Report AKL2010-025 prepared for the University of Auckland.

Lorrey, A., M., Vandergoes, M., Almond, P., Renwick, J., Stephens, T., Bostock, H., Mackintosh, A., Newnham, R., Williams, P., W., Ackerley, D., Neil, H., and Fowler, A. M. (2012). Palaeocirculation across New Zealand during the last glacial maximum at ~21 ka, Quaternary Science Reviews, Vol. 36, pp. 189-213, doi.org/10.1016/j.quascirev.2011.09.025.

Lorrey, A., Fauchereau, N., Stanton, C., Chappell, P., Phipps, S., Mackintosh, A., Renwick, J., Goodwin, I. and Fowler, A. (2014). The Little Ice Age climate of New Zealand reconstructed from Southern Alps cirque glaciers: a synoptic type approach. Climate Dynamics, 42, 3039–3060. doi.org/10.1007/s00382-013-1876-8.

Lorrey, A. M., and Bostock, H. (2017). The Climate of New Zealand Through the Quaternary. In: Shulmeister J. (eds) Landscape and Quaternary Environmental Change in New Zealand. Atlantis Advances in Quaternary Science, vol 3. Atlantis Press, Paris. doi.org/10.2991/978-94-6239-237-3_3.

Lorrey, A., Vargo, L., Purdie, H., Anderson, B., Cullen, N., Sirguey, P., Mackintosh, A., Willsman, A., Macara, G., and Chinn, W. (2022). Southern Alps equilibrium line altitudes: Four decades of observations show coherent glacier–climate responses and a rising snowline trend. Journal of Glaciology, 1-14. doi:10.1017/jog.2022.27.

Lüthi, D., Le Floch, M., Bereiter, B., Blunier, T., Barnola, J.-M., Siegenthaler, U., Raynaud, D., Jouzel, J., Fischer, H., Kawamura, K., et al. (2008). High-resolution carbon dioxide concentration record 650,000–800,000 years before present. Nature, 453(7193):379–382. doi.org/10.1038/nature06949.

Macara, G. R. 2018. The Climate and Weather of Southland. Second edition. Niwa Science and Technology Series, Number 63. 40 pp. ISSN 1173-0382.

Mackintosh, A. N., Barrows, T. T., Colhoun, E. A., and Fifield, L. K. (2006). Exposure dating and glacial reconstruction at Mt. Field, Tasmania, Australia, identifies MIS 3 and MIS 2 glacial advances and climatic variability. J. Quaternary Sci., Vol. 21 pp. 363–376. doi.org/10.1002/jqs.989.

Mackintosh, A. N., Anderson, B. M., and Pierrehumbert, R. T. (2017). Reconstructing climate from glaciers. Annu. Rev. Earth Planet. Sci. 45:649–80. doi.org/10.1146/annurev-earth-063016-020643.

Manley, G. (1959). The late-glacial climate of north-west England. Liverpool and Manchester Geological Journal 2, 188-215. doi.org/10.1002/gj.3350020207.

Martin, H. E. and Whalley, W. B. (1987). Rock glaciers: part 1: rock glacier morphology: classification and distribution. Progress in Physical Geography: Earth and Environment. Vol. 11 issue: 2, pp. 260-282. doi.org/10.1177/030913338701100205.

Marcott, S., Bauska, T., Buizert, C. et al. Steig, E. J., Rosen, J. L., Cuffey, K. M., Fudge, T. J., Severinghaus, J. P., Ahn, J., Kalk, M. L., McConnell, J. R., Sowers, T., Taylor, K. C., White, J. W. C. and Brook, E. J. (2014). Centennial-scale changes in the global carbon cycle during the last deglaciation. Nature 514, 616–619, doi:10.1038/nature13799.

Markle, B., Steig, E., Buizert, C. Schoenemann, S. W., Bitz, C. M., Fudge, T. J., Pedro, J. B., Ding, Q., Jones, T. R., White, J. W. C. and Sowers, T. (2017). Global atmospheric teleconnections during Dansgaard–Oeschger events. Nature Geosci 10, 36–40. doi.org/10.1038/ngeo2848.

McColl, S. T., and Davies, T. R. (2011). Evidence for a rock-avalanche origin for 'The Hillocks'"moraine", Otago, New Zealand. Geomorphology, 127(3-4), pp.216-224. doi.org/10.1016/j.geomorph.2010.12.017.

McGlone, M. S. (1995). Lateglacial landscape and vegetation change and the Younger Dryas climate oscillation in New Zealand. Quaternary Science Reviews 14, 867-881. doi.org/10.1016/0277-3791(95)00068-2.

McGlone, M. S., Turney, C. S. M., and Wilmshurst, J. M. (2004). Late-glacial and Holocene vegetation and climatic history of the Cass Basin, central South Island, New Zealand. Quaternary Research 62, 267-279. doi.org/10.1016/j.yqres.2004.09.003.

McKinnon, K. A., Mackintosh, A. N., Anderson, B. M., Barrell, D. J. A. (2012). The influence of sub-glacial bed evolution on ice extent: a model-based evaluation of the Last Glacial Maximum Pukaki glacier, New Zealand. Quaternary Science Reviews. 57, 46-57. doi.org/10.1016/j.quascirev.2012.10.002.

McManus, J. F., Francois, R., Gherardi, J. M., Keigwin, L. D. and Brown-Leger, S. (2004). Collapse and rapid resumption of Atlantic meridional circulation linked to deglacial climate changes. nature, 428(6985), pp.834-837. doi.org/10.1038/nature02494.

Mendelová, M., Hein, A. S., Rodés, Á., Smedley, R. K., and Xu, S. (2020). Glacier expansion in central Patagonia during the Antarctic Cold Reversal followed by retreat and stabilisation during the Younger Dryas, Quaternary Science Reviews. Vol. 227, 106047. doi.org/10.1016/j.quascirev.2019.106047.

Menviel, L., Spence, P., Yu, J., Chamberlain, M.A., Matear, R.J., Meissner, K.J. and England, M.H. (2018). Southern Hemisphere westerlies as a driver of the early deglacial atmospheric CO_2 rise. Nature Communications, 9(1), pp.1-12. doi.org/10.1038/s41467-018-04876-4.

Meier, M. F. and Post, A. S. (1962). Recent variations in mass net budgets of glaciers in western North America. Union Gèodèsique et Géophysique Internationale. Association Internationale d'Hydrologie Scientifique Commission des Neiges et des Glaces. Colloque d'Obergurgl, 10/9-18/9 1962, 63-77. Publication no. 58 de l'Association Internationale d'Hydrologie Scientifique.

Meierding, T. C. (1982). Late Pleistocene glacial equilibrium-line in the Colorado Front Range: A comparison of methods. Quaternary Research 18, 289-310. doi.org/10.1016/0033-5894(82)90076-X.

Milankovitch, M. (1920). Theorie mathematique des phenomenes thermiques produits par la radiation solaire. Gauthier-Villars, Paris, France.

Milankovitch, M. (1941). Kanon der Erdbestrahlung und seine Anwendung auf das Eiszeitenproblem. Royal Serbian Academy, Belgrade.

Mix, Alan C., Bard, E., and Schneider, R. (2001). Environmental processes of the ice age: land, oceans, glaciers (EPILOG), Quaternary Science Reviews, Vol. 20, Issue 4, pp. 627-657, doi.org/10.1016/S0277-3791(00)00145-1.

Moore, E. M. M., Eaves, S. R., Norton, K. P., Mackintosh, A. N. Anderson, B. M., Dowling, L. H., Hidy, A. J. (2022). Climate reconstructions for the Last Glacial Maximum from a simple cirque glacier in Fiordland, New Zealand. Quaternary Science Reviews 275, 107281. doi.org/10.1016/j.quascirev.2021.107281.

Murray, D. R. and Locke, W. W. (1989). Dynamics of the Late Pleistocene Big Timber Glacier, Crazy Mountains, Montana, U.S.A. Journal of Glaciology. 35, 183-190. doi.org/10.3189/S0022143000004470.

NEEM community members. Eemian interglacial reconstructed from a Greenland folded ice core. Nature 493, 489–494 (2013). doi.org/10.1038/nature11789.

Nesje A. and Dahl S. O. (2000). Glaciers and Environmental Change. New York: Oxford University Press. 216 pp. ISBN 9780340706343.

Newnham, R. M. and Lowe, D. J. (2000). Fine-resolution pollen record of late-glacial climate reversal from New Zealand. Geology 28, 759-762. doi.org/10.1130/0091-7613(2000)28<759:FPROLC>2.0.CO;2.

Newnham, R. M., Vandergoes, M. J., Sikes, E., Carter, L., Wilmshurst, J. M., Lowe, D. J., McGlone, M. S., and Sandiford, A. (2012). Does the bipolar seesaw extend to the terrestrial southern mid-latitudes?, Quaternary Science Reviews, Vol. 36, pp. 214-222, doi.org/10.1016/j.quascirev.2011.04.013.

Newnham, R., McGlone, M., Moar, N., Wilmshurst, J. and Vandergoes, M. (2013). The vegetation cover of New Zealand at the Last Glacial Maximum: Quaternary Science Reviews, v. 74, p. 202–214, doi.org/10.1016/j.quascirev.2012.08.022.

New Zealand Geological Survey (1973). Quaternary geology South Island, 1:1 000 000. New Zealand Geological Survey miscellaneous series map 6. Wellington, New Zealand. Department of Scientific and Industrial Research.

Nishiizumi K., Imamura M., Caffee M. W., Southon J. R., Finkel R. C. and McAninch J. (2007). Absolute calibration of ^{10}Be AMS standards. Nucl. Instrum. Methods Phys. Res. Sect. B Beam Interact. Mater. Atoms. 258, 403-413. doi.org/10.1016/j.nimb.2007.01.297.

NIWA (National Institute of Water and Atmospheric Research). (2012). New Zealand median annual average temperature based on 30 year period 1981-2010.

Norris, R. J., and Cooper, A. F. (2001). Late quaternary slip rates and their significance for slip partitioning on the Alpine Fault. Journal of Structural Geology, 23(2/3): 507-520. doi.org/10.1016/S0191-8141(00)00122-X.

Norton, K. P., von Blanckenburg, F., Schlunegger, F., Schwab, M., and Kubik, P. W. (2008). Cosmogenic nuclide-based investigation of spatial erosion and hillslope channel coupling in the transient foreland of the Swiss Alps. Geomorphology, 95 (3–4), pp. 474-486. doi.org/10.1016/j.geomorph.2007.07.013.

Norton, D. (1985). A multivariate technique for estimating New Zealand temperature normals. Weather and Climate 5, 64-74. doi:10.2307/44279988.

Nyenhuis, M. (2006). Permafrost und Sedimenthaushalt in Einem Alpinen Geosystem. Bonner Geographische Abhandlungen, Nr. 116. Bonn: Asgard-Verlag. 142 pp.

Ochs, M. and Ivy-Ochs, S. (1997). The chemical behavior of Be, Al, Fe, Ca and Mg during AMS target preparation from terrestrial silicates modeled with chemical speciation calculations. Nuclear Instruments and Methods in Physics Research Section B: Beam Interactions with Materials and Atoms. Vol. 123, 1–4, pp. 235-240. doi.org/10.1016/S0168-583X(96)00680-5.

Oerlemans, J. and Fortuin, J. P. F. (1992). Sensitivity of glaciers and small ice caps to greenhouse warming, Science, 258, 115–117, doi:10.1126/science.258.5079.115.

Oerlemans J. (2001). Glaciers and Climate Change. Rotterdam: A.A. Balkema.

Oerlemans, J. (2005). Extracting a Climate Signal from 169 Glacier Records. Science. Vol. 308, Issue 5722, pp. 675-677. doi:10.1126/science.1107046.

Ohmura, A., Kasser, P. and Funk, M. (1992). Climate at the equilibrium line of glaciers. Journal of Glaciology 38, 397–411. doi.org/10.3189/S0022143000002276.

Østrem, G. (1966). The height of the glaciation limit in southern British Colombia and Alberta. Geografiska Annaler 48, A, 126-138. doi.org/10.2307/520522.

Pedro, J. B., van Ommen, T. D., Rasmussen, S. O., Morgan, V. I., Chappellaz, J., Moy, A. D., Masson-Delmotte, V., and Delmotte, M. (2011). The last deglaciation: timing the bipolar seesaw, Clim. Past, 7, 671–683, doi.org/10.5194/cp-7-671-2011.

Pedro, J., Bostock, H., Bitz, C. He, F., Vandergoes, M. J., Steig, E. J., Chase, B. M., Krause, C. E., Rasmussen, S. O., Markle, B. R., and Cortese, G. (2016). The spatial extent and dynamics of the Antarctic Cold Reversal. Nature Geosci 9, 51–55. doi.org/10.1038/ngeo2580.

Pedro, J. B., Jochum, M., Buizert, C., He, F., Barker, S., and Rasmussen, S. O. (2018). Beyond the bipolar seesaw: Toward a process understanding of interhemispheric coupling, Quaternary Science Reviews, Vol. 192, pp. 27-46, doi.org/10.1016/j.quascirev.2018.05.005.

Pellitero R., Rea B. R., Spagnolo M., Bakke J., Hughes P., Ivy-Ochs S., Lukas S., and Ribolini A. (2015). A GIS tool for automatic calculation of glacier equilibrium-line altitudes, Computers and Geosciences. Vol. 82, pp. 55-62. doi.org/10.1016/j.cageo.2015.05.005.

Petit, J. R., Jouzel, J., Raynaud, D., Barkov, N. I., Barnola, J. ., Basile, I., Bender, M., Chappellaz, J., Davis, M., Delaygue, G., Delmotte, M., Kotiyakov, V. M., Legrand, M., Lipenkov, V. Y., Lorius, C., Ppin, L., Ritz, C., Saltzman, E., and Stievenard, M. (1999). Climate and atmospheric history of the past 420,000 years from the Vostok ice core, Antarctica. Nature, 399(6735):429–436. doi.org/10.1038/20859.

Pfeffer, W. T., Arendt, A. A., Bliss, A., Bolch, T., Cogley, J. G., Gardner, A. S., Hagen, J., Hock, R., Kaser, G., Kienholz, C., Miles, E. S., Moholdt, G., Mölg, N., Paul, F., Radic V., Rastner, P., Raup, B. H., Rich, J., Sharp, M. J., and The Randolph Consortium (2014). The Randolph Glacier Inventory: a globally complete inventory of glaciers, Journal of Glaciology, 60, 537–552, doi.org/10.3189/2014JoG13J176.

Pahnke, K., Zahn, R., Elderfield, H., and Schulz, M. (2003). 340,000-year centennial- scale marine record of Southern Hemisphere climatic oscillation: Science, v. 301, p. 948–952, doi:10.1126/science.1084451.

Phillips, F. M., Zreda, M. G., Benson, L. V., Plummer, M. A., Elmore, D., and Sharma, P. (1996). Chronology for Fluctuations in Late Pleistocene Sierra Nevada Glaciers and Lakes, Science, 274, 5288, (749-751), doi/10.1126/science.274.5288.749.

Pillans, B. (1991). New Zealand Quaternary stratigraphy: An overview. Quaternary Science Reviews. Vol. 10. pp. 405-418. doi.org/10.1016/0277-3791(91)90004-E.

Porter, S. C. (1975). Equilibrium-line altitudes of late Quaternary glaciers in the Southern Alps, New Zealand. Quaternary Research 5, 27-47. doi.org/10.1016/0033-5894(75)90047-2.

Porter, S. C. (1981). Glaciological evidence of Holocene climatic change. In: Wigley, T. M. L., Ingram, M. J., Farmer, G. (eds.), Climate and History Studies on Past Climates and their Impact on Man, pp. 82-110. Cambridge University Press, Cambridge.

Preusser, F., Andersen, B. G., Denton, G. H., and Schlüchter, C. (2005). Luminescence chronology of Late Pleistocene glacial deposits in North Westland, New Zealand. Quaternary Science Reviews. Vol. 24, Issue 20-21. pp. 2207–2227. doi.org/10.1016/j.quascirev.2004.12.005.

Putnam, A., Denton, G., Schaefer, J. Barrell, D. J. A., Andersen, B. G., Finkel, R. C., Schwartz, R., Doughty, A. M., Kaplan, M., and Schlüchter, C. (2010a). Glacier advance in southern middle-latitudes during the Antarctic Cold Reversal. Nature Geosci 3, 700–704. doi.org/10.1038/ngeo962.

Putnam, A. E., Schaefer, J. M., Barrell, D. J. A., Vandergoes, M., Denton, G. H., Kaplan, M. R., Schwartz, R., Finkel, R. C., Goehring, B. M., Kelley, S. E. (2010b). In situ cosmogenic ^{10}Be production rate calibration from the Southern Alps, New Zealand. Quaternary Geochronology. 5, 392–409. doi.org/10.1016/j.quageo.2009.12.001.

Putnam A. E., Schaefer, J. M., Denton G. H. et al. (2012). Regional climate control of glaciers in New Zealand and Europe during the preindustrial Holocene. Nature Geoscience 5: 627-630. doi.org/10.1038/ngeo1548.

Putnam, A. E., Schaefer, J. M., Denton, G. H., et al. (2013a). Warming and glacier recession in the Rakaia valley, Southern Alps of New Zealand, during Heinrich Stadial 1. Earth and Planetary Science Letters 382: 98–110. doi.org/10.1016/j.epsl.2013.09.005.

Putnam, A. E., Schaefer, J. M., Denton, G. H., Barrell, D. J. A., Birkel, S. A., Andersen, B. G., Kaplan, M. R., Finkel, R. C., Schwartz, R., Doughty, A. M. (2013b). The Last Glacial Maximumat 44°S documented by a moraine chronology at Lake Ohau, Southern Alps of

New Zealand. Quaternary Science Reviews 62, 114–141. doi.org/10.1016/j.quascirev.2012.10.034.

Purdie, H., Anderson, B., Chinn, T., Owen, I., Mackintosh, A. and Lawson, W. (2014). Franz Josef and Fox Glaciers, New Zealand: Historic length records. Global and Planetary Change. Vol. 121, pp. 41-52. doi.org/10.1016/j.gloplacha.2014.06.008.

Rączkowska, Z. and Zwoliński, Z. (2015). Digital geomorphological map of Poland. Geogr. Pol. 88 (2), 205–210. doi.org/GPol.0025.

Rahmstorf, S., and Schellnhuber, H. J. (2006). Der Klimawandel. Beck Verlag, Munich, 144 pp.

Rattenbury, M.S.; Jongens, R.; Cox, S.C. (compilers) 2010: Geology of the Haast area: scale 1:250,000. Lower Hutt: Institute of Geological & Nuclear Sciences Limited. Institute of Geological & Nuclear Sciences 1:250,000 geological map 14. 67 p. + 1 folded map.

Richardson, C., and Holmlund, P. (1996). Glacial cirque formation in northern Scandinavia. Annals of Glaciology 22, 102-106. doi.org/10.3189/1996AoG22-1-102-106.

Robinson, G., Peterson, J. A., and Anderson, P. M. (1971). Trend surface analysis of corrie altitudes in Scotland. Scottish Geographical Magazine 87, 142-146. doi.org/10.1080/00369227108736188.

Rother, H., Fink, D., Shulmeister, J., Mifsud, C., M. Evans and Pugh, J. (2014). The early rise and late demise of New Zealand's last glacial maximum. Proceedings of the National Academy of Science, 111, 11630-11635. doi.org/10.1073/pnas.1401547111.

Röthlisberger, R., Mulvaney, R., Wolff, E. W., Hutterli, M. A., Bigler, M., Sommer, S., and Jouzel, J. (2002). Dust and sea salt variability in central East Antarctica (Dome C) over the last 45 kyrs and its implications for southern high-latitude climate, Geophys. Res. Lett., 29(20), 1963, doi:10.1029/2002GL015186.

Rowan, A. V., Brocklehurst, S.H. Schultz, D. M. Plummer, M. A. Anderson, L. S. and Glasser, N. F. (2014). Late Quaternary glacier sensitivity to temperature and precipitation distribution in the Southern Alps of New Zealand, J. Geophys. Res. Earth Surf., 119, 1064–1081, doi:10.1002/2013JF003009.

Sagredo, E. A., Kaplan, M. R., Araya, P. S., Lowell, T. V., Aravena, J. C., Moreno, P. I., Kelly, M. A. and Schaefer, J. M., (2018). Trans-pacific glacial response to the Antarctic Cold Reversal in the southern mid-latitudes. Quaternary Science Reviews, Vol. 188, pp. 160-166. doi.org/10.1016/j.quascirev.2018.01.011.

Sattler, K., Anderson, B., Mackintosh, A., Norton, K., and de Róiste M. (2016) Estimating Permafrost Distribution in the Maritime Southern Alps, New Zealand, Based on Climatic

Conditions at Rock Glacier Sites. Frontiers in Earth Science. Vol 4. pp. 1-17. doi.org/10.3389/feart.2016.00004.

Schaefer, J. M., Putnam, A. E., Denton, G. H., Kaplan, M. R., Birkel, S., Doughty, A. M., Kelley, S., Barrell, D. J. A., Finkel, R. C., Winckler, G., Anderson, R. F., Ninneman, U. S., Barker, S., Schwartz, R., and Schl ¨ uchter, C. (2015). The Southern Glacial Maximum 65000 years ago and its Unfinished Termination. Quaternary Science Reviews. Vol. 114, pp. 52-60. doi.org/10.1016/j.quascirev.2015.02.009.

Schildgen, T. F., Phillips, W. M. and Purves, R. S. (2005). Simulation of snow shielding corrections for cosmogenic nuclide surface exposure studies. Geomorphology, 64, pp.67-85. doi.org/10.1016/j.geomorph.2004.05.003.

Schmid, M. O., Baral, P., Gruber, S., Shahi, S., Shrestha, T., Stumm, D., and Wester, P. (2015). Assessment of permafrost distribution maps in the Hindu Kush Himalayan region using rock glaciers mapped in Google Earth. The Cryosphere, 9, 2089–2099. doi.org/10.5194/tc-9-2089-2015.

Seijmonsbergen, A. C. (2013). The Modern Geomorphological Map, Editor(s): John F. Shroder, Treatise on Geomorphology, Academic Press, 2013, pp. 35-52. doi.org/10.1016/B978-0-12-374739-6.00371-7.

Schmittner, A., Saenko, O. A., and Weaver, A. J. (2003). Coupling of the hemispheres in observations and simulations of glacial climate change, Quaternary Science Reviews, Vol. 22, pp. 659-671, doi.org/10.1016/S0277-3791(02)00184-1.

Shulmeister, J., Thackray, G., Rieser, U., Hyatt, O., Rother, H., Smart, C., and Evans, D. (2010). The stratigraphy, timing and climatic implications of glaciolacustrine deposits in the middle Rakaia Valley, South Island, New Zealand. Quaternary Science Reviews, 29(17):2362–2381. doi.org/10.1016/j.quascirev.2010.06.004.

Shulmeister, J. Fink, D. Winkler, S. Thackray, G. D. Borsellino, R. Hemmingsen, M. and Rittenour, T. M. (2018a). Evidence for slow late-glacial ice retreat in the upper Rangitata Valley, South Island, New Zealand, Quaternary Science Reviews, Vol. 185, pp. 102-112. doi.org/10.1016/j.quascirev.2018.01.006.

Shulmeister, J., Thackray, G. D., Rittenour, T., and Hyatt, O. M. (2018b). Multiple glacial advances in the Rangitata Valley, South Island, New Zealand, during the last glaciation imply substantial extent and duration of MIS 3 glaciation. Quaternary Research. 89, 375-393, doi:10.1017/qua.2017.108.

Siegenthaler, U., Stocker, T. F., Monnin, E., L¨ uthi, D., Schwander, J., Stauffer, B., Raynaud, D., Barnola, J.-M., Fischer, H., Masson Delmotte, V., et al. (2005). Stable carbon cycle–

climate relationship during the late Pleistocene. Science, 310(5752):1313–1317. doi:10.1126/science.1120130.

Sime, L. C., Kohfeld, K. E., Le Quéré, C., Wolff, E. W., de Boer, A. M., Graham, R. M., and Bopp, L. (2013). Southern Hemisphere westerly wind changes during the Last Glacial Maximum: model-data comparison. Quaternary Science Reviews, 64, 104-120. Doi: doi.org/10.1016/j.quascirev.2012.12.008.

Soteres, R. L., Peltier, C., Kaplan, M. R., and Sagredo, E. A. (2020). Glacial geomorphology of the Strait of Magellan ice lobe, southernmost Patagonia, South America. Journal of Maps, 16(2), 299–312. doi.org/10.1080/17445647.2020.1736197.

Soteres, R.L., Sagredo, E.A., Kaplan, M.R. Martini, M. A., Moreno, P. I., Reynhout, S. A., Schwartz, R., and Schaefer, J. M. (2022). Glacier fluctuations in the northern Patagonian Andes (44°S) imply wind-modulated interhemispheric in-phase climate shifts during Termination 1. Sci Rep 12, 10842. doi.org/10.1038/s41598-022-14921-4.

Stenni, B., Buiron, D., Frezzotti, M., Albani, S., Barbante, C., Bard, E., Barnola, J. M., Baroni, M., Baumgartner, M., Bonazza, M., Capron, E., Castellano, E., Chappellaz, J., Delmonte, B., Falourd, S., Genoni, L., Iacumin, P., Jouzel, J., Kipfstuhl, S., Landais, A., Lemieux-Dudon, B., Maggi, V., Masson-Delmotte, V., Mazzola, C., Minster, B., Montagnat, M., Mulvaney, R., Narcisi, B., Oerter, H., Parrenin, F., Petit, J. R., Ritz, C., Scarchilli, C., Schilt, A., Sch´upbach, S., Schwander, J., Selmo, E., Severi, M., Stocker, T. F., and Udisti, R. (2011). Expression of the bipolar seesaw in Antarctic climate records during the last deglaciation, Nat. Geosci., 4, 46–49, doi:10.1038/ngeo1026.

Stocker, T. F. and Johnsen, S. J. (2003). A minimum thermodynamic model for the bipolar seesaw, Paleoceanography, 18, 1087, doi:10.1029/2003PA000920.

Stone, J. (2000). Air pressure and cosmogenic isotope production. Journal of Geophysical Research. Solid Earth, Vol. 105. NO. B10, 23,753-23,759. doi.org/10.1029/2000JB900181.

Strand, P. D. Schaefer, J. M., Putnam, A. E., Denton, G. H., Barrell, D. J. A., Koffman, T. N. B. and Schwartz, R. (2019). Millennial-scale pulsebeat of glaciation in the Southern Alps of New Zealand. Vol. 220, pp.165-177. doi.org/10.1016/j.quascirev.2019.07.022.

Suggate, R. P. (1965). Late Pleistocene geology of the northern part of the South Island, New Zealand. N.Z. Geological Survey Bulletin, n.s. 77.

Suggate, R. P. (1990). Pliocene and Pleistocene glaciations of New Zealand. Quaternary Science Reviews 9:175–198. doi.org/10.1016/0277-3791(90)90017-5.

Suggate, R. P. (2004). South Island, New Zealand: ice advances and marine shorelines. In: Ehlers, J., Gibbard, P. L. (Eds.), Quaternary Glaciations—Extent and Chronology, Part III. Elsevier, Amsterdam, pp. 285–291. doi.org/10.1016/S1571-0866(04)80134-9.

Suggate, R. P., and Almond, P. C. (2005). The Last Glacial Maximum (LGM) in western South Island, New Zealand: implications for the global LGM and MIS 2. Quaternary Science Reviews 24: 1923-1940. doi.org/10.1016/j.quascirev.2004.11.007.

Sutherland, R., Kim, K., Zondervan, A. and McSaveney, M. (2007). Orbital forcing of mid-latitude Southern Hemisphere glaciation since 100 ka inferred from cosmogenic nuclide ages of moraine boulders from the Cascade Plateau, southwest New Zealand. Geological Society of America Bulletin, 119(3-4), pp.443-451. doi.org/10.1130/B25852.1.

Sutherland, J. L., Carrivick, J. L., Evans, D. J.A., Shulmeister, J., and Quincey, D. J. (2019a). The Tekapo Glacier, New Zealand, during the Last Glacial Maximum: An active temperate glacier influenced by intermittent surge activity. Vol. 343, pp. 183-210, doi.org/10.1016/j.geomorph.2019.07.008.

Sutherland, J. L., Carrivick, J. L., Shulmeister, J., Quincey, D. J. and James, W. H. M. (2019b). Ice-contact proglacial lakes associated with the Last Glacial Maximum across the Southern Alps, New Zealand, Quaternary Science Reviews, Vol. 213, pp. 67-92, doi.org/10.1016/j.quascirev.2019.03.035.

Tait, A. and Macara, G. (2014). Evaluation of interpolated daily temperature data for high elevation areas in New Zealand. Weather and Climate, Vol. 34. pp. 36-49. doi.org/10.2307/26169743.

Thomas, A. M. (2018). Glacio-lacustrine sedimentation in newly discovered paleo-lakes, Westland, New Zealand. Unpublished M.Sc. thesis. Victoria University of Wellington, New Zealand. http://hdl.handle.net/10063/7827.

Tielidze L. G., and Wheate, R. D. (2018). The greater Caucasus glacier inventory (Russia, Georgia and Azerbaijan). Cryosphere, 12, pp. 81-94, doi.org/10.5194/tc-12-81-2018.

Tielidze L. G., Eaves S. R., Norton, K. P., and Mackintosh A. N. (2021). Glacial geomorphology of the Ahuriri River valley, central Southern Alps, New Zealand, Journal of Maps, 17:2, 73-86, doi:10.1080/17445647.2021.1876777.

Tielidze, L., Eaves, S., Norton, K., Mackintosh, A. and Hidy, A. (2022). Cosmogenic ^{10}Be constraints on deglacial snowline rise in the Southern Alps, New Zealand. Quaternary Science Reviews. doi.org/10.1016/j.quascirev.2022.107548.

Tielidze L. G., Eaves S. R., Norton, K. P., Mackintosh A. N. Pedro, J. B., and Hidy, A. J. (2022). Early glacier advance in New Zealand during the Antarctic Cold Reversal. Journal of Quaternary Science. Accepted for final publication.

Tierney, J. E., Poulsen, C. J., Montañez, I. P., Bhattacharya, T., Feng, R., Ford, H. L., Hönisch, B., Inglis, G. N., Petersen, S. V., Sagoo, N., Tabor, C. R., Thirumalai, K., Zhu, J., Burls, N. J., Foster, G. L., Goddéris, Y., Huber, B. T., Ivany, L. C., Turner, S. K., Lunt, D. J., McElwain, J. C., Mills, B. J. W., Otto-Bliesner, B. L., Ridgwell, A., and Zhang, Y. G. (2020). Past climates inform our future. Science, Vol 370, Issue 6517. doi:10.1126/science.aay3701.

Turnbull, I. M. (compiler) 2000: Geology of the Wakatipu area: scale 1:250,000. Lower Hutt: Institute of Geological & Nuclear Sciences. Institute of Geological & Nuclear Sciences 1:250,000 geological map 18. 72 p. + 1 folded map.

Turney, C. S. M., McGlone, M. S., and Wilmshurst, J. M. (2003). Asynchronous climate change between New Zealand and the North Atlantic during the last deglaciation. Geology 31, 223.226. doi.org/10.1130/0091-7613(2003)031<0223:ACCBNZ>2.0.CO;2.

Wagner, T., Pleschberger, R., Kainz, S., Ribis, M., Kellerer-Pirklbauer, A., Krainer, K., Philippitsch, R., and Winkler, G. (2020). The first consistent inventory of rock glaciers and their hydrological catchments of the Austrian Alps, Austrian Journal of Earth Sciences, 113(1), 1-23. doi:doi.org/10.17738/ajes.2020.0001.

Wallace, S. 2001. Mapping glacial landforms in the Pukaki and Tekapo Lake basins. Unpublished PGDipSci dissertation, in Geography, at the University of Otago, New Zealand.

Whitehouse, I. E. (1988). Geomorphology of the central Southern Alps, New Zealand: the interaction of plate collision and atmospheric circulation. Zeitschrift für Geomorphologie 69:105–116.

Williams, P. W. (1991). Tectonic geomorphology, uplift rates and geomorphic response in New Zealand. CATENA. Vol. 18, Issue 5, pp. 439-452. doi.org/10.1016/0341-8162(91)90048-3.

Wittmeier, H. E., Schaefer, J. M., Bakke, J., Rupper, S., Paasche, Ø. Schwartz, R., Finkel, R. C. (2020). Late Glacial mountain glacier culmination in Arctic Norway prior to the Younger Dryas, Quaternary Science Reviews, Vol. 245, 106461, doi.org/10.1016/j.quascirev.2020.106461.

Vandergoes, M. J., Dieffenbacher Krall, A. C., Newnham, R. M., Denton, G. H., and Blaauw, M. (2008). Cooling and changing seasonality in the southern Alps, New Zealand during the

Antarctic cold reversal. Quaternary Science Reviews, 27(5):589–601. doi.org/10.1016/j.quascirev.2007.11.015.

von Blanckenburg, F., Hewawasam, T., and Kubik, P. W. (2004). Cosmogenic nuclide evidence for low weathering and denudation in the wet, tropical highlands of Sri Lanka, J. Geophys. Res., 109, F03008, doi:10.1029/2003JF000049.

von Blanckenburg, F. and Willenbring, J., K. (2014). Cosmogenic Nuclides: Dates and Rates of Earth-Surface Change. Elements; 10 (5): 341–346. doi.org/10.2113/gselements.10.5.341.

WAIS Divide Project Members. (2013). Onset of deglacial warming in West Antarctica driven by local orbital forcing. Nature 500, 440–444. doi.org/10.1038/nature12376.

Whittaker, T. E., Hendy, C. H., and Hellstrom, J. C. (2011). Abrupt millennial-scale changes in intensity of Southern Hemisphere westerly winds during marine isotope stages 2–4. Geology 2011; 39 (5): 455–458. doi.org/10.1130/G31827.1.

Yan, Y., Bender, M. L., Brook, E. J., Clifford, H. M., Kemeny, P. C., Kurbatov, A. V., Mackay, S., Mayewski, P. A., Ng, J., Severinghaus, J. P., and Higgins, J. A. (2019). Two-million-year-old snapshots of atmospheric gases from Antarctic ice. Nature 574, 663–666. doi.org/10.1038/s41586-019-1692-3.

Supplement

The exact data blocks that were entered into the online calculator for age calculation

Table S1. Moraine belt-3 (outer) (44°24'36"S, 169°40'25"E).

AL-19-18	-44.409645	169.678879	756.702	std	1.94	2.7	0.990779	0	2019;
AL-19-20	-44.410053	169.677258	758.623	std	2.00	2.7	0.998955	0	2019;
AL-19-21	-44.410519	169.677116	758.52	std	2.29	2.7	0.998955	0	2019;
AL-19-27	-44.41137	169.67104	761.423	std	2.66	2.7	0.998955	0	2019;
AL-19-28	-44.41184	169.67271	757.434	std	4.27	2.7	0.998955	0	2019;
AL-20-29	-44.41072	169.68034	753.255	std	2.12	2.7	0.998955	0	2019;
AL-20-33	-44.41117	169.67877	761.859	std	2.04	2.7	0.974704	0	2019;
AL-20-37	-44.41179	169.67583	754.543	std	2.85	2.7	0.998955	0	2019;
AL-20-39	-44.41282	169.67349	755.554	std	2.34	2.7	0.99868	0	2019;
AL-20-40	-44.41389	169.6703	757.739	std	2.64	2.7	0.998955	0	2019;
AL-20-41	-44.41443	169.6712	752.659	std	2.10	2.7	0.976371	0	2019;

AL-19-18	Be-10	quartz	150774.2844	3320.704595	07KNSTD;
AL-19-20	Be-10	quartz	151541.1593	3904.736521	07KNSTD;
AL-19-21	Be-10	quartz	154896.02	4503.161493	07KNSTD;
AL-19-27	Be-10	quartz	147683.1506	3342.568996	07KNSTD;
AL-19-28	Be-10	quartz	149495.7997	3713.529839	07KNSTD;
AL-20-29	Be-10	quartz	150469.5717	3433.215923	07KNSTD;
AL-20-33	Be-10	quartz	150702.9519	3638.537977	07KNSTD;
AL-20-37	Be-10	quartz	148572.3649	3465.59781	07KNSTD;
AL-20-39	Be-10	quartz	152072.3696	3470.500118	07KNSTD;
AL-20-40	Be-10	quartz	148670.1283	3402.753957	07KNSTD;
AL-20-41	Be-10	quartz	145691.9371	3162.660911	07KNSTD;

Table S2. Moraine belt-3 (inner) (44°23'54"S, 169°39'48"E).

AL-26-49	-44.395441	169.666723	773.708	std	2.28	2.7	0.998195	0	2020;
AL-26-53	-44.393977	169.669205	773.839	std	4.05	2.7	0.990586	0	2020;
AL-26-55	-44.393104	169.668986	768.468	std	2.78	2.7	0.993362	0	2020;
AL-26-57	-44.391977	169.666613	764.711	std	2.86	2.7	0.998693	0	2020;
AL-27-59	-44.394375	169.655063	769.395	std	1.72	2.7	0.996929	0	2020;
AL-27-61	-44.395731	169.658087	766.378	std	2.36	2.7	0.998627	0	2020;
AL-27-63	-44.400109	169.657308	766.993	std	2.44	2.7	0.995922	0	2020;
AL-27-64	-44.401301	169.659033	769.03	std	2.53	2.7	0.992318	0	2020;
AL-27-65	-44.401771	169.659769	769.221	std	2.69	2.7	0.998846	0	2020;
AL-27-66	-44.403993	169.659257	773.914	std	2.81	2.7	0.995555	0	2020;
AL-27-68	-44.396934	169.660573	768.123	std	3.77	2.7	0.991419	0	2020;

AL-26-49	Be-10	quartz	158168.4262	3489.457823	07KNSTD;
AL-26-53	Be-10	quartz	155003.6314	3452.235005	07KNSTD;
AL-26-55	Be-10	quartz	153704.2253	3395.678878	07KNSTD;
AL-26-57	Be-10	quartz	161563.8736	3558.92749	07KNSTD;

AL-27-59 Be-10 quartz 157922.6756 3479.784293 07KNSTD;

AL-27-61 Be-10 quartz 136196.3919 3017.087745 07KNSTD;

AL-27-63 Be-10 quartz 148226.2562 3163.21186 07KNSTD;

AL-27-64 Be-10 quartz 158794.6177 3486.357 07KNSTD;

AL-27-65 Be-10 quartz 154453.0576 3487.18959 07KNSTD;

AL-27-66 Be-10 quartz 159370.1512 5238.645501 07KNSTD;

AL-27-68 Be-10 quartz 156929.5717 3544.674768 07KNSTD;

Table S3. Moraine belt-2 (44°21'46"S, 169°38'15"E).

AML-28-102 -44.36261335 169.6379867 737.788 std 1.1 2.7 0.996832 0 2020;

AML-28-103 -44.36285818 169.637718 738.028 std 4.11 2.7 0.994472 0 2020;

AML-28-104 -44.36322871 169.6379153 735.968 std 2.23 2.7 0.994472 0 2020;

AML-28-105 -44.36304369 169.6371831 730.683 std 2.57 2.7 0.992993 0 2020;

AML-28-106 -44.36249735 169.6370826 727.313 std 2.96 2.7 0.997196 0 2020;

AML-28-102 Be-10 quartz 85528.18912 2411.028972 07KNSTD;

AML-28-103 Be-10 quartz 89619.30817 3661.786942 07KNSTD;

AML-28-104 Be-10 quartz 79489.59312 2139.706487 07KNSTD;

AML-28-105 Be-10 quartz 72247.33249 2076.958293 07KNSTD;

AML-28-106 Be-10 quartz 78190.41683 2740.857019 07KNSTD;

Table S4. Moraine belt-1 (44°15'44"S, 169°36'41"E).

AM-17-01 -44.264579 169.605771 774.896 std 1.12 2.7 0.927932 0 2019;

AM-18-11 -44.241326 169.614783 800.328 std 1.43 2.7 0.984798 0 2019;

AM-18-13 -44.239497 169.616435 812.503 std 1.26 2.7 0.986981 0 2019;

AM-18-15 -44.239671 169.619302 862.545 std 0.85 2.7 0.976531 0 2019;

AM-18-16 -44.239705 169.619328 862.854 std 0.93 2.7 0.969833 0 2019;

AM-18-17 -44.25119 169.61516 803.631 std 2.57 2.7 0.979546 0 2019;

AM-17-01 Be-10 quartz 122332.5256 2959.330551 07KNSTD;

AM-18-11 Be-10 quartz 135177.6665 3474.86293 07KNSTD;

AM-18-13 Be-10 quartz 133921.4523 2743.548058 07KNSTD;

AM-18-15 Be-10 quartz 137056.6653 3196.625408 07KNSTD;

AM-18-16 Be-10 quartz 137423.1927 3116.285387 07KNSTD;

AM-18-17 Be-10 quartz 129302.0479 2944.472945 07KNSTD;

Table S5. Moraine belt-1 (44°15'44"S, 169°36'41"E).

AM-18-08b -44.241709 169.614529 798.419 std 1.6 2.7 0.988486 0 2019;

AM-18-09b -44.241693 169.614466 797.685 std 1.59 2.7 0.981724 0 2019;

AM-18-10b -44.241688 169.61446 797.488 std 2.5 2.7 0.944171 0 2019;

AM-18-12b -44.241384 169.614766 799.609 std 1.2 2.7 0.991202 0 2019;

AM-18-14b -44.23724 169.617903 819.969 std 1.31 2.7 0.985638 0 2019;

AM-18-08b Be-10 quartz 130445.8207 2945.569939 07KNSTD;

AM-18-09b Be-10 quartz 127742.9492 2906.679437 07KNSTD;

AM-18-10b Be-10 quartz 126157.4572 2859.26079 07KNSTD;

AM-18-12b Be-10 quartz 131325.5253 2957.158896 07KNSTD;

AM-18-14b Be-10 quartz 134528.2446 3024.874426 07KNSTD;

Table S6. Outer moraine ridge (44°7'57"S, 169°38'34"E).

Z3	-44.13210653	169.6413434	1314.645	std	3.7	2.7	0.941083	0	2020;
Z6	-44.13243034	169.6422272	1287.459	std	1.2	2.7	0.941901	0	2020;
Z7	-44.13243032	169.6423142	1285.667	std	1.6	2.7	0.946035	0	2020;
Z9	-44.13266613	169.6431523	1263.642	std	2.4	2.7	0.952138	0	2020;
Z3	Be-10 quartz	159530.0028	4094.563927		07KNSTD;				
Z6	Be-10 quartz	157440.2270	4136.369668		07KNSTD;				
Z7	Be-10 quartz	161391.4333	4213.581266		07KNSTD;				
Z9	Be-10 quartz	162148.7655	3750.056461		07KNSTD;				

Table S7. Inner moraine ridge (44°7'55"S, 169°38'30"E).

Z1	-44.13183791	169.6400655	1338.852	std	1.2	2.7	0.943362	0	2020;
Z2	-44.13191951	169.6409091	1323.553	std	3.3	2.7	0.928704	0	2020;
Z4	-44.13227443	169.6422048	1292.165	std	3.9	2.7	0.941555	0	2020;
Z5	-44.13236732	169.6426147	1281.391	std	1.4	2.7	0.948823	0	2020;
Z8	-44.13251268	169.6429465	1269.618	std	2.5	2.7	0.951419	0	2020;
Z10	-44.13242441	169.6432118	1263.392	std	4.5	2.7	0.949802	0	2020;
Z1	Be-10 quartz	158971.7797	3493.236439		07KNSTD;				
Z2	Be-10 quartz	147101.5843	3372.508033		07KNSTD;				
Z4	Be-10 quartz	166519.0768	5114.905851		07KNSTD;				
Z5	Be-10 quartz	156621.4675	3617.311778		07KNSTD;				
Z8	Be-10 quartz	145349.0074	3206.984973		07KNSTD;				
Z10	Be-10 quartz	142741.9832	3403.260027		07KNSTD;				

Table S8. Terminal moraine ridge (44°7'54"S, 169°38'42"E).

U1	-44.13172573	169.6439527	1202.722	std	3.08	2.7	0.938499	0	2020;
U2	-44.13172565	169.6445155	1188.378	std	2.46	2.7	0.946756	0	2020;
U3	-44.13183358	169.6446179	1186.102	std	1.17	2.7	0.946756	0	2020;
U4	-44.13173049	169.6450973	1177.7	std	6.10	2.7	0.952172	0	2020;
U5	-44.13198012	169.6452539	1174.866	std	1.21	2.7	0.952172	0	2020;
U6	-44.13211462	169.6454296	1171.279	std	3.19	2.7	0.955393	0	2020;
U8	-44.1310547	169.6454376	1178.565	std	1.64	2.7	0.952291	0	2020;
U9	-44.13095732	169.6454462	1178.173	std	3.67	2.7	0.951371	0	2020;
U10	-44.13087978	169.6452395	1180.736	std	2.73	2.7	0.952522	0	2020;
U11	-44.13087926	169.6452281	1180.925	std	2.55	2.7	0.952522	0	2020;
U12	-44.13075063	169.6452283	1181.969	std	3.19	2.7	0.952291	0	2020;
U1	Be-10 quartz	126961.6315	3091.246098		07KNSTD;				
U2	Be-10 quartz	129052.3706	3272.558394		07KNSTD;				
U3	Be-10 quartz	128314.3219	2987.835831		07KNSTD;				
U4	Be-10 quartz	124176.5381	3805.951569		07KNSTD;				
U5	Be-10 quartz	133718.0417	3086.313284		07KNSTD;				
U6	Be-10 quartz	128587.0669	3242.734254		07KNSTD;				
U8	Be-10 quartz	111066.3952	2840.678874		07KNSTD;				
U9	Be-10 quartz	122758.8447	3162.310947		07KNSTD;				
U10	Be-10 quartz	128043.6048	3501.132216		07KNSTD;				

U11	Be-10 quartz	129222.1131	3222.518336	07KNSTD;				
U12	Be-10 quartz	19985.03226	1672.926332	07KNSTD;				

Table S9. Riegel-bedrock near the inner terminal moraine ridge (44°7'56''S, 169°38'44''E).

U7	-44.13222567	169.6457674	1162.931	std	7.00	2.7	0.955393	0	2020;
U7	Be-10 quartz	133986.438	4586.864599		07KNSTD;				

Table S10. Canyon Creek bedrock (44°11'22''S, 169°35'28''E).

B1	-44.18607841	169.5932067	1306.73	std	1.84	2.7	0.957296	0	2020;
B2	-44.18628963	169.593209	1307.23	std	2.49	2.7	0.957296	0	2020;
B3	-44.18644085	169.5937835	1313.953	std	2.48	2.7	0.957296	0	2020;
B4	-44.18664003	169.5942687	1317.586	std	1.88	2.7	0.957296	0	2020;
B5	-44.18825448	169.5952064	1353.252	std	2.01	2.7	0.894639	0	2020;
B6	-44.18825448	169.5952064	1353.252	std	2.02	2.7	0.894639	0	2020;
B1	Be-10 quartz	142098.4345	4748.195722		07KNSTD;				
B2	Be-10 quartz	144191.7561	6433.474907		07KNSTD;				
B3	Be-10 quartz	118195.3639	2691.463159		07KNSTD;				
B4	Be-10 quartz	151478.7478	3405.034458		07KNSTD;				
B5	Be-10 quartz	149669.5959	3830.767986		07KNSTD;				
B6	Be-10	quartz	143626.6252		3234.792014		07KNSTD;		

Map of Glacial Geomorphology of the Ahuriri River valley

Glacial Geomorphology of the Ahuriri River Valley, Southern Alps, New Zealand

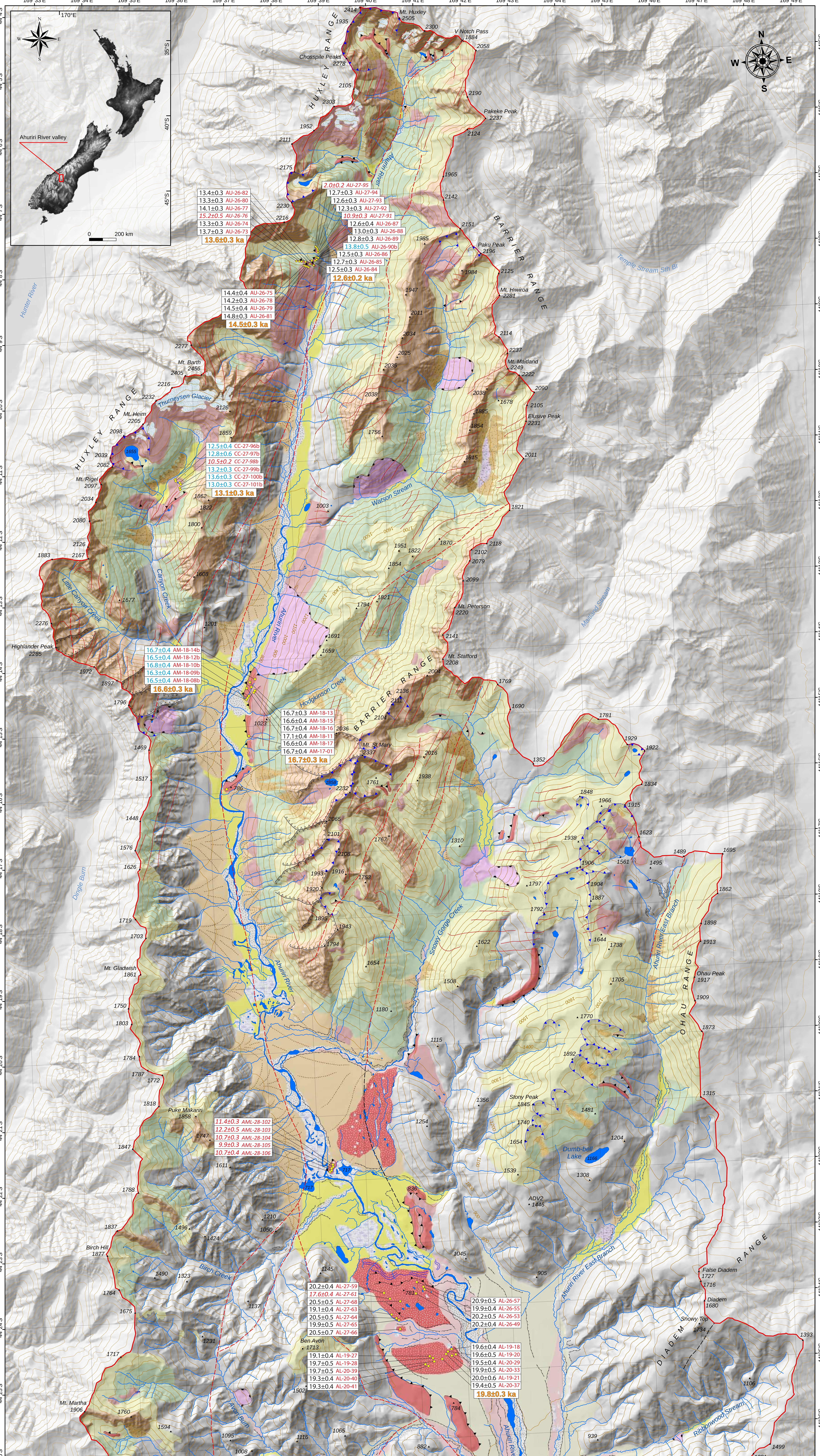

Geomorphological units

Hillslope landform features

- Ice sculpted bedrock surface
- General bedrock terrain
- Steep eroded slope
- Active scree slope
- Vegetated scree slope

Moraine landform features

- Moraine ridge
- Hummocky moraine

Fluvial landform features

- Outwash plain
- Alluvial plain
- Alluvial fan
- Debris cone
- River terrace

Other landforms

- Glacier
- Rock glacier
- Landslide
- Rock avalanche deposit
- Active river plain

Linear features

- Cirque
- Ice contact slope
- Hanging valley
- Palaeo shoreline
- Landslide margin
- Cliff and terrace edge
- Alluvial fan formline
- Active fault
- Inactive fault
- Formline

Water bodies

- Waterfall
- River
- Lake and large river
- Swamp

Topographic features

- Mt. Huxley 2505 — Peak
- 800 — Contour line
- Basin border

^{10}Be exposure ages

20.2±0.4	Age from the boulder	Thousand years old
16.7±0.4	Age from the bedrock	
11.4±0.3	Outlier age	
13.6±0.3	Summary age	
AL-27-59	Sample name	
	Sample location	

0 2 km

0 2 mi

Map scale 1: 38,000 when displayed as ISO A0 size
Coordinate system: GSC_NZGD_2000
Projection: New Zealand Transverse Mercator 2000

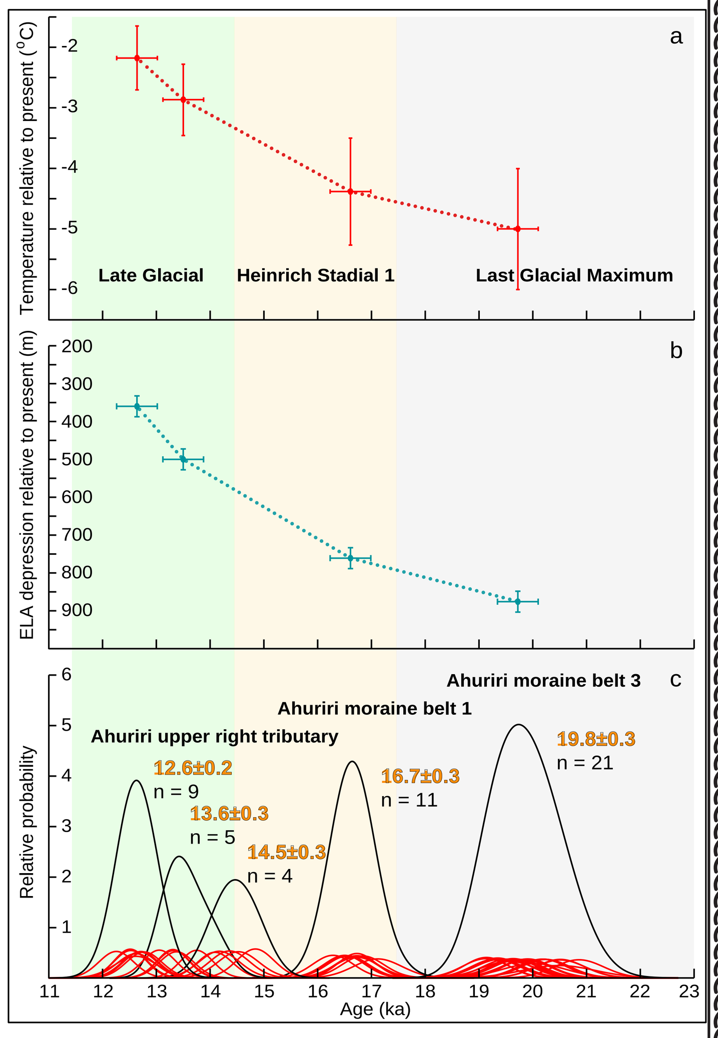

Glacier-based temperature reconstruction from the Ahuriri River valley from 19.8 to 12.6 ka (a). Equilibrium Line Altitude (ELA) depression relative to present from 19.8 to 12.6 ka (b). A normal Kernel density plots from the Ahuriri River valley (c).

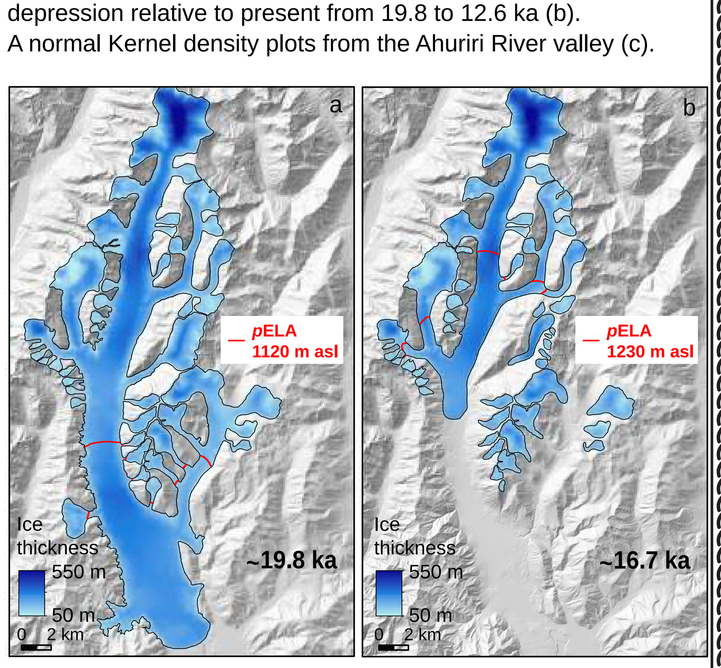

Ahuriri Glacier decrease and palaeo Equilibrium Line Altitude (*p*ELA) increase between ~19.8 (a) and ~16.7 ka (b).

This work was supported by Victoria University of Wellington (Doctoral Scholarship) and Marsden Fund - Royal Society of New Zealand (E3230).

Levan Tielidze[1,2], Shaun Eaves[1,2], Kevin Norton[2], Andrew Mackintosh[3]

[1] *Antarctic Research Centre, Victoria University of Wellington, Wellington, New Zealand*
[2] *School of Geography, Environmental and Earth Sciences, Victoria University of Wellington, Wellington, New Zealand*
[3] *School of Earth, Atmosphere and Evironment, Monash University, Melbourne, Australia*

Correspondence: *TielidzeLevan@gmail.com*